

**Fluid Phase Thermodynamics: I) Nucleate Pool Boiling of Oxygen  
Under Magnetically Enhanced Gravity and II) Superconducting  
Cavity Resonators for High-Stability Frequency References and  
Precision Density Measurements of Helium-4 Gas**

Thesis by  
Theodore Allen Corcovilos

In Partial Fulfillment of the Requirements  
for the Degree of  
Doctor of Philosophy



California Institute of Technology  
Pasadena, California

2008

(Defended June 11, 2007)

©2008

Theodore Allen Corcovilos

All Rights Reserved

## Acknowledgements

Coffee just wasn't strong enough to defend itself.

---

Tom Waits,  
intro to "Eggs and Sausage"\*

**W**HEN you've been in school as long as I have, a lot of people deserve credit when you finally graduate. First, I'd like to thank my parents and my sister for keeping me going all along the way, and my grandparents.

I'd like to thank Nai-Chang Yeh for giving me the research opportunities and providing encouragement when things in the lab got difficult. Don Strayer and Nils Asplund were great helps to me; most graduate students learn lab skills from senior grad students and postdocs, but I was fortunate to work side by side with these two expert researchers and learn the tools of my trade from them. Thanks to the rest of the Yeh Group members, past and present, for all of their help along the way.

The next group I'd like to acknowledge is all of my teachers; they encouraged my curiosity, and I'm at Caltech because of them. From Maryville High School I thank Linda Best, John Roop, Cynthia Freeman, Barbara Inscho, John Smith, and Tom Delozier; and from the University of Tennessee: Al Sanders, Jim Parks, Soren Sorensen, the rest of the Physics Department faculty, Raj Pal Soni and the late Jack Reese. Thanks also to THE PRIDE OF THE SOUTHLAND BAND.

Thanks, too, to my friends from back home who keep me grounded and my spirits high: Don McMahon, Frederick Grim, Greg Grim, and Brandon and Karoline Berg, and to my many friends here, especially Tim Best, Neal Oldham and Ushma Shukla, Matt Matuszewski, Meg Wessling, and Micol Christopher, and to Jason, Dave, Steve, Gretchen, and the rest of the poker gang. Thanks to my outstanding roommates over my stay here: Benjamin Lev, James Petersson, Greg Drummond, Jonathan Hart, Ali Husain, and Jonathan Owen; men of quality, all. Thanks especially to Janet Sheung, for making me smile.

I couldn't have kept sane without some nonscience outlets. Thanks to Bill Bing and the Caltech-Occidental Concert Band for giving me the chance to play my horn, make some music, and make some friends. And just to keep things balanced, I must also thank the guys of the Caltech Rugby Football Club; there's nothing like being on the bottom of a ruck to straighten out your priorities in life.

Thanks to all of my students. The only way to learn to teach is by doing, and it helps when you have the best students in the world to learn from.

Lastly, I thank coffee.

---

\*T. Waits. In *Nighthawks at the Diner*, Elektra/Asylum Records (1975). Recording number 7559-60620-2, compact disk, track 5.

## Abstract

Although fluids are typically the first systems studied in undergraduate thermodynamics classes, we still have only a rudimentary phenomenological understanding of these systems outside of the classical and equilibrium regimes. Two experiments will be presented. First, we present progress on precise measurements of helium-4 gas at low temperatures (1 K–5 K). We study helium because at low densities it is an approximately ideal gas but at high densities the thermodynamic properties can be predicted by numerical solutions of Schrödinger’s equation. By utilizing the high resolution and stability in frequency of a superconducting microwave cavity resonator we can measure the dielectric constant of helium-4 to parts in  $10^9$ , corresponding to an equivalent resolution in density. These data will be used to calculate the virial coefficients of the helium gas so that we may compare with numerical predictions from the literature. Additionally, our data may allow us to measure Boltzmann’s constant to parts in  $10^8$ , a factor of 100 improvement over previous measurements. This work contains a description of the nearly-completed apparatus and the methods of operation and data analysis for this experiment. Data will be taken by future researchers.

The second experiment discussed is a study of nucleate pool boiling. To date, no adequate quantitative model exists of this everyday phenomenon. In our experiment, we vary one parameter inaccessible to most researchers, gravity, by applying a magnetic force to our test fluid, oxygen. Using this technique, we may apply effective gravities of 0–80 times Earth’s gravitational acceleration ( $g$ ). In this work we present heat transfer data for the boiling of oxygen at one atmosphere ambient pressure for effective gravity values between 1g and 16g. Our data describe two relationships between applied heat flux and temperature differential: at low heat flux the system obeys a power law and at high heat flux the behavior is linear. We find that the transition heat flux between these two regimes scales as the 4th root of the gravitational acceleration, which may indicate a relationship to the critical heat flux. Additionally, we find that the low heat flux power law exponent is independent of gravity and the power law scale coefficient increases linearly with gravity.

# Contents

|   |            |
|---|------------|
| <b>Acknowledgements</b>   | <b>iii</b> |
| <b>Abstract</b>   | <b>iv</b>  |
| <b>Contents</b>   | <b>v</b>   |
| <b>List of Figures</b>  | <b>xi</b>  |
| <b>List of Tables</b>   | <b>xiv</b> |
| <b>1 Introduction</b>   | <b>1</b>   |
| 1.1 Part I, Boiling of Oxygen in Enhanced Effective Gravity . . . . .               | 1          |
| 1.2 Part II, Superconducting Cavity Resonators and Measurements of Helium-4 . . . . | 2          |
| 1.2.1 Some Apologetics . . . . .  | 2          |
| Bibliography . . . . .  | 4          |
| <b>I Nucleate Pool Boiling of Oxygen under Enhanced Effective Gravity</b>           | <b>5</b>   |
| <b>Notation for part I</b>  | <b>6</b>   |
| <b>2 Introduction to Part</b>   | <b>9</b>   |
| 2.1 Qualitative Description of Boiling . . . . .                                    | 9          |
| 2.1.1 Equilibrium . . . . .   | 10         |
| 2.1.2 Convection . . . . .  | 14         |
| 2.1.3 Nucleate Boiling . . . . .  | 15         |
| 2.1.4 Transition and Film Boiling . . . . .   | 16         |
| 2.2 Prior Work . . . . .  | 16         |

|          |  |           |
|----------|--|-----------|
| 2.2.1    | Theoretical Work . . . . .                             | 17        |
| 2.2.2    | Recent Experimental Work on General Boiling . . . . .  | 19        |
| 2.2.3    | Experiments at Nonstandard Gravity . . . . .           | 20        |
| 2.3      | This Work . . . . .                                    | 21        |
|          | Bibliography . . . . .                                 | 22        |
| <b>3</b> | <b>Hardware</b>  | <b>25</b> |
| 3.1      | Magnet . . . . .                                       | 25        |
| 3.1.1    | Field Profile . . . . .                                | 25        |
| 3.1.2    | Force Calculations . . . . .                           | 28        |
| 3.2      | Cryogenic Probe . . . . .                              | 30        |
| 3.2.1    | Heater . . . . .                                       | 32        |
| 3.2.2    | Temperature Sensors . . . . .                          | 33        |
| 3.2.3    | Magnetic-Field Sensors . . . . .                       | 34        |
| 3.2.4    | Optics . . . . .                                       | 34        |
| 3.3      | Auxiliary Systems . . . . .                            | 35        |
| 3.3.1    | Vacuum System . . . . .                                | 35        |
| 3.3.2    | Computer Control . . . . .                             | 36        |
|          | Bibliography . . . . .                                 | 38        |
| <b>4</b> | <b>Procedures</b>                                      | <b>39</b> |
| 4.1      | Sample Filling . . . . .                               | 40        |
| 4.2      | Data Collection . . . . .                              | 42        |
| 4.2.1    | Choice of Heater Power Sequence . . . . .              | 42        |
| 4.2.2    | Transient Effects at Boiling Outset . . . . .          | 49        |
|          | Bibliography . . . . .                                 | 50        |
| <b>5</b> | <b>Data</b>  | <b>51</b> |
| 5.1      | Raw Data . . . . .                                     | 51        |
| 5.1.1    | Measurement of the Quiescent Heat Leak . . . . .       | 51        |
| 5.1.2    | Determination of Steady-State Temperatures . . . . .   | 52        |
| 5.1.3    | Relationship between Superheat and Heat Flux . . . . . | 54        |
|          | Bibliography . . . . .                                 | 58        |

|          |  |           |
|----------|--|-----------|
| <b>6</b> | <b>Analysis</b>  | <b>59</b> |
| 6.1      | Gravity-Independent Effects . . . . .                            | 60        |
| 6.1.1    | Comparison with Correlations . . . . .                           | 60        |
| 6.1.2    | High Heat-Flux Behavior . . . . .                                | 63        |
| 6.2      | Gravity Dependence . . . . .                                     | 65        |
| 6.2.1    | Comparison with Empirical Correlations . . . . .                 | 66        |
| 6.2.2    | Comparison with Other Experiments . . . . .                      | 68        |
|          | Bibliography . . . . .   | 69        |
| <b>7</b> | <b>Conclusion to Part I</b>                                      | <b>71</b> |
| 7.1      | Summary . . . . .  | 71        |
| 7.2      | Suggestions for Future Work . . . . .                            | 72        |
| 7.2.1    | Expanding the Oxygen Boiling Investigation . . . . .             | 72        |
| 7.2.2    | Applying the Magnetic Force Technique to Other Systems . . . . . | 73        |
| 7.3      | Acknowledgments . . . . .  | 74        |
|          | Bibliography . . . . .   | 75        |
|          | <b>Appendices to Part I</b>                                      | <b>76</b> |
| <b>A</b> | <b>Calibration Procedure for Temperature Sensors</b>             | <b>77</b> |
|          | Bibliography . . . . .   | 79        |
| <b>B</b> | <b>Oxygen Experiment Data</b>                                    | <b>80</b> |
| B.1      | Oxygen Data Run Parameters . . . . .                             | 80        |
| B.2      | Steady-State Temperature Data . . . . .                          | 81        |
| B.3      | Plots and Fits . . . . .   | 86        |
| <b>C</b> | <b>Miscellaneous Derivations from the Boiling Experiment</b>     | <b>96</b> |
| C.1      | Explicit Expressions for the Magnetic Field . . . . .            | 96        |
| C.2      | Oxygen Experiment Uncertainty Derivations . . . . .              | 98        |
|          | Bibliography . . . . .   | 101       |

|   |            |
|---|------------|
| <b>II Superconducting Cavities and Measurements of Helium-4</b> | <b>102</b> |
| Notation for part II  | 103        |
| <b>8 Introduction to Superconducting Cavity Resonators</b>      | <b>108</b> |
| 8.1 Electromagnetic Resonant Cavities . . . . .                 | 109        |
| 8.2 Properties of Superconducting Cavities . . . . .            | 110        |
| 8.2.1 Resonance Mode Characterization . . . . .                 | 110        |
| 8.2.2 Limits on Frequency Stability . . . . .                   | 112        |
| 8.2.3 Phase-Locked Loop . . . . .                               | 113        |
| 8.2.4 Allan Variance . . . . .                                  | 116        |
| 8.3 Frequency Standards . . . . .                               | 117        |
| Bibliography . . . . .  | 120        |
| <b>9 Hardware</b>   | <b>122</b> |
| 9.1 Superconducting Cavities . . . . .                          | 122        |
| 9.1.1 Physical Properties . . . . .                             | 122        |
| 9.1.2 Expected Frequency Fluctuations . . . . .                 | 125        |
| 9.1.3 Processing and Handling . . . . .                         | 125        |
| 9.1.4 Annealing . . . . .                                       | 127        |
| 9.2 Cryogenic System . . . . .                                  | 129        |
| 9.2.1 Temperature Control . . . . .                             | 129        |
| 9.2.2 Additions for Helium Measurements . . . . .               | 134        |
| 9.3 Microwave System . . . . .                                  | 135        |
| 9.3.1 Transmission Spectroscopy . . . . .                       | 135        |
| 9.3.2 Phase-Locked Loop System . . . . .                        | 137        |
| 9.4 Auxiliary Systems . . . . .                                 | 141        |
| 9.4.1 Acoustic Noise Abatement . . . . .                        | 141        |
| 9.4.2 Computer Control and Software . . . . .                   | 141        |
| Bibliography . . . . .  | 142        |
| <b>10 Data for Superconducting Cavities</b>                     | <b>143</b> |
| 10.1 Cavity Characterization . . . . .                          | 143        |

|           |   |            |
|-----------|---|------------|
| 10.2      | Frequency Stability . . . . .                             | 144        |
| 10.2.1    | Single Mode . . . . .                                     | 145        |
| 10.2.2    | Dual Mode . . . . .                                       | 145        |
| 10.3      | Environmental Noise Sources . . . . .                     | 146        |
|           | Bibliography . . . . .                                    | 150        |
| <b>11</b> | <b>Thermodynamic Measurements of Helium</b>               | <b>151</b> |
| 11.1      | General Properties of Helium-4 . . . . .                  | 153        |
| 11.2      | Equations of State . . . . .                              | 153        |
| 11.2.1    | Ideal Gas Law . . . . .                                   | 153        |
| 11.2.2    | Virial Equation . . . . .                                 | 153        |
| 11.2.3    | Theoretical Equations of State . . . . .                  | 156        |
| 11.3      | Dielectric Constant–Density Relations . . . . .           | 158        |
| 11.4      | Dielectric Constant Gas Thermometry . . . . .             | 158        |
| 11.5      | Virial Coefficients . . . . .                             | 160        |
| 11.6      | Boltzmann Constant . . . . .                              | 161        |
|           | Bibliography . . . . .                                    | 163        |
| <b>12</b> | <b>Analysis and Preliminary Results</b>                   | <b>165</b> |
| 12.1      | Perturbation Theory on the EM Wave Equation . . . . .     | 165        |
| 12.1.1    | Unperturbed Solution . . . . .                            | 167        |
| 12.1.2    | First-Order Perturbation . . . . .                        | 167        |
| 12.1.3    | Second-Order Perturbation . . . . .                       | 170        |
| 12.2      | Gravity Effect on the Local Dielectric Constant . . . . . | 171        |
| 12.2.1    | Dead-Space Correction to Density . . . . .                | 172        |
| 12.2.2    | Liquid Phases . . . . .                                   | 176        |
| 12.3      | Equation of State Uncertainties . . . . .                 | 177        |
| 12.4      | Proof-of-Concept Data . . . . .                           | 178        |
|           | Bibliography . . . . .                                    | 181        |
| <b>13</b> | <b>Future Work and Conclusions</b>                        | <b>183</b> |
| 13.1      | Frequency Stability Measurements . . . . .                | 183        |
| 13.2      | Gas-Phase Measurements . . . . .                          | 183        |

|                              |  |            |
|------------------------------|--|------------|
| 13.2.1                       | Unsaturated Vapor . . . . .                                  | 183        |
| 13.2.2                       | Saturated Vapor Curve . . . . .                              | 185        |
| 13.3                         | Conclusions . . . . .  | 186        |
|                              | Bibliography . . . . .                                       | 187        |
| <b>Appendices to Part II</b> |  | <b>188</b> |
| <b>D</b>                     | <b>Miscellaneous Constructions for the Helium Experiment</b> | <b>189</b> |
| D.1                          | Low Temperature Vacuum Feedthroughs . . . . .                | 189        |
| D.2                          | Quarter-Wavelength Microwave Heat Sinks . . . . .            | 191        |
| D.3                          | Superconducting Coax Loops . . . . .                         | 193        |
|                              | Bibliography . . . . .                                       | 195        |
| <b>14</b>                    | <b>Concluding Remarks</b>                                    | <b>196</b> |
|                              | Bibliography . . . . .                                       | 198        |

## List of Figures

|     |  |    |
|-----|--|----|
| 2.1 | Qualitative boiling curve . . . . .                              | 10 |
| 2.2 | Equilibrium phase diagram of oxygen in $P$ - $T$ plane . . . . . | 11 |
| 2.3 | Equilibrium phase diagram of oxygen in $P$ - $V$ plane . . . . . | 12 |
| 3.1 | Magnetic field of the solenoid. . . . .                          | 27 |
| 3.2 | Magnetic acceleration of the solenoid. . . . .                   | 29 |
| 3.3 | Oxygen probe schematic . . . . .                                 | 31 |
| 3.4 | Borescope schematic . . . . .                                    | 35 |
| 3.5 | Oxygen experiment controls . . . . .                             | 37 |
| 4.1 | Oxygen sample filling . . . . .                                  | 41 |
| 4.2 | Typical data run . . . . .                                       | 43 |
| 4.3 | Hysteresis between convection and boiling modes . . . . .        | 45 |
| 4.4 | Decreasing “stairstep” sequence . . . . .                        | 46 |
| 4.5 | Increasing “stairstep” sequence . . . . .                        | 47 |
| 4.6 | Constant heater power data . . . . .                             | 48 |
| 5.1 | Example data set with fits . . . . .                             | 53 |
| 5.2 | Fitting parameters . . . . .                                     | 56 |
| 6.1 | Fits to aggregate data sets . . . . .                            | 62 |
| 6.2 | Conjectured boiling curve . . . . .                              | 65 |
| 6.3 | Fitting functions of aggregate fits . . . . .                    | 66 |
| 6.4 | Transition heat flux versus effective gravity . . . . .          | 67 |
| B.1 | Data from 20061103, $g_{\text{eff}} = 1g$ . . . . .              | 87 |
| B.2 | Data from 20061119, $g_{\text{eff}} = 1g$ . . . . .              | 88 |

|      |  |     |
|------|--|-----|
| B.3  | Data from 20070213, $g_{\text{eff}} = 1g$ . . . . .                          | 89  |
| B.4  | Data from 20061213, $g_{\text{eff}} = 6g$ . . . . .                          | 90  |
| B.5  | Data from 20061214, $g_{\text{eff}} = 6g$ . . . . .                          | 91  |
| B.6  | Data from 20070214, $g_{\text{eff}} = 6g$ . . . . .                          | 92  |
| B.7  | Data from 20061216, $g_{\text{eff}} = 16g$ . . . . .                         | 93  |
| B.8  | Data from 20061217, $g_{\text{eff}} = 16g$ . . . . .                         | 94  |
| B.9  | Data from 20070215, $g_{\text{eff}} = 16g$ . . . . .                         | 95  |
| 8.1  | Cartoon schematic of the phase-locked loop . . . . .                         | 115 |
| 8.2  | Phase-locked loop error signal . . . . .                                     | 116 |
| 9.1  | Drawing of the niobium cavity . . . . .                                      | 123 |
| 9.2  | Intrinsic surface resistance and maximum $Q$ of the niobium cavity . . . . . | 127 |
| 9.3  | Schematic of the UHV annealing system, side cutaway view. . . . .            | 128 |
| 9.4  | Schematic of the superconducting cavity probe . . . . .                      | 130 |
| 9.5  | Germanium resistance thermometer readout circuit . . . . .                   | 131 |
| 9.6  | Example temperature data . . . . .   | 133 |
| 9.7  | Temperature-induced frequency fluctuations . . . . .                         | 134 |
| 9.8  | Schematic for transmission spectroscopy of cavity modes. . . . .             | 136 |
| 9.9  | Detailed block diagram of the phase-locked loop . . . . .                    | 139 |
| 10.1 | Example spectrum of the cavity in the $TE_{011}$ mode. . . . .               | 144 |
| 10.2 | Phase-locked loop time series . . . . .                                      | 145 |
| 10.3 | Frequency stability of the 14 GHz mode . . . . .                             | 146 |
| 10.4 | Frequency stability of the dual-mode configuration . . . . .                 | 147 |
| 10.5 | Power spectrum of air conditioner noise . . . . .                            | 148 |
| 11.1 | Helium-4 phase diagram . . . . .   | 152 |
| 11.2 | Temperature dependence of the helium-4 second virial coefficient . . . . .   | 155 |
| 11.3 | Helium interaction potential . . . . .                                       | 157 |
| 12.1 | Gas-induced frequency shift . . . . .  | 169 |
| 12.2 | Sample can drawing . . . . .   | 175 |
| 12.3 | Gravity-induced frequency shift . . . . .                                    | 176 |

|   |     |
|---|-----|
| 12.4 Helium density proof-of-concept data . . . . .       | 180 |
| D.1 Cryogenic vacuum feedthrough . . . . .                | 190 |
| D.2 Quarter-wave heat sink tee . . . . .                  | 191 |
| D.3 Transmission maxima for short-circuit tees . . . . .  | 192 |
| D.4 Construction of superconducting signal loops. . . . . | 194 |

## List of Tables

|      |   |     |
|------|---|-----|
| 2.1  | Thermophysical properties of oxygen and copper . . . . .          | 13  |
| 3.1  | Superconducting magnet specifications . . . . .                   | 26  |
| 5.1  | Fitting parameters . . . . .                                      | 57  |
| 6.1  | Reparametrization of fits . . . . .                               | 61  |
| 6.2  | Values of correlation coefficients . . . . .                      | 61  |
| A.1  | Calibration coefficients for Cernox temperature sensors . . . . . | 78  |
| B.1  | Oxygen data run summary . . . . .                                 | 80  |
| B.2  | Steady-state fits 20061103 . . . . .                              | 81  |
| B.3  | Steady-state fits 20061118 . . . . .                              | 81  |
| B.4  | Steady-state fits 20070213 . . . . .                              | 82  |
| B.5  | Steady-state fits 20061213 . . . . .                              | 82  |
| B.6  | Steady-state fits 20061214 . . . . .                              | 83  |
| B.7  | Steady-state fits 20070214 . . . . .                              | 83  |
| B.8  | Steady-state fits 20061216 . . . . .                              | 84  |
| B.9  | Steady-state fits 20061217 . . . . .                              | 84  |
| B.10 | Steady-state fits 20070215 . . . . .                              | 85  |
| 8.1  | Dependence of the Allan variance on noise type . . . . .          | 117 |
| 9.1  | Properties of niobium . . . . .                                   | 124 |
| 9.2  | Parameters of the superconducting cavity . . . . .                | 125 |
| 9.3  | Sources of resonance frequency fluctuations . . . . .             | 126 |
| 9.4  | Nominal device settings for the phase-locked loop . . . . .       | 140 |

|      |  |     |
|------|--|-----|
| 10.1 | Best measured parameters of the superconducting cavity . . . . .             | 144 |
| 11.1 | Temperature coefficients of the helium-4 second virial coefficient . . . . . | 154 |
| 12.1 | Estimated uncertainties for helium equation of state measurements . . . . .  | 179 |
| 12.2 | Helium density proof-of-concept data . . . . .                               | 180 |
| D.1  | Transmission maxima for short-circuit tees . . . . .                         | 192 |

Dieses vor allem: fragen Sie sich in der stillsten Stunde Ihrer Nacht: *muß* ich schreiben? Graben Sie in sich nach einer tiefen Antwort. Und wenn diese zustimmend lauten sollte, wenn Sie mit einem starken und einfachen *ich muß* dieser ernstesten Frage begegnen dürfen, dann bauen Sie Ihr Leben nach dieser Notwendigkeit.\*

---

Rainer Maria Rilke,  
letter to F. X. Kappus<sup>†</sup>

## Chapter 1

### Introduction

“**E**XPERIMENTAL low-temperature physicist” must surely rank as one of the most complicated jobs in the world. He or she is at various times a plumber, electrician, carpenter, chef, computer programmer, engineer, salesman, accountant, librarian, almost anything but a “scientist”. . . but only a scientist can bring such diverse skills together with the focus, foresight, and fortitude needed to answer the simple but prickly question, “How does the universe work?”

This thesis is my modest attempt to answer this question or, perhaps, show how to properly ask the question within my field of study. The general topic under consideration is the thermodynamics of fluids. Two distinct experiments are discussed, in reverse chronological order. Part I investigates the effect of gravity on boiling dynamics. Part II looks at using high-Q superconducting resonators to precisely measure the density of helium-4 gas. This introductory chapter will conclude with a brief explanation of why there are two experiments.

#### 1.1 Part I, Boiling of Oxygen in Enhanced Effective Gravity

Boiling is a phenomenon taken for granted by most of us when we cook pasta or make tea, but from a scientific viewpoint, little is still known about this complex behavior. Because a boiling system is far from thermodynamic equilibrium and involves a wide range of macro- and microscopic effects, there is little theoretical understanding of the boiling process. What is known

---

\*This above all—ask yourself in the stillest hour of the night: *must* I write? Delve into yourself for a deep answer. And if this should be affirmative, if you may meet this earnest question with a strong and simple *I must* then build your life according to this necessity. (Translation by M. D. Herter Norton [1])

<sup>†</sup>Ref. [2]

about boiling comes from almost a century of empirical studies of various quality. Attempts to condense these data into a phenomenological model have had only modest success.

We approach the problem of boiling by investigating changes in a parameter that has been inaccessible to most researchers: gravity. We study “gravity” by substituting for it a different force: magnetism. By using a superconducting magnet, we apply a magnetic force to a sample of liquid oxygen. We boil the oxygen and measure the heat transport of the boiling liquid for effective gravity values between one and sixteen times the Earth’s gravity.

## **1.2 Part II, Superconducting Cavity Resonators and Their Use for Thermodynamic Measurements of Helium-4**

Frequency measurements are the cornerstone of modern metrology because they can be performed more precisely than any other fundamental measurement. Superconducting cavity microwave resonators are particularly useful for frequency measurements because they can have line widths as fine as one trillionth of their frequency. Coupled with suitable electronics, superconducting cavity resonators can function as precise frequency references with frequency drifts of parts in  $10^{15}$  or less over measurements times of one thousand seconds. We leverage such a system for density measurements of helium-4 gas and develop a method of measuring the equation of state of helium to high precision.

### **1.2.1 Some Apologetics**

Before progressing, the reader should be forewarned that the work presented in part II of the thesis is incomplete, although close to yielding interesting data. Some historical context is appropriate here to help the reader understand why the story of this work ends in a cliffhanger.

Despite the belief of many low temperature physicists, science is not done in a vacuum. Our superconducting cavity experiment was a victim of some real-world circumstances that altered our scientific goals and slowed down the project. As will be related later, the largest source of uncertainty in our helium equation of state measurements is caused by gravity. The only way to overcome this perturbation is to remove gravity by operating the experiment in space. Our original intent was to operate the experiment on the International Space Station (ISS) in the module known as the Low Temperature Physics Facility (LTPF). The LTPF was originally scheduled to

begin operation in 2003 [3].

The LTPF installation experienced several postponements because of lagging construction schedules on the ISS, but these delays were not significant enough to affect our experimental plans. However, the tragic loss of the space shuttle *Columbia* on February 1, 2003 [4] put an indefinite halt to the space station construction. We proceeded with the ground-based phase of our experiments with the hope that the ISS eventually would be completed, even if this occurred after the tenure of the present author. The most immediate change in the project was the shift in emphasis from liquid-phase measurements to gas-phase measurements, where the gravity perturbation is approximately one thousand times smaller. Much of the discussion in following chapters considers the question of how much science can be done in the gas phase with our apparatus.

Unfortunately, the *coup de grâce* for this project came a year later when President George W. Bush ordered the restructuring of NASA to prepare for future human missions to the moon and Mars [5], effectively eliminating NASA's basic research programs and hence our funding. (This shift did, however, provide funding for the boiling experiments described in part I of this thesis.) Although we attempted to secure funding from other sources, ultimately the project stalled. We were not able to complete our intended scientific measurements before our funding expired, so the present work contains feasibility studies and some basic calibration and proof-of-concept measurements using the mostly completed experimental apparatus. At the time of our postponement we had just concluded some infrastructure upgrades to reduce acoustic noise and temperature drifts in the laboratory, but we were unable to finish measurements to determine the effects of these improvements before our money ran out. Our hope is to resume the project at some later date when the funding environment is more favorable. These plans are discussed in the concluding chapter of part II.

## Bibliography

- [1] R. M. Rilke. *Letters to a Young Poet*. New York: Norton (1962). Translated by M. D. Herter Norton.
- [2] R. M. Rilke. Letter to F. X. Kappus (February 17, 1903). <http://www.rilke.de/briefe/170203.htm>.
- [3] U. E. Israelsson and M. C. Lee. “The NASA/JPL program in microgravity fundamental physics.” *Low Temperature Physics*, **24**(2):140–143 (1998). <http://link.aip.org/link/?LTP/24/140/1>.
- [4] H. W. Gehman, Jr., J. L. Barry, D. W. Deal, J. N. Hallock, K. W. Hess, G. S. Hubbard, J. M. Logsdon, et al. *Columbia Accident Investigation Board Report*. Washington: National Aeronautics and Space Administration (2003). <http://caib.nasa.gov>.
- [5] G. W. Bush. “Renewed spirit of discovery.” Speech at NASA headquarters, Washington, DC (January 14, 2004). <http://www.whitehouse.gov/news/releases/2004/01/20040114-3.html>.

**Part I**

**Nucleate Pool Boiling of Oxygen under  
Enhanced Effective Gravity**

## Notation for part I

Notation used in part I. The sections listed indicate the first use of each symbol.

| Notation             | Description   | Section |
|----------------------|---|---------|
| <b>Greek symbols</b> |   |         |
| $\chi$               | Magnetic susceptibility, in SI units  | 3.1     |
| $\chi^2$             | Chi-squared error function  | 5.1     |
| $\kappa$             | Exponential decay coefficient, in inverse seconds   | 5.1     |
| $\kappa_l$           | Thermal diffusivity   | 2.2     |
| $\mu_0$              | Vacuum permeability, $4\pi \times 10^{-7} \text{ NA}^{-2}$  | 3.1     |
| $\rho$               | Mass density  | 3.1     |
| $\sigma$             | Surface tension   | 2.1     |
| $\sigma_{Ts}$        | Uncertainty in steady-state temperature   | 5.1     |
| $\tau$               | Elapsed time  | 5.1     |
| $\tau_0$             | Elapsed time at which the heater power changes  | 5.1     |
| <b>Roman symbols</b> |   |         |
| $A$                  | Surface area of the heater, $16.6 \text{ cm}^2$   | 5.1     |
| $a$                  | Acceleration  | 3.1     |
| $a$                  | Effective length of the solenoid, in meters; a fitting parameter in the magnetic field expression | 3.1     |
| $a$                  | Fitting parameter from equation (5.3): the scale parameter for the power law                      | 5.1     |
| $B$                  | Magnetic field, in tesla  | 3.1     |

| <b>Notation</b>  | <b>Description</b>  | <b>Section</b> |
|------------------|---|----------------|
| $b$              | Effective radius of the solenoid, in meters; a fitting parameter in the magnetic field expression | 3.1            |
| $b$              | Fitting parameter from equation (5.3): the exponent for the power law                             | 5.1            |
| $C$              | Scale factor in the magnetic field expression   | 3.1            |
| $C_s$            | Rohsenow coefficient  | 2.2            |
| $c$              | Fitting parameter from equation (5.3): the constant term in the linear function                   | 5.1            |
| $D_d$            | Bubble diameter   | 2.2            |
| $g$              | Gravitational acceleration at Earth's surface, 9.8 m/s <sup>2</sup>                               | 2.2            |
| $g_{\text{eff}}$ | Effective net gravity   | 5.1            |
| $h_{lg}$         | Latent heat per unit mass   | 2.1            |
| $I$              | Magnet current, in amperes  | 3.1            |
| $K$              | Exponential scale coefficient, in kelvin  | 5.1            |
| $L$              | Length of quarter-wave heat sink stub   | D.2            |
| $M$              | Molecular mass  | 2.2            |
| $m$              | Fitting parameter from equation (5.3): the slope in the linear function                           | 5.1            |
| $m$              | Mass  | 3.1            |
| $n$              | Rohsenow exponent   | 2.2            |

| Notation         | Description  | Section |
|------------------|--|---------|
| $P$              | Pressure   | 2.1     |
| $P_{\text{sat}}$ | Saturation pressure  | 2.1     |
| $Q$              | Heater power   | 5.1     |
| $Q_0$            | Quiescent heater power   | 5.1     |
| $q$              | Heat flux (power per unit area)  | 2.1     |
| $q_t$            | Fitting parameter from equation (5.3): the transition heat flux between power-law and linear regions | 5.1     |
| $R$              | Heater surface roughness   | 2.2     |
| $r$              | Radial position inside the solenoid, in meters   | 3.1     |
| $T$              | Temperature  | 2.1     |
| $T_{\text{sat}}$ | Saturation temperature   | 2.1     |
| $T_s$            | Quasi-static temperature   | 5.1     |
| $\Delta T$       | Superheat  | 2.1     |
| $t$              | Reduced superheat: $t = (T/T_b) - 1$   | 5.1     |
| $U$              | Potential energy   | 3.1     |
| $V$              | Volume   | 2.1     |
| $X_n$            | Dimensionless quantity   | 2.2     |
| $z$              | Axial position inside the solenoid, in meters  | 3.1     |

... the order in creation which you see is that which you have put there, like a string in a maze, so that you shall not lose your way. For existence has its own order and that no man's mind can compass, that mind itself being but a fact among others.

---

Cormac McCarthy, *Blood Meridian*\*

## Chapter 2

### Introduction to Part I

**N**UCLEATE pool boiling is one of the enduring problems in fluid mechanics and thermal physics. The large number of physical variables, many of them not directly measurable or controllable, and the difficulty in reproducing exact experimental conditions have thwarted attempts at constructing an accurate theoretical description, or even phenomenological description, of this everyday process. In an attempt to shed more light on this difficult topic, we have chosen to study the effect of varying one particular parameter which has been inaccessible to most investigators: gravity. Experimentally, we simulate altered gravity conditions by taking advantage of the large magnetic susceptibility of molecular oxygen ( $O_2$ ). By applying a magnetic force to the oxygen we simulate effective gravities between 1 and 16 times the Earth's gravity. In this chapter we briefly review the various behaviors seen in a boiling system and describe previous theoretical and experiment results from the literature.

#### 2.1 Qualitative Description of Boiling

Although no universal quantitative model of boiling behavior exists, qualitatively the boiling process occurs in several possible modes depending on the heater temperature and applied heater power. Either heater temperature or heater power may be controlled in general, although in this experiment the heater power is the control variable. To ease comparison among different experimental systems, these two parameters are usually reexpressed as the superheat and heat flux. The superheat  $\Delta T$  is the difference between the heater temperature  $T$  (which we assume is equal to

---

\*Reference [1]

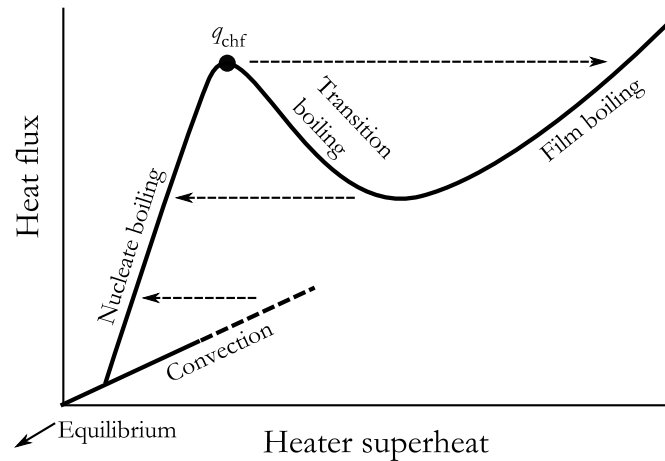


Figure 2.1. Qualitative boiling curve for an arbitrary liquid and heater, adapted from [2] and [3], showing the relationship between applied heat flux and heater superheat, on a log-log scale (solid lines). The labels indicate the various modes of boiling observed along regions of the curve; these modes are described in section 2.1. Irreversible transitions between modes possible when heat flux is used as the control variable are indicated by the dashed arrows. Equilibrium conditions do not appear on this plot but are off scale to the bottom left. The critical heat flux between nucleate and transition boiling is also shown as the point labeled  $q_{\text{CHF}}$ .

the liquid temperature at the heater surface) and the saturation temperature of the liquid  $T_{\text{sat}}$ . The heat flux  $q$  is the ratio of the heater power  $Q$  and the heater surface area  $A$ . The heat-flux–superheat relation of the various modes for a typical system (fluid and heater combination) is depicted in figure 2.1 and discussed in the following section, starting at the low heat flux portion of the curve.

### 2.1.1 Equilibrium

At equilibrium (off of the bottom left of figure 2.1), the liquid and gas phases of the test substance have a common temperature, pressure, and chemical potential. Under equilibrium conditions where the liquid and gas phases coexist, the system is said to be saturated. The pressure-temperature relation under these conditions is known as the saturation curve (see the solid line in figure 2.2), with a one-to-one relationship existing between the saturation pressure ( $P_{\text{sat}}$ ) and the saturation temperature ( $T_{\text{sat}}$ ). The mass density (and its reciprocal, the specific volume) of the saturated substance is dual valued; the high density case yields the liquid phase and the low density case yields the gas phase. The equilibrium phase diagram for oxygen is shown in figures 2.2 and 2.3.

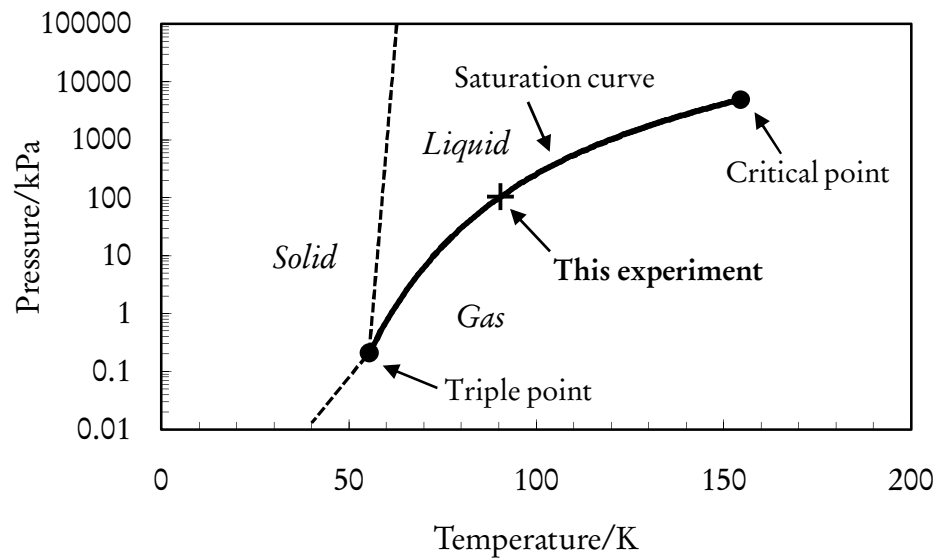


Figure 2.2. Equilibrium phase diagram of oxygen in the pressure-temperature plane. The saturation curve separating the liquid and gas phases is shown by the solid black line, data from [4]. The triple point (54.4 K, 148 Pa) and critical point (155 K, 5.04 MPa) are shown as dots. The beginning equilibrium condition for this experiment (90.2 K, 101 kPa) is shown by a cross in the top panel. The dotted lines are approximate boundaries between the other phases.

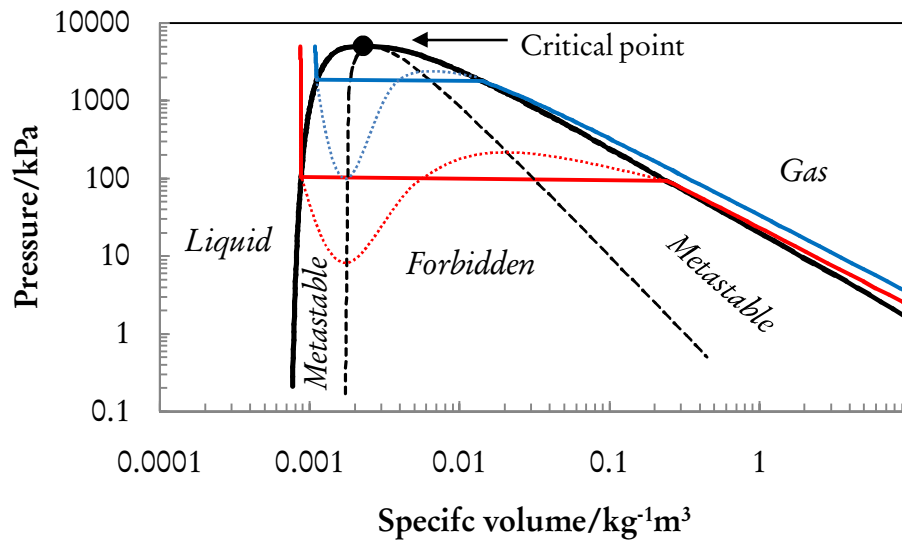


Figure 2.3. Equilibrium phase diagram of oxygen in the pressure-volume plane, discussed in more detail in section 2.1.2. The solid black line is the saturation curve (see also figure 2.2). The dashed black lines are the spinodal curves approximated from the van der Waals equation (equation (2.3)) that separate the metastable states from mechanically forbidden states (equation (2.1)). The solid red line is the isotherm at 90.2 K (starting condition for this experiment) and the solid blue line is another isotherm at a 130 K, for comparison. The colored dotted lines represent approximate extensions of the equation of state isotherms into the nonequilibrium region, assuming the van der Waals approximation (equation (2.2)). The saturation curve and isotherm data are from [4].

Table 2.1. Thermophysical properties of oxygen and copper at 90.2 K

| Property  | Symbol         | Value                                     |
|---|----------------|---|
| <i>Oxygen at normal boiling point (From [4], except where noted):</i> |                |   |
| Latent heat   | $h_{lg}$       | $2.12 \times 10^5$ J/kg                   |
| Mass density (gas)  | $\rho_g$       | 4.483 kg/m <sup>3</sup>                   |
| Mass density (liquid)   | $\rho_l$       | 1141 kg/m <sup>3</sup>                    |
| Specific heat (gas)   | $c_{p,g}$      | 979.6 J/kgK                               |
| Specific heat (liquid)  | $c_{p,l}$      | 1694 J/kgK                                |
| Viscosity (liquid)  | $\mu_l$        | 194.7 $\mu$ Pa $\cdot$ s                  |
| Thermal conductivity (liquid)   | $\lambda_l$    | 0.1518 W/m $\cdot$ K                      |
| Molecular mass  | $M$            | 32 a.m.u.                                 |
| Surface tension [5]   | $\sigma$       | 0.013 N/m                                 |
| Contact angle with Cu [6]   | $\phi$         | $\sim 1^\circ$                            |
| Specific magnetic susceptibility [7]                                  | $\chi/\rho$    | $+3.02 \times 10^{-6}$ m <sup>3</sup> /kg |
| <i>Copper at 90 K:</i>  |                |   |
| Specific heat [8]   | $c_{p,Cu}$     | 0.21 J/kgK                                |
| Thermal conductivity [8]  | $\lambda_{Cu}$ | 500 W/m $\cdot$ K                         |
| Density [7]   | $\rho_{Cu}$    | 8900 kg/m <sup>3</sup>                    |

We use the empirical saturation curve of our test substance, oxygen, provided by the National Institute of Standards and Technology (NIST) [4], which is a numerical computer model based on a compilation of many experimental data sets. Other quantities specific to the liquid-gas equilibrium are the latent heat (per unit mass),  $h_{lg}$ , and the surface tension of the interface between the two phases,  $\sigma$ . A summary of these properties and others for our test fluid, oxygen, is given in table 2.1.

Upon adding a small quantity of heat to the system (slowly, while holding pressure constant) and waiting for the system to re-equilibrate, the added heat goes into converting some fraction of the liquid into gas; this heat is, of course, the latent heat of evaporation. This slow addition of small amounts of heat can be repeated until all of the substance is the gas phase. Throughout this process, the temperature remains constant and uniform throughout the sample. The readers will recognize this quasi-static process as the picture of boiling or evaporation typically taught

in introductory thermodynamics textbooks, (e.g., chapter 9 of [9]). However, most real-world examples of boiling are far from equilibrium, including the experiment discussed in this work. The remainder of this section will describe some of the nonequilibrium phenomena associated with boiling.

Although equilibrium conditions are useful for comparison, the heating power in our experiment is too great to satisfy the equilibrium approximation. For sufficiently large heat flux values, a temperature gradient develops between our heater and the liquid–gas interface. We quantify this behavior with two parameters. We represent the power in terms of the incident heat flux (heater power per unit area,  $q$ ). The temperature gradient is quantified in terms of the heater superheat ( $\Delta T$ ), which is the temperature difference between the heater surface and the equilibrium saturation temperature (again, assuming pressure remains constant).

### 2.1.2 Convection

For small heat fluxes (or equivalently, small superheats), the system develops convection. In this metastable configuration, liquid is heated by the heater, expands, and rises to the surface, where some molecules escape into the gas phase, carrying off latent heat. The superheated liquid can exist at temperatures above the saturation temperature so long as the extended equation of state for the fluid obeys the mechanical stability criterion of having positive compressibility. The forbidden region is given by the condition

$$\left. \frac{\partial P}{\partial V} \right|_T < 0, \quad (2.1)$$

which would imply that the fluid expands as pressure is increased. The extended equation of state is the relation between pressure  $P$ , temperature  $T$ , and volume  $V$  for the equilibrium fluid extended into the non-equilibrium region of the pressure-volume plane where phase separation would normally occur in equilibrium; typically for this purpose the extended equation of state is approximated by the van der Waals equation of state *without* Maxwell’s correction [10]:

$$\frac{P}{P_c} = -\frac{3}{(V/V_c)^2} + \frac{8(T/T_c)}{3(V/V_c) - 1}, \quad (2.2)$$

where  $P_c$ ,  $V_c$ , and  $T_c$  are the critical point values of the pressure, volume, and temperature, respectively.

The boundary lines of zero compressibility are referred to as spinodal lines [11] and represent

the theoretical maximum superheat for the liquid as a function of pressure. For the van der Waals equation of state, the spinodal lines are given by

$$\frac{P}{P_c} = \frac{3}{(V/V_c)^2} - \frac{2}{(V/V_c)^3}. \quad (2.3)$$

In practice, however, the superheated fluid will begin boiling below this theoretical limit, as described below. Convection of superheated fluid is only a metastable configuration; small perturbations can cause the system to collapse into the energetically favorable boiling mode, as described below. In our experiment, we use heater powers large enough that convection appears only as a transient behavior upon the initial heating of the system (see section 4.2.1).

### 2.1.3 Nucleate Boiling

As we increase the superheat, the next heat transfer mode is nucleate boiling. Our experiment is primarily concerned with this particular mode of boiling heat transfer. Nucleate boiling is characterized by the presence of discrete vapor bubble nucleation sites on the heater surface. These nucleation sites typically occur at concave spots on the heater surface when thermal fluctuations create microscopic vapor bubbles which attach to the potential nucleation site. At low heat fluxes, individual bubbles form, grow, detach, and rise. At higher heat fluxes, the individual bubbles merge into vertical jets.

The literature contains several models for how nucleation sites form and become active [3]. A typical example, by Dhir, for the necessary superheat for nucleation is

$$\Delta T = \frac{4\sigma T_{\text{sat}}}{\rho_v h_{lg} D_c},$$

where  $\Delta T$  is the superheat,  $\sigma$  is the surface tension of the vapor-liquid interface,  $T_{\text{sat}}$  is the saturation temperature of the fluid,  $\rho_v$  is the mass density of the vapor,  $h_{lg}$  is the latent heat,  $D_c$  is the size of the surface defect. Inserting the values for our experiment (from table 2.1), the minimum nucleation superheat is only about  $\Delta T = 70$  mK, or equivalently, the reduced superheat needed to nucleate vapor bubbles is  $\Delta T/T_{\text{sat}} = 8 \times 10^{-4}$ . This value is comparable to the smallest superheats measured in our experiment (see chapter 5).

### 2.1.4 Transition and Film Boiling

If we continue increasing the heater power, eventually the liquid at the heater surface will vaporize more quickly than it can be replaced from the bulk liquid. At this critical heat flux, a film of vapor forms over the entire heater surface, inhibiting heat transfer to the fluid. This configuration is known as film boiling [3; 12].

The transition from nucleate boiling to film boiling is abrupt and irreversible (see the top arrow in figure 2.1). The heat flux value where this transition occurs is called the critical heat flux  $q_{\text{CHF}}$ . This quantity is usually determined empirically, although some modestly successful models exist. The most commonly used model for predicting the value of  $q_{\text{CHF}}$  is that of Zuber [13]:

$$q_{\text{CHF}} = 0.131 \rho_g^{1/2} h_{lg} [\sigma g (\rho_l - \rho_g)]^{1/4}. \quad (2.4)$$

For our system (see table 2.1) under Earth gravity the predicted  $q_{\text{CHF}}$  is approximately  $2 \times 10^5 \text{ W/m}^2$ . This is well above our maximum applied heat flux of approximately  $3000 \text{ W/m}^2$ , so we do not anticipate transition or film boiling to occur in our experiment. However, as explained in chapter 6, our data suggest a possible alternative boiling curve and a much lower value for the critical heat flux.

If we decrease the heater power of a system in film boiling, eventually the heater power will be insufficient to maintain the vapor film. Once this point is reached, the system will suddenly collapse back into the nucleate boiling mode (the middle arrow in figure 2.1).

The hysteretic shift between nucleate and film boiling modes can be avoided if the heater temperature is held constant rather than the heater power. In this case, an additional boiling mode is accessible, called transition boiling. Transition boiling is an inhomogeneous and fluctuating mixture of heater regions with nucleate and film boiling. The various regions may move and fluctuate in size. The transition boiling mode is inherently unstable; without precise control of the heater temperature the system will collapse into either the film boiling or nucleate boiling modes.

## 2.2 Prior Work

Research into boiling has been ongoing for more than a century, but understanding of this common behavior is still largely phenomenological. The large number of system variables and the difficulty in reproducing experimental data have thwarted attempts to develop a unified model

(see, for example, the reviews in [12] and [3]).

### 2.2.1 Theoretical Work

Early work (prior to about 1950) attempted to study as many experimental configurations as possible, particularly by varying the fluid and the heater geometry. At this time, research was primarily intended to collect data for engineering applications; tables of data were sufficient for this purpose and few models proposed. A breakthrough paper in 1952 by W. M. Rohsenow [14] is the first credible attempt to explain the mechanism of heat transfer in nucleate pool boiling. Rohsenow focuses attention on the growth of bubbles on the heater surface, incorporating bubble size and interactions with the heater surface into the model. Rohsenow's end result is

$$\frac{q}{\mu_l h_{lg}} \sqrt{\frac{\sigma}{g(\rho_l - \rho_g)}} = \frac{1}{C_s^3} \left( \frac{c_{p,l} \Delta T}{h_{lg}} \right)^3 \left( \frac{\mu_l c_{p,l}}{\lambda_l} \right)^n, \quad (2.5)$$

where  $C_s$  is an empirical parameter relating to the surface-liquid interaction ( $C_s \approx 0.02$  for oxygen [15]) and the values of other parameters for our system are listed in table 2.1. The exponent  $n = 3.0$  for water and  $n = 5.1$  for other liquids [3].

After Rohsenow many alternative models appeared in the literature. Some of the more noteworthy of these correlations are those by Forster and Zuber [16], Engleberg-Forster and Grief [17], and Judd and Hwang [18].

The large number of proposed models must have been frustrating to experimentalists, who often had to compare their data to as many as a dozen different models. Works on cryogenic fluids by Kosky and Lyon [19] and Drayer [20] demonstrate diligent efforts to include as many models as possible. Drayer, for example, in experiments on the boiling of hydrogen shows how some of the eleven models tested predict heat flux values which deviate from experimental results by as much as *six orders of magnitude*.

With the emergence of computing power in the late twentieth century, the modeling emphasis shifted from mechanisms to statistics. Stephan and Abdelsalam [6] performed a massive regression analysis on approximately five thousand data points from seventy-two separate experiments. Stephan and Abdelsalam began their model with fourteen dimensionless combinations of material

parameters ( $X_n$ ) and assumed these were related by a power law:

$$\prod_{n=1}^{14} X_n^{b_n} = 1.$$

By keeping only those factors which were shown by the fitting process to be statistically significant, they reduced the above expression to

$$\frac{qD_d}{\Delta T \lambda_l} = 0.23 \left( \frac{R}{\mu\text{m}} \right)^{0.133} \left( \frac{qD_d}{\lambda_l T_{\text{sat}}} \right)^{0.624} \left( \frac{[\rho c_p \lambda]_{\text{heater}}}{\rho_l c_{p,l} \lambda_l} \right)^{0.117} \\ \times \left( \frac{\rho_g}{\rho_l} \right)^{0.257} \left( \frac{c_{p,l} T_{\text{sat}} D_d^2}{\alpha_l^2} \right)^{0.374} \left( \frac{h_{lg} D_d^2}{\alpha_l^2} \right)^{-0.329}, \quad (2.6)$$

where the equation is assumed to only be applicable to cryogenic liquids. The various material parameters are listed in table 2.1;  $\alpha_l = \lambda_l / \rho_l c_{p,l}$  is the thermal diffusivity of the liquid,  $R$  is the heater surface roughness ( $\sim 60 \mu\text{m}$  for our heater), and  $D_d$  is the empirically determined bubble diameter. Stephan and Abdelsalam give the mean absolute error of their correlation to be 14.3%. They also calculate correlations for several other classes of fluids: water, hydrocarbons, and refrigerants, and an overall correlation. The class-based correlations have errors of 10%–15% and the overall correlation has an error of 22.3%. It should be noted the above equation is *independent of gravity*. For the specific combination of a copper heater and oxygen at a saturation pressure of 1 atm, Stephan and Abdelsalam give (see equation (13a) and table 2 of [6]):

$$\frac{\Delta T}{\text{K}} = 12.3 \left( \frac{R}{\mu\text{m}} \right)^{0.133} \left( \frac{q}{\text{Wm}^{-2}} \right)^{0.376}. \quad (2.7)$$

The complexity of Stephan and Abdelsalam's correlation and similar works inspired Cooper [21; 22] to take a different approach in 1984. Cooper set out to compose a correlation using only the most basic material parameters (for example, the molecular mass), in particular noting that because the thermodynamic properties of a specific substance are not independent, some simplification must be possible. For example, Cooper noted that properties such as the density and surface tension could be described in terms of the critical pressure. Other properties can be

related to the molecular mass. After these simplifications, Cooper's end result is

$$\left(\frac{q}{\text{Wm}^{-2}}\right)^{1/3} = 55.0 \frac{\Delta T}{\text{K}} \left(\frac{P}{P_c}\right)^{0.12-0.21\log(R/\mu\text{m})} \left(-\log\frac{P}{P_c}\right)^{-0.55} \left(\frac{M}{\text{a.m.u.}}\right)^{-0.50}, \quad (2.8)$$

where  $P_c$  is the critical pressure,  $R$  is the heater surface roughness, and  $M$  is the molecular mass. Cooper does not claim that this correlation is more accurate than others, but invoking an Occam's-Razor-type argument, claims that the scatter in existing experimental data is too large to justify a more elaborate correlation; therefore, by Cooper's reasoning, this simpler expression is more desirable.

Theoretical progress stalled in the 1980s because of the inadequacy of the existing experimental data. The irreproducibility of bulk boiling measurements limits their usefulness. New understanding would come from a shift of emphasis to microscopic behavior in the form of experiments with improved spatial and temporal resolution and new numerical simulation techniques. The frustrating inability to find a mechanistic model is summarized in Vijay K. Dhir's acceptance article for the American Society of Mechanical Engineers' 2004 Max Jakob award for "eminent achievement in heat transfer"; the title of the paper is telling: "Mechanistic prediction of nucleate boiling heat transfer—achievable or a hopeless task?" [23]. Despite the dire sound of his title, Dhir concludes on an optimistic note, saying that boiling behavior can be predicted but only with numerical simulations.

### 2.2.2 Recent Experimental Work on General Boiling

Experiments representative of the improved methodology in recent years are those by Kim and colleagues [24–27] and by Dhir and colleagues [15; 28; 29]. The Kim group's experiments attempt to study the small-scale behavior at the heater surface by using an array of 96 small heaters, each heater a square of side 0.27 mm in early experiments and 0.100 mm in later experiments. The power and temperature of each heater can be individually monitored and controlled, with a sample rate of up to 1130 Hz when all heaters are operating. In some studies, only a subset of the heaters was used, resulting in a faster sampling rate. Kim et al. also observe the heater surface from above using a high-speed camera synchronized with the heater measurement electronics.

With this configuration, the researchers were able to resolve the growth and motion of individual vapor bubbles. They also observed quasi-periodic temperature oscillations in individual

heater elements, correlated with the nucleation and departure of individual bubbles. In particular, this experiment can measure microlayer evaporation. This phenomenon occurs when a thin layer of liquid forms between a bubble and the heater surface and was suspected to be the dominant heat transport mechanism in low-gravity conditions. Kim's later experiments [27] discount microlayer evaporation as an efficient heat transport mechanism in favor of transient heat conduction into the liquid as the heater surface rewets before each bubble nucleation event.

The approach by Dhir and colleagues [28; 29] is to study single nucleation sites using high-speed photography and to compare these images with numerical simulations. Individual nucleation sites are formed by micromachining cavities into the heater surface, each cavity being 10  $\mu\text{m}$  in diameter and 20  $\mu\text{m}$  deep. These studies investigate particularly the growth and merger of bubbles. Dhir finds that at low superheat, the heat flux is a function of the number of active nucleation sites and the waiting time between bubble formation events on an individual site. Also, at high superheat, frequent bubble merger events cause transient drying out of the heat surface, reducing heat transport efficiency. These experimental results corroborate numerical simulations also done by the group.

### 2.2.3 Experiments at Nonstandard Gravity

Experiments at high effective gravities using centrifuges [30; 31] and parabolic-trajectory aircraft [26] show results which vary depending on the applied heat flux. At low heat fluxes, increasing gravity increases heat transfer efficiency. At high heat fluxes, however, increasing gravity decreases heat transfer efficiency [30].

Low gravity studies show an even wider range of results. The general consensus among investigators is that the factors influencing nucleate boiling can be qualitatively divided into macroscopic and microscopic phenomena. Macroscopic effects, such as buoyancy, bubble dynamics, and thermocapillary effects, tend to depend on gravity. Microscopic effects at the heater surface, such as intermolecular forces, microlayer evaporation and transient microlayer conduction, are independent of gravity. As gravity is reduced, the microscopic phenomena begin to dominate over the macroscopic effects and compete with one another, resulting in varying experimental results depending on the details of the experiments [2; 30; 32; 33].

Many of the widely used empirical correlations of boiling heat transfer neglect gravity. Several make no mention of gravity at all [6; 22]. Those that do include the gravitational acceleration  $g$

[14; 17], often do so only as a dimensional constant, not as a physical variable. In these models varying the value of  $g$  yields unphysical predictions [3]. Modern interpretation is that these correlations are only valid when  $g$  is held constant at its Earth value of  $9.8 \text{ m/s}^2$ , regardless of the actual gravity in the experiment. To develop adequate models which account for gravity variations, more experimental data are needed. Our goal in this experiment is to measure some gravity dependence in the heat-flux–superheat relationship, particularly in the value of the critical heat flux.

## 2.3 This Work

The experiment discussed in this work originated with modest goals. The original idea was proposed by our collaborator Dr. Donald Strayer of the Jet Propulsion Laboratory as a proof-of-concept test for their new Variable Gravity Testbed Facility [34]. Our system was designed to be inexpensive and utilize as much preexisting equipment as possible. Additionally, the straightforward nature of this experiment makes it an excellent research project for undergraduate students. Much of the design and construction of the test probe were done by Caltech undergraduates Michael Kwun Hung Cheung and Michael E. Turk under the author’s supervision.

We are performing bulk experiments on nucleate pool boiling of oxygen (some thermophysical properties of oxygen appear in table 2.1). In particular, we are measuring the effects of gravity on the heat transport properties of the process by monitoring the heat flux through the sample and the temperature differential across the sample. We change the effective gravity by applying a magnetic force to our test fluid, oxygen having a high magnetic susceptibility. Details of the experimental setup are given in chapter 3.

Data were collected for boiling of oxygen under atmospheric pressure (760 torr) with effective gravitational accelerations of 1, 6, and 16 times that of the Earth, for heat fluxes between approximately  $10 \text{ W/m}^2$  and  $3000 \text{ W/m}^2$ , corresponding to superheats up to approximately 3 K. The experimental procedures appear in chapter 4. The data are described in chapter 5 and appendix B and the results discussed in chapter 6.

## Bibliography

- [1] C. McCarthy. *Blood Meridian: Or the Evening Redness in the West*. New York: Vintage (1985).
- [2] P. DiMarco. "Review of reduced gravity boiling heat transfer: European research." *Japan Society of Microgravity Application Journal*, **20**:252–263 (2003).  
<http://www.glue.umd.edu/~kinjh/Documents%20and%20movies/European%20Research.pdf>.
- [3] V. K. Dhir, S. G. Kandlikar, Y. Fujita, Y. Iida, and R. Heist. In S. Kandlikar, M. Shoji, and V. K. Dhir, editors, *Handbook of Phase Change: Boiling and Condensation*, Philadelphia: Taylor and Francis, pp. 63–99 (1999).
- [4] D. G. Friend. *NIST Thermophysical Properties of Pure Fluids Database, NIST Standard Reference Databases*, volume 12. Gaithersburg, MD: U.S. Department of Commerce (1992). PC software version 3.1.
- [5] S. D. Bembenek. "Calculation of the surface tension of oxygen using molecular-dynamics simulations." *Journal of Chemical Physics*, **124**:014709 (2006). doi:1030363/1.2136872.
- [6] K. Stephan and M. Abdelsalam. "Heat-transfer correlations for natural convection boiling." *International Journal of Heat and Mass Transfer*, **23**:73–87 (1980).
- [7] D. R. Lide, editor. *CRC Handbook of Chemistry and Physics*. New York: CRC Press, 79th edition (1998).
- [8] G. K. White and P. J. Meeson. *Experimental Techniques in Low-Temperature Physics*. New York: Oxford UP, fourth edition (2002).
- [9] P. M. Morse. *Thermal Physics*. Redwood City: Addison, second edition (1969).
- [10] J. L. Lebowitz and O. Penrose. "Rigorous treatment of the van der Waal-Maxwell theory of liquid–vapor transition." *Journal of Mathematical Physics*, **7**:98–113 (1966).
- [11] Y. Fujita and S. G. Kandlikar. In S. G. Kandlikar, M. Shoji, and V. K. Dhir, editors, *Handbook of Phase Change: Boiling and Condensation*, Philadelphia: Taylor and Francis, pp. 1–40 (1999).
- [12] V. K. Dhir. "Boiling heat transfer." *Annual Reviews of Fluid Mechanics*, **30**:365–401 (1998).  
doi:10.1146/annurev.fluid.30.1.365.
- [13] N. Zuber. *Hydrodynamic Aspects of Boiling Heat Transfer*. Ph.D. thesis, University of California, Los Angeles (1959).
- [14] W. M. Rohsenow. "A method of correlating heat-transfer data for surface boiling of liquids." *Transactions of the American Society of Mechanical Engineers*, **74**:969–976 (1952).
- [15] S. P. Liaw and V. K. Dhir. "Void fraction measurement during saturated pool boiling of water on partially wetted surfaces." *Journal of Heat Transfer*, **111**:731–738 (1989).

- [16] H. K. Forster and N. Zuber. "Dynamics of vapor bubbles and boiling heat transfer." *American Institute of Chemical Engineers Journal*, 1:531–535 (1955).  
<http://www3.interscience.wiley.com/cgi-bin/abstract/109074537/ABSTRACT>.
- [17] K. Engleberg-Forster and R. Greif. "Heat transfer to a boiling liquid—mechanism and correlations." *Journal of Heat Transfer*, 81:43–53 (1959).
- [18] R. L. Judd and K. S. Hwang. "A comprehensive model for nucleate pool boiling heat transfer including microlayer evaporation." *Journal of Heat Transfer*, 98:623–629 (1976).
- [19] P. G. Kosky and D. N. Lyon. "Pool boiling heat transfer to cryogenic liquids." *American Institute of Chemical Engineers Journal*, 14:372–387 (1968).  
<http://www3.interscience.wiley.com/cgi-bin/abstract/109074109/ABSTRACT>.
- [20] D. E. Drayer. "Nucleate boiling of hydrogen." *Industrial and Engineering Chemistry Fundamentals*, 4:167–171 (1965).
- [21] M. G. Cooper. *Industrial and Chemical Engineering Symposium Series*, 86:786–793 (1984).
- [22] M. G. Cooper. "Heat flow rates in saturated nucleate pool boiling—a wide-ranging examination using reduced properties." *Advances in Heat Transfer*, 16:155–239 (1984).
- [23] V. K. Dhir. "Mechanistic prediction of nucleate boiling heat transfer—achievable or a hopeless task?" *Journal of Heat Transfer*, 128:1–12 (2006).
- [24] C. D. Henry and J. Kim. "A study of the effects of heater size, subcooling, and gravity level on pool boiling heat transfer." *International Journal of Heat and Fluid Flow*, 25:262–273 (2004).
- [25] C. D. Henry, J. Kim, B. Chamberlain, and T. G. Hartman. "Heater size and heater aspect ratio effects on subcooled pool boiling heat transfer in low-g." *Experimental Thermal and Fluid Sciences*, 29:773–782 (2005).
- [26] J. Kim, J. F. Benton, and D. Wisniewski. "Pool boiling heat transfer on small heaters: effect of gravity and subcooling." *International Journal of Heat and Mass Transfer*, 45:3919–3932 (2002).  
doi:10.1016/S0017-9310(02)00108-4.
- [27] J. G. Myers, V. K. Yerramilli, S. W. Hussey, G. F. Yee, and J. Kim. "Time and space resolved wall temperature and heat flux measurements during nucleate boiling with constant heat flux boundary conditions." *International Journal of Heat and Mass Transfer*, 48:2429–2442 (2005). doi:10.1016/j.ijheatmasstransfer.2004.12.050.
- [28] A. Mukherjee and V. K. Dhir. "Study of lateral merger of vapor bubbles during nucleate pool boiling." *Journal of Heat Transfer*, 126(6):1023–1039 (2004). doi:10.1115/1.1834614.
- [29] G. Son and V. K. Dhir. "Numerical simulation of nucleate boiling on a horizontal surface at high wall superheats." *International Journal of Heat and Mass Transfer* (2007). Submitted.

- [30] H. Merte. "Nucleate pool boiling in variable gravity." In J. N. Koster and R. L. Sani, editors, *Low-Gravity Fluid Dynamics and Transport Phenomena, Progress in Astronautics and Aeronautics*, volume 130, Washington: American Institute of Astronautics and Aeronautics, pp. 15–72 (1990).
- [31] M. E. Ulucakli and H. Merte. "Nucleate boiling with high gravity and large subcooling." *Journal of Heat Transfer*, 112:451–457 (1990).
- [32] J. Kim. "Review of reduced gravity boiling heat transfer: US research." *Japan Society of Microgravity Application Journal*, 20:264–271 (2003).  
<http://www.glue.umd.edu/~kimjh/Documents%20and%20movies/US%20Research.pdf>.
- [33] H. Ohta. "Review of reduced gravity boiling heat transfer: Japanese research." *Japan Society of Microgravity Application Journal*, 20:272–285 (2003).  
<http://www.glue.umd.edu/~kimjh/Documents%20and%20movies/JapaneseResearch.pdf>.
- [34] T. Chui, B. Zhang, M. Barmatz, I. Hahn, K. Penanen, C. Hays, D. Strayer, et al. "Cryogenics for lunar exploration." *Cryogenics*, 46:74–81 (2006). doi:10.1016/j.cryogenics.2005.10.006.

## Chapter 3

We had a kettle; we let it leak:  
 Our not repairing made it worse.  
 We haven't had any tea for a week...  
 The bottom is out of the Universe.

---

Rudyard Kipling, "Natural Theology"\*

## Hardware

**S**IMPLE things can inspire us. Looking at a tea kettle through the lens of thermodynamics, we see the following: the water is being heated from below at atmospheric pressure. This is exactly what we need for our experiment. The differences between a tea kettle and our experiment are the technicalities. For example, our apparatus has to fit inside a superconducting magnet.

### 3.1 Magnet

The magnet we use was originally purchased for a different experiment. However, the large bore and strong field make it ideal for our application. The magnet is a NbTi superconducting solenoid, manufactured by American Magnetics (Oak Ridge, TN). The magnet is cooled by liquid helium and may be run in a persistent-current configuration. The key design parameters of the magnet are listed in table 3.1.

#### 3.1.1 Field Profile

The important quantity for our experiment is the field profile of the magnet. The magnetic force on our test fluid is proportional to  $(\mathbf{B} \cdot \nabla)\mathbf{B}$ , as described below. The magnitude of the axial magnetic force increases sharply as one moves away from the center along the axis of the solenoid because of the large field gradient. The force reaches maximum magnitude near the ends of the solenoid—this is where we place our experiment (see figure 3.2 and the next section).

---

\*Reference [1]

Table 3.1. Superconducting magnet specifications

|                           |                               |
|---------------------------|-------------------------------|
| Maximum central field     | 9.0 T                         |
| Maximum current           | 84.0 A                        |
| Field to current ratio    | 0.1072 T/A                    |
| Central field homogeneity | $\pm 0.1\%$ over 1 cm d.s.v.* |
| Inductance                | 38.8 H                        |
| Bore diameter             | 4.0"                          |
| Outer diameter            | 8.1"                          |
| Length                    | 12.0"                         |

\*d.s.v. = diameter spherical volume

To calculate the field profile of the magnet, and hence the magnetic force, we begin with some calibration data provided by the magnet's manufacturer. The manufacturer tabulated the radial and axial fields for axial positions  $z$  between  $-10$  cm and  $+10$  cm and radial positions  $r$  between  $0$  and  $+10$  cm, where  $z = 0, r = 0$  represents the center of the magnet. Unfortunately, we need to know the field at larger  $z$  values. By assuming a particular functional form for the magnetic field, we extrapolate out to larger values of  $z$ .

The on-axis magnetic field (shown in figure 3.1(a)) is approximately that of a uniformly wound finite solenoid:

$$B_z(z) \approx IC \left( \frac{z + a/2}{\sqrt{(z + a/2)^2 + b^2}} - \frac{z - a/2}{\sqrt{(z - a/2)^2 + b^2}} \right),$$

with parameters  $a = 25.5$  cm,  $b = 7.78$  cm and  $C = 6.28 \times 10^{-2}$  T/A. We determined these parameters by fitting the equation to the data provided by the manufacturer. The current is shown as  $I$  (maximum of 84 A for this magnet), and the axial position  $z$  is measured relative to the center of the magnet. The off-axis fields at the heater surface ( $z = 8.8$  cm) are calculated using formulas from [2] for uniformly wound solenoids of finite volume, and are shown in figure 3.1(b). (See also, appendix C.)

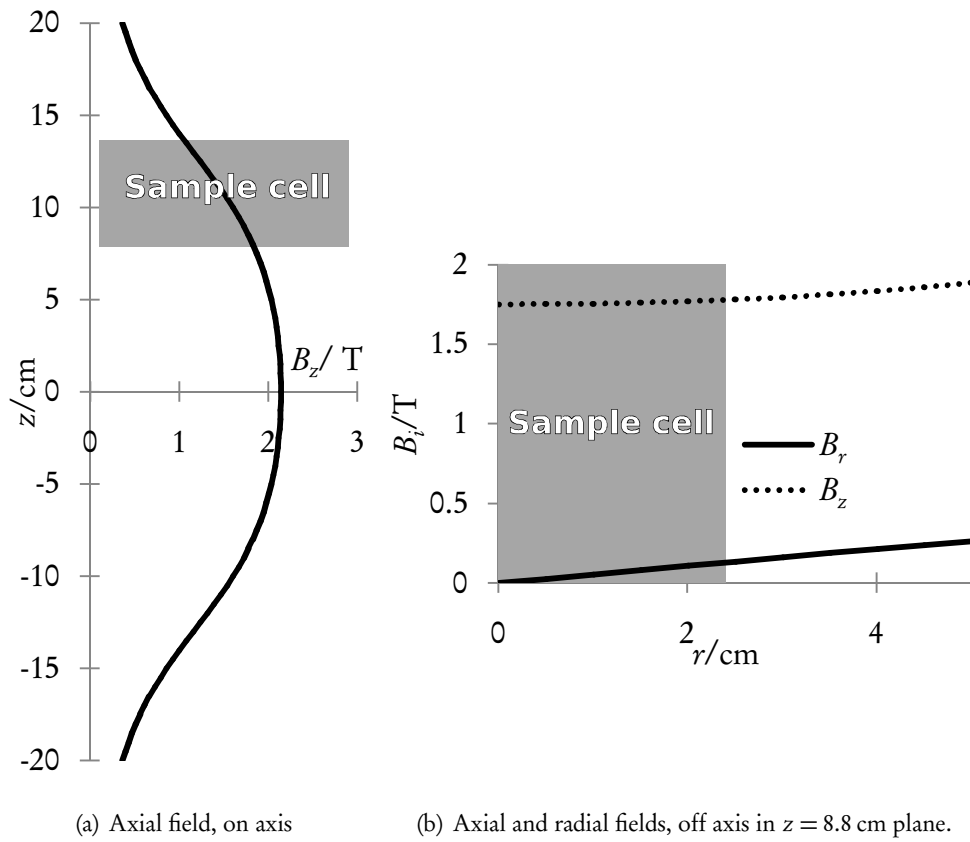


Figure 3.1. Magnetic field of the solenoid in tesla for magnet current  $I = 20$  A. Approximate sample cell position is shown in gray.

### 3.1.2 Force Calculations

The acceleration  $\mathbf{a}$  experienced by a magnetic fluid with susceptibility  $\chi$  in the presence of an applied field  $\mathbf{B}$  is given by

$$\mathbf{a} = \frac{1}{\mu_0 \rho} \chi (\mathbf{B} \cdot \nabla) \mathbf{B}, \quad (3.1)$$

where  $\rho$  is the mass density of the fluid (liquid or gas),  $\mu_0$  is the vacuum permeability, and all quantities are in SI units (adapted from [3]).

An equivalent expression can be derived by considering the energy in the system. The magnetostatic potential energy of the fluid in a field is

$$\begin{aligned} U &= -\frac{1}{2} \int dV \mathbf{H} \cdot \mathbf{B}, \\ &= -\frac{1}{2\mu_0} \chi \int dV B^2, \\ &= -\frac{1}{2\mu_0} \frac{\chi}{\rho} \int dm B^2 \\ \frac{U}{m} &= -\frac{1}{2\mu_0} \frac{\chi}{\rho} B^2. \end{aligned}$$

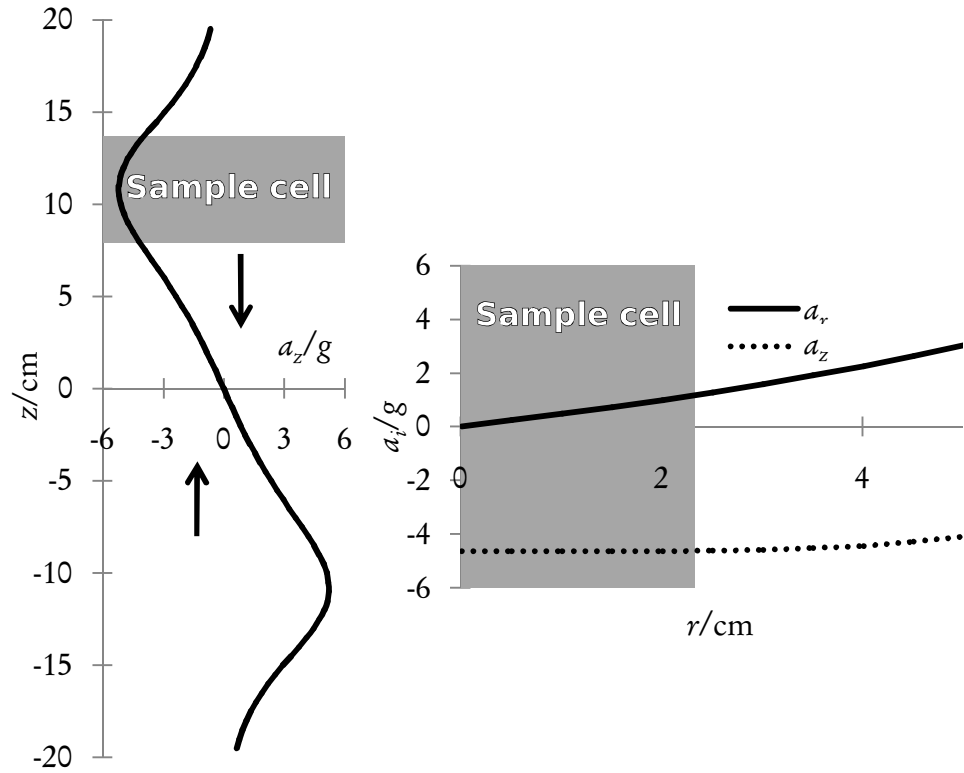
Taking the gradient

$$\mathbf{a} = -\frac{1}{m} \nabla U = \frac{1}{2\mu_0} \frac{\chi}{\rho} \nabla (B^2). \quad (3.2)$$

These final two expressions are preferred for their ease of use numerically; the potential energy is a scalar quantity and the gradient is simple to calculate.

For oxygen near the normal boiling point (90.2 K) the ratio  $\chi/\rho$  equals  $+3.02 \times 10^{-6} \text{ m}^3/\text{kg}$  for both liquid and gas phases [4]. We assume any temperature dependence in  $\chi/\rho$  is negligible over our temperature range of 90–95 K. To achieve 1g of acceleration on oxygen at the normal boiling point requires  $|(\mathbf{B} \cdot \nabla) \mathbf{B}| = 4.5 \text{ T}^2/\text{m}$ . The magnetic force causes an acceleration that is independent of the fluid density and therefore independent of the phase of the fluid. The end result is an applied acceleration which, like gravitational acceleration, is independent of mass.

The magnetic acceleration of oxygen as a function of position within the magnet is shown in figure 3.2. The graphics show acceleration for the case in which the solenoid current is at its maximal value of  $I = 84 \text{ A}$ . For other current values the acceleration is proportional to  $I^2$  (see equation (3.3) and (3.4), below). Although plotted in figure 3.2(b) for completeness, we ignore the radial force in our analysis.



(a) Axial acceleration, on axis      (b) Axial and radial acceleration, off axis in  $z = 8.8$  cm plane.

Figure 3.2. Magnetic acceleration of oxygen as a function of position in the magnet for magnet current  $I = 20$  A, with direction indicated by the arrows. Approximate sample position is shown in gray. The values show only the magnetic acceleration; the ambient gravitational acceleration from the Earth is not shown, but would be  $1g$  in the negative- $z$  direction.

To obtain an approximately flat force profile over the volume of the liquid, we place the sample cell near the end of the magnet where the force obtains its maximum magnitude, with the center of the sample cell 11.0 cm above the magnet center (equivalent to placing the heater surface at 8.8 cm), as illustrated by the gray boxes in figures 3.1 and 3.2. The force varies over the volume of the sample cell by about  $\pm 5\%$  relative to its average value.

The net effective gravity ( $g_{\text{eff}}$ ) for oxygen in our magnet on axis at the heater surface is related to the current  $I$  by

$$g_{\text{eff}}(I; z = 8.8 \text{ cm}, r = 0) = g \left[ \left( \frac{I}{9.28 \text{ A}} \right)^2 + 1 \right], \quad (3.3)$$

where positive values indicate downward acceleration.

Future studies at reduced effective gravity may be performed by placing the sample at the bottom end of the magnet, where the magnetic force counteracts the Earth's gravity. In this configuration, the net effective gravity on axis at the heater surface is

$$g_{\text{eff}}(I; z = -12.8 \text{ cm}, r = 0) = g \left[ \left( \frac{I}{9.33 \text{ A}} \right)^2 - 1 \right], \quad (3.4)$$

with positive values being directed downward. To completely cancel the Earth's gravity requires 9.33 A in this configuration. To simulate lunar gravity (0.16g) and Martian gravity (0.38g) requires 8.54 A and 7.35 A, respectively. Unfortunately, we are not able to conduct experiments at reduced effective gravity at this time because it requires building a longer cryogenic probe or raising the magnet inside the dewar, a nontrivial adjustment.

## 3.2 Cryogenic Probe

A drawing of the cryogenic probe is given in figure 3.3. The primary challenge of the cryogenic probe design is the thermal isolation of the sample (at 90 K) from the external liquid helium bath (at 4.2 K). To this end, the sample cell is surrounded by vacuum and is mechanically supported by insulating G-10 epoxy posts (not shown). Vacuum is maintained by a charcoal pot located in the vacuum space on the bottom exterior flange. Under optimal conditions, less than 50 mW of heat is transferred from the sample cell to the helium bath. This heat leak is measured during each experimental run, as described in sections 4.2 and 5.1.

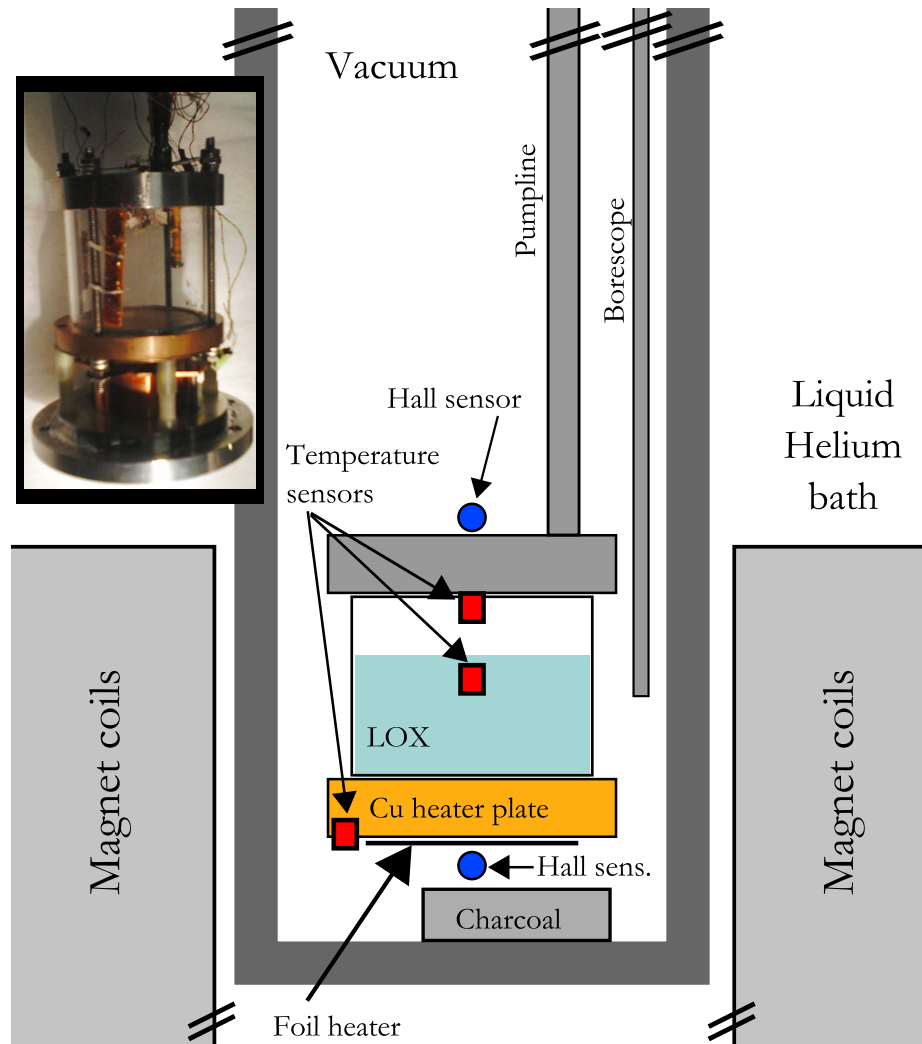


Figure 3.3. Schematic of the oxygen experiment cryogenic probe. A photograph of the sample cell appears in the inset. For a description, see the text.

The exterior of the cryogenic probe is thin-walled stainless-steel tubing, 200  $\mu\text{m}$  thick and 85 mm in diameter. The top (room-temperature) plate (not shown in the figure) is made of stainless steel and welded to the tubing. The top plate contains ports for two electrical feedthroughs (similar to those in appendix D.1), the vacuum-space pump line, the sample pump/fill line, and a feedthrough for the fiberoptic borescope. All of the feedthroughs are made of brass, attached to the plate using indium gaskets. The bottom plate is stainless steel, also sealed to the probe body with an indium gasket. To offset thermal contraction, the screws holding the bottom seal also use Belleville washers to apply additional force. Attached to the interior of the bottom plate is a copper pot filled with charcoal. This charcoal absorbs any residual gas in the vacuum space after the probe is submerged in liquid helium.

The sample cell itself is a hollow cylinder. The top end is a stainless-steel plate with an electrical feedthrough (for the temperature sensor wires) and with a port for the sample pump/fill line. The side of the cylinder is 50 mm O.D., 2 mm thick, 40 mm tall quartz tubing. The ends of the tubing must be mutually parallel and ground smooth to ensure proper mating with the end plates and to minimize mechanical stress in the quartz under compression. The quartz is mated to the end plates by indium gaskets. The bottom plate is copper, described in more detail in the following section. Compression of the gaskets is provided by four brass 6-32 threaded rods, with stainless-steel Belleville washers and hex nuts tightened to 5 N·m of torque. Equal torques on the nuts are necessary to prevent anisotropic mechanical stresses which may break the quartz, particularly under thermal contraction.

### 3.2.1 Heater

The design of the heater is crucial in boiling experiments, as was described in section 2.2. We do not wish to study heater surface effects in our experiment, so we give special consideration to maintaining a consistent heater surface between experimental runs. Heater factors which may change the boiling dynamics include material composition, surface roughness, and trapping of non-sample gasses [5; 6].

The heater is a 10 mm thick plate of oxygen-free high-conductivity (OFHC) copper. This plate is 60 mm in diameter. The section of the heater in contact with the sample fluid has a diameter of 46 mm. The surface of the plate which contacts the sample was initially prepared by machining the copper flat and then polishing to a mirrorlike finish. Because smooth surfaces inhibit the

formation of boiling nucleation sites, we complete the heater preparation by roughening the heating surface with 240 grit sandpaper, yielding a surface roughness of approximately  $60\ \mu\text{m}$  [7]. We repeat the sanding process approximately once per month or whenever the heater is exposed to air for extended periods to remove any oxidation or other contamination from the surface. After sanding or other handling the heater is washed with successive baths of detergent, acetone, and isopropanol in an ultrasonic agitator to remove any debris and grease from the surface. To slow the degrading of the heater surface and to reduce the amount of absorbed gasses or solvents on the surface, the sample cell is kept under vacuum when not in use.

The heat source is a Minco  $70\ \Omega$  thin-foil resistor attached to the copper plate on the outside of the sample cell. We hold the resistor in place with a thin layer of Apiezon N grease and a beryllium-copper clamp to improve the thermal contact between the resistor and the copper plate. The resistor is measured using a four-lead configuration so that we can accurately monitor the power dissipated by the resistor.

### 3.2.2 Temperature Sensors

For temperature measurements we use four Lakeshore Cernox resistive temperature sensors, model CX-1050-SD, connected in a four-lead configuration. We calibrated these sensors prior to installation by comparing with a previously calibrated sensor over the range of 20–110 K; details are given in appendix A.

The magnetic field dependence of the Cernox sensors is given by the manufacturer as a parts-in- $10^4$  effect in the resistance at our operating temperatures and fields [8]. We neglect this effect.

The temperature sensors are located throughout the sample cell. Two sensors are attached to interior of the top plate of the sample cell, stood off from the top plate itself so they measure the temperature of the sample at this position. One is located on a screw near the center of the cell, on axis. A fourth sensor is embedded in a copper mounting screw which is attached to the outside surface of copper heater plate.

The bottom sensor resistance is measured using a Lakeshore LS-340 temperature controller, which is also used to power the heater resistor. The resistance of the three other temperature sensors are measured in a four-lead configuration. We excite these sensors with a current of  $10\ \mu\text{A}$ , provided by a Keithley 220 current source. We measure the voltage across the sensors with a

Keithley 182 nanovoltmeter. Switching between the sensors is provided by a Keithley 705 scanner.

Only the sensor in the heater is used for quantitative data during the boiling phase of the experiment. The other sensors are used to indicate the liquid level during the filling phase—the sensor temperatures drop suddenly once immersed in liquid, thus indicating the liquid level—and for qualitative observations during boiling. These in-cell sensors can not be used for quantitative data during boiling because the temperature is sensitive to the liquid level, which fluctuates violently during boiling. However, these sensors are still useful for diagnostics.

### 3.2.3 Magnetic-Field Sensors

For magnetic field measurements in the cryogenic probe we use a pair of Toshiba THS-122 Hall-effect magnetic field sensors. We mount the Hall sensors on either end of the sample cell, on axis, approximately 1 cm above and below the sample cell on standoff plates. The standoffs are necessary to thermally isolate the magnetic sensors from the sample cell; these semiconducting sensors are sensitive to temperature. The magnetic field sensors are excited using the same equipment as the upper temperature sensors (Keithley 220 current source and Keithley 182 nanovoltmeter). We were unable to calibrate these sensors because we have no way of directly measuring their temperature. They are used only in a qualitative sense to verify that the solenoid is functioning.

### 3.2.4 Optics

A fiberoptic borescope built by Myriad Fiber (Dudley, MA) is positioned adjacent to the quartz sample cell wall to provide imaging of the experiment. The borescope image is output via a Panasonic GP-KS162HD CCD camera to a television monitor. The temporal and spatial resolutions of the camera are insufficient for quantitative measurements of bubble dynamics but serve nicely for diagnostic purposes and qualitative observations such as the level of the liquid during filling and identification of bubbles to confirm boiling. A schematic of the borescope is shown in figure 3.4.

We had to specify some design parameters to the manufacturer to ensure the borescope would operate at low temperature and in vacuum. All of the focusing optics are in the room-temperature portion of the borescope, so that thermal contraction of the optics will not alter the focus of the device. All of the vacuum seals are also at room temperature. The shaft of the borescope contains vent holes along its length to facilitate pumping out of the borescope interior and reduce virtual

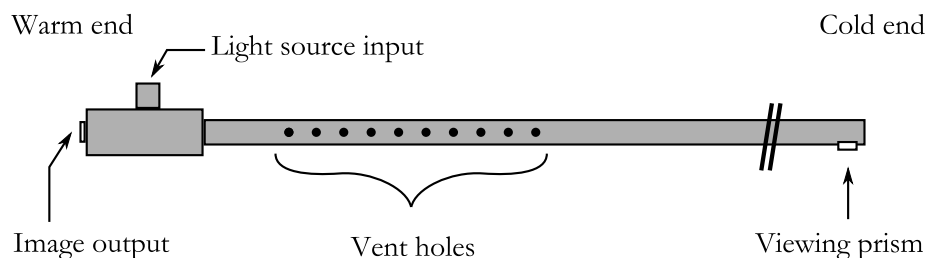


Figure 3.4. Drawing of the borescope, not to scale. The left side of the borescope is the room-temperature end. The focusing optics, camera, and light source connect to this end. The right side the active end, with a  $90^\circ$  imaging prism at the end. For the location of the borescope with respect to the sample cell, see figure 3.3.

leaks. One remaining problem with the optical setup is the nuisance of condensation on the low-temperature window, obscuring the image. The condensation can be prevented by adequately pumping before the probe is submerged in liquid helium and eliminating any vacuum leaks.

### 3.3 Auxiliary Systems

#### 3.3.1 Vacuum System

A 6 mm O.D. stainless-steel pump line extends from the top of the sample cell to room-temperature gas handling equipment. Pumping of the oxygen sample gas is performed by four Varian Vacorb sorption pumps, filled with zeolite getter and cooled by liquid nitrogen. In consideration of the safety challenges of working with oxygen gas at potentially high pressures, we chose these pumps for their low cost and ease of use relative to using mechanical pumps filled with fluorinated lubricant.

Typically, a single sorption pump has sufficient capacity for one experimental run. Having multiple pumps allows us to run experiments for several days before stopping to regenerate the pumps. Before regenerating the sorption pumps after an experimental run, we first vent them to atmosphere overnight. This allows air to dilute the oxygen in the pumps, reducing the fire danger of heating the pumps. The following day the pumps may be safely baked out using an electrical heating jacket.

An MKS 651C pressure controller, actuating an MKS 253A butterfly valve, controls the system

pressure. The pressure is measured by an MKS 626A Baratron sensor placed in front of the butterfly valve. We assume the pressure measured at the pumps is the same as the sample pressure. This control setup allows us to specify any boiling pressure between 10 torr and 1000 torr. For the data presented in this work, we use a nominal pressure of 760 torr, which can be maintained with  $\pm 2$  torr accuracy.

### **3.3.2 Computer Control**

All of the above electronic sensing and control equipment are connected via GPIB to a PC running National Instruments LABVIEW 7.0 software. The sensors are polled sequentially with a cycle of approximately 10 seconds. The control relationships between the various components are summarized in figure 3.5.

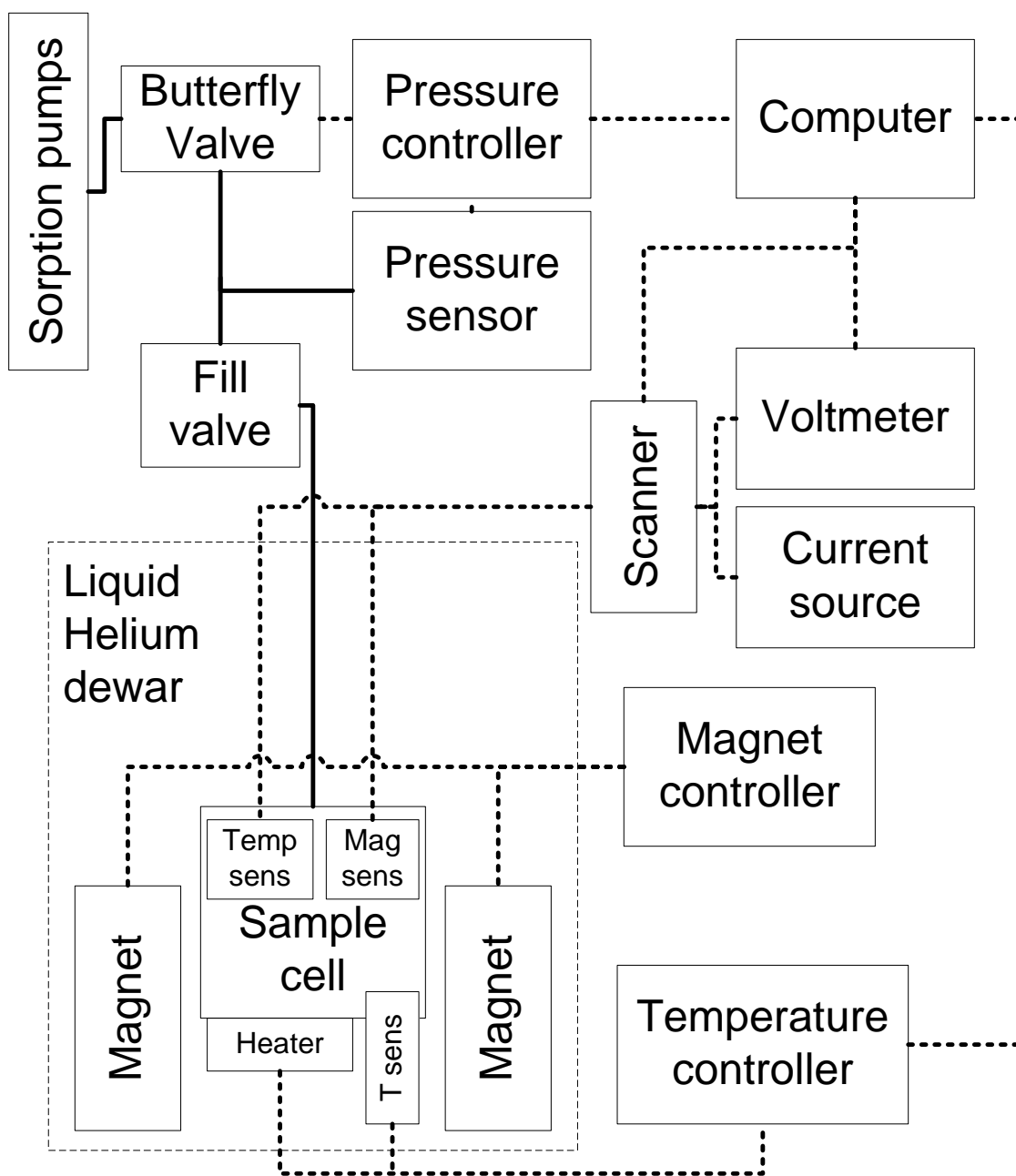


Figure 3.5. A block diagram of controls. The pump lines are indicated by solid lines. Electronic connections are shown by thick dashed lines.

## Bibliography

- [1] R. Kipling. “Natural theology.” In *The Years Between*, Garden City, NY: Doubleday (1919).  
<http://whitewolf.newcastle.edu.au/words/authors/K/KiplingRudyard/verse/p1/theology.html>.
- [2] J. T. Conway. “Exact solutions for the magnetic fields of axisymmetric solenoids and current distributions.” *IEEE Transactions on Magnetics*, **37**:2977–2988 (2001).
- [3] J. D. Jackson. *Classical Electrodynamics*. New York: Wiley, third edition (1999).
- [4] D. R. Lide, editor. *CRC Handbook of Chemistry and Physics*. New York: CRC Press, 79th edition (1998).
- [5] V. K. Dhir. “Boiling heat transfer.” *Annual Reviews of Fluid Mechanics*, **30**:365–401 (1998).  
doi:10.1146/annurev.fluid.30.1.365.
- [6] V. K. Dhir, S. G. Kandlikar, Y. Fujita, Y. Iida, and R. Heist. In S. Kandlikar, M. Shoji, and V. K. Dhir, editors, *Handbook of Phase Change: Boiling and Condensation*, Philadelphia: Taylor and Francis, pp. 63–99 (1999).
- [7] *Coated Abrasives—Grain Size Analysis*. Standard 6334-2, International Organization for Standardization (1998).  
<http://www.iso.org>.
- [8] *Temperature Measurement and Control Catalog*. Westerville, OH: Lakeshore Cryogenics (ca. 2000).

## Chapter 4

### Procedures

**W**E spent much of the first year of this project developing the proper procedures for preparing the experiment and for taking data in a self-consistent manner. These procedures are of crucial importance because of the stochastic nature of boiling dynamics. Historically, boiling experiments have been plagued with irreproducibility [2]. The large variability among data taken under supposedly identical conditions stifles any attempt to develop a predictive model of boiling dynamics. The spreads in the body of data in the literature are so bad (typically 30% in any given experiment e.g., references [3; 4]) that any reasonable model fits, hence the profligation of empirical and phenomenological correlations in the literature [5–12].

Our contribution to the body of work is to isolate one parameter of interest, the effective gravity, and fix all other variables to the extent possible. In particular, we study only one sample fluid (oxygen), have only one type of heater (a horizontal plate of OFHC copper, roughened with 240 grit sandpaper), use only one ambient pressure (one atmosphere), and follow a particular sequence of heater powers, as explained below. Even with all of our precautions, we still have some residual irreproducibility in our data; we identify suspected causes of this residual irreproducibility below in section 4.2.2.

---

\*Used by linotype operators to mark a typographic error, indicating the line of type was to be removed before printing. The letters are the order of keys on a linotype machine, corresponding to the frequency of their use in the English language. (The modern equivalent would be the familiar QWERTY of the computer keyboard.) Sometimes type compositors would miss the marked lines, allowing the mysterious phrase ETAOIN SHRDLU to appear erroneously in newspaper articles. The phrase became an inside joke in the newspaper business. See, for example, an April Fool's Day article in *Time*, 1929 [1].

## 4.1 Sample Filling

An early vexing problem in the development of this project was choosing a method to load the sample fluid into the sample cell. To fill our sample cell with liquid oxygen we must cool the sample cell and then condense oxygen gas into the cell from a cylinder at room temperature until the cell is full. According to [13], the specific enthalpy of oxygen gas at 1 atm and 300 K is  $2.7 \times 10^5$  J/kg, and the specific enthalpy of liquid oxygen at its normal boiling point (1 atm, 90.2 K) is  $-1.3 \times 10^5$  J/kg, for a net change in specific enthalpy of  $-4.0$  J/kg for condensation of liquid from room-temperature gas. To fill our sample cell (volume of  $95 \text{ cm}^3$ ) with liquid oxygen (mass density of  $1100 \text{ kg/m}^3$ ) requires 110 g of oxygen. The key result is that we must remove 44 kJ of heat from room-temperature oxygen gas to condense enough liquid to fill the sample cell. Our initial (admittedly naïve) plan was to use a weak thermal link between the sample cell and the liquid helium bath surrounding the cryogenic probe to remove the heat from the oxygen, perhaps using a measured quantity of helium thermal exchange gas or a heat switch as the thermal link. However, even assuming we could build a suitable thermal link, dumping 44 kJ into the helium bath would boil off 17 L of liquid helium (or in perhaps more relevant units,  $\sim$  \$100). A better method was needed.

Our solution is to use a secondary dewar of liquid nitrogen to cool the probe for the purpose of filling the oxygen cell. Once the sample cell is filled, we move the probe to the liquid helium magnet dewar for the boiling measurements. For thermal exchange we add a sizable amount of helium gas to the vacuum space of the probe ( $\sim$  1 torr). The normal boiling point of liquid nitrogen (77 K) is cold enough to condense oxygen, but still above the triple point of the oxygen (54.4 K), so we do not have to worry about the oxygen freezing (and blocking the pump line, etc.). Using liquid nitrogen also has the advantage that it is inexpensive, so the amount of nitrogen we boil off is irrelevant.

There are some difficulties with this technique of using two dewars. First, we must move the probe between dewars, causing jostling which can disturb wires, pumplines, etc. Secondly, we must repeatedly subject the probe exterior to thermal cycles between 77 and 4 K. Early on, this cycling had a tendency to loosen the screws holding the indium gasket on the bottom flange of the probe. We solved this problem by adding Belleville washers to the screws to maintain compression on the gasket. Cooling the probe from 77 to 4 K also boils off some liquid helium. We estimate we lose 2 L of liquid helium per cool down, an order of magnitude improvement over our initial

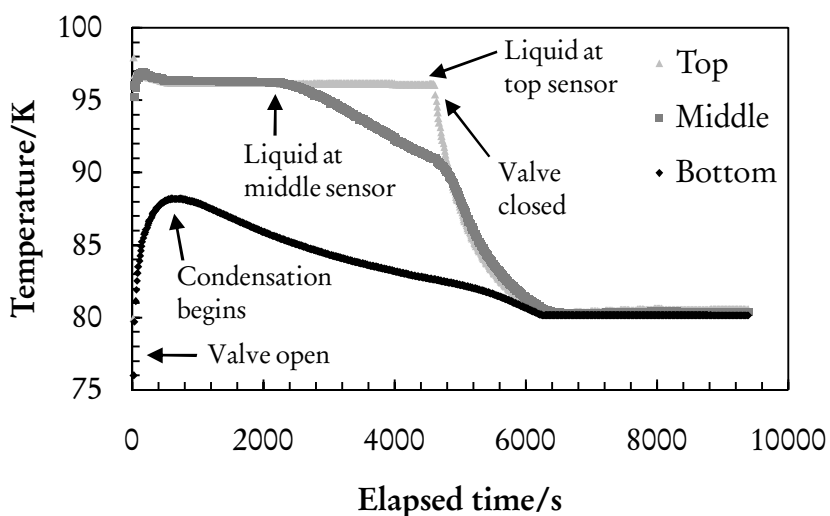


Figure 4.1. Temperature sensor readings of the sample cell as a function of time during the oxygen filling procedure. Notice the decrease in temperature as the liquid level rises above each sensor. (Data taken 20060910.)

strategy.

The third, most serious, issue with our two-dewar method is the difficulty in removing the helium thermal exchange gas before transferring the probe to the liquid helium dewar. This gas must be removed to guarantee good thermal isolation between the sample cell and the helium bath. Using less helium exchange gas during filling does not help; it only makes the condensation process slower. We pump out the exchange gas overnight using a turbomolecular pump, typically yielding pressures in the microtorr range, but this is not low enough pressure. To finish the job of pumping out the exchange gas, we installed a small ( $5 \text{ cm}^3$ ) charcoal pot inside the vacuum space on the bottom flange, see figure 3.3. Upon moving the probe to the helium dewar, this charcoal cools to liquid helium temperature and begins absorbing the remaining exchange gas.

The actual sample condensation process is straightforward. We begin with the probe in the liquid nitrogen dewar and add about 1 torr of helium gas to the probe vacuum space. We connect an oxygen gas cylinder to the fill/pump line valve of the probe and open the valve. As the oxygen condenses and the liquid level in the cell rises, we infer the liquid level by monitoring the sample cell temperature sensors. The temperature of the sensors drops when they come into contact with the liquid, as shown in figure 4.1. We may also monitor the liquid level optically with the borescope. The filling process typically takes about two hours.

After filling the sample cell, we close the fill valve and disconnect the oxygen gas cylinder. We pump on the probe vacuum space with a turbomolecular pump for several hours (typically, overnight) to remove as much helium thermal exchange gas as possible. Next, we disconnect the pump and transfer the probe to the liquid helium dewar.

## 4.2 Data Collection

After transferring the probe we reconnect all sensor wires and connect the sample pump line to our external sorption pumps and pressure controller. At this point we begin logging the sample temperatures, heater power, and pressure. Example time series of these data are shown in figure 4.2. The experimental sequence is described through the next few paragraphs.

To prevent the sample from freezing, we initially set the Lakeshore LS-340 temperature controller to maintain a constant heater temperature slightly below our intended boiling point, typically 90.0 K. We allow the temperature to stabilize, typically waiting 30–60 minutes. We record the heater power required to maintain this constant temperature ( $Q_0$ , usually  $\sim 50$  mW) and interpret it as the heat leak rate from the sample to the helium bath. During this stabilization period we also energize our superconducting magnet to the appropriate current for our desired effective gravity (see section 3.1).

After the temperature stabilizes, we set the pressure controller to our desired pressure (760 torr). Because we are performing constant heater power measurements, we disable the control loop on the temperature controller and set it to output a constant power. For the runs presented here, our initial heater power is 5 W. This choice is discussed further in section 4.2.1, below.

At each value of the heater power, we wait approximately five minutes for the heater temperature to stabilize. We record the heater temperature and heater power. We then change heater power to our next desired value and wait again for the system to stabilize. We repeat this sequence several times until we have collected our desired amount of data.

### 4.2.1 Choice of Heater Power Sequence

Because boiling is an inherently non-equilibrium process, it is reasonable to assume it involves some hysteretic behavior. The possibility of history dependence in the system requires us to carefully select and justify the sequence of events, particularly how we add heat to the system.

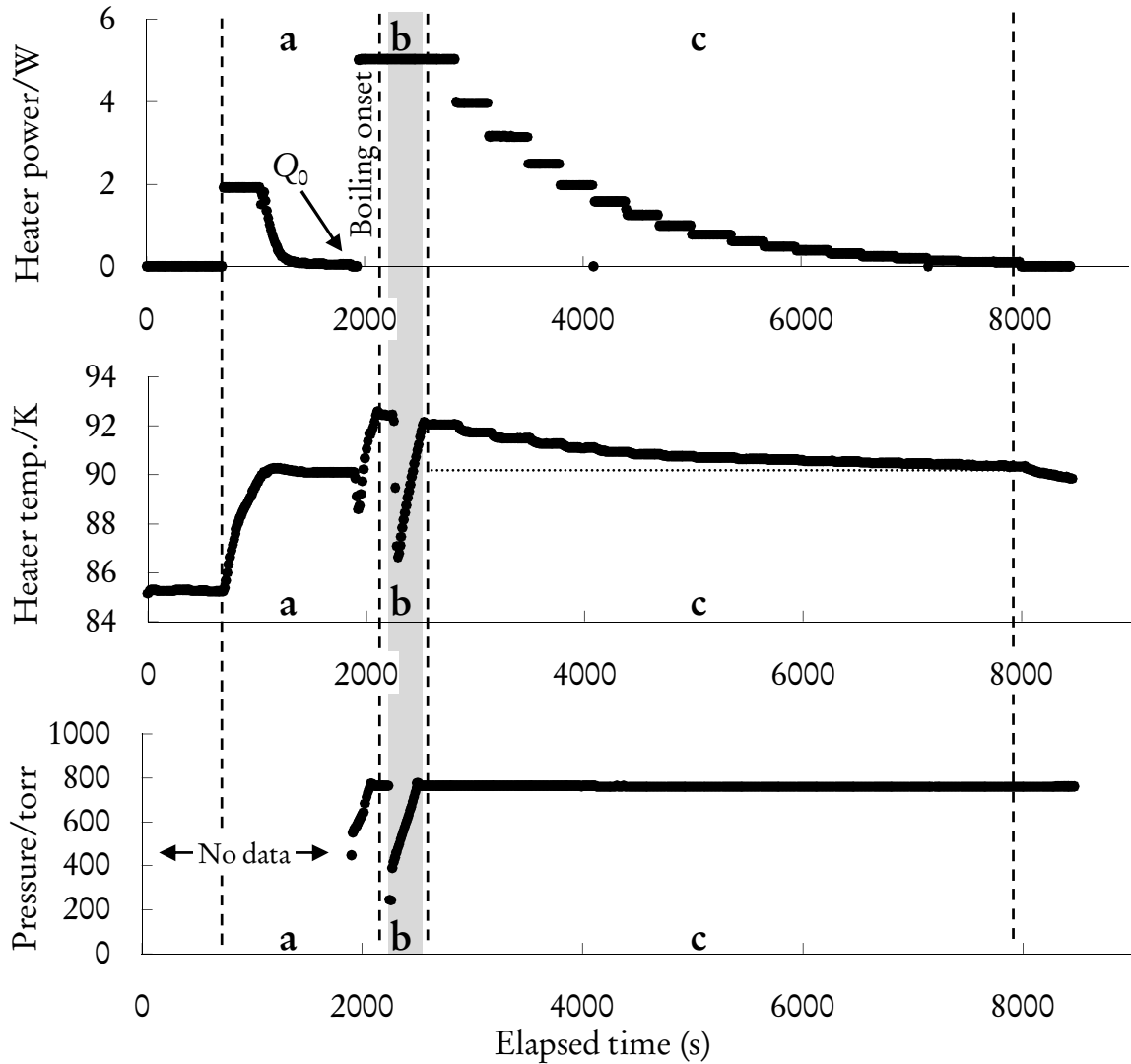


Figure 4.2. A typical data run. The horizontal axis (common to all three frames) shows elapsed time in seconds. The vertical axes show (from top to bottom) heater power, heater temperature, and pressure. Some regions of interest are separated by dashed lines and labeled: (a) warm-up and stabilization, (b) transient behavior (see section 4.2.2), and (c) data collection. The quiescent power ( $Q_0$ ) measurement and the onset of boiling are denoted in the top panel. The horizontal dotted line in the center panel indicates the nominal saturation temperature. (Data taken 20061213.)

Specifically, we have identified at least two times in the course of each experimental run where the history of the system can affect the heater superheat versus heat flux relationship.

The first of these situations is the onset of boiling. If we start with the system in thermal equilibrium under saturated conditions and increase the temperature of the liquid, the liquid will not immediately begin to boil. For small values of heat flux the system will be in a metastable convective mode (see section 2.1.2). So long as the convective heat transport is sufficiently good, the system can remain in the convective mode indefinitely. We are not interested in measuring convection, so we try to avoid this mode. Only when the heat flux is increased beyond some critical value will nucleation sites form on the surface of the heater and boiling commence. Energetically, boiling is the preferred mode because the heat transport is more efficient; the heater temperature is lower for boiling than convection at a given heat flux value. Because we are not interested in the convective mode, we begin our experiments at a relatively high heater power (5 W). This power is sufficient to quickly enter the boiling regime without being trapped in the convection mode for long periods of time.

Some comparison data for the convective and boiling modes in our experiment are shown in figure 4.3. The arrows in the figure show the time sequence of the data points. Initially, heater power is slowly increased from zero and the system stays in a convective mode. At some critical power, the system collapses into the boiling mode and the heater temperature decreases.

The transition from convection to boiling is abrupt and irreversible. Once the system is in the boiling mode, the convective mode can only be regained by stopping the heater power and letting the system re-equilibrate. Also, the heat flux at which the onset of boiling occurs is not very reproducible. An upper bound for the critical superheat can be calculated from an equation of state (see section 2.1.2), but in practice the system cannot reach this value. Because the system is only metastable under conditions sufficiently far from equilibrium, disturbances such as shaking can cause the collapse into boiling so long as there is sufficient energy in the system to form nucleation sites.

An additional irreversible behavior in our system is an apparent dependence on the maximum applied heater power (or, perhaps, maximum heater superheat). The system retains some memory of the maximum heater power used on a given experimental run. This effect is exemplified in a pair of runs with an alternating sequence of applied heater powers, which we have dubbed “stairstep” runs.

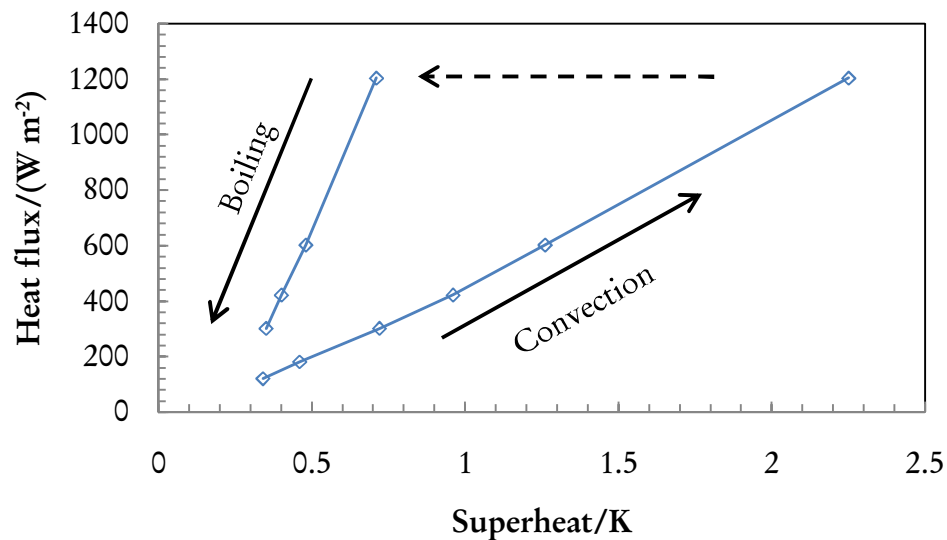


Figure 4.3. Hysteresis between convection and boiling modes. The horizontal axis shows the superheat of the heater and the vertical axis shows the applied heat flux. The arrows indicate the time sequence of the data points. (Data from 20060921)

For the first run, shown in figure 4.4, we begin at a nominal heater power of 5 W. After the temperature stabilizes, we decrease the heater power to 3 W, wait, return to 5 W, wait, decrease the power to an even lower value, return to maximum power, and repeat several times. The top two panels of the figure show the time sequence of heater power and heater temperature. The bottom panel shows the relationship between heater power and heater temperature, with the time sequence indicated by arrows. At every return to maximum power the heater temperature returns to approximately the same value; the system displays no hysteresis.

For the second run, figure 4.5, we invert the power sequence, starting at a low power level (2 W), then increasing to a higher power (3 W). Upon returning to the original low power level, we see that the heater temperature settles at a different value; there is some irreversibility in the system. However, so long as we do not exceed previous values of the maximum power, the power-temperature relationship stays consistent.

The combination of these “stairstep” runs suggests that we should only use monotonically decreasing heater powers during our experimental runs (e.g., region (c) of figure 4.2). We suspect the hysteresis is caused by an increase in number of nucleation sites at higher powers, resulting in improved heat transport and hence lower superheats; the number nucleation sites remains

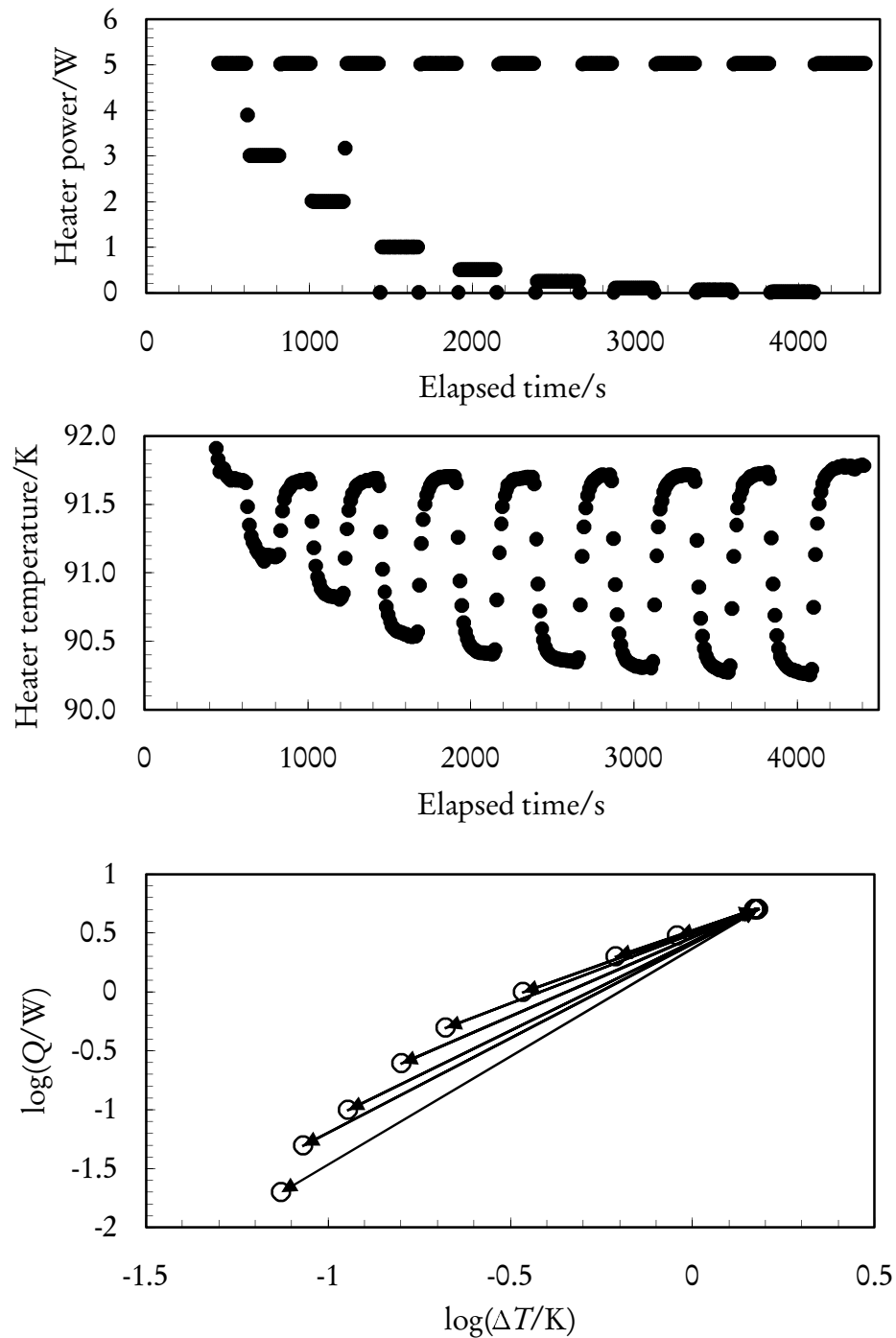


Figure 4.4. Decreasing “stairstep” sequence. The top two panels show heater power and heater temperature, respectively, as functions of elapsed time. The bottom panel plots heater power and heater temperature. (Data taken 20060927)

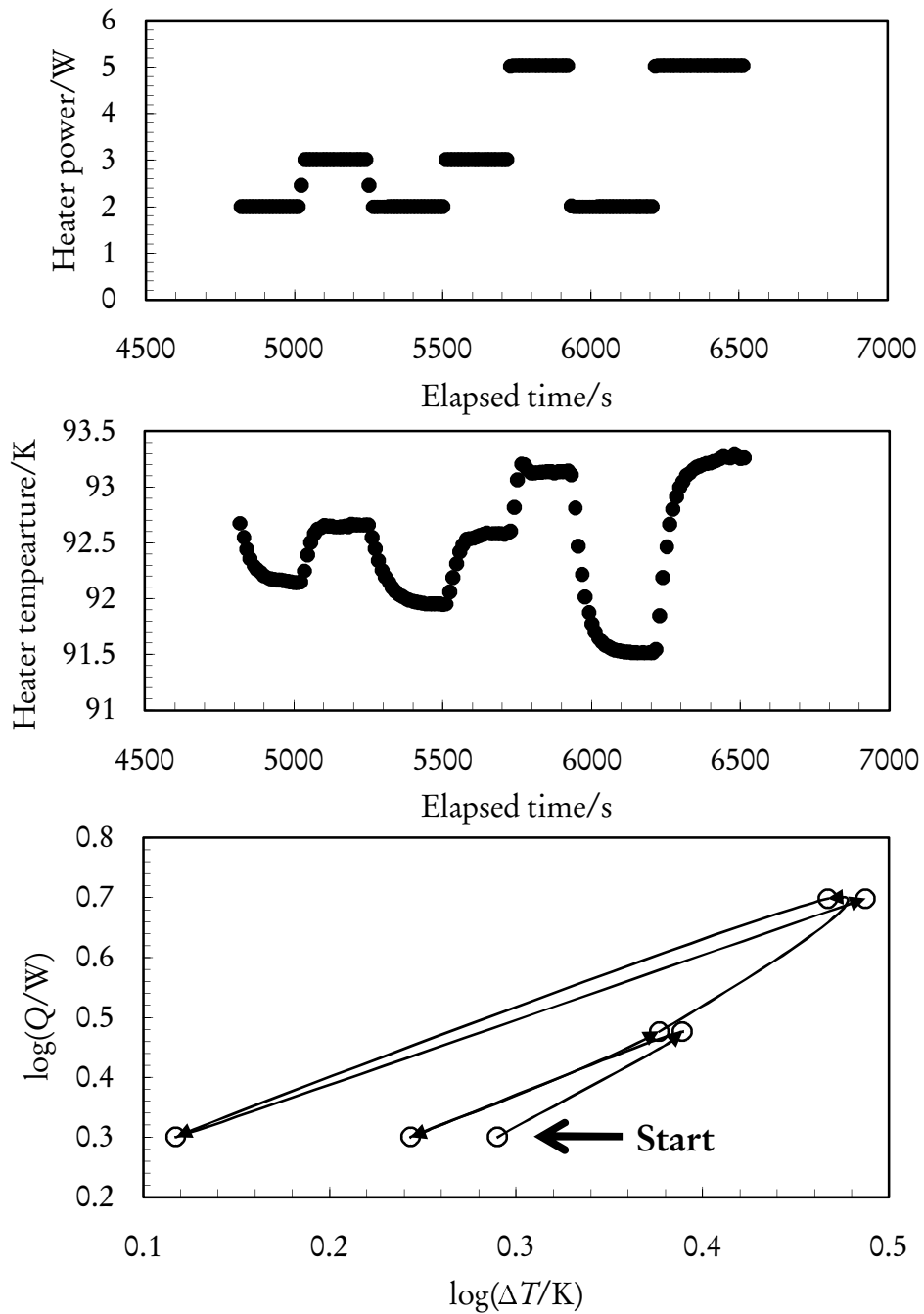


Figure 4.5. Increasing “stairstep” sequence. The top two panels show heater power and heater temperature, respectively, as functions of elapsed time. The bottom panel plots heater power and heater temperature. (Data taken 20060928)

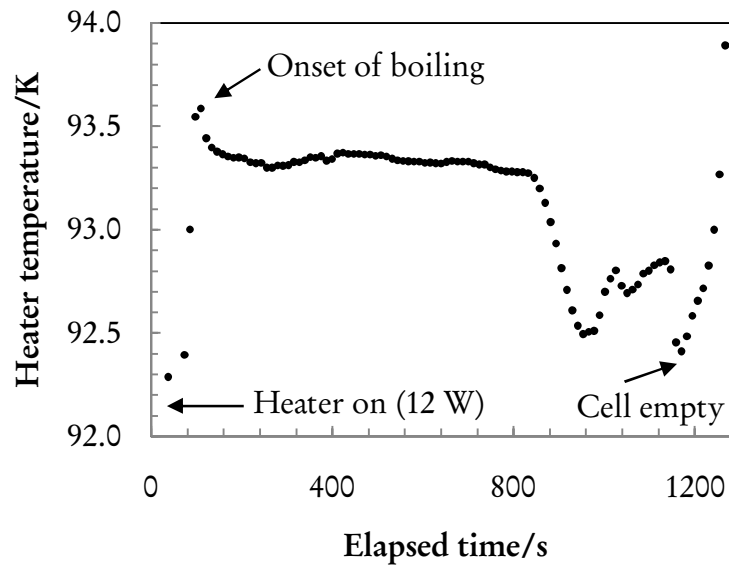


Figure 4.6. Run at constant heater power, to demonstrate long-term steady state behavior. The temperature is approximately constant between 150 and 800 s.

constant when the power decreases, but increases if the power exceeds its previous maximum value. To avoid changing the number of nucleation sites, we only change the heater power by lowering it. In particular, we choose a geometrically decreasing power sequence (with the addition of the constant quiescent heat loss), which allows for better fitting of our low-power power-law relationship between heat flux and superheat (see chapter 6). In our largest data sets the heater power sequence contains ten points per decade, for about three decades.

Also, we neglect any dependence of the heater temperature on the volume of the sample liquid. We assume that for a sufficiently large sample volume, any change in temperature is slow compared to the time scale of the experiment. We validate this assumption by taking a long data run at constant heater power and observing the change in heater temperature to be small, at least when the sample cell is sufficiently full. These data are shown in figure 4.6. Note that the power for this diagnostic data set is 12 W, compared with the maximum value of 5 W used for our experimental data. For lower powers, particular the decreasing power sequence described above, we expect even less drift in the temperature.

### 4.2.2 Transient Effects at Boiling Outset

Occasionally, immediately after the initiation of boiling, the system undergoes control-related pressure and temperature fluctuations. The onset of boiling increases the flow of gas to the pumps which can temporarily destabilize the feedback loop in the pressure controller, causing pressure oscillations for several seconds until the controller reestablishes control. An example of this behavior can be seen in the region “b” (the shaded area) of figure 4.2.

The most immediate effect of this pressure oscillation is that the temperature of the sample also oscillates. But perhaps the more important effect is the drop in the saturation temperature caused by the drop in pressure. The net result of the decreased sample temperature is an intermittently increased superheat, undoing our careful choice of the heat flux sequence (or equivalently, exceeding our maximum desired superheat). Unfortunately, during these transient fluctuations the pressure can fall below the resolution of our pressure gauge, so we are unable to know the actual pressure or superheat, preventing us from quantifying this effect.

## Bibliography

- [1] “Etaoin Shurdlu.” *Time* (April 1, 1929).  
<http://www.time.com/time/magazine/article/0,9171,881281,00.html>.
- [2] V. K. Dhir, S. G. Kandlikar, Y. Fujita, Y. Iida, and R. Heist. In S. Kandlikar, M. Shoji, and V. K. Dhir, editors, *Handbook of Phase Change: Boiling and Condensation*, Philadelphia: Taylor and Francis, pp. 63–99 (1999).
- [3] D. E. Drayer. “Nucleate boiling of hydrogen.” *Industrial and Engineering Chemistry Fundamentals*, **4**:167–171 (1965).
- [4] P. G. Kosky and D. N. Lyon. “Pool boiling heat transfer to cryogenic liquids.” *American Institute of Chemical Engineers Journal*, **14**:372–387 (1968).  
<http://www3.interscience.wiley.com/cgi-bin/abstract/109074109/ABSTRACT>.
- [5] M. G. Cooper. *Industrial and Chemical Engineering Symposium Series*, **86**:786–793 (1984).
- [6] M. G. Cooper. “Heat flow rates in saturated nucleate pool boiling—a wide-ranging examination using reduced properties.” *Advances in Heat Transfer*, **16**:155–239 (1984).
- [7] K. Engleberg-Forster and R. Greif. “Heat transfer to a boiling liquid—mechanism and correlations.” *Journal of Heat Transfer*, **81**:43–53 (1959).
- [8] H. K. Forster and N. Zuber. “Dynamics of vapor bubbles and boiling heat transfer.” *American Institute of Chemical Engineers Journal*, **1**:531–535 (1955).  
<http://www3.interscience.wiley.com/cgi-bin/abstract/109074537/ABSTRACT>.
- [9] R. L. Judd and K. S. Hwang. “A comprehensive model for nucleate pool boiling heat transfer including microlayer evaporation.” *Journal of Heat Transfer*, **98**:623–629 (1976).
- [10] B. B. Mikic and W. M. Rohsenow. *Journal of Heat Transfer*, **91**:245–250 (1969).
- [11] W. M. Rohsenow. “A method of correlating heat-transfer data for surface boiling of liquids.” *Transactions of the American Society of Mechanical Engineers*, **74**:969–976 (1952).
- [12] K. Stephan and M. Abdelsalam. “Heat-transfer correlations for natural convection boiling.” *International Journal of Heat and Mass Transfer*, **23**:73–87 (1980).
- [13] D. G. Friend. *NIST Thermophysical Properties of Pure Fluids Database, NIST Standard Reference Databases*, volume 12. Gaithersburg, MD: U.S. Department of Commerce (1992). PC software version 3.1.

Whom the gods notice, they destroy. Be small...and you will escape the jealousy of the great.

---

Philip K. Dick,  
*The Man in the High Castle*\*

## Chapter 5

### Data

**A**<sub>FTER</sub> collecting the raw data from a particular experimental run, a fair amount of processing is needed to reduce the raw temperature and heater power time-series data into an interpretable set of quantities. The two parameters temperature and power are the core of the experiment. We are interested in the quasi-static values of these quantities; we can neglect the transient behavior and long time-scale drifts in the data.

Next, we turn to the task of correlating these quantities. Traditionally, the relationship between temperature and heater power has been described by power laws (see chapter 2 and references [2-5]), but this form does not completely describe our data. Our choice of fitting function and the physical implications of this choice are discussed below.

### 5.1 Raw Data

#### 5.1.1 Measurement of the Quiescent Heat Leak

Before collecting the heat flux and temperature data, one additional measurement is needed. The recorded heater power value must be corrected to account for the quiescent heat loss  $Q_0$ , which is measured as the amount of heater power needed to maintain constant temperature under constant volume conditions (i.e., without pumping). We interpret this power as heat leaked into the helium bath. To measure  $Q_0$  we set the heater temperature at a point below the saturation temperature using the Lakeshore LS-340 temperature controller, typically 90.0 K. We identify the heater power

---

\*Reference [1]

required to maintain this temperature as the quiescent heat and subtract its value from the other heat measurements. An example of this measurement is shown in region (a) of figure 4.2. The values of  $Q_0$  for the various data runs are given in appendix B.1, typically about 50 mW.

### 5.1.2 Determination of Steady-State Temperatures

The data collection phase of each experimental run follows the pattern of region (c) in figure 4.2. This same data set is shown in more detail as figure 5.1; similar plots for the other data sets are given in appendix B.3. The measured temperature as a function of time for each of our data sets is given in the top panels of these figures. The center and bottom panels demonstrate the steady-state data and fits, described in detail in the next section.

As seen in the top panel of figure 5.1, upon each change of the heater power, the heater temperature settles to some quasi-static value. This settling approximately follows an exponential decay law:

$$T(\tau) = K \exp[-\chi(\tau - \tau_0)] + T_s, \quad (5.1)$$

where  $T$  is the heater temperature,  $\tau$  is elapsed time from the beginning the experiment,  $\tau_0$  is the elapsed time at which the heater power changes. The variables  $K$ ,  $\chi$ , and  $T_s$  are fitting parameters, with  $T_s$  being the steady-state temperature of the heater, our desired quantity. Typically,  $\chi$  is on the order of  $0.03 \text{ s}^{-1}$ . The value of  $K$  depends on the previous value of the heater power.

To perform the fits, we first manually determine the value of  $\tau_0$  by looking at the time series for the heater power, which changes in discrete steps. Then we find the parameter values for equation (5.1) which minimize the  $\chi^2$  error function for the data, where  $\chi^2$  obeys the usual statistical definition:

$$\chi^2 = \sum_{\tau} \frac{[T_{\text{data}}(\tau) - T_{\text{fit}}(\tau)]^2}{\sigma_T^2(\tau)}.$$

The uncertainty in the steady-state temperature,  $\sigma_{T_s}$ , is

$$\frac{1}{\sigma_{T_s}} = \sqrt{\sum_{\tau} \frac{1}{\sigma_T^2}}.$$

We assume  $T_s$  only depends on the applied heat flux ( $q = Q/A$ , with  $Q$  being the heater

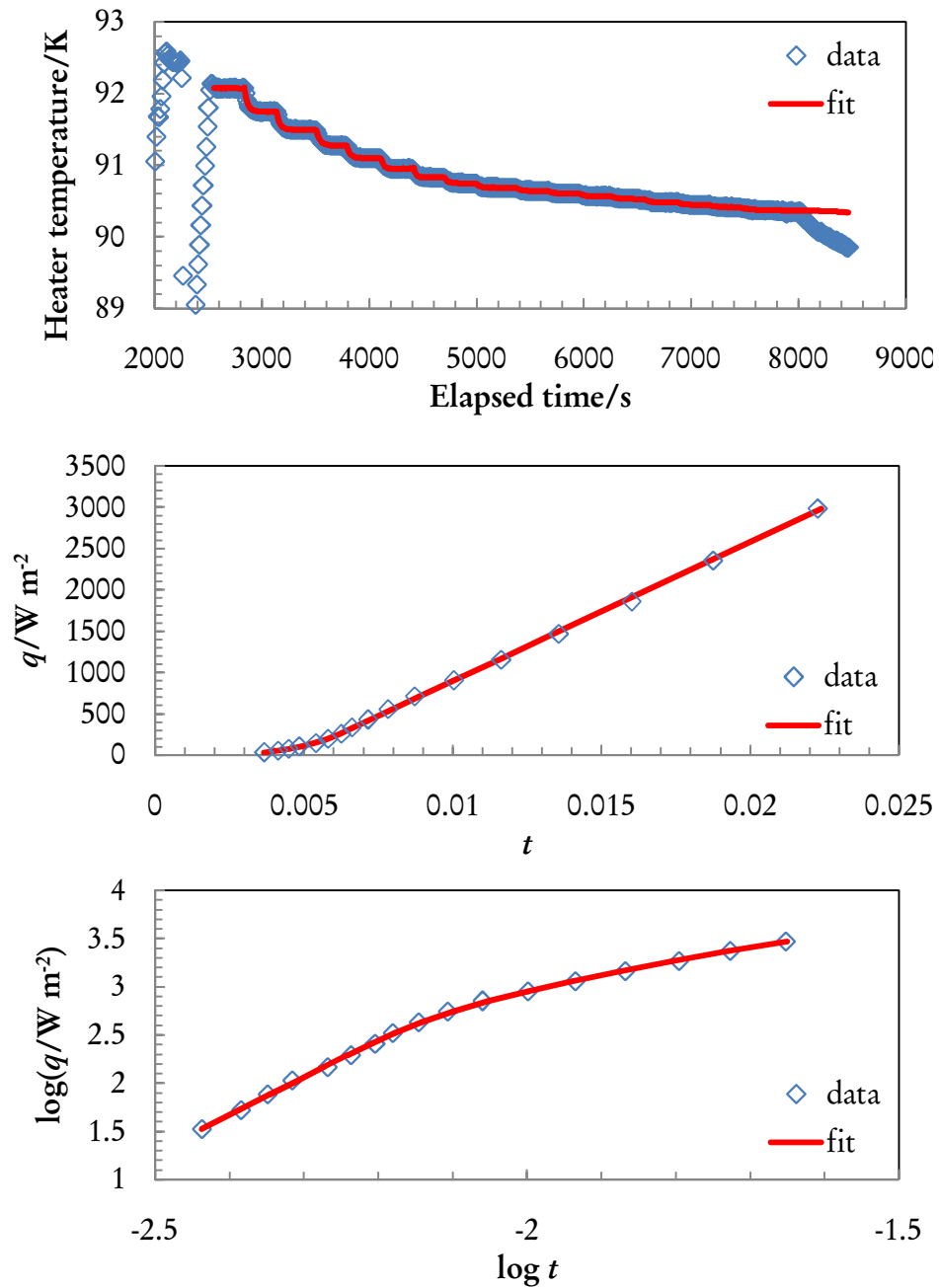


Figure 5.1. An example data set with an effective gravity value of  $g_{\text{eff}} = 6g$ , shown previously in figure 4.2. The top panel shows the heater temperature as a function of elapsed time. The middle and bottom panels show the heat-flux-reduced-superheat data and fits to equation (5.3) on linear and log-log scales, respectively. (Data from 20061213).

power and  $A$  being the area of the heater,  $16.6 \text{ cm}^2$ ) for a fixed value of the saturation pressure ( $760 \pm 2 \text{ torr}$  for all data presented here). In general, the steady-state temperature also depends on the history of the system, but we've chosen our sequence of declining heater powers to maintain a reproducible relationship between  $T_s$  and  $q$ , as discussed previously in section 4.1.

### 5.1.3 Relationship between Superheat and Heat Flux

The literature typically describes boiling dynamics as the relationship between the heater heat flux and the heater superheat (see reviews in [6; 7]). The superheat is defined as the difference between the heater temperature,  $T$  (denoted  $T_s$  in the previous section, but dropping the subscript from here on for brevity), and the saturated boiling temperature of the fluid at the ambient pressure of the experiment,  $T_{\text{sat}}$ . We desire a dimensionless temperature quantity so that our data may be directly compared with other experiments. Also, we wish to somehow remove the ambient pressure as a factor in our analysis. To accomplish these goals, we introduce a new quantity, the reduced superheat:

$$t = \frac{T - T_{\text{sat}}}{T_{\text{sat}}}. \quad (5.2)$$

We cannot directly measure the saturation temperature, but we can calculate its value by measuring the pressure of the system. Using an empirical model of the oxygen equation of state compiled by the National Institute of Standards and Technology (NIST) [8], we calculate the saturation temperature by assuming the measured system pressure is the saturation pressure. We approximate the NIST saturation temperature-pressure relation by a polynomial series near our nominal system pressure of 760 torr (1 atm):

$$\frac{T_{\text{sat}}(P)}{\text{K}} = 80.060 + 1.3332 \times 10^{-2} \left( \frac{P}{\text{torr}} \right) - 1.5964 \times 10^{-11} \left( \frac{P}{\text{torr}} \right)^2 + 7.1054 \times 10^{-15} \left( \frac{P}{\text{torr}} \right)^3.$$

The calculated saturation temperature goes into equation (5.2) along with the measured heater temperature to yield the reduced superheat  $t$ . The steady-state heater temperature (expressed as the reduced superheat) and the applied heat flux for all of our experimental runs are tabulated in appendix B.2.

Next, we need some equation to describe the relationship between these quantities. Our reduced superheat and heat flux data are well described by a piecewise function of the applied heat

flux  $q$ :

$$t(q) = \begin{cases} t_0 + a \left(\frac{q}{q_t}\right)^b & \text{for } q < q_t, \\ t_0 + m \left(\frac{q}{q_t}\right) + c & \text{for } q \geq q_t, \end{cases} \quad (5.3)$$

where the fitting parameter  $q_t$  represents some transition heat flux, and the dimensionless quantities  $a$ ,  $b$ ,  $m$ , and  $c$  are also fitting parameters. To correct for any measurement bias in the temperature, we include an additional constant fitting parameter,  $t_0$ , so that  $t \rightarrow 0$  as  $q \rightarrow 0$ . The values of  $t_0$  for the various data runs are listed in appendix B.2. Also, we require the function to be smooth, with  $t(q)$  and  $\partial t(q)/\partial q$  continuous at  $q = q_t$ . These constraints are equivalent to

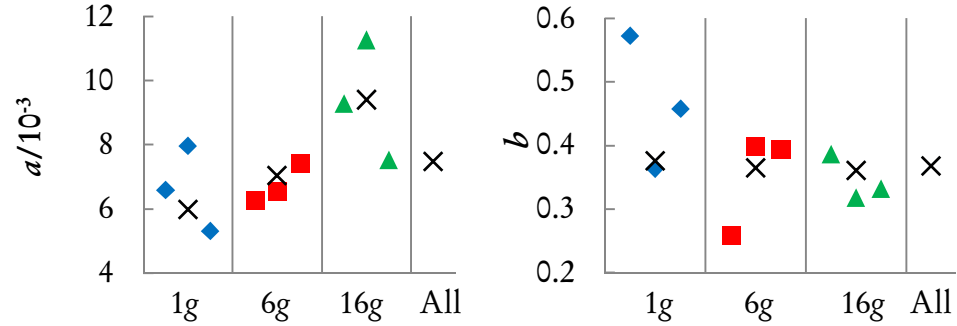
$$m = ab \quad \text{and} \quad c = a(1 - b), \quad (5.4)$$

leaving three independent free parameters per fit. The physical significance of this functional form is discussed in chapter 6, but it should be noted that we are attempting to parametrize the nucleate boiling region of the prototype boiling curve shown previously in figure 2.1 and described in section 2.1.

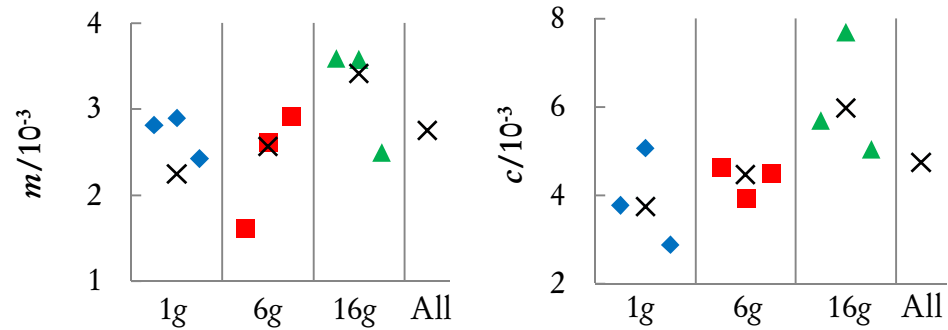
We perform the fitting to equation (5.3) by minimizing the  $\chi^2$  error function of the  $(t, q)$  data with respect to the parameters  $q_t$ ,  $a$ ,  $b$ ,  $m$ , and  $c$ , using the *Solver* function of Microsoft Excel. The uncertainties in the parameters are calculated by finding the deviation in each parameter that increases  $\chi^2$  by unity [9; 10]. We find a closed-form expression for the uncertainties by assuming that the function  $\chi^2(q_t, a, b, m, c)$  can be approximated by a quadratic function in the parameters near the  $\chi^2$  minimum. Details of the uncertainty derivations are given in appendix C.2.

Experimental data sets and the resulting fits to equation (5.3) are shown in appendix B.1 and B.3. Additionally, we performed fits to aggregate data sets, combining all of the data for each value of  $g_{\text{eff}}$  into a single fit. For the aggregates fits, the uncertainties were increased by a factor to account for the scatter in the data. This correction factor is chosen to make the  $\chi^2$  per degree of freedom equal to unity for these aggregate fits. We believe the scatter in the data between runs is caused by transient pressure fluctuations at the onset of boiling, as described previously in section 4.2.2. The fitting parameters, their uncertainties, and fits to aggregates over the various  $g_{\text{eff}}$  summarized in table 5.1 and figure 5.2.

Power-law fit parameters:



Linear fit parameters:



Transition heat flux:

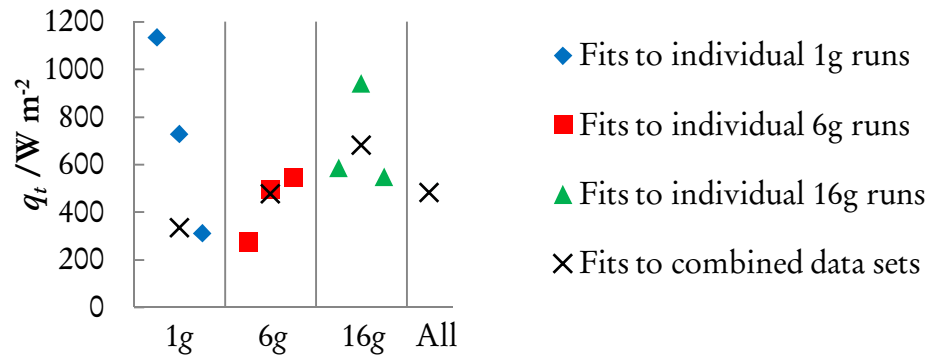


Figure 5.2. Fitting parameters ( $q_t$ ,  $a$ ,  $b$ ,  $c$ , and  $m$ ) from equation (5.3), also in table 5.1. The filled polygons represent individual runs. The crosses indicate fits to aggregate data sets at the specified  $g_{\text{eff}}$ . A fit to the entirety of the data (i.e., neglecting gravity) is included at the right of each panel. The uncertainties in the data are not shown in the graph but are given in table 5.1.

Table 5.1. Fitting parameters ( $q_t$ ,  $a$ ,  $b$ ,  $c$ , and  $m$ ) from equation (5.3) for various data runs and fits to aggregate data sets for each  $g_{\text{eff}}$

| Run date           | Current/A | $g_{\text{eff}}$ | $q_t/\text{Wm}^{-2}$ | $a/10^{-3}$        | $b$                 | $c/10^{-3}$       | $m/10^{-3}$       |
|--------------------|-----------|------------------|----------------------|--------------------|---------------------|-------------------|-------------------|
| 20061103           | 0         | 1                | $1135 \pm 12$        | $6.58 \pm 0.05$    | $0.572 \pm 0.009$   | $3.77 \pm 0.03$   | $2.81 \pm 0.06$   |
| 20061119           | 0         | 1                | $729 \pm 6$          | $7.96 \pm 0.03$    | $0.363 \pm 0.005$   | $5.07 \pm 0.03$   | $2.89 \pm 0.02$   |
| 20070213           | 0         | 1                | $311.1 \pm 0.5$      | $5.299 \pm 0.0074$ | $0.4568 \pm 0.0008$ | $2.879 \pm 0.006$ | $2.421 \pm 0.013$ |
| Combined data set  |           | 1                | $334 \pm 7$          | $5.98 \pm 0.09$    | $0.375 \pm 0.009$   | $3.74 \pm 0.09$   | $2.24 \pm 0.03$   |
| 20061213           | 20        | 6                | $272.2 \pm 0.7$      | $6.27 \pm 0.01$    | $0.2586 \pm 0.0008$ | $4.65 \pm 0.01$   | $1.621 \pm 0.003$ |
| 20061214           | 20        | 6                | $497.4 \pm 1.1$      | $6.55 \pm 0.01$    | $0.3983 \pm 0.0012$ | $3.94 \pm 0.01$   | $2.609 \pm 0.004$ |
| 20070214           | 20        | 6                | $548 \pm 2$          | $7.43 \pm 0.02$    | $0.3938 \pm 0.0018$ | $4.50 \pm 0.01$   | $2.925 \pm 0.007$ |
| Combined data set  |           | 6                | $477 \pm 7$          | $7.03 \pm 0.06$    | $0.364 \pm 0.006$   | $4.47 \pm 0.05$   | $2.56 \pm 0.02$   |
| 20061216           | 34        | 16               | $586 \pm 2$          | $9.3 \pm 0.02$     | $0.386 \pm 0.001$   | $5.69 \pm 0.01$   | $3.585 \pm 0.006$ |
| 20061217           | 34        | 16               | $940 \pm 4$          | $11.3 \pm 0.02$    | $0.317 \pm 0.001$   | $7.69 \pm 0.01$   | $3.574 \pm 0.009$ |
| 20070215           | 34        | 16               | $548 \pm 2$          | $7.53 \pm 0.01$    | $0.331 \pm 0.002$   | $5.035 \pm 0.008$ | $2.493 \pm 0.006$ |
| Combined data set  |           | 16               | $681 \pm 17$         | $9.4 \pm 0.1$      | $0.36 \pm 0.01$     | $5.97 \pm 0.07$   | $3.41 \pm 0.05$   |
| Combined, all runs |           |                  | $482 \pm 7$          | $7.48 \pm 0.06$    | $0.367 \pm 0.006$   | $4.74 \pm 0.05$   | $2.75 \pm 0.02$   |

## Bibliography

- [1] P. K. Dick. *The Man in the High Castle*. New York: Vintage (1962).
- [2] M. G. Cooper. "Heat flow rates in saturated nucleate pool boiling—a wide-ranging examination using reduced properties." *Advances in Heat Transfer*, **16**:155–239 (1984).
- [3] K. Engleberg-Forster and R. Greif. "Heat transfer to a boiling liquid—mechanism and correlations." *Journal of Heat Transfer*, **81**:43–53 (1959).
- [4] W. M. Rohsenow. "A method of correlating heat-transfer data for surface boiling of liquids." *Transactions of the American Society of Mechanical Engineers*, **74**:969–976 (1952).
- [5] K. Stephan and M. Abdelsalam. "Heat-transfer correlations for natural convection boiling." *International Journal of Heat and Mass Transfer*, **23**:73–87 (1980).
- [6] V. K. Dhir, S. G. Kandlikar, Y. Fujita, Y. Iida, and R. Heist. In S. Kandlikar, M. Shoji, and V. K. Dhir, editors, *Handbook of Phase Change: Boiling and Condensation*, Philadelphia: Taylor and Francis, pp. 63–99 (1999).
- [7] H. Merte. "Nucleate pool boiling in variable gravity." In J. N. Koster and R. L. Sani, editors, *Low-Gravity Fluid Dynamics and Transport Phenomena, Progress in Astronautics and Aeronautics*, volume 130, Washington: American Institute of Astronautics and Aeronautics, pp. 15–72 (1990).
- [8] D. G. Friend. *NIST Thermophysical Properties of Pure Fluids Database, NIST Standard Reference Databases*, volume 12. Gaithersburg, MD: U.S. Department of Commerce (1992). PC software version 3.1.
- [9] P. R. Bevington and D. K. Robinson. *Data Reduction and Error Analysis for the Physical Sciences*. New York: McGraw-Hill, third edition (2003).
- [10] W. H. Press, W. T. Vetterling, S. A. Teukolsky, and B. P. Flannery. *Numerical Recipes in C*. New York: Cambridge, second edition (1992).

It's not easy working with a piece of data that could kill you.

---

Neal Stephenson, *Snow Crash*\*

## Chapter 6

### Analysis

**R**EDUCING megabytes of raw data to a small number of meaningful parameters is perhaps the most difficult part of understanding an experiment. This is particularly true when there is no pre-existing theory for the experiment. As was related in chapter 2, no mechanistic model of nucleate pool boiling exists to date. Those models which do exist are constricted by caveats and special conditions—obtaining even order-of-magnitude agreement with experiment is considered victory. This paucity of definitiveness in the literature is in some ways a boon to the experimentalist: we can propose our own models for our data, provided we can defend their plausibility. Critics can only shrug their shoulders and say, “maybe...”

As mentioned in the previous chapter, the fitting function we use to model our boiling data is

$$t(q) = \begin{cases} t_0 + a \left(\frac{q}{q_t}\right)^b & \text{for } q < q_t, \\ t_0 + m \left(\frac{q}{q_t}\right) + c & \text{for } q \geq q_t, \end{cases}$$

subject to the smoothness constraints

$$m = ab \quad \text{and} \quad c = a(1 - b).$$

The low heat flux power law form of the above fitting function was chosen for comparison with many empirical and theoretical correlations in the literature, such as references [2–5]. However, this form alone can not fit the full heat flux range of our data. This is most apparent in the log-log

---

\*Reference [1]

plots where the data have a definite bend near  $q \sim 500 \text{ W/m}^2$  (see plots in figure 5.1 and appendix B.3). For initial comparisons, we neglect the high heat flux portion of the data and consider only the low heat flux power law behavior below this transition heat flux. Having chosen the low heat flux parameters, the values of the high heat flux parameters of the fitting equation are fixed by the smoothness constraints (equation (5.4)). Below we compare our fitting parameters with models and experiments in the literature and offer suggestions to explain the deviation of our data from the accepted models.

## 6.1 Gravity-Independent Effects

### 6.1.1 Comparison with Correlations

One robust result is that the power law exponent at low heat flux,  $b$ , has a value of 0.37 which is independent of the effective gravity, as shown in table 5.1 and figure 5.2. This value is very similar to the exponent in most empirical correlations of  $b \sim 1/3$  [2–6].

To compare the measured value of  $a$  with the correlations from the literature requires rewriting the correlations and our fitting function (equation (5.3)) into similar forms:

$$\Delta T = \tilde{a} q^b, \quad (6.1)$$

where the new coefficient  $\tilde{a}$  is related to the original fitting parameters by

$$\tilde{a} = a T_{\text{sat}} / q_t^b, \quad (6.2)$$

and SI units are assumed. The calculated values of  $\tilde{a}$  for the aggregate data sets at each value of effective gravity are given in table 6.1. Our goal is to calculate the values of  $\tilde{a}$  and  $b$  predicted by the various correlations in section 2.2.1 and compare to the values for our experimental data.

Rearranging terms of the Rohsenow (equation (2.5)), Stephan-Abdelsalam (equation (2.6)), and Cooper (equation (2.8)) yield the following expressions, respectively:

$$\Delta T_R = 0.029 g^{-1/6} q^{1/3}, \quad (6.3)$$

$$\Delta T_{SA} = 21.2 q^{0.376}, \quad (6.4)$$

$$\Delta T_C = 0.051 q^{1/3}. \quad (6.5)$$

Table 6.1. Reparametrization of fits to experimental data, for ease of comparison with results from the literature

|                      | 1g                | 6g                | 16g             |
|----------------------|-------------------|-------------------|-----------------|
| $a/10^{-3}$          | $5.95 \pm 0.09$   | $7.03 \pm 0.06$   | $9.4 \pm 0.1$   |
| $b$                  | $0.375 \pm 0.009$ | $0.364 \pm 0.006$ | $0.36 \pm 0.01$ |
| $q_t/\text{Wm}^{-2}$ | $334 \pm 7$       | $477 \pm 7$       | $681 \pm 17$    |
| $\tilde{a}$          | 0.0607            | 0.0672            | 0.081           |

Table 6.2. Values of the coefficients  $\tilde{a}$  and  $b$  from equation (6.1) from our experiment and calculated from references [4–6]

|                          | 1g                | 6g                | 16g             |
|--------------------------|-------------------|-------------------|-----------------|
| $\tilde{a}_{\text{exp}}$ | 0.0607            | 0.0672            | 0.081           |
| $b_{\text{exp}}$         | $0.375 \pm 0.009$ | $0.364 \pm 0.006$ | $0.36 \pm 0.01$ |
| $\tilde{a}_{\text{R}}$   | 0.029             | 0.022             | 0.018           |
| $b_{\text{R}}$           | ←————             | 1/3               | ————→           |
| $\tilde{a}_{\text{SA}}$  | ←————             | 21.2              | ————→           |
| $b_{\text{SA}}$          | ←————             | 0.376             | ————→           |
| $\tilde{a}_{\text{C}}$   | ←————             | 0.051             | ————→           |
| $b_{\text{C}}$           | ←————             | 1/3               | ————→           |

The dependence of the Rohsenow correlation on gravity is explicitly shown above; the Stephan-Abdelsalam and Cooper correlations neglect gravity. Note that the Stephan-Abdelsalam coefficient is three orders of magnitude larger than Rohsenow, Cooper, and our experiment. This is somewhat surprising because equation (2.7) was taken directly from [5] as an equation for oxygen boiling on a copper plate. We have no explanation for this discrepancy at this time.

The predicted coefficients and the experimentally determined values are summarized in table 6.2. Our values of  $b$  agree quite well with all of the correlations, and the experimental values of  $\tilde{a}$  agree within a factor of three with Rohsenow and Cooper. The disagreement with Stephan-Abdelsalam is several orders of magnitude, however. The various correlations and fits to equation (5.3) are displayed with the experimental data in figure 6.1.

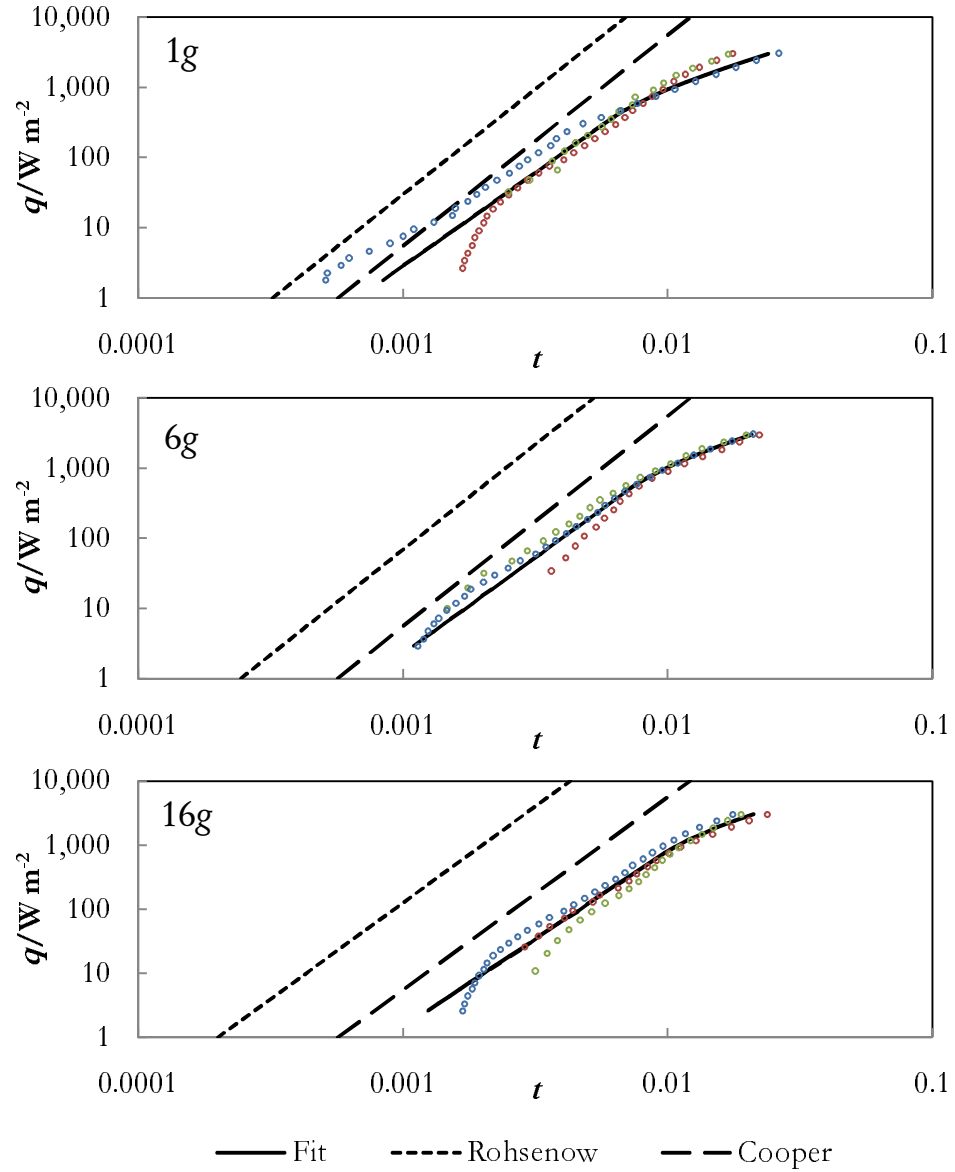


Figure 6.1. Fits of equation (5.3) (solid and dashed lines) to aggregate data sets (open dots, colors representing individual experimental runs) for each value of effective gravity and predictions of Rohsenow (equation (2.5)) and Cooper (equation (2.8)). The prediction of Stephan and Abdelsalam (equation (2.6)) is off scale to the right. See also table 5.1 and figures 5.2 and 6.3.

### 6.1.2 High Heat-Flux Behavior

We append the linear portion of the fitting function and smoothness constraints to remedy the poor fits at high heat flux without adding an excessive number of free parameters. Clues to this change in heat transport behavior appear in some of the more recent literature. Experiments by Kim and colleagues [7] using microheater arrays (see section 2.2.2) also show a linear heat-flux–superheat relationship at high superheat values (see figure 15 of reference [7]) when they remove data corresponding to regions of the heater array which dry out. In more recent work, the Kim group proposes a transient conduction model which predicts  $q$  is proportional to  $\Delta T$  for the case where the heater surface contains transient dry spots [8]. As the dry spot moves or changes in size, liquid re-wets the heater. The primary heat transfer in the system during this re-wetting is by conduction into the newly formed liquid layer as it covers previously dry regions. Kim et al. argue that because conduction is a less efficient heat transfer mechanism than nucleate boiling or convection, the overall heat transfer efficiency will be linear in this configuration.

Other interesting data from the literature are numerical simulations by Son and Dhir [9], which show a kink in the boiling curve at high heat flux values. For low heat flux, they see  $\Delta T$  proportional to  $q^{1/3}$ , which agrees with our measurements and the empirical correlations. At high heat fluxes, however, the data show linear behavior similar to our experiment. In these simulations the linear regime corresponds to configurations where the nucleation site density and waiting time between individual bubble nucleation events is independent of heat flux. We cannot observe individual nucleation sites with our current experimental setup, but confirmation of the number of nucleation sites and waiting time may be possible with improved optics and a high-speed camera. If the number of nucleation sites is indeed fixed at high heat flux, this could possibly explain the “stairstep” runs of section 4.2.1 (see figures 4.4 and 4.5): at high heat flux the number of nucleation sites is fixed, but at low heat flux the number of nucleation sites may vary, resulting in hysteresis.

In personal conversation with Dhir [10], he suggested that our linear behavior at high heat fluxes may also be due to partial transient dry out of the heater surface, similar to the effect seen in the Kim experiments described above. Furthermore, Dhir describes this condition as essentially a form of transition boiling (see section 2.1.4). Because the conduction heat transfer in the gas is much lower than the liquid, under partially dry conditions the total heat transfer is less efficient, resulting in the change from a power law to a linear relation.

Our experiment is fundamentally different than most other experiments in the literature

because our heater has a large heat capacity. Our heater is a copper block with a volume of approximately  $30 \text{ cm}^3$ . Using the properties in table 2.1, the heat capacity of the heater block at  $90.2 \text{ K}$  is calculated to be approximately  $50 \text{ J/K}$ . This is in comparison to the heat capacity of the liquid oxygen sample, which is about  $180 \text{ J/K}$  for a full sample cell. Because the heat capacity of the heater and the sample are similar in magnitude, especially after a sizable fraction of the liquid boils away, the heater temperature will not respond quickly to changes in the fluid temperature, effectively time averaging the temperature data. Also, because of the high thermal conductivity of the copper, the heater temperature will be approximately uniform across the heater surface, resulting in effective spatial averaging of the heater temperature as measured by the embedded temperature sensor. In contrast, other experiments typically use a heater with as little heat capacity as possible (e.g., thin plates or wires [7; 11]) to decouple the thermal properties of the heater from the sample and allow the boiling dynamics to be more visible.

We conjecture (based on discussions with Dhir [10]) that this averaging effect in our system may smooth out the dip in the boiling curve through the transition boiling regime, because transition boiling itself is essentially a fluctuation between nucleate and film boiling modes. This implies a boiling curve similar to that depicted in figure 6.2. Our linear boiling curve at high heat flux could be indicative of this new transition boiling mode. The occurrence of this mode could be confirmed by observing transient drying out of the heater surface, but this observation would require changes to our optics.

Our conjecture would also imply that the transition heat flux  $q_t$  from our fitting equation (see equation (5.3)) is in fact the critical heat flux which separates nucleate boiling from transition boiling. In the typical boiling curve, the critical heat flux is defined as the local maximum in  $q(t)$  curve (figure 6.2). Models exist for predicting the critical heat flux  $q_{\text{CHF}}$ , the most commonly used being the Zuber correlation [12] (see also equation (2.4)):

$$q_{\text{CHF}} = 0.131 \rho_g^{1/2} h_{lg} \left[ \sigma g (\rho_l - \rho_g) \right]^{1/4}. \quad (6.6)$$

For our system under Earth gravity the predicted  $q_{\text{CHF}}$  is approximately  $2 \times 10^5 \text{ W/m}^2$ . This is about 1000 times our measured value of  $q_t$ , casting doubt on our conjecture that  $q_t$  is equivalent to  $q_{\text{CHF}}$ . However, equation (6.6) notably does not contain any heater parameters such as heat capacity, surface roughness, or contact angle. This negligence of the heater properties may invalidate the Zuber model, particularly under low-gravity conditions when microscopic effects become more

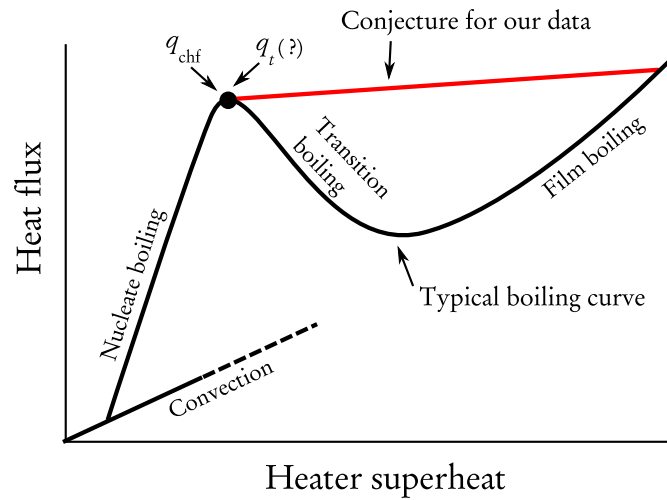


Figure 6.2. Conjectured boiling curve for our experiment (plotted on a log-log scale), based on a suggestion by Dhir [10]. The typical qualitative boiling curve is shown in black (also shown in figure 2.1). Our conjecture appears in red.

important [13]. This may effect the magnitude of  $q_{CHF}$ , but Zuber's functional form is determined by dimensional analysis, so the magnitude is suspect anyway. In particular, Zuber does predict dependence of  $q_{CHF}$  on gravity. As shown below, we can compare this dependence to our data for  $q_t$  to give some insight into the relation between  $q_{CHF}$  and  $q_t$ .

## 6.2 Gravity Dependence

Following the data reduction described in the previous chapter, we have a manageable set of parameters with which we can assess the role of gravity on the experiment. A brief glance at figure 5.2 and table 5.1 shows scatter in the data between individual runs. Despite this scatter, we can still make some judgment about gravity dependence, particularly if we consider the fits to aggregations of data sets at each value of  $g_{eff}$  (figures 6.3, 6.1, and the crosses in figure 5.2). The curves which fit the aggregate data sets are summarized in figure 6.3. The values of the fitting parameters for these fits are shown earlier in table 5.1 and figure 5.2.

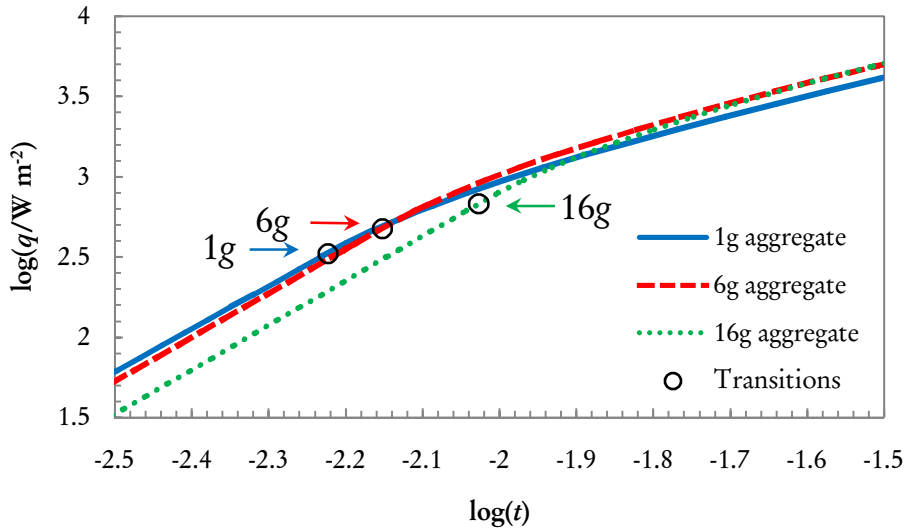


Figure 6.3. A summary plot of the fitting of equation (5.3) (lines) to aggregate data sets (data not shown) for each value of effective gravity. The calculated transition heat flux values  $q_t$  for the various  $g_{\text{eff}}$  are indicated by circles and arrows. Note the general trend between  $q_t$  and  $g_{\text{eff}}$ .

### 6.2.1 Comparison with Empirical Correlations

As noted earlier, the value of the power law exponent,  $b$ , appears to be independent of gravity, having a value of 0.37 when averaged over all data. This is consistent with various correlations in the literature which have this exponent at the fixed value of  $b = 1/3$  [2–6].

The gravity dependence of the other parameters in our fits is less certain because of scatter in the data. Using the fitting parameters for the combined data sets, figure 5.2 and table 5.1 suggest the power law coefficient  $a$  increases linearly with increasing  $g_{\text{eff}}$ :

$$a/10^{-3} = 0.23 g_{\text{eff}}/g + 5.71, \quad (6.7)$$

with an  $R^2$  fitting correlation of 0.9992. If instead we use the reparametrization given above in equation (6.2) the relation between  $\tilde{a}$  and  $g_{\text{eff}}$  becomes

$$\tilde{a}/10^{-3} = 1.34 g_{\text{eff}}/g + 59.5, \quad (6.8)$$

with an  $R^2$  fitting correlation of 0.99996. The literature generally predicts a power-law relation between the coefficient  $\tilde{a}$  and gravity [4; 5]. Of the correlations considered here, only Rohsenow

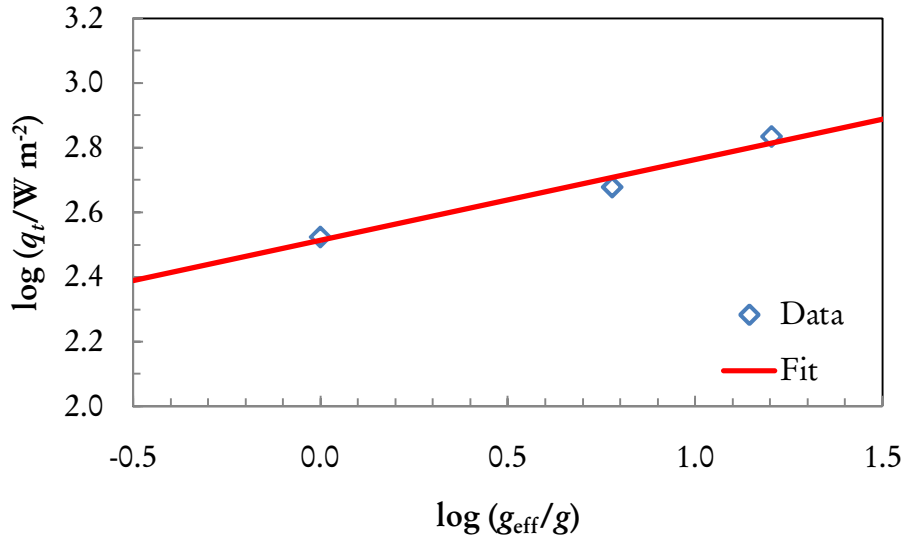


Figure 6.4. Transition heat flux  $q_t$  as a function of effective gravity  $g_{\text{eff}}$  on a log-log plot. The line indicates the fitting function  $\log(q_t/\text{Wm}^{-2}) = 2.5 + 0.25 \log(g_{\text{eff}}/g)$ .

predicts gravity dependence, predicting  $\tilde{a}$  to vary as  $g^{-1/6}$  [4] (see equations (2.5) and (6.3)). Interestingly, the form of a power law fit to our  $\tilde{a}(g)$  experimental data fails, having an  $R^2$  value of only 0.88.

The final free parameter in our fitting function is the transition heat flux  $q_t$ , also described briefly in the previous section. The value of  $q_t$  seems to increase with an increase in effective gravity. This trend supports the conjecture of the previous section that  $q_t$  is the critical heat flux,  $q_{\text{chf}}$ . The Zuber model for critical heat flux (equation (6.6)), predicts  $q_{\text{chf}}$  is proportional to  $g^{1/4}$ . Recent consensus in the literature is that the factor of  $g$  in the equation should be treated only as a dimensional constant, not a variable [14]. However, our data do show that  $q_t$  scales approximately as  $g^{1/4}$ , as shown in figure 6.4. Specifically, our data obey

$$q_t = \left(320 \text{ W/m}^2\right) \left(\frac{g_{\text{eff}}}{g}\right)^{0.25}. \quad (6.9)$$

Because  $q_t$  has the same gravity dependence as that predicted for  $q_{\text{chf}}$ , the conjecture that  $q_t$  is the same as  $q_{\text{chf}}$  has more credence. The disparity in the magnitude is less important, especially since the Zuber model for  $q_{\text{chf}}$  neglects the heater parameters.

Combining equations (5.3), (5.4), (6.7) and (6.9) yields our complete expression for the depen-

dence of the superheat on the heat flux, for arbitrary gravities (all units in SI):

$$\frac{\Delta T}{T_{\text{sat}}} = \begin{cases} \left[ 2.7 \times 10^{-5} \left( \frac{g_{\text{eff}}}{g} \right) + 6.8 \times 10^{-4} \right] \left( \frac{g_{\text{eff}}}{g} \right) q^{0.37} & \text{for } q < q_t; \\ \left( \frac{g_{\text{eff}}}{g} \right)^{-0.25} \left[ 2.7 \times 10^{-7} \left( \frac{g_{\text{eff}}}{g} \right) + 6.60 \times 10^{-6} \right] q \\ + \left[ 1.4 \times 10^{-4} \left( \frac{g_{\text{eff}}}{g} \right) + 3.74 \times 10^{-3} \right] & \text{for } q > q_t. \end{cases} \quad (6.10)$$

## 6.2.2 Comparison with Other Experiments

The most comparable experiment in the literature to the present work is that of Merte and colleagues (reviewed in [15; 16], pp. 48–50) on nucleate pool boiling of nitrogen in a centrifuge, for accelerations between  $-1g$  and  $+20g$ . The thermodynamic properties of nitrogen (e.g., boiling point, latent heat, density) are similar to oxygen, so we should be able to compare our data with Merte’s data, at least qualitatively. Merte finds that increasing the effective gravity above Earth gravity increases the superheat at higher heat flux, but decreases the superheat at low heat flux ( $q \lesssim 10^4 \text{ W/m}^2$ ). By analyzing Merte’s data, we see that these data do not fit our model, but rather a simple power law,  $t \propto q^b$ , with exponents ranging from  $b = 0.17$  at  $g_{\text{eff}} = 1g$  to  $b = 0.28$  at  $g_{\text{eff}} = 20g$ . This is in contrast to our measured value of  $b = 0.37$  at all gravity levels. The disagreement in the exponent  $b$  could be related to our choice of heater. While Merte also uses a large copper block for his heater body, the surface of his heater is coated with stainless steel. Also, Merte does not specify the roughness of the heater surface.

Other experiments at increased gravity have not developed quantitative models of the effect of gravity on boiling, the majority of these being aircraft flight experiments with necessarily short durations [7]. Most of the work at altered gravity has focused on microgravity conditions using drop towers, parabolic-trajectory aircraft, and space-based experiments [13; 17; 18]. Our data are not directly applicable to these low- $g$  experiments, although with modest modifications to the magnet dewar we could take data in this regime, as described in sections 3.1.2 and 7.2.

## Bibliography

- [1] N. Stephenson. *Snow Crash*. New York: Bantam (1992).
- [2] M. G. Cooper. "Heat flow rates in saturated nucleate pool boiling—a wide-ranging examination using reduced properties." *Advances in Heat Transfer*, **16**:155–239 (1984).
- [3] K. Engleberg-Forster and R. Greif. "Heat transfer to a boiling liquid—mechanism and correlations." *Journal of Heat Transfer*, **81**:43–53 (1959).
- [4] W. M. Rohsenow. "A method of correlating heat-transfer data for surface boiling of liquids." *Transactions of the American Society of Mechanical Engineers*, **74**:969–976 (1952).
- [5] K. Stephan and M. Abdelsalam. "Heat-transfer correlations for natural convection boiling." *International Journal of Heat and Mass Transfer*, **23**:73–87 (1980).
- [6] M. G. Cooper. *Industrial and Chemical Engineering Symposium Series*, **86**:786–793 (1984).
- [7] J. Kim, J. F. Benton, and D. Wisniewski. "Pool boiling heat transfer on small heaters: effect of gravity and subcooling." *International Journal of Heat and Mass Transfer*, **45**:3919–3932 (2002).  
doi:10.1016/S0017-9310(02)00108-4.
- [8] J. G. Myers, V. K. Yerramilli, S. W. Hussey, G. F. Yee, and J. Kim. "Time and space resolved wall temperature and heat flux measurements during nucleate boiling with constant heat flux boundary conditions." *International Journal of Heat and Mass Transfer*, **48**:2429–2442 (2005). doi:10.1016/j.ijheatmasstransfer.2004.12.050.
- [9] G. Son and V. K. Dhir. "Numerical simulation of nucleate boiling on a horizontal surface at high wall superheats." *International Journal of Heat and Mass Transfer* (2007). Submitted.
- [10] V. K. Dhir (2007). Personal communication, 13 Apr. 2007.
- [11] A. Mukherjee and V. K. Dhir. "Study of lateral merger of vapor bubbles during nucleate pool boiling." *Journal of Heat Transfer*, **126**(6):1023–1039 (2004). doi:10.1115/1.1834614.
- [12] N. Zuber. *Hydrodynamic Aspects of Boiling Heat Transfer*. Ph.D. thesis, University of California, Los Angeles (1959).
- [13] J. Kim. "Review of reduced gravity boiling heat transfer: US research." *Japan Society of Microgravity Application Journal*, **20**:264–271 (2003).  
<http://www.glue.umd.edu/~kimjh/Documents%20and%20movies/US%20Research.pdf>.
- [14] V. K. Dhir, S. G. Kandlikar, Y. Fujita, Y. Iida, and R. Heist. In S. Kandlikar, M. Shoji, and V. K. Dhir, editors, *Handbook of Phase Change: Boiling and Condensation*, Philadelphia: Taylor and Francis, pp. 63–99 (1999).

- [15] H. Merte. "Nucleate pool boiling in variable gravity." In J. N. Koster and R. L. Sani, editors, *Low-Gravity Fluid Dynamics and Transport Phenomena, Progress in Astronautics and Aeronautics*, volume 130, Washington: American Institute of Astronautics and Aeronautics, pp. 15–72 (1990).
- [16] M. E. Ulucakli and H. Merte. "Nucleate boiling with high gravity and large subcooling." *Journal of Heat Transfer*, 112:451–457 (1990).
- [17] P. DiMarco. "Review of reduced gravity boiling heat transfer: European research." *Japan Society of Microgravity Application Journal*, 20:252–263 (2003).  
<http://www.glue.umd.edu/~kimjh/Documents%20and%20movies/European%20Research.pdf>.
- [18] H. Ohta. "Review of reduced gravity boiling heat transfer: Japanese research." *Japan Society of Microgravity Application Journal*, 20:272–285 (2003).  
<http://www.glue.umd.edu/~kimjh/Documents%20and%20movies/JapaneseResearch.pdf>.

Science may be described as the art of systematic over-simplification.

---

Karl R. Popper, in an interview with *The Observer (London)*\*

## Chapter 7

### Conclusion to Part I

**T**HE original intent of this experiment was simply to demonstrate that magnetic levitation is a feasible method to study materials properties under altered effective gravity. We have succeeded in this modest task and acquired useful science data from our simple homemade apparatus. Our results are summarized below and some suggestions for future studies are offered.

#### 7.1 Summary

We collect heat flux ( $q$ ) versus superheat ( $\Delta T$ ) data for the saturated nucleate pool boiling of oxygen at its normal boiling point using a horizontal roughened copper plate as the heater. Heat flux values up to  $3 \text{ kW/m}^2$  are applied to the system, resulting in superheat values of up to 3 K. By applying a magnetic force to the test fluid we simulate effective gravity values of 1, 6, and 16 times the Earth's gravity.

The heat-flux versus superheat data are found to obey a piecewise relationship (equation (5.3)). At low heat flux values the superheat is proportional to  $q^{0.37}$  for all effective gravities. At high heat flux the relation between heat flux and superheat becomes linear. This piece-wise behavior is consistent with experiments by Kim et al. [2] and numerical simulations by Son and Dhir [3], but contrary to standard empirical correlations of nucleate boiling which predict a simple power-law behavior [4–6]. However, the power-law exponent we find for the low heat flux portion of our data of 0.37 is consistent with these correlations of approximately 1/3.

Based on our data, we propose a modified boiling curve at high high heat flux (figure 6.2)

---

\*Reference [1]

which omits the negatively sloping transition boiling regime. Our new boiling curve predicts the superheat to be a monotonically increasing function of heat flux for all heat flux values, in particular, with the transition boiling mode represented by a linear relationship. We hypothesize that this behavior is related to the large heat capacity of our heater, which spatially and temporally averages the superheat preventing the unstable fluctuations between nucleate and film boiling typically associated with transition boiling.

Varying the effective gravity in our experiment weakly affects the scale parameter  $a$  of our low heat flux power law, which obeys a linear function with respect to the gravity (equation (6.7)). The transition heat flux separating the power-law and linear behaviors is found to scale as  $g^{0.25}$  (equation (6.9)). This gravity dependence is identical with that predicted in the literature [7] for the critical heat flux which, in the traditional picture of boiling, separates the nucleate and transition boiling modes. The identification of our transition heat flux with the critical heat flux supports our conjectured boiling curve.

## 7.2 Suggestions for Future Work

Any well-done experiment not only answers questions but also suggests new avenues for exploration. The current work from its inception was intended to be a gateway into more interesting future projects. While some additional work can be performed with the apparatus described in chapter 3, the methods presented here require a more sophisticated purpose-built system to reach their full potential.

### 7.2.1 Expanding the Oxygen Boiling Investigation

The most obvious addition to any experiment is more data. In particular, this experiment, like all boiling experiments, contains some degree of irreproducibility. As shown earlier in table 5.1 and figure 5.2, there is considerable variation in the heat-flux–temperature data between experimental runs done under supposedly identical conditions. Although the most desirable outcome would be to eliminate this irreproducibility, we are likely limited by the inability of our pressure controller to handle transient spikes in the gas flow, as described previously in section 4.2.2. However, by repeating the experiment several times and averaging the results (in our case, implicitly averaging by forming aggregate data sets) we can get useful quantitative information. Additional experimental runs would likely further reduce the uncertainties in the fitting parameters, perhaps unmasking

more subtle gravity-dependent effects. In particular, by adjusting the magnet current we can expand the range of effective gravities measured, potentially up to 80g.

Moreover, with some modest modifications to the magnet dewar, the experiment can be performed using reduced effective gravities. The change required is to adjust the magnet support structure to raise the magnet within the dewar, allowing the sample cell to be positioned at the bottom end of the solenoid. In this configuration the magnetic force is antiparallel to the Earth's gravity, resulting in a reduced net effective gravity (see equation (3.4) and the accompanying text). By reducing the effective gravity, macroscopic forces such as buoyancy are also reduced, allowing microscopic effects to manifest themselves in the boiling dynamics. Several experiments by other researchers have been performed under microgravity conditions (see reviews in references [8–10]); these experiments do see qualitatively different behavior than those performed under terrestrial gravity. Most importantly, the traditional correlation functions fail under microgravity conditions. The value of gravitational acceleration at which the traditional correlations begin to fail is currently unknown.

Our experiment has the advantage of being able to run over much longer time scales (tens of minutes) in comparison to aircraft and drop tower experiments (up to tens of seconds) [9]. Also, our method can be used to investigate *small but finite* values of effective gravity, unlike the experiments from the literature which only probe microgravity conditions. In particular, we can study boiling dynamics of oxygen at some values of gravity important to space exploration, such as lunar gravity (0.16g) or Martian gravity (0.38g). These studies could prove critical to the design of life support and fuel storage systems for future human missions to these heavenly bodies. Oxygen in particular must be studied carefully because of its inherent fire danger; poor thermal design of a storage vessel, for example, could result in a sudden release of oxygen gas, a potentially disastrous situation.

### 7.2.2 Applying the Magnetic Force Technique to Other Systems

The primary limitation of our current system is that the maximum magnetic field is too weak to study most materials. Oxygen is unique among fluids in having a large magnetic susceptibility ( $+3 \times 10^{-6} \text{ m}^3/\text{kg}$  at 90 K [11]). This is about 3 orders of magnitude larger than most substances. For example, the magnetic susceptibility of water at 20 °C is  $-9 \times 10^{-9} \text{ m}^3/\text{kg}$  [12], requiring  $|(\mathbf{B} \cdot \nabla)\mathbf{B}|$  on the order of  $10^3 \text{ T}^2/\text{m}$  to generate 1g of acceleration (see equation (3.1)). This is

beyond the capability of our magnet. However, such a magnet has recently been installed by our collaborators at the Jet Propulsion Laboratory. The new Variable Gravity Testbed Facility (VGTF) [13] has a room-temperature bore magnet with a maximum  $|(\mathbf{B} \cdot \nabla)\mathbf{B}|$  of  $1450 \text{ T}^2/\text{m}$ , sufficient to levitate water or biological systems. Alternatively, this system could be used to study boiling of oxygen with effective gravity values up to  $300g$ . By studying more fluids over larger temperature and effective gravity ranges, the VGTF can expand on the work presented in this text and bring better understanding of the role of gravity in boiling.

### 7.3 Acknowledgments

Finally, we would like to thank all those who contributed to the construction and operation of this experiment: Professor Nai-Chang Yeh, Dr. Donald Strayer, Nils Asplund, Michael Kwun Hung Cheung, Scott Medling, and, especially, Michael Turk. Funding for this project was provided by a contract with the National Aeronautics and Space Administration, through the Jet Propulsion Laboratory's Low Temperature Science and Quantum Sensor Group.

## Bibliography

- [1] *The Observer (London)* (August 1, 1982). Interview with Karl R. Popper.
- [2] J. Kim, J. F. Benton, and D. Wisniewski. "Pool boiling heat transfer on small heaters: effect of gravity and subcooling." *International Journal of Heat and Mass Transfer*, **45**:3919–3932 (2002). doi:10.1016/S0017-9310(02)00108-4.
- [3] G. Son and V. K. Dhir. "Numerical simulation of nucleate boiling on a horizontal surface at high wall superheats." *International Journal of Heat and Mass Transfer* (2007). Submitted.
- [4] M. G. Cooper. "Heat flow rates in saturated nucleate pool boiling—a wide-ranging examination using reduced properties." *Advances in Heat Transfer*, **16**:155–239 (1984).
- [5] W. M. Rohsenow. "A method of correlating heat-transfer data for surface boiling of liquids." *Transactions of the American Society of Mechanical Engineers*, **74**:969–976 (1952).
- [6] K. Stephan and M. Abdelsalam. "Heat-transfer correlations for natural convection boiling." *International Journal of Heat and Mass Transfer*, **23**:73–87 (1980).
- [7] N. Zuber. *Hydrodynamic Aspects of Boiling Heat Transfer*. Ph.D. thesis, University of California, Los Angeles (1959).
- [8] P. DiMarco. "Review of reduced gravity boiling heat transfer: European research." *Japan Society of Microgravity Application Journal*, **20**:252–263 (2003). <http://www.glue.umd.edu/~kimjh/Documents%20and%20movies/European%20Research.pdf>.
- [9] J. Kim. "Review of reduced gravity boiling heat transfer: US research." *Japan Society of Microgravity Application Journal*, **20**:264–271 (2003). <http://www.glue.umd.edu/~kimjh/Documents%20and%20movies/US%20Research.pdf>.
- [10] H. Ohta. "Review of reduced gravity boiling heat transfer: Japanese research." *Japan Society of Microgravity Application Journal*, **20**:272–285 (2003). <http://www.glue.umd.edu/~kimjh/Documents%20and%20movies/JapaneseResearch.pdf>.
- [11] D. R. Lide, editor. *CRC Handbook of Chemistry and Physics*. New York: CRC Press, 79th edition (1998).
- [12] R. Cini and M. Torrini. "Temperature dependence of magnetic susceptibility of water." *Journal Chemical Physics*, **49**:2826–2830 (1968). doi:10.1016/0017-9310(72)90028-2.
- [13] T. Chui, B. Zhang, M. Barmatz, I. Hahn, K. Penanen, C. Hays, D. Strayer, et al. "Cryogenics for lunar exploration." *Cryogenics*, **46**:74–81 (2006). doi:10.1016/j.cryogenics.2005.10.006.

## **Appendices to Part I**

## Appendix A

### Calibration Procedure for Temperature Sensors

The calibration data for the Cernox temperature sensors were taken at intervals of 0.25 K using an excitation current of 10  $\mu\text{A}$ . Following the suggestion of the manufacturer [1], these data were condensed into a Chebychev series for each sensor, in the form

$$\log T(R) = \sum_n a_n T_n \left( \frac{(\log R - \log R_{\min}) - (\log R_{\max} - \log R)}{\log R_{\max} - \log R_{\min}} \right), \quad (\text{A.1})$$

where  $T$  is temperature in kelvin,  $R$  is the sensor resistance in ohms, and  $R_{\min}$  and  $R_{\max}$  are the minimum and maximum sensor resistances over the calibration range. It should be noted that Lakeshore does not use the logarithm on the left-hand side of equation (A.1). We made this amendment after noticing that the calibration data approximately follow a power law; this change reduces the residuals in the calibration fits.

The Chebychev polynomials  $T_n(x)$  are given by the usual definition

$$T_n(x) = \cos[n \arccos x], \quad (\text{A.2})$$

or the equivalent recursion relations

$$T_{n+1}(x) = 2xT_n(x) - T_{n-1}(x); \quad (\text{A.3})$$

$$T_0(x) = 1; \quad \text{and} \quad T_1(x) = x. \quad (\text{A.4})$$

For each sensor we calculate the coefficients  $a_n$  by fitting the calibration data to equation (A.1). We truncate the series after six or seven terms, depending on the  $\chi^2$  error function of each fit.

The coefficient values are given in table A.1, along with the sensor identification numbers and their location within the sample cell.

Table A.1. Calibration coefficients for Cernox temperature sensors, for use in equation (A.1)

| Sensor #               | 1            | 2            | 3            | 4            | 5            | 6            |
|------------------------|--------------|--------------|--------------|--------------|--------------|--------------|
| Location               | Center       | Top          | Top          | Unused       | Heater       | Unused       |
| Serial #               | x38152       | x38153       | x38154       | x38186       | x38191       | x38192       |
| $T_{\min}/\text{K}$    | 14.25        | 14.25        | 8.25         | 8.25         | 13.75        | 13.75        |
| $T_{\max}/\text{K}$    | 107.021      | 107.021      | 105.915      | 105.915      | 110.001      | 110.001      |
| $\log R_{\min}$        | 2.19262      | 2.23177      | 2.2232       | 2.18078      | 2.17799      | 2.20056      |
| $\log R_{\max}$        | 2.95237      | 3.02476      | 3.23307      | 3.12664      | 2.9539       | 2.99559      |
| $a_0$                  | 1.59695      | 1.5976       | 1.47114      | 1.47329      | 1.59614      | 1.59652      |
| $a_1$                  | -4.37506E-01 | -4.36769E-01 | -5.56615E-01 | -5.56574E-01 | -4.50976E-01 | -4.50645E-01 |
| $a_2$                  | -5.50092E-03 | -5.94917E-03 | -2.04367E-03 | -4.15307E-03 | -6.24557E-03 | -6.49723E-03 |
| $a_3$                  | -9.60662E-04 | -2.14011E-03 | 1.27178E-03  | 9.92464E-04  | -1.08486E-03 | -1.49225E-03 |
| $a_4$                  | 1.11931E-05  | -2.71339E-04 | 2.08823E-03  | 2.16478E-03  | -1.05931E-04 | -2.49905E-04 |
| $a_5$                  | 6.33286E-04  | 9.16360E-04  | 1.35911E-03  | 1.33516E-03  | 4.71381E-04  | 5.32595E-04  |
| $a_6$                  | 3.35364E-04  | 6.65689E-04  | -5.02736E-04 | -4.47060E-04 | 2.17901E-04  | 2.95971E-04  |
| $a_7$                  | -3.45855E-04 | -6.18338E-04 | -7.15087E-04 | -7.70539E-04 | -2.28708E-04 | -2.82395E-04 |
| $a_8$                  | -4.64044E-05 | -7.13521E-05 | 0.000786118  | 0.000737387  | -4.37555E-05 | -5.63403E-05 |
| $\chi^2/\text{d.o.f.}$ | 2.18E-02     | 1.05E-01     | 2.54E-01     | 1.55E-01     | 1.29E-02     | 2.74E-02     |

## Bibliography

- [1] *Temperature Measurement and Control Catalog*. Westerville, OH: Lakeshore Cryogenics (ca. 2000).

## Appendix B

### Oxygen Experiment Data

This appendix contains tables of the raw data for the oxygen experiment.

#### B.1 Oxygen Data Run Parameters

The data runs discussed in chapter 5 are summarized in table B.1 below.

Table B.1. Oxygen data run summary

| Date     | Current/A | $g_{\text{eff}}/g$ | $Q_0/\text{mW}$ | $t_0/10^{-3}$ |
|----------|-----------|--------------------|-----------------|---------------|
| 20061103 | 0         | 1                  | 50              | -0.3          |
| 20061119 | 0         | 1                  | 47              | -2.5          |
| 20070213 | 0         | 1                  | 50              | -1.5          |
| 20061213 | 20        | 6                  | 70              | -1.7          |
| 20061214 | 20        | 6                  | 46              | -1.2          |
| 20070214 | 20        | 6                  | 50              | -2.0          |
| 20061216 | 34.2      | 16                 | 36              | -2.5          |
| 20061217 | 34.4      | 16                 | 45              | -3.9          |
| 20070215 | 34.3      | 16                 | 46              | -2.2          |

## B.2 Steady-State Temperature Data

The following tables give the results of the fitting of the raw experimental data to equation (5.1) for each run.

Table B.2. Reduced superheat fits for run of 20061103, with  $g_{\text{eff}} = 1g$

| $q/\text{Wm}^{-2}$ | $t/10^{-3}$ | $\sigma_t/10^{-3}$ | $q/\text{Wm}^{-2}$ | $t/10^{-3}$ | $\sigma_t/10^{-3}$ |
|--------------------|-------------|--------------------|--------------------|-------------|--------------------|
| 3216               | 13.48       | 0.11               | 233.9              | 2.76        | 0.33               |
| 1989               | 9.66        | 0.38               | 173.8              | 2.26        | 0.25               |
| 1386               | 7.43        | 0.36               | 113.8              | 1.84        | 0.32               |
| 775.0              | 5.04        | 0.47               | 54.23              | 1.26        | 0.20               |
| 474.0              | 3.98        | 0.27               | 30.15              | 0.76        | 0.14               |
| 353.7              | 3.26        | 0.29               | 12.10              | 0.55        | 0.18               |
| 293.5              | 3.03        | 0.28               |                    |             |                    |

Table B.3. Reduced superheat fits for run of 20061118, with  $g_{\text{eff}} = 1g$

| $q/\text{Wm}^{-2}$ | $t/10^{-3}$ | $\sigma_t/10^{-3}$ | $q/\text{Wm}^{-2}$ | $t/10^{-3}$ | $\sigma_t/10^{-3}$ |
|--------------------|-------------|--------------------|--------------------|-------------|--------------------|
| 2997               | 14.45       | 0.22               | 347.7              | 3.65        | 0.16               |
| 2367               | 12.19       | 0.19               | 270.4              | 3.21        | 0.17               |
| 1872               | 10.03       | 0.12               | 208.5              | 2.56        | 0.16               |
| 1480               | 8.34        | 0.13               | 159.8              | 2.06        | 0.19               |
| 1166               | 7.17        | 0.10               | 121.2              | 1.62        | 0.15               |
| 918.0              | 6.35        | 0.11               | 90.11              | 1.20        | 0.32               |
| 728.0              | 5.11        | 0.58               | 66.56              | 1.37        | 0.45               |
| 568.3              | 4.87        | 0.22               | 47.29              | 0.56        | 0.38               |
| 444.8              | 4.13        | 0.24               | 31.61              | 0.06        | 0.49               |

Table B.4. Reduced superheat fits for run of 20070213, with  $g_{\text{eff}} = 1g$ 

| $q/\text{Wm}^{-2}$ | $t/10^{-3}$ | $\sigma_t/10^{-3}$ | $q/\text{Wm}^{-2}$ | $t/10^{-3}$ | $\sigma_t/10^{-3}$ |
|--------------------|-------------|--------------------|--------------------|-------------|--------------------|
| 3020               | 24.75       | 0.04               | 59.80              | 1.02        | 0.08               |
| 2396               | 20.13       | 0.08               | 47.42              | 0.78        | 0.09               |
| 1898               | 16.61       | 0.11               | 37.68              | 0.56        | 0.09               |
| 1509               | 13.69       | 0.14               | 29.93              | 0.40        | 0.09               |
| 1196               | 11.23       | 0.12               | 23.77              | 0.26        | 0.10               |
| 946.0              | 9.18        | 0.12               | 18.82              | 0.09        | 0.22               |
| 751.0              | 7.52        | 0.14               | 14.98              | 0.04        | 0.11               |
| 596.3              | 6.18        | 0.14               | 11.86              | -0.19       | 0.10               |
| 472.9              | 5.13        | 0.10               | 9.418              | -0.40       | 0.10               |
| 375.7              | 4.13        | 0.12               | 7.458              | -0.50       | 0.09               |
| 298.5              | 3.28        | 0.13               | 5.932              | -0.60       | 0.08               |
| 236.6              | 2.66        | 0.10               | 4.677              | -0.76       | 0.11               |
| 187.9              | 2.32        | 0.12               | 3.665              | -0.87       | 0.10               |
| 149.1              | 2.13        | 0.11               | 2.931              | -0.92       | 0.10               |
| 118.2              | 1.77        | 0.08               | 2.278              | -0.98       | 0.08               |
| 93.87              | 1.47        | 0.10               | 1.798              | -0.99       | 0.11               |
| 75.29              | 1.26        | 0.10               |                    |             |                    |

Table B.5. Reduced superheat fits for run of 20061213, with  $g_{\text{eff}} = 6g$ 

| $q/\text{Wm}^{-2}$ | $t/10^{-3}$ | $\sigma_t/10^{-3}$ | $q/\text{Wm}^{-2}$ | $t/10^{-3}$ | $\sigma_t/10^{-3}$ |
|--------------------|-------------|--------------------|--------------------|-------------|--------------------|
| 2983               | 20.57       | 0.06               | 334.0              | 4.91        | 0.07               |
| 2353               | 17.05       | 0.10               | 256.7              | 4.56        | 0.05               |
| 1858               | 14.32       | 0.14               | 194.8              | 4.10        | 0.07               |
| 1466               | 11.86       | 0.07               | 146.1              | 3.70        | 0.05               |
| 1152               | 9.92        | 0.09               | 107.5              | 3.13        | 0.06               |
| 904.2              | 8.33        | 0.08               | 76.48              | 2.78        | 0.07               |
| 711.8              | 7.02        | 0.07               | 52.90              | 2.43        | 0.05               |
| 554.5              | 6.12        | 0.05               | 33.68              | 1.96        | 0.11               |
| 431.1              | 5.45        | 0.08               |                    |             |                    |

Table B.6. Reduced superheat fits for run of 20061214, with  $g_{\text{eff}} = 6g$ 

| $q/\text{Wm}^{-2}$ | $t/10^{-3}$ | $\sigma_t/10^{-3}$ | $q/\text{Wm}^{-2}$ | $t/10^{-3}$ | $\sigma_t/10^{-3}$ |
|--------------------|-------------|--------------------|--------------------|-------------|--------------------|
| 2997               | 18.59       | 0.05               | 270.9              | 3.89        | 0.06               |
| 2367               | 15.07       | 0.07               | 209.0              | 3.46        | 0.07               |
| 1873               | 12.27       | 0.06               | 160.4              | 3.04        | 0.10               |
| 1481               | 10.54       | 0.07               | 121.7              | 2.61        | 0.07               |
| 1166               | 9.07        | 0.07               | 90.69              | 2.21        | 0.06               |
| 918.4              | 7.77        | 0.08               | 67.14              | 1.76        | 0.08               |
| 725.8              | 6.72        | 0.08               | 47.87              | 1.39        | 0.09               |
| 568.7              | 5.75        | 0.07               | 32.20              | 0.83        | 0.11               |
| 445.3              | 5.02        | 0.06               | 19.82              | 0.58        | 0.09               |
| 348.2              | 4.38        | 0.08               | 10.08              | 0.29        | 0.11               |

Table B.7. Reduced superheat fits for run of 20070214, with  $g_{\text{eff}} = 6g$ 

| $q/\text{Wm}^{-2}$ | $t/10^{-3}$ | $\sigma_t/10^{-3}$ | $q/\text{Wm}^{-2}$ | $t/10^{-3}$ | $\sigma_t/10^{-3}$ |
|--------------------|-------------|--------------------|--------------------|-------------|--------------------|
| 3020               | 19.06       | 0.22               | 75.49              | 1.51        | 0.06               |
| 2397               | 15.50       | 0.12               | 59.88              | 1.21        | 0.09               |
| 1898               | 12.53       | 0.08               | 47.28              | 0.82        | 0.07               |
| 1509               | 10.56       | 0.08               | 37.74              | 0.54        | 0.06               |
| 1196               | 8.93        | 0.06               | 29.90              | 0.27        | 0.08               |
| 946.0              | 7.58        | 0.07               | 23.75              | 0.07        | 0.07               |
| 750.9              | 6.64        | 0.08               | 18.80              | -0.14       | 0.07               |
| 596.3              | 5.69        | 0.10               | 14.97              | -0.25       | 0.07               |
| 472.8              | 4.97        | 0.08               | 11.84              | -0.36       | 0.09               |
| 375.6              | 4.38        | 0.07               | 9.398              | -0.49       | 0.07               |
| 298.4              | 3.88        | 0.07               | 7.103              | -0.58       | 0.07               |
| 236.6              | 3.49        | 0.06               | 6.068              | -0.64       | 0.07               |
| 187.9              | 3.01        | 0.06               | 4.664              | -0.71       | 0.08               |
| 149.2              | 2.58        | 0.06               | 3.659              | -0.75       | 0.08               |
| 118.1              | 2.18        | 0.09               | 2.919              | -0.81       | 0.12               |
| 93.82              | 1.82        | 0.06               |                    |             |                    |

Table B.8. Reduced superheat fits for run of 20061216, with  $g_{\text{eff}} = 16g$ 

| $q/\text{Wm}^{-2}$ | $t/10^{-3}$ | $\sigma_t/10^{-3}$ | $q/\text{Wm}^{-2}$ | $t/10^{-3}$ | $\sigma_t/10^{-3}$ |
|--------------------|-------------|--------------------|--------------------|-------------|--------------------|
| 3003               | 21.28       | 0.09               | 276.9              | 4.66        | 0.08               |
| 2373               | 17.90       | 0.09               | 215.1              | 4.02        | 0.08               |
| 1879               | 14.90       | 0.08               | 166.4              | 3.03        | 0.06               |
| 1487               | 12.35       | 0.06               | 127.7              | 2.76        | 0.06               |
| 1173               | 10.34       | 0.06               | 96.70              | 1.89        | 0.12               |
| 924.4              | 8.75        | 0.06               | 73.15              | 1.58        | 0.08               |
| 731.8              | 7.61        | 0.11               | 53.89              | 1.09        | 0.07               |
| 574.7              | 6.60        | 0.19               | 38.21              | 0.78        | 0.06               |
| 451.3              | 5.90        | 0.14               | 25.84              | 0.39        | 0.08               |
| 354.2              | 5.16        | 0.08               |                    |             |                    |

Table B.9. Reduced superheat fits for run of 20061217, with  $g_{\text{eff}} = 16g$ 

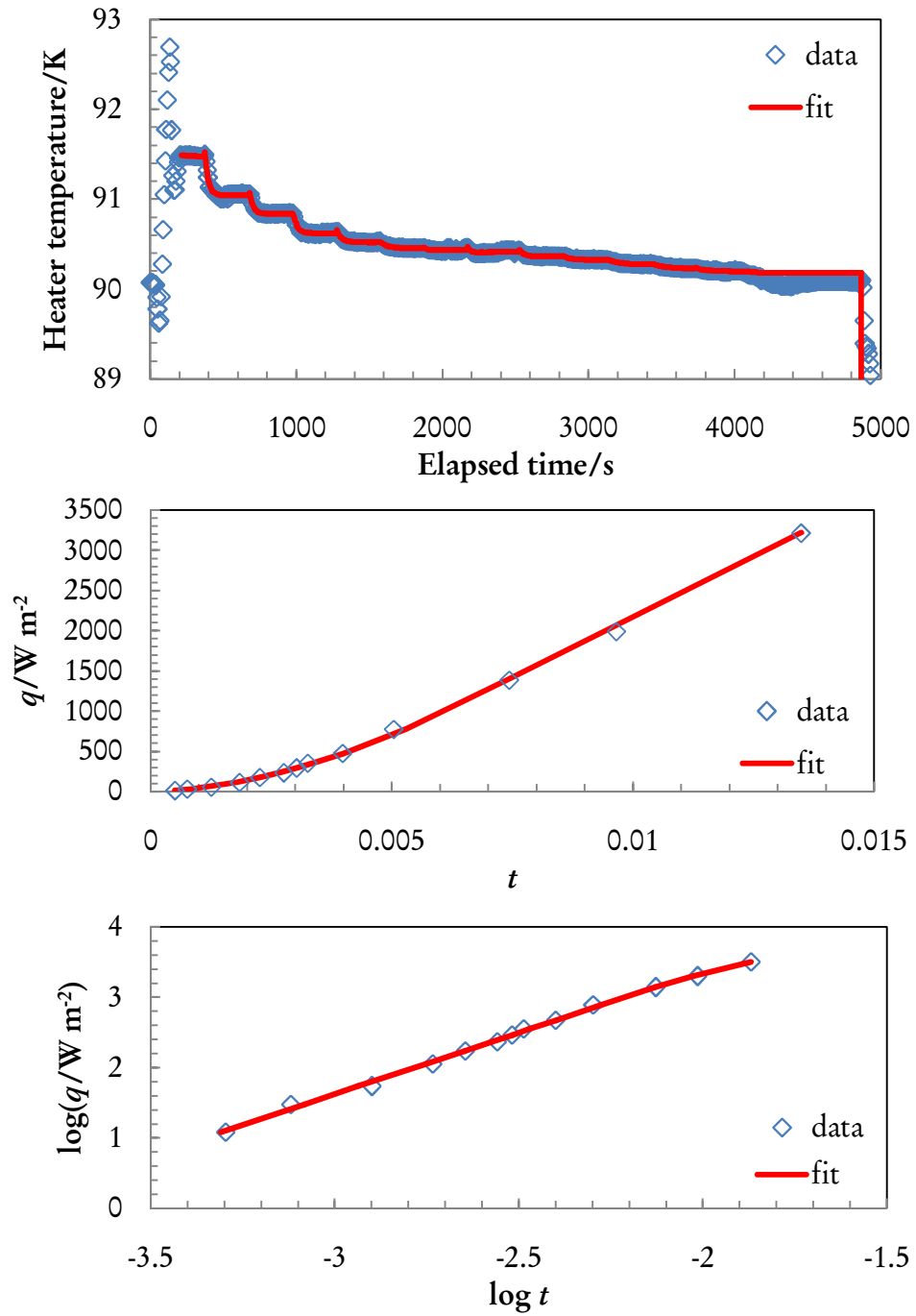
| $q/\text{Wm}^{-2}$ | $t/10^{-3}$ | $\sigma_t/10^{-3}$ | $q/\text{Wm}^{-2}$ | $t/10^{-3}$ | $\sigma_t/10^{-3}$ |
|--------------------|-------------|--------------------|--------------------|-------------|--------------------|
| 2997               | 15.04       | 0.09               | 271.5              | 3.88        | 0.06               |
| 2368               | 12.93       | 0.11               | 209.6              | 3.25        | 0.08               |
| 1873               | 11.02       | 0.10               | 161.0              | 2.63        | 0.07               |
| 1481               | 9.55        | 0.07               | 122.3              | 1.94        | 0.07               |
| 1167               | 8.28        | 0.07               | 91.28              | 1.29        | 0.07               |
| 919.0              | 7.15        | 0.07               | 67.73              | 0.80        | 0.07               |
| 726.4              | 6.31        | 0.08               | 48.47              | 0.34        | 0.08               |
| 569.3              | 5.63        | 0.07               | 32.80              | -0.06       | 0.06               |
| 445.9              | 5.01        | 0.06               | 20.42              | -0.39       | 0.07               |
| 348.7              | 4.42        | 0.05               | 10.68              | -0.72       | 0.15               |

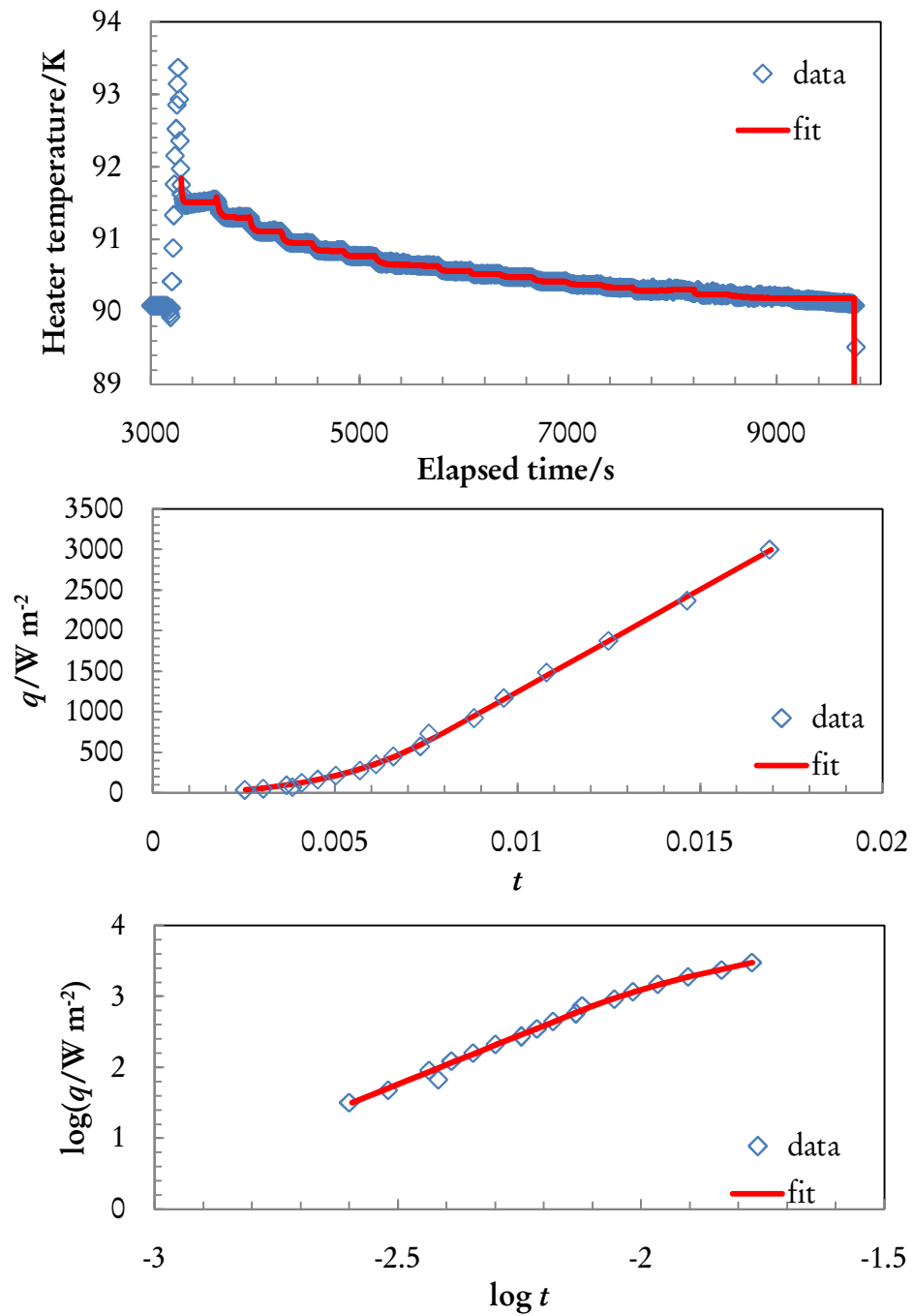
Table B.10. Reduced superheat fits for run of 20070215, with  $g_{\text{eff}} = 16g$ 

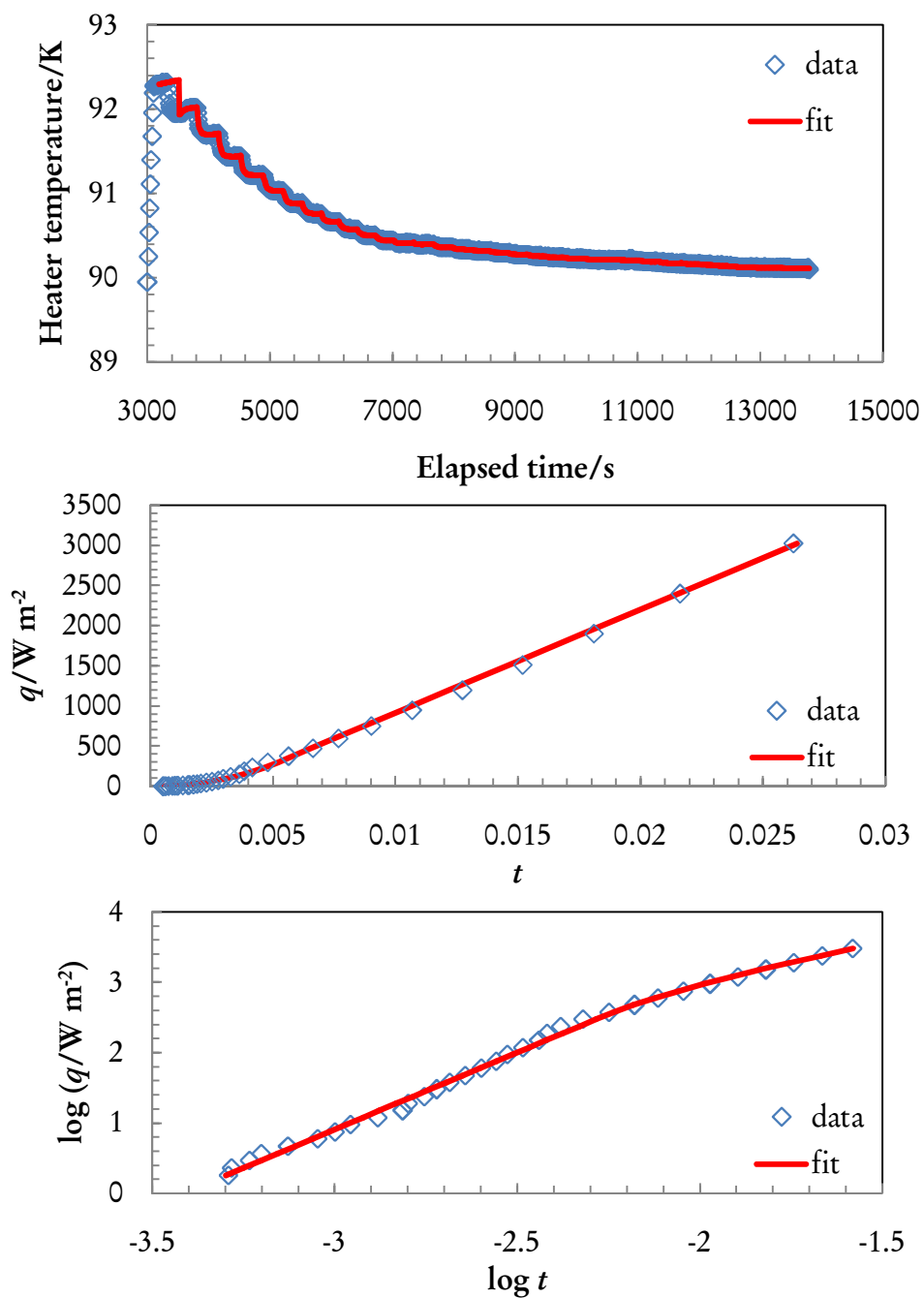
| $q/\text{Wm}^{-2}$ | $t/10^{-3}$ | $\sigma_t/10^{-3}$ | $q/\text{Wm}^{-2}$ | $t/10^{-3}$ | $\sigma_t/10^{-3}$ |
|--------------------|-------------|--------------------|--------------------|-------------|--------------------|
| 3022               | 15.40       | 0.14               | 74.95              | 1.39        | 0.07               |
| 2398               | 13.11       | 0.13               | 59.47              | 1.05        | 0.07               |
| 1899               | 10.96       | 0.09               | 47.10              | 0.75        | 0.06               |
| 1504               | 9.44        | 0.11               | 37.35              | 0.51        | 0.07               |
| 1198               | 8.34        | 0.06               | 29.60              | 0.31        | 0.06               |
| 946.1              | 7.39        | 0.06               | 23.45              | 0.13        | 0.05               |
| 750.9              | 6.59        | 0.06               | 18.57              | 0.00        | 0.06               |
| 596.2              | 5.85        | 0.06               | 14.65              | -0.13       | 0.06               |
| 472.9              | 5.20        | 0.06               | 11.54              | -0.18       | 0.06               |
| 375.0              | 4.72        | 0.03               | 9.103              | -0.25       | 0.07               |
| 297.9              | 4.16        | 0.13               | 7.144              | -0.33       | 0.08               |
| 236.6              | 3.63        | 0.08               | 5.618              | -0.37       | 0.08               |
| 187.5              | 3.13        | 0.06               | 4.364              | -0.44       | 0.08               |
| 149.1              | 2.68        | 0.07               | 3.359              | -0.49       | 0.07               |
| 118.2              | 2.24        | 0.07               | 2.619              | -0.52       | 0.15               |
| 93.30              | 1.85        | 0.07               |                    |             |                    |

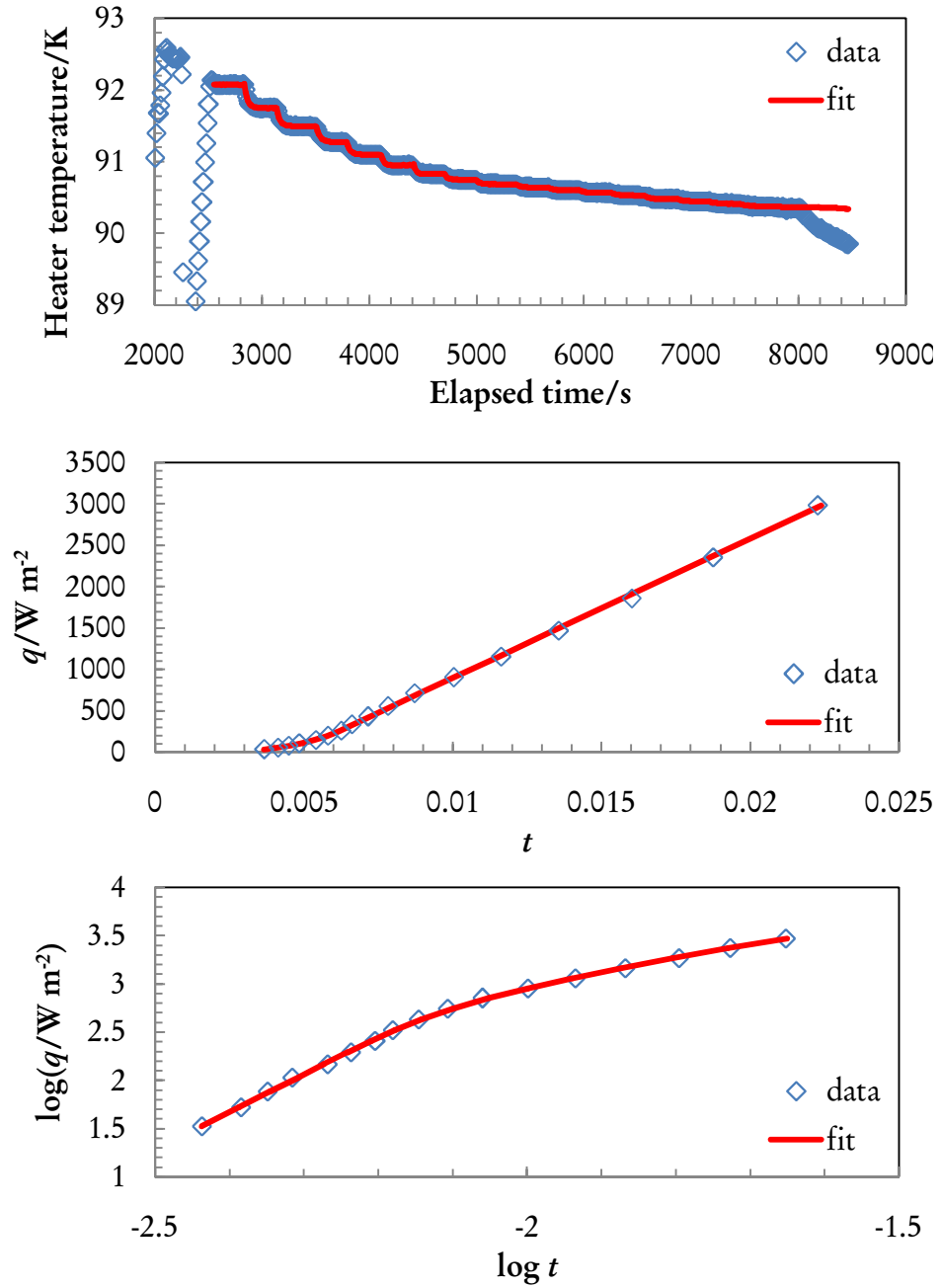
### B.3 Plots and Fits

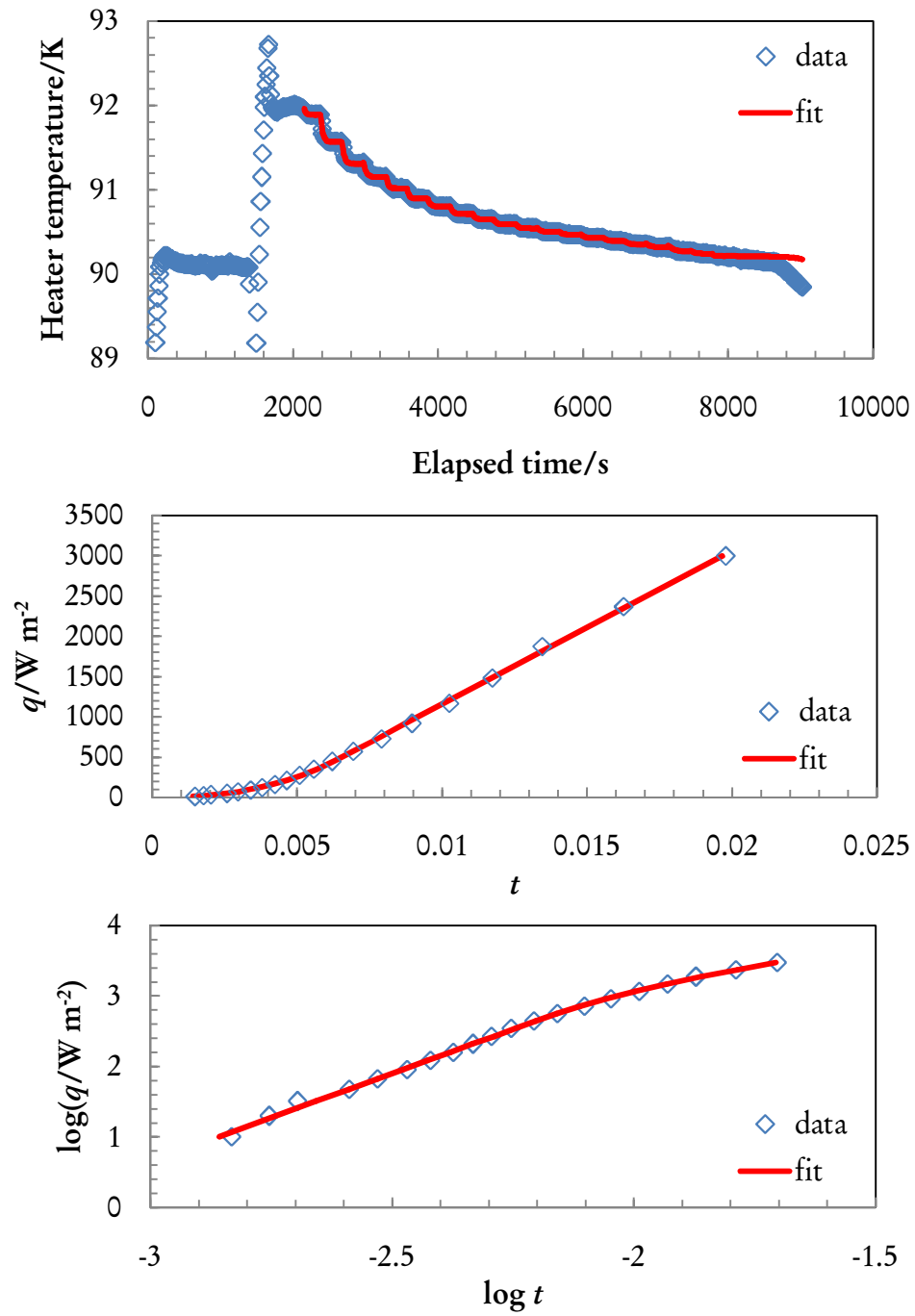
The following section contains the times series data plots and heat flux versus reduced superheat plots (the same data as the tables in appendix B.2) for all of the oxygen boiling experiment runs. The top panel on each page contains the heater temperature (vertical axis) as a function of elapsed time (horizontal axis); the data are blue open diamonds and the fits to equation (5.1) (from page 52) are red lines. The middle panel on the page shows the reduced temperature (horizontal axis) as a function of heat flux (vertical axis); the data are blue open diamonds and the fits to equation (5.3) (from page 55) are red lines. The bottom panel contains the same data as the middle panel, but on a log-log scale.

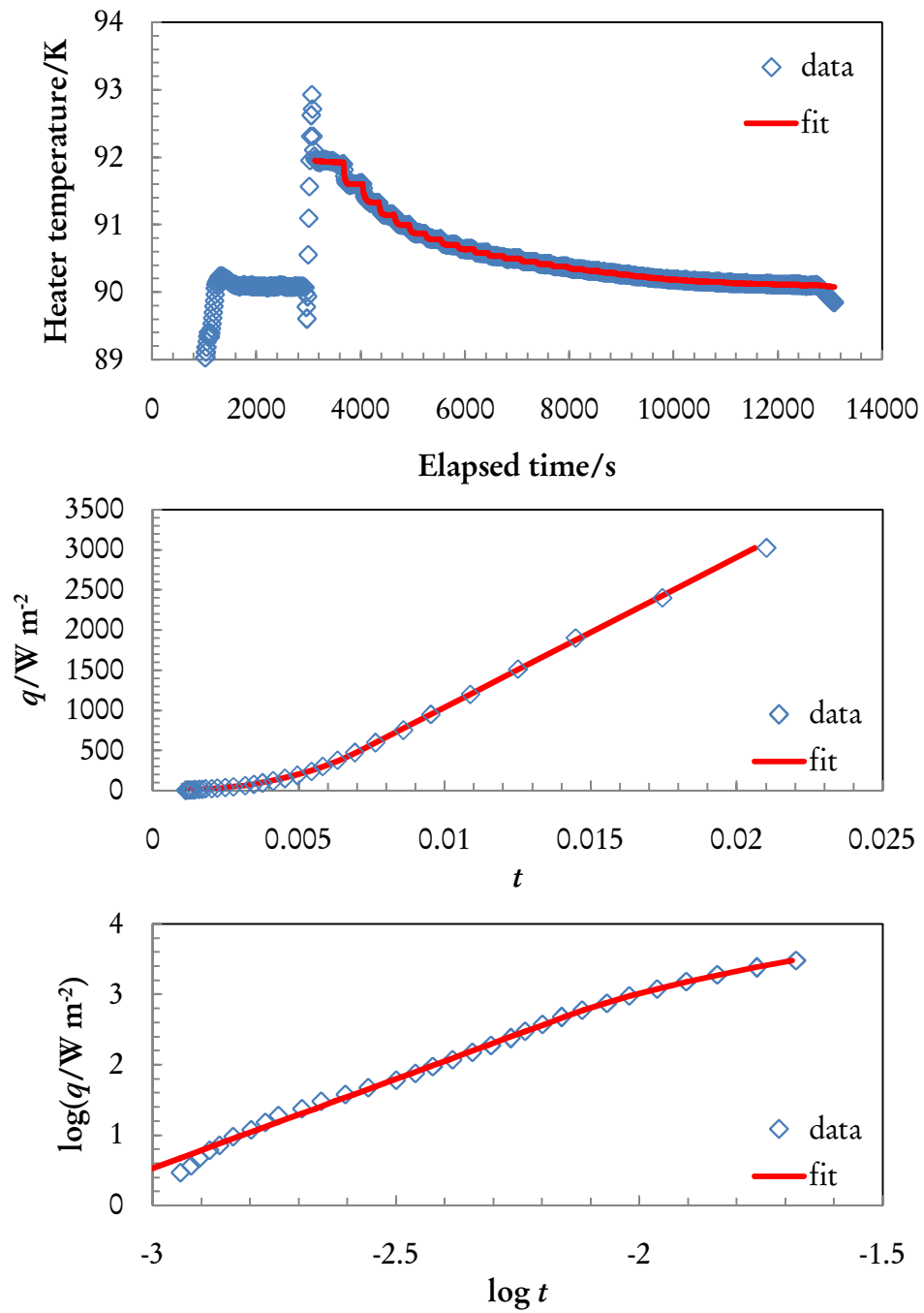
Figure B.1. Data from 20061103,  $g_{\text{eff}} = 1\text{g}$

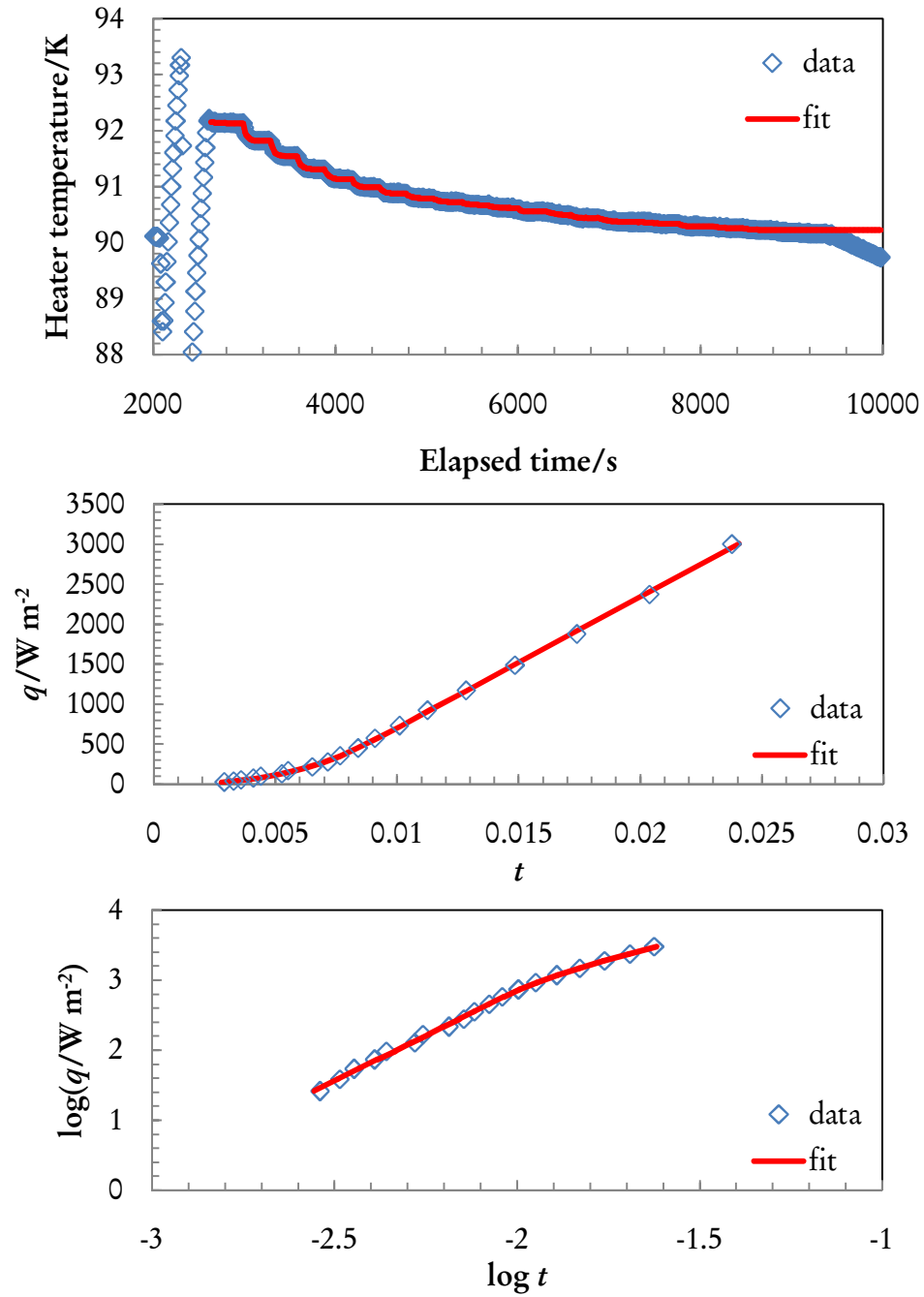
Figure B.2. Data from 20061119,  $g_{\text{eff}} = 1g$

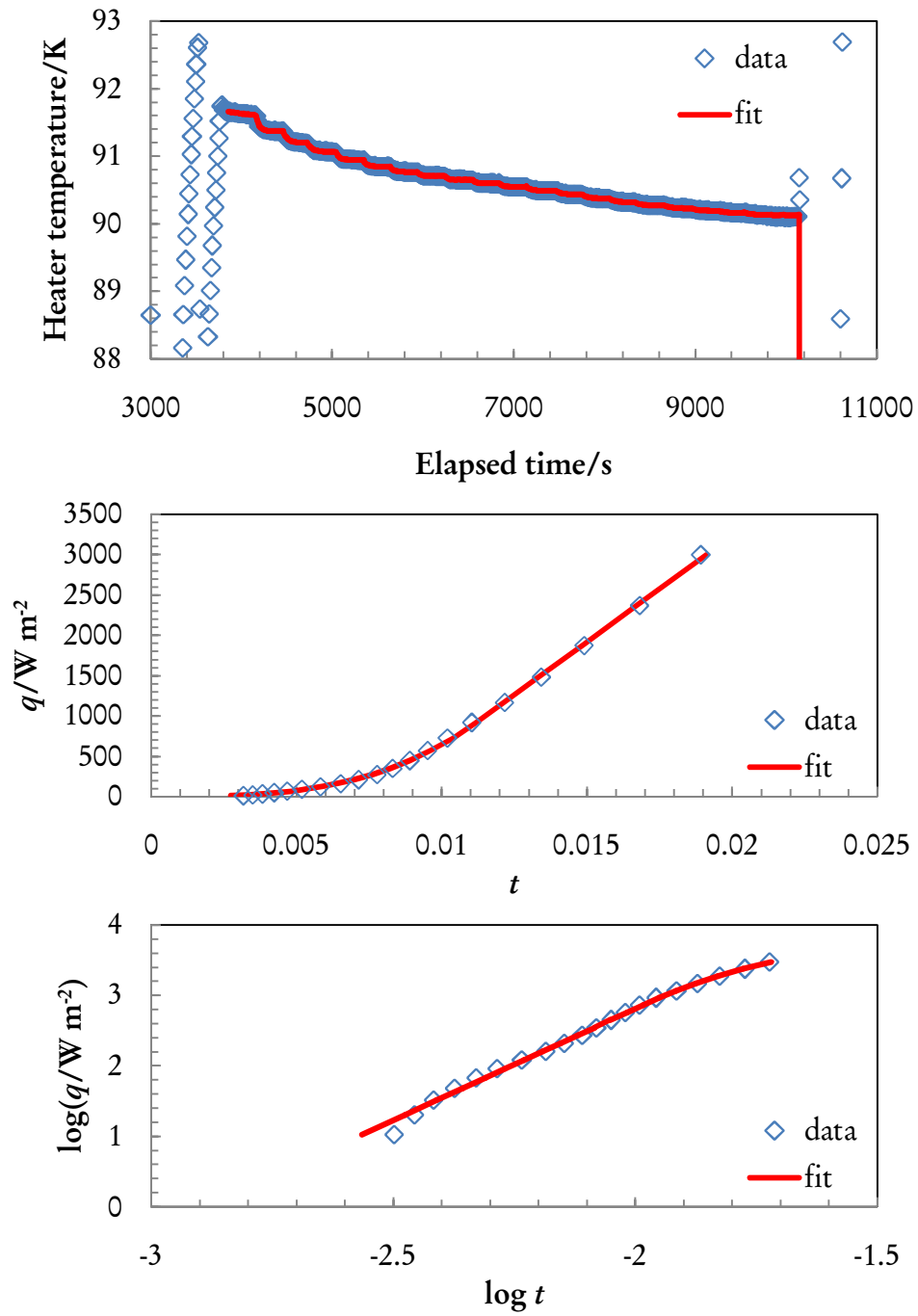
Figure B.3. Data from 20070213,  $g_{\text{eff}} = 1g$

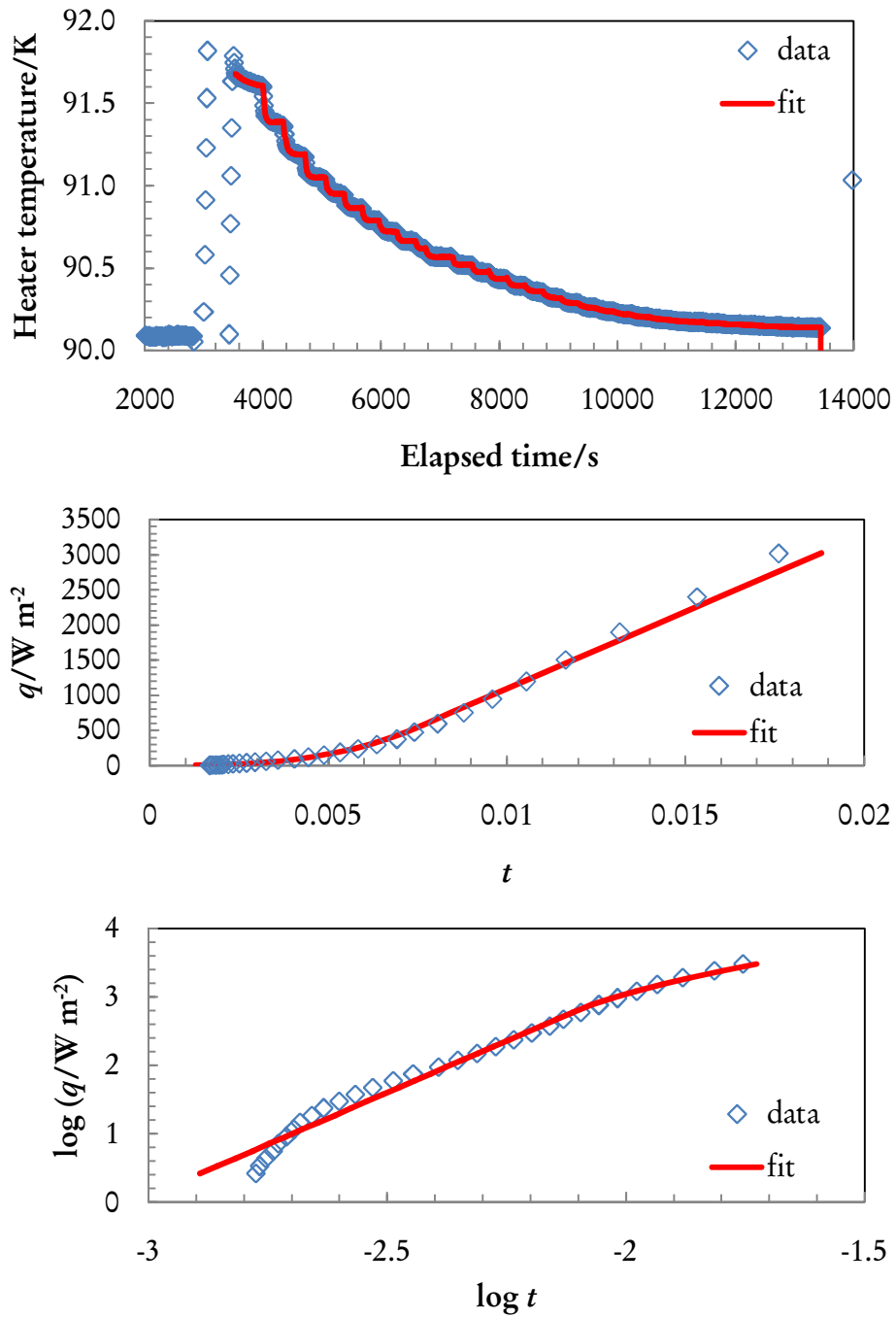
Figure B.4. Data from 20061213,  $g_{\text{eff}} = 6g$

Figure B.5. Data from 20061214,  $g_{\text{eff}} = 6\text{ g}$

Figure B.6. Data from 20070214,  $g_{\text{eff}} = 6g$

Figure B.7. Data from 20061216,  $g_{\text{eff}} = 16g$

Figure B.8. Data from 20061217,  $g_{\text{eff}} = 16g$

Figure B.9. Data from 20070215,  $g_{\text{eff}} = 16g$

## Appendix C

### Miscellaneous Derivations from the Boiling Experiment

#### C.1 Explicit Expressions for the Magnetic Field

These explicit closed-form expressions for the magnetic field of a uniformly wound finite solenoid are taken from Conway [1]. It is interesting to note that these expressions only appeared in print in 2001. Conway acknowledges that these formulas did not originate with his work, but he cannot identify specific references. Earlier published methods relied on power series expansions of the integrals which only converged near the center of the magnet [2; 3]. Conway's expressions are valid over all space.

The magnetic field  $\mathbf{B}$  at location  $(r, z)$  generated by a thin, finite, uniform solenoid of radius  $R$  and ends located at  $Z_1$  and  $Z_2$ , with current  $I$  is given by the following expressions:

$$B_z(r, z, R, Z_1, Z_2) = \begin{cases} \frac{\mu_0 IR}{2} \left[ I_{(0,1,0)}(R, r, |Z_1 - z|) \right. \\ \quad \left. - I_{(0,1,0)}(R, r, |Z_2 - z|) \right] & \text{for } z < Z_1, \\ \frac{\mu_0 IR}{2} \left[ 2I_{(0,1,0)}(R, r, 0) \right. \\ \quad - I_{(0,1,0)}(R, r, |Z_1 - z|) \\ \quad \left. - I_{(0,1,0)}(R, r, |Z_2 - z|) \right] & \text{for } Z_1 < z < Z_2, \\ \frac{\mu_0 IR}{2} \left[ I_{(0,1,0)}(R, r, |Z_2 - z|) \right. \\ \quad \left. - I_{(0,1,0)}(R, r, |Z_1 - z|) \right] & \text{for } z > Z_2, \end{cases}$$

$$B_r(r, z, R, Z_1, Z_2) = \frac{\mu_0 IR}{2} \left[ I_{(0,1,1)}(R, r, |Z_2 - z|) - I_{(0,1,1)}(R, r, |Z_1 - z|) \right].$$

The functions  $I_{(\lambda,\mu,\nu)}$  are the Bessel-Laplace integrals, defined as

$$I_{(\lambda,\mu,\nu)}(R, r, |z|) = \int_0^\infty s^\lambda J_\mu(sR) J_\nu(sr) e^{-s|z|} ds,$$

where  $J_\mu(x)$  are Bessel functions of the first kind. Explicit expressions of  $I_{(\lambda,\mu,\nu)}$  for the equations above are

$$I_{(0,1,0)}(R, r, |z|) = \begin{cases} \frac{1}{R} \left[ 1 - \frac{|z|k\mathbf{K}(k)}{2\pi\sqrt{rR}} - \frac{\Lambda_0(|\beta|, k)}{2} \right] & \text{for } r < R, \\ \frac{1}{R} \left[ -\frac{|z|k\mathbf{K}(k)}{2\pi\sqrt{rR}} + \frac{\Lambda_0(|\beta|, k)}{2} \right] & \text{for } r > R, \end{cases}$$

$$I_{(0,1,1)}(R, r, |z|) = \frac{1}{\pi k \sqrt{rR}} \left[ (2 - k^2)\mathbf{K}(k) - 2\mathbf{E}(k) \right].$$

In the above,  $\mathbf{K}(k)$  and  $\mathbf{E}(k)$  are the complete elliptic integrals of the first and second kind, respectively. The auxiliary variables are defined as

$$k = \sqrt{\frac{4rR}{(r+R)^2 + z^2}},$$

and

$$\beta = \arcsin \left( \frac{z}{\sqrt{(r-R)^2 + z^2}} \right).$$

Lastly, the Heuman Lambda function  $\Lambda_0(\beta, k)$  may be defined in terms of the elliptic integrals by

$$\Lambda_0(\beta, k) = \frac{2}{\pi} \left[ \mathbf{E}(k)F(\beta, k') + \mathbf{K}(k)E(\beta, k') - \mathbf{K}(k)F(\beta, k') \right],$$

where  $k' = \sqrt{1 - k^2}$  and  $F(\beta, k)$  and  $E(\beta, k)$  are the incomplete elliptic integrals of the first and second kinds, respectively.

## C.2 Oxygen Experiment Uncertainty Derivations

As discussed in section 5.1.3, we choose a piecewise functional form to describe the reduced superheat  $t$  as a function of the applied heat flux  $q$ :

$$t(q) = \begin{cases} a \left(\frac{q}{q_t}\right)^b & \text{for } q < q_t, \\ m \left(\frac{q}{q_t}\right) + c & \text{for } q \geq q_t, \end{cases} \quad (\text{C.1})$$

where  $q_t$  is some transition heat flux (found by fitting), and the dimensionless quantities  $a, b, m$ , and  $c$  are fitting parameters subject to smoothness constraints that  $t(q)$  and  $\partial t(q)/\partial q$  are continuous at  $q = q_t$ . The constraints are equivalent to

$$m = ab, \quad c = a(1 - b). \quad (\text{C.2})$$

For a given set of data  $\{t_i, q_i\}$  we perform fits by minimizing the  $\chi^2$  error function in terms of the fitting parameters  $\{q_t, a, b, c, m\}$ :

$$\chi^2(q_t, a, b, c, m) = \sum_i \frac{[t_i - t(q_i; q_t, a, b, c, m)]^2}{\sigma_{t_i}^2}.$$

Once  $\chi^2$  has been minimized, we can approximate it as a quadratic function near the minimum point by Taylor expansion:

$$\chi^2(\delta q_t, \delta a, \delta b, \delta c, \delta m) \approx \chi^2|_{\min} + \frac{1}{2} \left[ \frac{\partial^2 \chi^2}{\partial a^2} \Big|_{\min} (\delta a)^2 + \frac{\partial^2 \chi^2}{\partial b^2} \Big|_{\min} (\delta b)^2 + \dots \right] + \dots$$

We associate the uncertainties in the fitting parameters with the increments which increase the above function by unity. If we assume the parameters vary independently,

$$1 = \frac{1}{2} \frac{\partial^2 \chi^2}{\partial a^2} \sigma_a^2, \\ \sigma_a^2 = 2 \left( \frac{\partial^2 \chi^2}{\partial a^2} \right)^{-1},$$

and similarly for the other parameters.

The derivatives of  $\chi^2$  with respect to the fitting parameters are given below.

$$\frac{\partial^2 \chi^2}{\partial a^2} = \sum_{q_i < q_t} \frac{2}{\sigma_{t_i}^2} \left( \frac{q_i}{q_t} \right)^{2b} + \sum_{q_i > q_t} \frac{2}{\sigma_{t_i}^2} (1-b)^2$$

$$\frac{\partial^2 \chi^2}{\partial b^2} = \sum_{q_i < q_t} \frac{2a}{\sigma_{t_i}^2} \left( \frac{q_i}{q_t} \right)^b \left[ 2a \left( \frac{q_i}{q_t} \right)^b - t_i \right] \left[ \ln \left( \frac{q_i}{q_t} \right) \right]^2 + \sum_{q_i > q_t} \frac{2a^2}{\sigma_{t_i}^2}$$

$$\frac{\partial^2 \chi^2}{\partial m^2} =$$

$$\sum_{q_i < q_t} \left( \frac{1}{\sigma_{t_i}^2} \right) \left\{ 2 \left( \frac{q_i}{q_t} \right)^{\frac{m}{m+c}} \left[ \left( \frac{q_i}{q_t} \right)^{\frac{m}{m+c}} + \frac{2c}{m+c} \left( \frac{q_i}{q_t} \right)^{\frac{m}{m+c}} \ln \left( \frac{q_i}{q_t} \right) + \frac{c^2}{(m+c)^3} \left( 2(m+c) \left( \frac{q_i}{q_t} \right) - t_i \right) \left( \ln \left( \frac{q_i}{q_t} \right) \right)^2 \right] \right\} + \sum_{q_i > q_t} \frac{2}{\sigma_{t_i}^2} \left( \frac{q_i}{q_t} \right)^2$$

$$\frac{\partial^2 \chi^2}{\partial c^2} =$$

$$\sum_{q_i < q_t} \frac{1}{\sigma_{t_i}^2} \frac{1}{(m+c)^3} \left( 2 \left\{ \left( \frac{q_i}{q_t} \right)^{\frac{m}{m+c}} \left[ m^2 \left[ (m+c) \left( \frac{q_i}{q_t} \right)^{\frac{m}{m+c}} - t_i \right] \ln \left[ \frac{q_i}{q_t} \right]^2 + [m+c] \left[ \frac{q_i}{q_t} \right]^{\frac{m}{m+c}} \left[ (m+c) - m \ln \left( \frac{q_i}{q_t} \right) \right]^2 \right] \right\} \right) + \sum_{q_i > q_t} \frac{2}{\sigma_{t_i}^2}$$

Assuming that  $q_t$  is not equal to any  $q_i$ :

$$\frac{\partial^2 \chi^2}{\partial q_t^2} = \sum_{q_i < q_t} \frac{2}{\sigma_{t_i}^2} \frac{ab}{q_t^2} \left[ \frac{q_i}{q_t} \right]^b \left[ a(1+2b) \left( \frac{q_i}{q_t} \right)^b - (1+b)t_i \right] \\ + \sum_{q_i > q_t} \frac{2}{\sigma_{t_i}^2} \frac{mq_i}{q_t^4} [3mq_i + 2q_t(c - t_i)]$$

## Bibliography

- [1] J. T. Conway. "Exact solutions for the magnetic fields of axisymmetric solenoids and current distributions." *IEEE Transactions on Magnetics*, **37**:2977–2988 (2001).
- [2] M. P. Janawadkar, M. C. Valsakumar, and T. S. Radhakrishnan. "Computation of minimum volume sixth order superconducting solenoids." *Cryogenics*, **21**:403–407 (1981).
- [3] D. B. Montgomery. *Solenoid Magnet Design*. New York: Wiley (1969).

## Part II

# Applications of Superconducting Cavity Microwave Resonators as Frequency References and for Thermodynamic Measurements of Helium-4

## Notation for part II

Notation used in part II. The sections listed indicate the first use of each symbol.

| Notation               | Description   | Section |
|------------------------|---|---------|
| <b>Greek symbols</b>   |   |         |
| $\Delta_0$             | Superconducting gap energy at zero temperature                  | 8.2     |
| $\Delta f$             | Resonance full width at half maximum                            | 8.2     |
| $\Gamma$               | Geometry factor (units of resistance)                           | 8.2     |
| $\Omega_\alpha$        | Eigenfrequency of the electric field wave equation              | 12.1    |
| $\alpha$               | Coupling coefficient  | 8.2     |
| $\alpha$               | Generic mode label  | 12.1    |
| $\alpha$               | Thermal expansion coefficient                                   | 8.2     |
| $\alpha_0$             | Atomic polarizability   | 11.6    |
| $\alpha_f$             | Fine structure constant   | 11.6    |
| $\chi_e$               | Electric susceptibility   | 12.1    |
| $\delta V$             | Voltage error signal  | 9.2     |
| $\delta_0$             | Superconducting penetration depth at zero temperature           | 8.2     |
| $\delta_l$             | Partial wave phase shift  | 11.2    |
| $\delta_{\alpha\beta}$ | Kronecker delta function  | 12.1    |
| $\epsilon$             | Electric permittivity   | 8.2     |
| $\epsilon_r$           | Relative dielectric constant                                    | 11.3    |
| $\eta$                 | Dimensionless constant equal to $\epsilon_r - 1/\epsilon_r + 2$ | 11.4    |
| $\gamma_{mn}$          | Normalized Bessel root  | 8.1     |
| $\lambda$              | Perturbation expansion parameter                                | 12.1    |

| Notation             | Description   | Section |
|----------------------|---|---------|
| $\lambda$            | Radiation wavelength  | 11.4    |
| $\lambda_t$          | Thermal wavelength  | 11.2    |
| $\mu$                | Magnetic permeability   | 8.2     |
| $\mu_0$              | Magnetic permeability of vacuum   | 8.2     |
| $\omega$             | Angular frequency   | 8.2     |
| $\omega_{mnl}$       | Angular frequency of the TE <sub><i>mnl</i></sub> mode                  | 8.1     |
| $\phi$               | Azimuthal vector component  | 8.1     |
| $\psi(r, \phi)$      | Intermediate function in field equations                                | 8.1     |
| $\bar{\rho}$         | Average density   | 12.2    |
| $\rho$               | Molar density   | 11.2    |
| $\rho_0$             | Gas density at the cavity floor   | 12.2    |
| $\sigma_y^2(\tau)$   | Allan variance of $y$ over time interval $\tau$                         | 8.2     |
| $\tau$               | Time measurement interval   | 8.2     |
| $\theta$             | Phase of modulated signal   | 8.2     |
| $\zeta$              | Dimensionless length  | 12.2    |
| <b>Roman symbols</b> |   |         |
| $A$                  | Fitting amplitude   | 8.2     |
| $A(z)$               | Cross-sectional area as a function of height                            | 12.2    |
| $A^*$                | Resistance correction factor  | 8.2     |
| $A_\epsilon$         | Molar polarizability  | 11.3    |
| $A_n$                | Coefficients in the dielectric constant gas thermometry equation (11.8) | 11.4    |
| $a_0$                | Bohr radius   | 11.2    |
| $a_1, a_2$           | Integration limits in deadspace correction                              | 12.2    |
| $B$                  | Second virial coefficient   | 11.2    |
| $B_n$                | Terms in temperature series for the second virial coefficient           | 11.2    |
| $B_{c2}$             | Upper critical magnetic field   | 9.1     |

| <b>Notation</b>            | <b>Description</b>   | <b>Section</b> |
|----------------------------|--|----------------|
| $b$                        | Second dielectric virial coefficient                                       | 11.3           |
| $C$                        | Empirical parameter for equation (8.8)                                     | 8.2            |
| $C$                        | Fitting constant   | 8.2            |
| $C$                        | Liquid level sensor capacitance  | 13.2           |
| $C$                        | Third virial coefficient   | 11.2           |
| $C_n$                      | Coefficients in the temperature expansion for the third virial coefficient | 11.5           |
| $c$                        | Third dielectric virial coefficient  | 11.3           |
| $\mathbf{E}$               | Electric field   | 8.1            |
| $\vec{\mathcal{E}}_\alpha$ | Eigenmode of electric field wave equation                                  | 12.1           |
| $e$                        | Magnitude of electron charge   | 8.2            |
| $E_0$                      | Electric field amplitude   | 8.1            |
| $\tilde{f}$                | Normalized offset frequency  | 8.2            |
| $f$                        | Frequency  | 8.2            |
| $f_0$                      | Resonance frequency  | 8.2            |
| $f_m$                      | Modulation frequency   | 8.2            |
| $g$                        | Gravitational acceleration   | 8.3            |
| $\hbar$                    | Planck's constant divided by $2\pi$  | 8.2            |
| $\mathbf{H}$               | Magnetic field   | 8.1            |
| $i$                        | Square root of $-1$  | 8.2            |
| $J_m(x)$                   | Bessel function  | 8.1            |
| $K$                        | Compressibility  | 11.4           |

| <b>Notation</b>  | <b>Description</b>               | <b>Section</b> |
|------------------|----------------------------------|----------------|
| $k$              | Wave number                      | 11.2           |
| $k_B$            | Boltzmann's constant             | 8.2            |
| $L$              | Length of heat sink tee          | D.2            |
| $L$              | Length of the cavity             | 8.1            |
| $l$              | Angular momentum quantum number  | 11.2           |
| $l$              | Axial mode label                 | 8.1            |
| $m$              | Azimuthal mode label             | 8.1            |
| $m$              | Mass of a helium-4 atom          | 12.2           |
| $m_\alpha$       | Alpha particle mass              | 11.6           |
| $m_e$            | Electron mass                    | 8.2            |
| $N$              | Number of measurements           | 8.2            |
| $N_A$            | Avogadro's number                | 11.2           |
| $n$              | Radial mode label                | 8.1            |
| $n_e$            | Electron carrier density         | 8.2            |
| $P$              | Power                            | 8.2            |
| $P_l$            | Power dissipated                 | 8.2            |
| $p$              | Pressure                         | 8.2            |
| $Q$              | Cavity quality factor            | 8.2            |
| $Q_e$            | External circuit quality factor  | 9.3            |
| $Q_l$            | Loaded cavity quality factor     | 9.3            |
| $R$              | Molar gas constant               | 11.2           |
| $R$              | Radius of the cavity             | 8.1            |
| $R_0$            | Impurity resistance              | 8.2            |
| $R_{\text{GRT}}$ | Germanium thermometer resistance | 9.2            |

| Notation         | Description  | Section |
|------------------|--|---------|
| $R_{\text{ref}}$ | Reference resistance                                 | 9.2     |
| $R_s$            | Surface resistance                                   | 8.2     |
| $R_{sc}$         | Intrinsic resistance                                 | 8.2     |
| $\mathcal{R}$    | Transformer ratio                                    | 9.2     |
| $r$              | Radial vector component                              | 8.1     |
| $s$              | Dimensionless density                                | 12.2    |
| $s_0$            | Dimensionless gas density at the floor of the cavity | 12.2    |
| $T$              | Temperature  | 8.2     |
| $T_\lambda$      | Superfluid transition temperature                    | 11.0    |
| $t$              | Cavity wall thickness                                | 8.2     |
| $U$              | Stored energy  | 8.2     |
| $V$              | Voltage amplitude                                    | 8.2     |
| $V_{\text{can}}$ | Volume of the sample can                             | 12.2    |
| $V_{\text{ex}}$  | Excitation voltage                                   | 9.2     |
| $v_f$            | Fermi velocity                                       | 8.2     |
| $X$              | Dummy parameter in table 9.3                         | 9.1     |
| $x'_{mn}$        | $n$ th root of $\partial J_m(x)/\partial x$          | 8.1     |
| $Y$              | Young's modulus                                      | 8.2     |
| $z$              | Axial vector component                               | 8.1     |
| $z$              | Height in the cavity                                 | 12.2    |

‘They all fall under the heading of

Tetrapyloctomy.’

‘What’s tetra...?’

‘The art of splitting a hair four ways.’

---

Umberto Eco, *Foucault’s Pendulum*\*

## Chapter 8

# Introduction to Superconducting Cavity Resonators

**P**RECISION metrology is one of the most difficult and subtle disciplines in physics. Crudely put, metrology is the quest for more digits, but more properly, it is the study of the uncertainties in measurement techniques and the reduction of those uncertainties. The most precise measurements available in table-top physics experiments are those involving frequency. In this part of the thesis, we describe work towards achieving a particularly precise device for measuring frequencies in the 10 GHz range, the superconducting cavity resonator, and discuss some applications of the device to thermodynamic measurements of helium-4.

In the remainder of this chapter we introduce superconducting cavity resonators for use as frequency references. Our goal is to use the superconducting cavity resonator as a microwave frequency reference with frequency stability of parts in  $10^{15}$  or better over measurement times up to 1000 s. Later chapters will discuss the hardware associated with our experiment (chapter 9) and the use of our experiment purely as a frequency source (chapter 10).

Given a working superconducting cavity resonator system, we can apply the frequency resolution of the system to performing precise thermodynamic measurements of helium-4, in particular the dielectric constant and density. In the remainder of this part of the thesis we will introduce the thermodynamic properties of helium-4 (chapter 11) and describe how our apparatus may be used for precise measurements of these properties (chapter 12). The concluding chapter of this part (chapter 13) will summarize our results and discuss future plans for this experiment. Work on the project prior to the arrival of this researcher appears in references [2–5].

---

\*Reference [1]

## 8.1 Electromagnetic Resonant Cavities

The following few paragraphs are mostly a restatement of section 8.7 in Jackson's *Classical Electrodynamics*, 3rd edition [6]. For a circular cylindrical cavity of length  $L$  and radius  $R$ , the  $\text{TE}_{mnl}$  modes have the form:

$$\begin{aligned}
 H_z &= \psi(r, \phi) \sin\left(\frac{l\pi z}{L}\right), \\
 E_z &= 0, \\
 \mathbf{H}_t &= \frac{l\pi}{L\gamma_{mn}^2} \cos\left(\frac{l\pi z}{L}\right) \nabla_t \psi, \\
 \mathbf{E}_t &= -\frac{i\omega\mu}{\gamma_{mn}^2} \sin\left(\frac{l\pi z}{L}\right) \hat{\mathbf{z}} \times \nabla_t \psi, \\
 \psi(r, \phi) &= E_0 J_m(\gamma_{mn} r) e^{\pm im\phi}, \\
 \gamma_{mn} &= x'_{mn}/R, \\
 \omega_{mnl} &= \frac{1}{\sqrt{\mu\epsilon}} \left( \gamma_{mn}^2 + \frac{l^2\pi^2}{L^2} \right)^{1/2},
 \end{aligned}$$

where  $x'_{mn}$  is the  $n$ th root of the derivative of the Bessel function  $J_m(x)$ . The positions coordinates in the axial, radial, and azimuthal directions are  $z$ ,  $r$ , and  $\phi$ , respectively, with  $z = 0$  corresponding to the bottom wall of the cavity. The amplitude of the electric field is  $E_0$ .

We are only interested in  $\text{TE}_{01l}$  modes, so these can be simplified:

$$\begin{aligned}
 H_z &= E_0 J_0(\gamma_{01} r) \sin\left(\frac{l\pi z}{L}\right), \\
 E_z &= 0, \\
 \mathbf{H}_t &= E_0 \frac{l\pi}{L\gamma_{01}} \cos\left(\frac{l\pi z}{L}\right) J'_0(\gamma_{01} r) \hat{\mathbf{r}}, \\
 \mathbf{E}_t &= -E_0 \frac{i\omega\mu}{\gamma_{01}} \sin\left(\frac{l\pi z}{L}\right) J'_0(\gamma_{01} r) \hat{\phi}, \\
 \omega_{01l} &= \frac{1}{\sqrt{\mu\epsilon}} \left( \gamma_{01}^2 + \frac{l^2\pi^2}{L^2} \right)^{1/2}, \\
 \gamma_{01} &\approx 3.832/R.
 \end{aligned}$$

## 8.2 Properties of Superconducting Cavities

The key element in our experimental system is a superconducting cavity resonator (SCR). The properties of these devices were first thoroughly studied by Turneure and colleagues in the 1970s [7–9]. A thorough theoretical description of SCRS is given in [10]. We summarize these works here.

### 8.2.1 Resonance Mode Characterization

The most common means used to characterize the resonance modes is transmission spectroscopy. A schematic of the transmission setup appears in figure 9.8. In this method, a microwave signal of specified frequency is sent into the cavity through one of the signal coaxes and is extracted through the other signal coax. The outgoing signal is then amplified and filtered before being displayed on an oscilloscope. The amplitude peak-to-peak voltage,  $V$ , of the outgoing signal is then plotted as a function of frequency,  $f$ . Under ideal conditions, resonance modes appear as a Lorentzian peak:

$$V(f) = C + A \frac{(\Delta f / 2)^2}{(f - f_0)^2 + (\Delta f / 2)^2}, \quad (8.1)$$

where  $C$  is an offset voltage,  $A$  is the amplitude of the resonance,  $f_0$  is the resonance frequency and  $\Delta f$  is the full width at half maximum of the resonance). The  $Q$  value is calculated by the expression  $Q = f_0 / \Delta f$ . The uncertainty of  $f_0$  is determined by the fitting statistics.

The key parameters of an SCR are the resonance frequency  $f_0$  and the quality factor  $Q$ , which is a measure of the energy storage capacity of the resonator:

$$Q = 2\pi f_0 \frac{U}{P_l},$$

where  $U$  is the time-averaged electromagnetic energy stored in the cavity and  $P_l$  is the time-averaged power dissipated in the cavity. Two equivalent expressions for  $Q$  are [10; 11]

$$Q = \frac{f_0}{\Delta f} = \frac{\Gamma}{R_s}, \quad (8.2)$$

where  $\Delta f$  is the full width at half maximum (FWHM) of the resonance power spectrum,  $\Gamma$  is a geometry factor dependent on the particular resonance mode, and  $R_s$  is the surface resistance of the cavity material at the resonance frequency. In general, the quality factor may be improved

by reducing the surface resistance through annealing and chemical etching. These procedures are described in section 9.1.3.

The resistance has two components, one from surface contamination and other cavity defects ( $R_0$ ), the second from the finite penetration depth of the superconductor ( $R_{sc}$ ). The latter can be approximated by [10]

$$R_{sc} = A^* \left( \frac{\sqrt{3} m_e \mu_0^2 v_f \omega^2}{16\pi e^2 n_e} \right)^{1/3} \frac{2}{3} \left( \frac{2}{\pi} \right)^{4/3} \left( \frac{\hbar \omega}{2\Delta_0} \right)^{4/3} \frac{2\Delta_0}{k_B T} \ln \left( \frac{4k_B T}{1.78 \hbar \omega} \right) \exp \left( -\frac{\Delta_0}{k_B T} \right), \quad (8.3)$$

where  $m_e$  is the electron mass,  $\mu_0$  is the vacuum permeability,  $e$  is the electron charge,  $k_B$  is Boltzmann's constant,  $\hbar$  is Planck's constant divided by  $2\pi$ ,  $\omega$  is  $2\pi$  times the resonance frequency, and the other material-dependent parameters  $\Delta_0$ ,  $n_e$ , and  $v_f$  are the superconducting gap energy at zero temperature, the electron carrier density, and the Fermi velocity, respectively. The line width of the resonance for a cavity with  $Q$  on the order of  $10^9$  and resonance frequency of 10 GHz is about 10 Hz. The line width is also an estimate of the uncertainty in the measurement of the resonance frequency  $f_0$ , although this uncertainty may be reduced by performing multiple measurements. Through standard spectroscopy techniques the uncertainty in the resonance frequency can be reduced to the order of  $\Delta f / \sqrt{N}$ , where  $N$  is the number of measurements. A much better method is to measure the resonance frequency for long time periods (on the order of 1000 s or more) by means of the phase-locked loop (PLL) technique to be described later. Under ideal conditions the relative uncertainty in the measurement of the resonance frequency can be reduced to parts in  $(Q \times 10^7)$  using the PLL technique (see sections 8.2.3 and 9.3.2). For example, to reach an uncertainty in frequency of parts in  $10^{15}$  or better requires  $Q$  of  $10^8$  or more.

The inherent frequency stability of the resonator is limited by noise sources which alter the dimensions or electromagnetic properties of the cavity. These sources include (but are not limited to) fluctuations in mechanical strain, temperature, internal gas pressure, and incident microwave power [10]. These effects are described in detail below.

### 8.2.2 Limits on Frequency Stability

Any fluctuation in the mechanical, thermodynamic, or electromagnetic properties of the cavity can result in fluctuations of the resonance frequency. In this section we enumerate some sources of frequency fluctuations, mostly based on work found in [10].

The obvious sources of noise are those that change the physical dimensions of the cavity. For example, mechanical vibrations may strain the cavity causing fluctuations in the dimensions of the cavity. The relative fluctuations in frequency ( $\delta f/f$ ) caused by a strain along the axial direction ( $\delta L/L$ ) are

$$\frac{\delta f/f}{\delta L/L} = \frac{\pi^2 l^2}{\mu \epsilon (2\pi f_0)^2 L^2}, \quad (8.4)$$

where  $\mu$  is the magnetic permeability of the cavity interior (e.g., vacuum or gas),  $\epsilon$  is the electric permittivity of the interior,  $f_0$  is the nominal resonance frequency, and  $l$  is the axial mode label. The corresponding formula for strains in the radial direction ( $\delta R/R$ ) is

$$\frac{\delta f/f}{\delta R/R} = -\frac{x'_{mn}{}^2}{\mu \epsilon (2\pi f_0)^2 R^2}, \quad (8.5)$$

where  $x'_{mn}$  is the  $n$ th root of the derivative of the Bessel function  $J_m(x)$ , and  $m$  and  $n$  are the mode labels in the azimuthal and radial directions, respectively. In particular,  $x'_{01} \approx 3.832$ . These strains can be minimized by proper mounting of the cavity and by building the cavity with thick walls. Our cavity is mounted by screw threads along the circumference of the exterior in the middle.

Gas pressure fluctuations ( $\delta p/p$ ) may also cause strains in the cavity. The frequency fluctuations related to pressure variations are

$$\frac{\delta f/f}{\delta p/p} \approx \left( \frac{\delta f/f}{\delta R/R} \right) \frac{p}{Y}, \quad (8.6)$$

where the first factor comes from equation (8.5) and  $Y$  is the Young's modulus of the cavity. The effect of pressure fluctuations is proportional to pressure; it is minimized by operating at a low base pressure, typically below microtorr. However, for the helium equation of state measurement discussed in later chapters, the pressure inside the cavity will be on the order of tens of torr. Although the base pressure will be high in this case, the pressure fluctuations themselves should be minimal because the volume is fixed and the temperature will be controlled to parts in  $10^6$  or better. Unfortunately, pressure fluctuations may still be caused by acoustic noise.

Thermal fluctuations ( $\delta T/T$ ) cause two effects. The first are strains from thermal expansion, with frequency fluctuations according to

$$\frac{\delta f/f}{\delta T/T} = \frac{\alpha T}{\mu\epsilon(2\pi f_0)^2} \left[ \left( \frac{\pi l}{L} \right)^2 - \left( \frac{x'_{mn}}{R} \right)^2 \right], \quad (8.7)$$

where  $\alpha$  is the thermal expansion coefficient of the cavity.

The second temperature effect is the change in the superconducting penetration depth of the cavity as a function of temperature. An increase in the penetration depth effectively increases the volume of the cavity, causing the resonance frequency to decrease:

$$\frac{\delta f/f}{\delta T/T} = -C \frac{2\pi f_0 \delta(0) \mu_0}{2\Gamma} \frac{\Delta(0)}{k_B T} \exp \left[ -\frac{\Delta(0)}{k_B T} \right], \quad (8.8)$$

where  $k_B$  is the Boltzmann constant,  $C$  is an empirically determined material parameter ( $C = 1.8$  for niobium [10]),  $\delta_0$  is the superconductor penetration depth at zero temperature,  $\Delta_0$  is the superconducting energy gap at zero temperature, and  $\Gamma$  is a geometric constant determined by the mode with units of resistance. The effects of the two temperature fluctuations effects (equations (8.7) and (8.8)) on the frequency of the TE<sub>011</sub> mode of our cavity are displayed in figure 9.7.

The last effect considered here is that caused by fluctuations in the incident microwave power on the cavity. The electromagnetic pressure of the microwave radiation may be sufficient to strain the cavity, causing a change in frequency. The relation between power fluctuations and frequency fluctuations is

$$\frac{\delta f/f}{\delta P/P} \approx -\frac{QPt}{8\pi^2 f_0 YR^4}. \quad (8.9)$$

Here  $t$  is the wall thickness of the cavity. This effect may be minimized by reducing the incident power. We estimate the power  $P$  in the cavity during our experiments to be approximately  $-20$  dBm or, equivalently,  $10^{-5}$  W.

### 8.2.3 Phase-Locked Loop

The phase-locked loop (PLL) technique utilized in this experiment is derived from the method originally presented by R. V. Pound in the 1940s [12]. Pound's idea was to correct the frequency of the microwave source to match that of the resonant cavity by modulating the input signal and

measuring the phase of the reflected signal to determine the offset between the input frequency and the resonance frequency.

A cartoon depiction of the PLL technique is shown in figure 8.1 to summarize the technique. Beginning at the bottom left of the diagram is the carrier frequency source in the synthesizer, which generates a continuous wave signal at  $f_0$ , nominally the resonance frequency of the superconducting cavity. This signal enters the phase modulator where sidebands are mixed in at frequencies  $\pm f_m$  relative to the carrier. The frequency spectrum at this point in the circuit is shown in the top-left corner. From here the signal goes through a circulator to the cavity. A portion of the signal is reflected by the cavity and returns out the third port of the circulator. Note that only one signal coax is used, but the system contains two coaxes. This allows us to operate two PLL simultaneously in the same cavity at two resonance frequencies.

The reflected signal is greatly attenuated relative to the input signal and each component frequency experiences a phase shift. The attenuation and phase shift for each frequency are functions of the difference between that frequency and the cavity resonance frequency. The reflected signal enters a crystal detector which rectifies the signal, essentially folding over the spectrum at the carrier frequency: the signal previously at  $f_0$  yields a DC signal and the sidebands add together to give a signal at  $f_m$ .

The detected signal at the modulation frequency seen by the lock-in amplifier is given by [12]

$$V(\tilde{f}) \propto e^{i\theta} \frac{\alpha^2 - \tilde{f}^2 - 1 - 2i\tilde{f}\alpha}{(\alpha + 1)^2 + \tilde{f}^2}, \quad (8.10)$$

where  $\tilde{f}$  is a normalized offset frequency,  $\tilde{f} = 2Q(f - f_0)/f_0$ ,  $\alpha$  is a dimensionless coupling coefficient and has a value  $0 < \alpha \ll 1$  in the weakly coupled limit,  $\theta$  is a phase, and  $i = \sqrt{-1}$ . Note that after adjusting the phase  $\theta$  to zero, the imaginary part of the signal is an odd function in  $\tilde{f}$  and is approximately linear when  $\tilde{f}$  is near zero. Equation (8.10) is plotted in figure 8.2.

After correcting for the phase  $\theta$ , the imaginary component of this signal is detected by the lock-in amplifier and converted into a DC error voltage. The error voltage adjusts the frequency of the quartz crystal inside the synthesizer, correcting the carrier frequency towards the cavity resonance frequency, thus completing the loop.

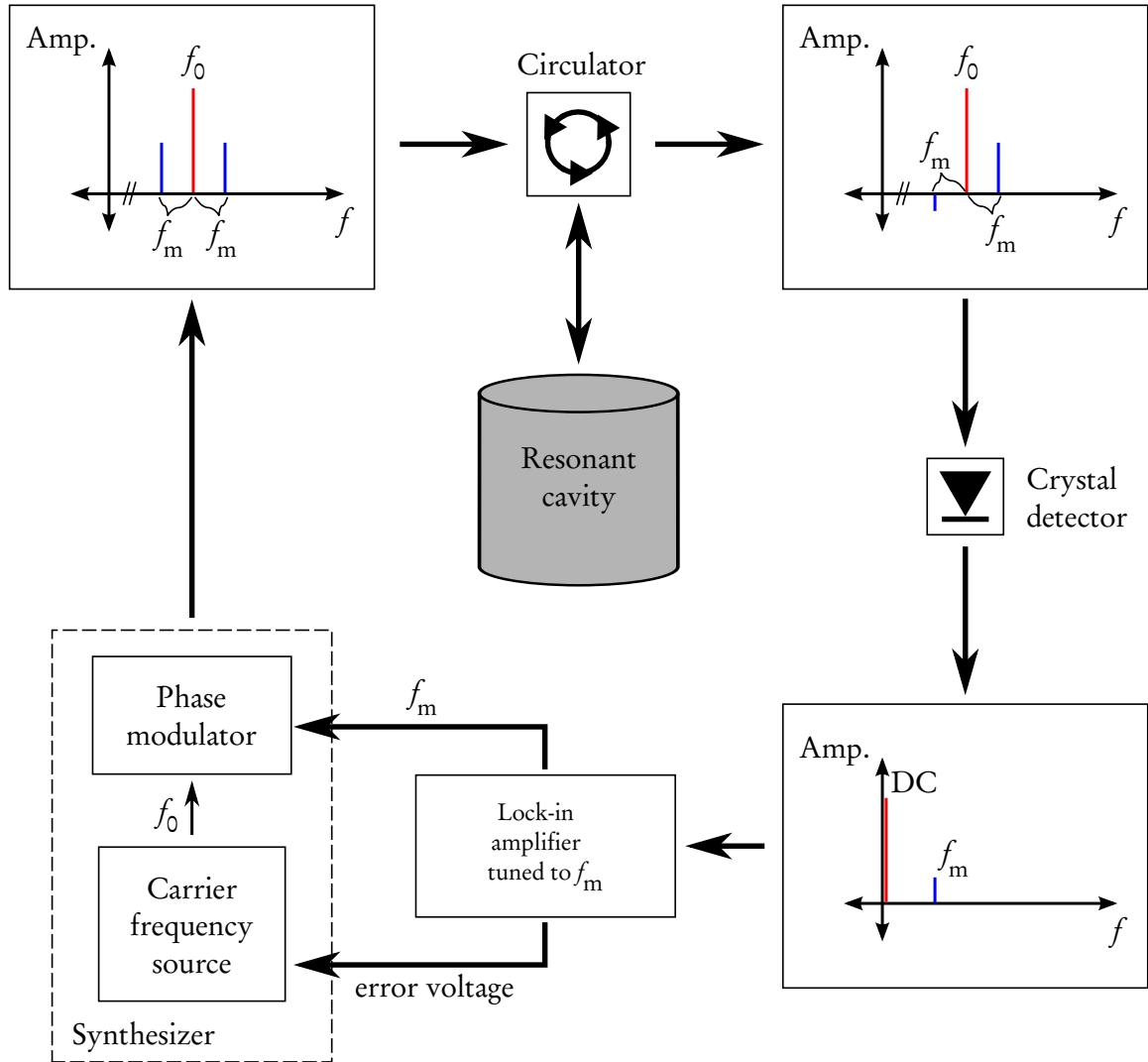


Figure 8.1. A cartoon schematic of the phase-locked loop. The graphs show the frequency spectrum of the signal at that point in the circuit. The carrier signal  $f_0$  is shown in red and the sidebands at  $f_0 \pm f_m$  are shown in blue. The height of these bars qualitatively show the real part of the amplitude, with the negative direction indicating a  $\pi$  phase shift. For more complete description of the circuit, see the text.

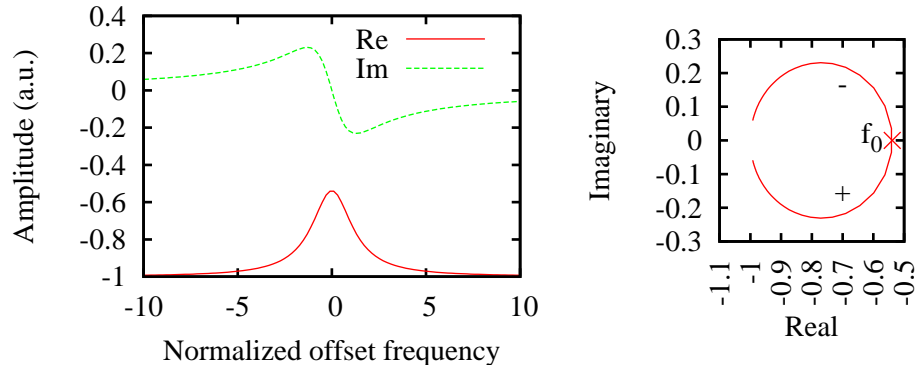


Figure 8.2. Phase-locked loop error signal, equation (8.10). The left panel shows the real and imaginary components of the error amplitude as a function of the normalized frequency  $\tilde{f}$ . The right panel shows the error signal plotted in the complex plane, with signal at resonance marked by  $f_0$  and the regions of the curve where  $f < f_0$  and  $f > f_0$  are labeled by  $-$  and  $+$ , respectively.

#### 8.2.4 Allan Variance

The metric of choice for describing frequency stability is the Allan variance [13; 14]. The Allan variance ( $\sigma_y^2(\tau)$ ) is a generalization of the normal statistical variance useful for quantities that vary over time. Essentially,  $\sigma_y^2(\tau)$  is the variance in the quantity  $y$  for measurements separated in time by the interval  $\tau$ . The Allan variance has two major advantages over the normal variance. First, the normal variance can diverge over long measurement times, for example, when the signal has a random walk; the Allan variance stays finite. Second, the functional form of  $\sigma_y^2(\tau)$  with respect to  $\tau$  gives information about the type of noise present in the system (described below).

To define the Allan variance, we first assume the quantity of interest is the frequency  $f$  with a nominal value of  $f_0$ . A series of  $N$  discrete measurements  $f_i$  for  $i \in \{1, \dots, N\}$  is made at equal time intervals  $\tau_0$ . The first step in calculating the Allan variance is to normalize the frequency measurements with respect to the nominal value:

$$y_i = \frac{f_i - f_0}{f_0}; \quad \text{for } i \in \{1, \dots, N\}, \quad (8.11)$$

where  $y_i$  is the relative error in the frequency measurement with respect to the nominal value.

Table 8.1. Dependence of the Allan variance on noise type [14]

| Noise source                | $\frac{\partial}{\partial(\log \tau)} \left( \log \sqrt{\sigma_y^2(\tau)} \right)$ |
|-----------------------------|--|
| White phase noise           | -1   |
| Flicker phase noise         | -1   |
| White frequency noise       | -1/2   |
| Flicker frequency noise     | 0  |
| Random walk frequency noise | +1/2   |

The Allan variance is then defined by

$$\sigma_y^2(n\tau_0) = \frac{1}{2} \sum_{k=1}^{\frac{N}{n}-1} (y_{nk} - y_{n(k+1)})^2. \quad (8.12)$$

The Allan variance is usually displayed in a log-log plot with  $\sqrt{\sigma_y^2(\tau)}$  (sometimes denoted by the acronym SRAV for “Square Root of Allan Variance”) on the vertical axis and  $\tau$  on the horizontal axis. The slope of the SRAV curve on the log-log plot indicates the type of noise which dominates the system over the time scale  $\tau$ . Some examples are given in table 8.1.

### 8.3 Frequency Standards

One the goals of this project is to use our highly stable superconducting cavity resonator as a frequency reference. The standard second is defined in terms of a cesium atom by international treaty. One second is *exactly* 9 192 631 770 times the period of the transition between the hyperfine states of the ground state of the cesium-133 atom [14]. The second is defined this way for two primary reasons: first, the cesium transition can be measured accurately in a laboratory, and second, so far as the atomic properties of the cesium atom are independent of time and place (which is true if Einstein’s Equivalence Principle holds) the second can be reproduced anywhere and anytime.

The current state-of-the-art frequency standard is the laser-cooled cesium fountain clock used by various government standards laboratories around the world [15]. These clocks have demonstrated relative frequency instabilities of  $2 \times 10^{-16}$  over measurement times of  $5 \times 10^4$  s. The major limit to long-term stability in these modern clocks is residual collisions in the cesium gas being measured.

Short-term stability is limited by instabilities in the local oscillator, which maintains the frequency of the clock between interrogations of the cesium atoms. This local oscillator has traditionally been a quartz crystal frequency source but cryogenic sapphire resonators have recently come into service. These sapphire resonators have relative frequency stabilities of  $3 \times 10^{-15}$  [15]. The sapphire resonator systems are almost identical to our superconducting cavity system; only the resonator itself is different.

Future frequency standards are likely to be based on optical atomic transitions, for example, in strontium atoms or mercury ions, because of the inherently fine linewidths (or high  $Q$ ) of these transitions. By leveraging the high precision and frequency span of femtosecond optical frequency combs (see, for example, the 2005 Nobel lecture by Theodor Hänsch [16]), optical and microwave frequencies are now directly comparable in the laboratory with  $1 \times 10^{-15}$  fractional uncertainty, thus opening up practical means of measuring optical frequencies to high accuracy [17; 18]. Researchers have already demonstrated parts in  $10^{15}$  stability for ensembles of  $^{87}\text{Sr}$  atoms in an optical lattice [19]. A competing technique is to measure transitions in single ions, thus avoiding collision broadening of the transition. Measurements of single  $^{199}\text{Hg}^+$  ions in a radio frequency trap have demonstrated relative frequency uncertainties of  $7 \times 10^{-17}$  [20].

To briefly explain how precise these measurements are, at this precision the researchers must account for effects as small as the gravitational redshift between frequency sources at different heights in the laboratory. The relative frequency shift between two clocks separated by a height  $h$  of 1 m at the Earth's surface is roughly  $gh/c^2 \sim 10^{-16}$ , an effect large enough to be seen by today's experiments. Tidal forces cause frequency shifts on the  $10^{-17}$  level throughout the course of a day [14]. In the near future, the very idea of synchronizing clocks will be obsolete, thanks to Einstein and modern technology. With these advancements in optical clock technology, the redefinition of the second in terms of an optical transition is imminent; the only uncertainty is the choice of which optical transition. The reign of cesium is ending.

Many of these advanced techniques have developed in the short time spanned by the work in this thesis. Unfortunately, our predicted ultimate frequency stability is only parts in  $10^{15}$  making our technology already obsolete for clock applications. However, superconducting resonators could still be useful as subsystems of a larger atomic frequency apparatus, for example as local oscillators in cesium clocks, replacing the sapphire resonators currently used. And, as will be explained beginning in chapter 11, our apparatus is still a state-of-the-art tool for measuring

materials properties.

## Bibliography

- [1] U. Eco. *Foucault's Pendulum*. New York: Ballantine (1989). Trans. William Weaver.
- [2] W. Jiang, D. M. Strayer, N.-C. Yeh, J. Huynh, N. Asplund, J. Gatewood, and M. J. Lysek. "Integration of high-resolution frequency control and thermometry for high-precision measurements of physical properties of helium." *Japan Society of Microgravity Application Journal*, **15 Supp.** II:157 (1999).
- [3] N.-C. Yeh, W. Jiang, and D. M. Strayer. "Application of high-resolution frequency measurements to studies of critical phenomena in helium." *Japan Society of Microgravity Application Journal*, **15 Supp.** II:136 (1999).
- [4] N.-C. Yeh, W. Jiang, D. M. Strayer, and N. N. Asplund. "Precise measurements of the density and critical phenomena near the phase transitions in helium using high-Q niobium microwave cavities." *Czech Journal of Physics*, **46**(Suppl. S3) (1996).
- [5] N.-C. Yeh, D. M. Strayer, V. L. Anderson, and N. Asplund. "Superconducting-Cavity-Stabilized Oscillators (scso) for precise frequency measurements." *Physica B*, **280**:557–558 (2000).
- [6] J. D. Jackson. *Classical Electrodynamics*. New York: Wiley, third edition (1999).
- [7] S. R. Stein and J. P. Turneaure. "Superconducting-cavity stabilized oscillators with improved frequency stability." *Proceedings of the IEEE*, **63**(8):1249–1250 (1975).
- [8] J. P. Turneaure and N. T. Viet. "Superconducting Nb  $TM_{010}$  mode electron-beam welded cavities." *Applied Physics Letters*, **16**(9):333–335 (1970).
- [9] J. P. Turneaure and I. Weissman. "Microwave surface resistance of superconducting niobium." *Journal of Applied Physics*, **19**(9):4417–4427 (1968).
- [10] V. B. Braginsky, V. P. Mitrofanov, and V. I. Panov. *Systems with Small Dissipation*. Chicago: U. Chicago P. (1985).
- [11] D. M. Pozar. *Microwave Engineering*. Reading: Addison-Wesley (1990).
- [12] R. V. Pound. "Electronic frequency stabilization of microwave oscillators." *Review of Scientific Instruments*, **17**(11):490–505 (1946). <http://link.aip.org/link/?RSI/17/490/1>.
- [13] D. W. Allan. "Statistics of atomic frequency standards." *Proceedings of the IEEE*, **54**(2):221–231 (1966).
- [14] C. Audoin and B. Guinot. *The Measurement of Time: Time, Frequency, and the Atomic Clock*. Cambridge: Cambridge UP, English edition (2001). Translator Stephen Lyle.
- [15] S. Bize, P. Laurent, M. Abgrall, I. Maksimovic, L. Cacciapuoti, J. Grünert, C. Vian, et al. "Cold atom clocks and applications." *Journal of Physics B*, **38**(9):S449–S468 (2005). <http://stacks.iop.org/0953-4075/38/S449>.
- [16] T. W. Hänsch. "Nobel lecture: Passion for precision." *Reviews of Modern Physics*, **78**(4):1297 (2006). <http://link.aps.org/abstract/RMP/v78/p1297>.

- [17] S. A. Diddams, J. Ye, and L. Hollberg. “Femtosecond lasers for optical clocks and low noise frequency synthesis.” In J. Ye and S. T. Cundiff, editors, *Femtosecond Optical Frequency Comb Technology: Principle, Operation and Applications*, New York: Springer, chapter 9 (2005). <http://tf.nist.gov/timefreq/general/pdf/1992.pdf>. Also, NIST Time and Frequency Division publication bin #1992.
- [18] M. C. Stowe, M. J. Thorpe, A. Pe’er, J. Ye, J. E. Stalnaker, V. Gerginov, and S. A. Diddams. “Direct frequency comb spectroscopy.” In E. Arimondo, P. Berman, and C. Lin, editors, *Advances in Atomic, Molecular, and Optical Physics*, volume 55, Amsterdam: Elsevier, chapter 1 (2007). <http://tf.nist.gov/timefreq/general/pdf/2205.pdf>. Also, NIST Time and Frequency Division publication bin #2205.
- [19] M. M. Boyd, A. D. Ludlow, S. Blatt, S. M. Foreman, T. Ido, T. Zelevinsky, and J. Ye. “ $^{87}\text{Sr}$  lattice clock with inaccuracy below  $10^{-15}$ .” *Physical Review Letters*, **98**(8):083002 (2007). <http://link.aps.org/abstract/PRL/v98/e083002>.
- [20] W. H. Oskay, S. A. Diddams, E. A. Donley, T. M. Fortier, T. P. Heavner, L. Hollberg, W. M. Itano, et al. “Single-atom optical clock with high accuracy.” *Physical Review Letters*, **97**(2):020801 (2006). <http://link.aps.org/abstract/PRL/v97/e020801>.

Clocks slay time. Time is dead as long as it is being clicked off by little wheels; only when the clock stops does time come to life.

---

William Faulker,  
*The Sound and the Fury*\*

## Chapter 9

### Hardware

**T**HE hardware used for this experiment has two primary systems. The first is the superconducting cavity and the microwave system used to measure and track its resonance frequency. The second major system is the thermal system, consisting of the cryogenic probe, thermometers, cooling equipment, etc. used to maintain an optimal temperature.

#### 9.1 Superconducting Cavities

##### 9.1.1 Physical Properties

The cavities we use are right circular cylinders machined from two pieces of niobium (see table 9.1) and e-beam welded together. Niobium is chosen because of its high superconducting transition temperature of 9.3 K and its mechanical robustness. The inner diameter and inner height of the cavity are approximately 28 mm. A schematic of the cavity dimensions is shown in figure 9.1. Our microwave equipment allows us to operate the cavity at two resonance modes,  $TE_{011}$  and  $TE_{013}$ , with respective resonance frequencies of approximately 14.1 and 20.7 GHz. (The subscripts in the mode labels indicate the number of antinodes of  $E_t$  in the azimuthal (over  $0 < \phi < \pi$ ), radial, and axial directions, respectively.) These modes are chosen for their high  $Q$  and because they can be inductively coupled to coaxial cables through a loop antenna at the end of the coax. The electric and magnetic fields of the  $TE_{011}$  modes of a right-circular cylindrical cavity of length  $L$  and radius

---

\*Reference [1]

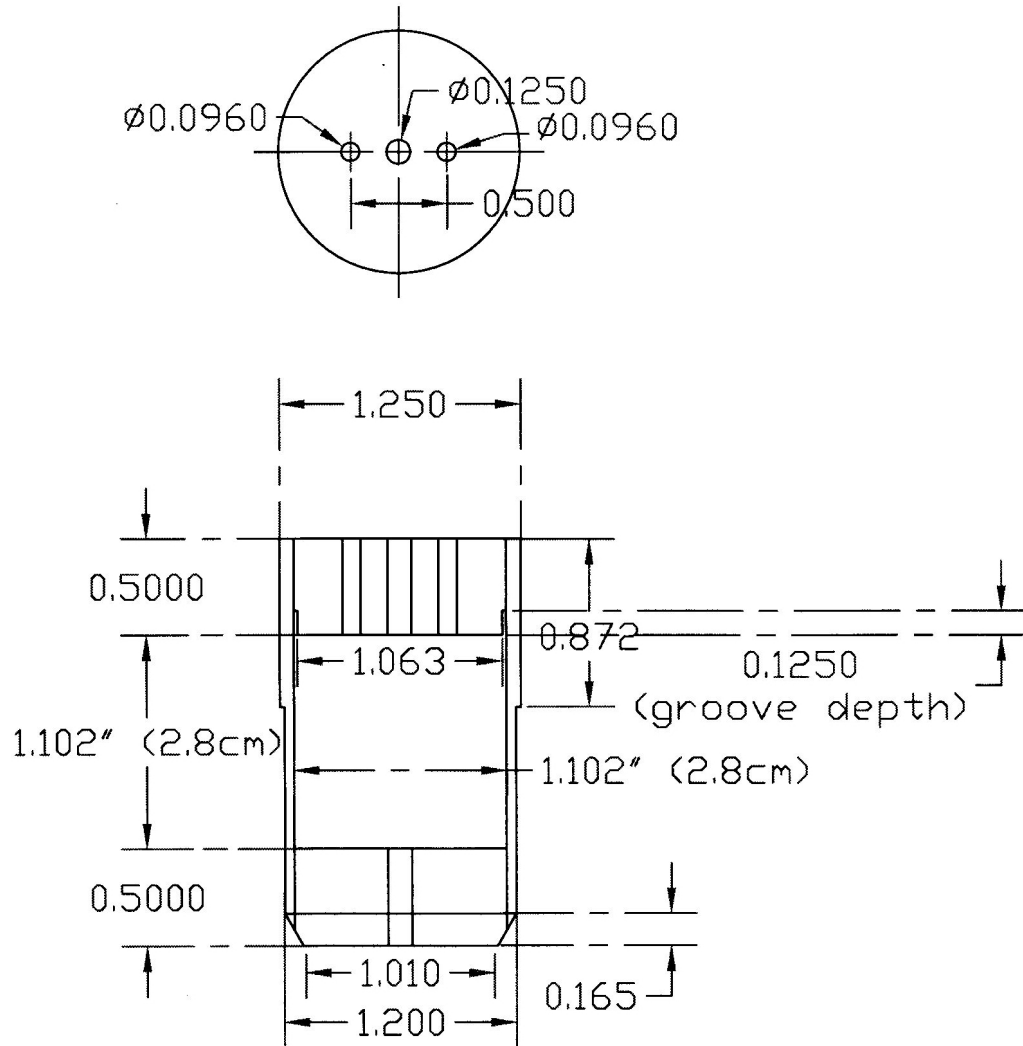


Figure 9.1. Drawing of the niobium cavity. Dimensions are in inches, except where noted. (By Wen Jiang).

Table 9.1. Mechanical and electromagnetic properties of the niobium at 1.4 K, from [3], except where noted

| Property                                | Symbol     | Value                                 |
|---|------------|---------------------------------------|
| Superconducting critical temperature    | $T_c$      | 9.25 K                                |
| Superconducting gap energy (0 K)        | $\Delta_0$ | 1.50 meV                              |
| Upper critical field (0 K) [4]          | $B_{c2}$   | 200 mT                                |
| Superconducting penetration depth (0 K) | $\delta_0$ | 35 nm                                 |
| Fermi velocity                          | $v_f$      | $2.9 \times 10^5$ m/s                 |
| Electron number density                 | $n_e$      | $2.4 \times 10^{28}$ m <sup>-3</sup>  |
| Thermal expansion coefficient           | $\alpha$   | $1.1 \times 10^{-10}$ K <sup>-1</sup> |
| Young's modulus                         | $Y$        | $\sim 10^{11}$ Pa                     |
| Constant for equation (8.3)             | $A^*$      | 0.97                                  |
| Constant for equation (8.8)             | $C$        | 1.8                                   |

$R$  are given by [2]

$$\begin{aligned}
 H_z &= E_0 J_0(\gamma_{01} r) \sin\left(\frac{l\pi z}{L}\right), \\
 E_z &= 0, \\
 \mathbf{H}_t &= E_0 \frac{l\pi}{L\gamma_{01}} \cos\left(\frac{l\pi z}{L}\right) J'_0(\gamma_{01} r) \hat{\mathbf{r}}, \\
 \mathbf{E}_t &= -E_0 \frac{i2\pi f_0 \mu}{\gamma_{01}} \sin\left(\frac{l\pi z}{L}\right) J'_0(\gamma_{01} r) \hat{\boldsymbol{\phi}}, \\
 \omega_{01l} &= \frac{1}{\sqrt{\mu\epsilon}} \left( \gamma_{01}^2 + \frac{l^2 \pi^2}{L^2} \right)^{1/2}, \\
 \gamma_{01} &\approx 3.832/R,
 \end{aligned}$$

where the axial position  $z$  is zero at the bottom of the cavity and  $L$  at the top of the cavity. Note that the electric field goes to zero at the cavity walls and that the magnetic field is parallel to the walls near the surface.

The properties of the cavities are summarized in table 9.2.

Table 9.2. Parameters of the superconducting cavity

| Property                 | Symbol      | Value (TE <sub>011</sub> ) | Value (TE <sub>013</sub> ) |
|--------------------------|-------------|----------------------------|----------------------------|
| Axial length             | $L$         | ~ 28 mm                    |                            |
| Radius                   | $R$         | ~ 14 mm                    |                            |
| Wall thickness           | $t$         | ~ 10 mm ends, ~ 2 mm sides |                            |
| Mode labels              | $(m, n, l)$ | (0, 1, 1)                  | (0, 1, 3)                  |
| Geometry coefficient [3] | $\Gamma$    | 780 $\Omega$               | 1200 $\Omega$              |
| Resonance frequency      | $f_0$       | 14.1 GHz                   | 20.7 GHz                   |

### 9.1.2 Expected Frequency Fluctuations

Table 9.3 summarizes the relative fluctuations in the cavity frequency generated by various effects earlier in section 8.2.2. Note that the best value of  $\delta f/f$  for all of these effects is less than our goal of  $10^{-15}$ , except for the pressure fluctuation effect in the helium experiment which has less stringent frequency uncertainty requirements (see chapter 11).

Not listed in the table are effects concerning components of the experiment other than the cavity itself, such as the microwave synthesizers, mixers, detectors, and amplifiers. These devices are also susceptible to temperature variations, humidity fluctuations, acoustic noise, external electromagnetic noise, and power supply noise (for the powered components) [5–7]. Although by using weak coupling to the cavity and the phase-locked loop technique we can reject most external noise sources, some of the sources indirectly affect the cavity, for example, by causing fluctuations in the power or temperature.

### 9.1.3 Processing and Handling

Because  $Q$  is inversely proportional to the surface resistance, minimizing the residual resistance is paramount. Figure 9.2 shows the theoretical intrinsic surface resistance and the resulting maximum  $Q$  as a function of temperature for the TE<sub>011</sub> mode of our cavity. In a real system, the  $Q$  saturates at  $1/R_0$  because of surface impurities. To reduce the residual surface resistance of the niobium cavity we use special preparation and handling procedures, particularly because niobium oxidizes easily in air. The processing procedures presented here are performed whenever the  $Q$  of the cavity begins to degrade (typically after several months) or whenever the cavity has been accidentally

Table 9.3. Order of magnitude estimates of resonance frequency fluctuations in the superconducting cavity, assuming a temperature of 1.4 K (except for the pressure fluctuations at the  $^4\text{He}$  lambda point of 2.17 K), from [3] and explained more fully in section 8.2.2

| Effect ( $X$ )   | Equation | Required $\delta X/X$ | $\frac{\delta f/f}{\delta X/X}$ | Best $\delta f/f$ |
|--|----------|-----------------------|---------------------------------|-------------------|
| Changes in cavity length   | (8.4)    | N/A                   | $10^{-1}$                       | N/A               |
| Changes in cavity radius   | (8.5)    | N/A                   | 1                               | N/A               |
| Thermal expansion  | (8.7)    | $10^{-8}$             | $10^{-10}$                      | $10^{-18}$        |
| Temperature dependence<br>of penetration depth                         | (8.8)    | $10^{-8}$             | $10^{-10}$                      | $10^{-18}$        |
| Pressure fluctuations at $10^{-6}$ torr<br>(clock experiment)          | (8.6)    | $10^{-3}$             | $10^{-12}$                      | $10^{-15}$        |
| Power fluctuations (best guess)  | (8.9)    | $10^{-3}$             | $10^{-13}$                      | $10^{-15}$        |
| <i>Goal (clock experiment)</i>   |          |                       |                                 | $< 10^{-15}$      |
| Pressure fluctuations at $^4\text{He}$ lambda point<br>(He experiment) | (8.6)    | $10^{-3}$             | $10^{-7}$                       | $10^{-10}$        |
| <i>Goal (helium experiment)</i>  |          |                       |                                 | $< 10^{-9}$       |

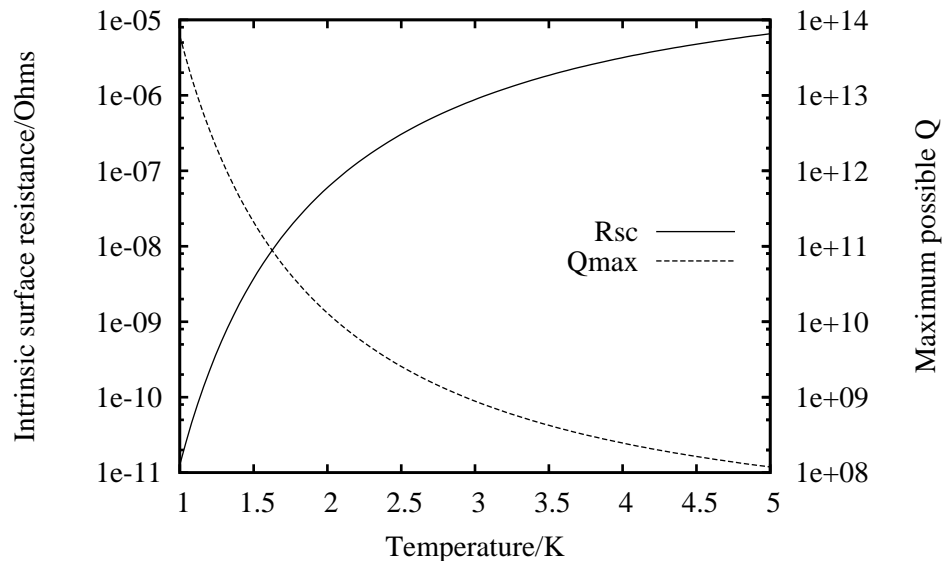


Figure 9.2. Theoretical intrinsic surface resistance  $R_{sc}$  (from equation (8.3), left scale) and theoretically maximum possible  $Q$  (right scale) of the  $TE_{011}$  mode of the niobium cavity, as a function of temperature.

exposed to air.

### Chemical cleaning and etching

The first step in processing the cavity is to degrease the surface to remove any condensed pump oil, fingerprints, etc. This is done by washes in an ultrasonic agitator with successive baths of mild detergent, acetone, isopropanol, and finally, deionized water. Each step is done for 30 minutes.

The second step is an acid etch to remove the oxide layer. The recipe for the acid bath is one part hydrofluoric acid, one part nitric acid, and two parts phosphoric acid. This cocktail removes approximately  $3 \mu\text{m}$  of niobium per minute. Typical etch times are 3–5 minutes, depending on the amount of oxide which must be removed. After the etch the cavity is rinsed in multiple baths of deionized water to remove any acid residue. The cavity is stored temporarily in deionized water until it can be installed in the annealing system.

#### 9.1.4 Annealing

The final step in the preparation of the niobium cavity is annealing under ultrahigh vacuum conditions. A schematic of the annealing setup is shown in figure 9.3. Before installing the niobium

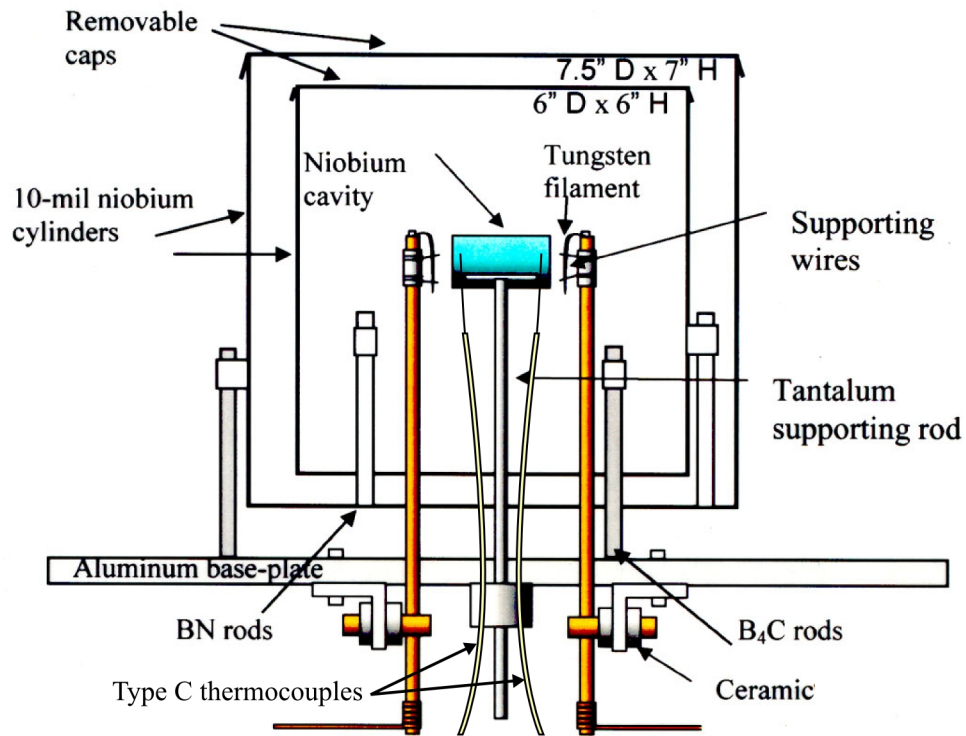


Figure 9.3. Schematic of the UHV annealing system, side cutaway view.

cavity into the vacuum system, a pair of type C thermocouples are spot welded to the ends of the cavity. The cavity is placed in the cradle between the two tungsten e-beam filaments. Then niobium radiation shields are placed around the cavity to keep the heat close to the cavity prevent damage to the chamber walls. Additionally, a water-cooled copper shroud goes around the niobium shields. The aluminum base plate and copper e-beam supports are also water cooled.

After installing the heat shields, the chamber is closed and rough pumped using a turbomolecular pump. Heating tapes are wrapped around the chamber and used to bake out the chamber overnight to remove water vapor from the chamber walls. After bake out, the heating tapes are removed. When the pressure drops below  $10^{-6}$  torr, ion pumps are started and liquid nitrogen is added to begin cooling a sorption pump in the base of the chamber. Then the turbomolecular pump is removed from the system. At this point, an ion gauge and a residual gas analyzer (Stanford Research RGA-200) are started to monitor the pressure and gas composition in the system. After the ion pumps have reached their lowest pressure, a titanium sublimation pump is started to further reduce the pressure.

When the pressure drops to  $\sim 10^{-9}$  torr, the heating of the cavity can begin. First, the cooling

water to the copper shroud, base plate, and e-beam posts is started. Next the e-beam system is energized and a small amount of current is applied to outgas the filament. After the pressure stabilizes, the current is increased until the cavity temperature (as measured by the thermocouples) reaches about 150 °C to drive off water vapor from the cavity. After the pressure drops again, the e-beam current is slowly increased until the cavity reaches the desired annealing temperature of 1500 °C. This temperature is maintained for 24–48 hours. After annealing the e-beam current is slowly reduced to zero and the e-beam system deenergized. The cavity is allowed to cool under vacuum until reaching room temperature.

In preparation for removing the cavity from the vacuum system, a shroud of plastic film is constructed around the vacuum chamber. This will be filled with helium gas to prevent air from reaching the newly processed cavity as it is being removed from the chamber. A portion of the shroud consists of a glove bag, to facilitate the cavity removal. After the chamber is opened, the cavity is placed inside a plastic bag which is heat-sealed closed. The process of installing the cavity in the cryogenic probe follows a similar procedure to the above, except in reverse.

## 9.2 Cryogenic System

The cavity must be cooled below its superconducting transition and maintained at a constant temperature. A schematic of the cryogenic probe containing the cavity and the other sample sensors is given in figure 9.4.

### 9.2.1 Temperature Control

As described in section 8.2.2, we require temperature stability of parts in  $10^5$  or better to avoid temperature-induced frequency fluctuations in the superconducting cavity. For clock applications, we also want to operate the system at as low a temperature as possible to reduce the surface resistance inside the cavity.

#### Helium Evaporation Pot

To cool our experiment below the normal boiling point of helium-4 (4.2 K), we use a helium evaporation pot, (item (e) in figure 9.4). By pumping on a small volume of helium liquid, we can lower the temperature of the pot to near 1.5 K.

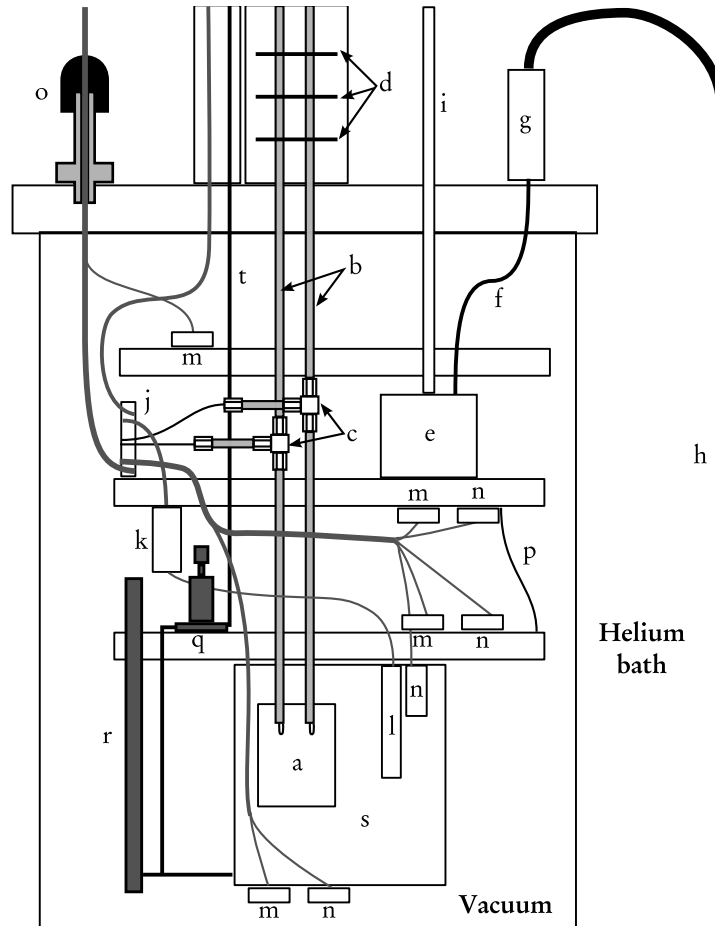


Figure 9.4. Schematic of the superconducting cavity probe. Relevant sections of the text are noted in parenthesis for the items depicted: (a) niobium cavity (9.1), (b) microwave signal coaxials (9.3, D.3), (c) quarter-wave heat sink tees (9.3, D.2), (d) radiation baffles (9.2.1), (e) helium evaporation pot (9.2.1), (f) impedance (9.2.1), (g) filter (9.2.1), (h) helium fill line (9.2.1), (i) pump line (9.2.1), (j) heat sink post, (k) SQUID (9.2.1), (l) high-resolution thermometer (9.2.1), (m) germanium resistance thermometers (9.2.1), (n) heaters, (o) electronics feedthrough (D.1), (p) thermal link (9.2.1), (q) helium fill valve (9.2.2), (r) capacitive liquid level sensor (9.2.2), (s) copper sample vessel (9.2.2), (t) sample fill line (9.2.2). Wires are shown as gray lines and gas lines as thick black lines.

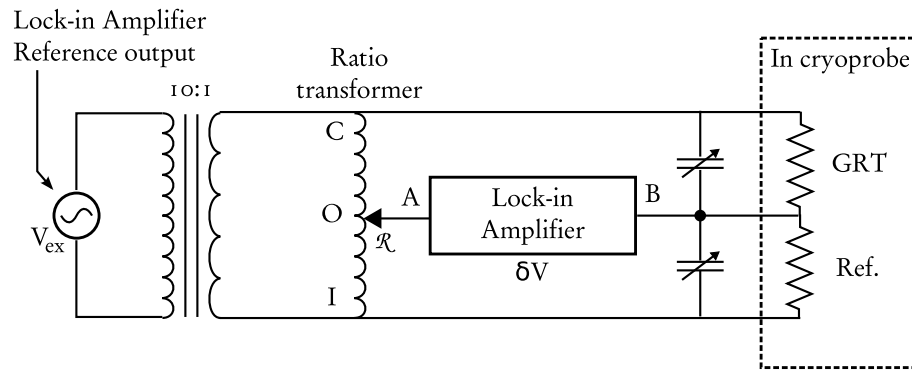


Figure 9.5. Germanium resistance thermometer readout bridge circuit, based on [8].

Helium from the external bath enters through a fill line (h), through a filter (g), and into a flow impedance (f), which limits the flow rate, setting the cooling power and base temperature of the pot (see next paragraph). From here the liquid flow into the pot (e), which is a hollow copper cylinder with a volume of about  $5 \text{ cm}^3$ . The inside of the pot contains copper fins to improve thermal conductivity between the helium and the pot. The pot is connected to a pumpline (i) leading to a pressure regulator and a mechanical pump.

The flow impedance controls the rate at which the helium is pumped through this system. The impedance is a 1 m long section of  $100 \text{ }\mu\text{m}$  I.D. stainless steel capillary tubing, giving a flow rate through the evaporation system of approximately  $300 \text{ }\mu\text{mol/s}$  of helium. This flow rate corresponds to cooling power of  $\sim 15 \text{ mW}$  and should allow the temperature of the probe to be reduced below  $2 \text{ K}$  [4].

### Temperature Sensors

The primary temperature measurement and control is performed using several calibrated germanium resistance thermometers (GRTs, (m) in figure 9.4). The temperature of each GRT is determined by measuring its resistance and inserting this into a Chebyshev series provided by the manufacturer (similar to the series explained in appendix A of part I).

The GRTs are mounted in copper blocks along with high-precision  $2.2 \text{ k}\Omega$  (nominal) resistors with a negligible temperature constant, which serve as reference resistances for the readout bridge circuit. The leads of the GRT are wrapped around the mounting block and secured with varnish for thermal anchoring.

The readout circuit is a basic inductance bridge, shown in figure 9.5 [8]. The bridge is excited

by the reference output of the lock-in amplifier. The bridge is balanced by adjusting the ratio transformer ratio,  $\mathcal{R}$ , until the difference signal in the lock-in amplifier  $\delta V$  is approximately zero. Any residual reactance in the circuit can be balanced using adjustable capacitors in parallel to the resistors. When the bridge is balanced, the resistance of the GRT is then given by the formula

$$R_{\text{GRT}} = \frac{\mathcal{R}}{1 - \mathcal{R}} R_{\text{Ref}} \quad (\text{balanced}). \quad (9.1)$$

The GRT resistance can be calculated to higher precision by measuring the residual out-of-balance signal on the lock-in amplifier,  $\delta V$ :

$$R_{\text{GRT}} = \frac{\mathcal{R}}{1 - \mathcal{R}} R_{\text{Ref}} - \frac{1}{\mathcal{R}^2} \frac{R_{\text{Ref}}}{V_{\text{ex}}/10} \delta V. \quad (9.2)$$

Unfortunately, the real excitation voltage across the resistors is not the value  $V_{\text{ex}}/10$  expected by the circuit diagram, but a different value due to lead resistance. In the formula above,  $V_{\text{ex}}$  must be replaced by an empirically determined value. This can be calculated by changing  $\mathcal{R}$  by a small amount. Assuming the  $R_{\text{GRT}}$  stays constant during this calibration measurement, equation (9.2) can be solved for  $V_{\text{ex}}$ .

To use the GRT circuit for temperature control, the transformer ratio  $\mathcal{R}$  is set at a value corresponding to the desired temperature (from equation (9.1)). The output signal of the lock-in amplifier is fed into a Linear Research LR-130 temperature controller, which in turn powers heater resistors (labelled (n) in figure 9.4). With this setup, temperature fluctuations can be reduced to less than  $10^{-5}$  K. Example temperature data is shown in figure 9.6. The effect of these temperature fluctuations on the cavity resonance frequency is shown in figure 9.7.

More precise temperature control is possible using paramagnetic-salt thermometers with Superconducting Quantum Interference Device (SQUID) readout. Previous researchers in the Yeh group demonstrated  $\sim 10^{-12}$  K temperature resolution at 1.8 K using this technique [9]. Future installation of this high resolution thermometry system will be necessary for the precise helium equation of state measurements described in later chapters, but is not necessary for clock applications where the temperature stability requirement is only parts in  $10^5$ .

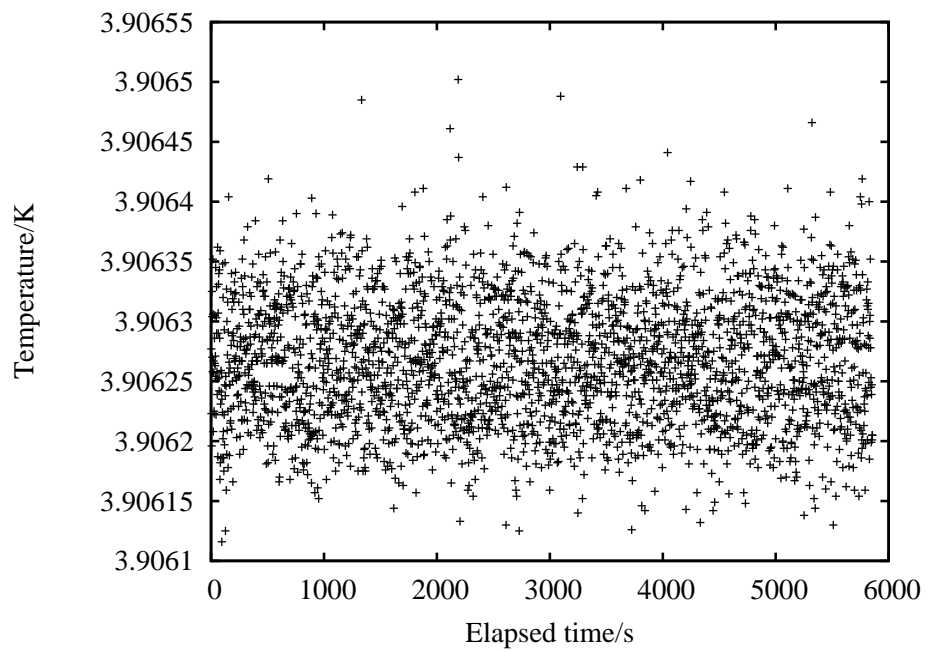


Figure 9.6. Example temperature data of the germanium resistance thermometer control circuit as a function of the elapsed time. The mean temperature of this data is 3.906275 K with a standard deviation of  $5.4 \times 10^{-5}$  K.

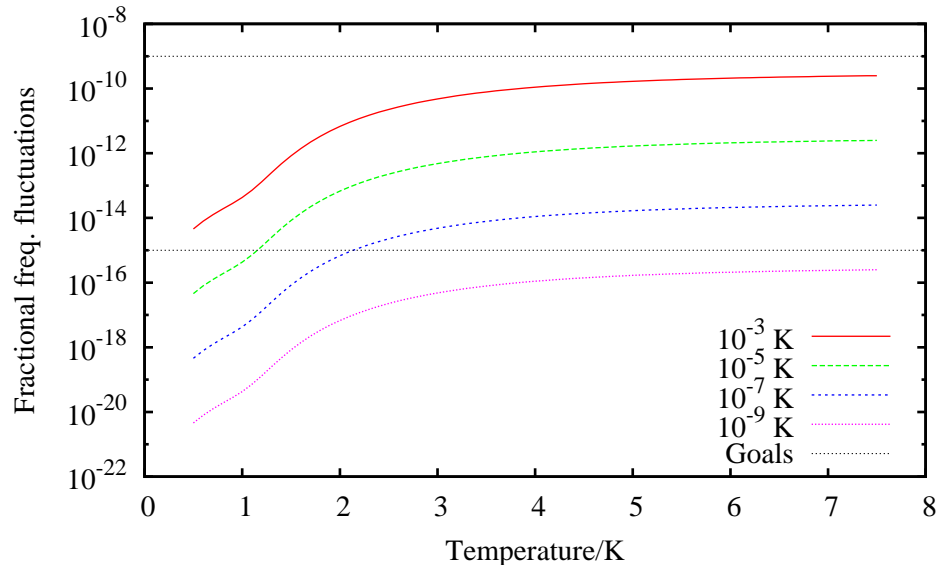


Figure 9.7. Temperature-induced frequency fluctuations for the  $TE_{011}$  mode of the superconducting cavity as a function of cavity temperature for various levels of temperature fluctuation. The maximum allowable frequency fluctuations are indicated by the horizontal dotted lines: the upper goal is for helium density measurements and the lower goal is for clock applications.

### Passive Thermal Control

In addition to the active elements mentioned above, several passive systems are installed to ensure proper temperature stability and control. Thermal links between the stages consist of measured lengths of goldplated oxygen-free high conductivity (OFHC) copper wire (e.g., item (p)). Heat sinking of the microwave coaxes is accomplished by thermally anchoring quarter-wave tees (items (c) in figure 9.4); these are explained in more detail in appendix D.2. To reduce any remaining heat down the coaxes toward the cavity, the bottom 15 cm of coax has a niobium center conductor; the superconductor has less thermal conductivity than the copper used in the rest of the coax sections. Copper-beryllium radiation baffles are installed in the pumplines (items (d) in figure 9.4).

### 9.2.2 Additions for Helium Measurements

Although it will not be discussed until chapter 11, the apparatus described here can also be used for thermodynamic measurements of gasses with a few modifications. Most importantly, the cavity must be enclosed in a sealed volume so that gas can be introduced into the cavity. This

vessel is a copper cylinder (item (s) in figure 9.4) with mounting holes for the niobium cavity, a heater, and the paramagnetic thermometer. The top and bottom plates are also copper and are sealed to the cylinder with indium gaskets. The microwave coaxes are soldered in place for helium measurements (although not fixed for clock applications) and the electrical and SQUID connections are also soldered in place. The can is filled with helium gas through a 1/16" stainless steel fill line (item (t) in figure 9.4) that enters the bottom of the can. This fill line is attached through an indium gasket flange so that it may be removed when necessary.

Also in the helium sample system are a capacitive liquid level sensor ((r) in figure 9.4) for use in future measurements of helium liquid phases. The sensor capacitance is monitored with a tunnel diode oscillator circuit. Further up on the fill line is a low-temperature needle valve (q) used to separate the sample from the room-temperature gas-handling equipment. This valve is operated with a removable control rod which extends upwards to room temperature.

With these additions, a set amount of helium gas or liquid may be added to the sample space and the cavity. This is necessary for the helium measurements described in chapters 11–13.

## 9.3 Microwave System

### 9.3.1 Transmission Spectroscopy

The primary means of cavity characterization and the initial determination of the resonance frequencies is transmission spectroscopy. In this technique, the output frequency of a synthesizer is scanned across the resonance. The synthesizer signal is carried to the cavity through one coax and returns through a second coax where the signal is amplified, filtered, and then the signal amplitude is measured using a high-frequency oscilloscope. The basic setup is shown in figure 9.8.

If the signal-to-noise ratio of the spectrum is too low to discern the resonance peaks, the signal coaxes can be moved further into the cavity by adjusting a micrometer at the room-temperature end to increase the coupling of the coaxes to the cavity. Increasing the coupling will increase the signal amplitude, but  $Q$  and  $f_0$  data are only meaningful in the weak-coupling limit. Strongly coupled coaxes will reduce the measured  $Q$  of the combined cavity-coax system. If the external circuit has an effective quality factor of  $Q_e$ , in the strong coupling limit the effective quality factor of the loaded cavity will be

$$Q_l = (Q^{-1} + Q_e^{-1})^{-1}. \quad (9.3)$$

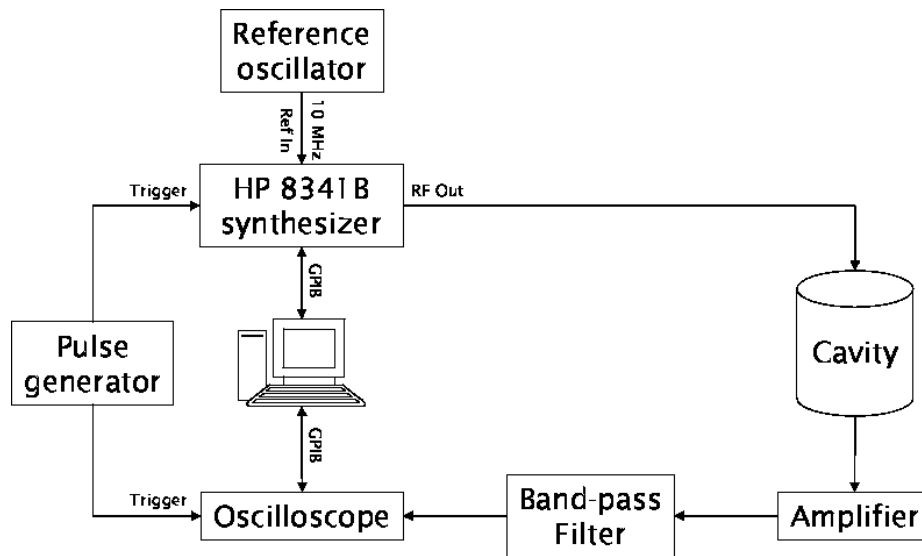


Figure 9.8. Schematic for transmission spectroscopy of cavity modes.

Reducing the coupling reduces  $1/Q_e$  [10]. In the weakly coupled limit that we are interested in,  $1/Q_e$  approaches zero, thereby eliminating the loading on the cavity at the cost of a loss of signal amplitude. Decoupling the external circuitry from the cavity is desirable because it also decouples any external noise sources from the cavity, although the cavity may still be indirectly affected by changes in incident microwave power or temperature, for example.

The coupling coaxes can also shift the resonance frequency of the system through dissipative loading (lowering  $f_0$ ) and by reducing the effective volume of the cavity (raising  $f_0$ ). Furthermore, if the coupling is excessive, the shape of the resonance peak may be distorted. Typical distortions indicative of over-coupling include asymmetric peaks, split peaks, peaks with nodes, and inverted peaks [10]. Although the effects of over-coupling are undesirable for determination of  $f_0$  and  $Q$ , increased coupling of the coaxes can be useful when trying to initially locate the modes because of the increased signal amplitude and broadened resonance peak. Once the desired resonance mode is located, the coupling can be reduced in increments until  $f_0$  ceases varying with the coupling strength, indicating the weak-coupling limit has been reached.

The microwave source for the transmission signal may be either continuous wave or pulsed. Continuous wave spectroscopy relies on the fact that the cavity will absorb radiation when excited off resonance (as in equation (8.1)).

Alternatively, the microwave source can be pulsed by connecting a pulse generator to the

amplitude modulation port of the Hewlett-Packard 8341B synthesizer. The pulse and the delay between pulses must be longer than the decay time of the cavity, which is equal to  $1/\Delta f = Q/f_0$ . (Incidentally, the preceding expression suggests using the decay time to determine  $Q$ , although difficulty in precisely measuring the decay time makes this method impractical.) If the pulses are too short, the amplitude modulation of the excitation signal causes side bands on the outgoing signal. The outgoing frequency spectrum is the product of the cavity spectrum and the Fourier transform of the input signal, by the convolution theorem; this is the time-domain analog of Fraunhofer diffraction. The convolution of the cavity spectrum with the input pulse shape makes determination of the peak width uncertain in this short-pulse limit. Note that for  $Q$  values in our optimal range of  $10^9$  and our frequency range of  $10^{10}$  Hz, the pulse lengths must be on the order of seconds long in order to avoid sidebands, thus slowing the measurements beyond the patience of the experimenters. Pulsed signal measurements are occasionally used as diagnostics, but most mode characterization is done with continuous wave measurements.

A third method of characterizing the cavity resonance modes is reflection spectroscopy. Although the resulting signal is more difficult to interpret, this method can be useful if, for example, one of the signal coaxes is damaged. The interpretation of the spectrum is similar to that of pulsed transmission spectroscopy, although inverted; the reflected amplitude is minimum on resonance. Unfortunately, distortions from over coupling are much more pronounced because the signal amplitudes are much larger in reflection mode. After the addition of quarter-wavelength heatsinking stubs to the signal coaxes (see section 9.2.1 and appendix D.1) reflection mode spectroscopy can no longer be used because reflections from the stubs dominate the spectrum. The phase-locked loop technique, however, is able to detect the reflected resonance signal despite the background.

### 9.3.2 Phase-Locked Loop System

A block diagram of the PLL setup appears in figure 9.9. The primary signal source is a custom-built synthesizer purchased from the National Institute of Standards and Technology (NIST) and built by Fred Walls and David Howe. The synthesizer output frequency has a narrow range of adjustment, so an additional frequency must be mixed in to reach the nominal resonance frequency of the superconducting cavity. This additional signal is supplied by a Hewlett-Packard 8341B synthesizer or a PTS (model 1A-3676) synthesizer. These synthesizers use a reference signal of 40 MHz from

the NIST synthesizer which is down converted to 10 MHz by a Stanford Research DS-345 digital synthesizer. Additional components needed for the full PLL setup are amplifiers and filters on the cavity output signal.

To monitor the performance of the PLL, a 100 MHz signal generated by the NIST synthesizer, which has a fixed frequency ratio with respect to the cavity resonance frequency, is compared to a reference oscillator, which may be a cesium beam clock or another PLL circuit. By design of the NIST synthesizer, the fractional frequency stability of this 100 MHz signal is equal to the fractional frequency stability of the PLL circuit. The signal is compared against a reference oscillator by mixing the two signals and measuring the beat frequency between the two nominally 100 MHz signals. The frequency of the beat signal is measured by a Stanford Research SR-620 frequency counter. In practice, the frequency of the PLL is slightly detuned to keep the beat frequency near 1 Hz so that it may be more easily counted. The measurements of the frequency counter are downloaded to a computer by a GPIB connection for storage and analysis.

### **PLL Acquisition and Optimization**

To establish phase-locking, the first step is to locate the resonance frequency of the cavity with spectroscopy (see section 9.3.1). Once the resonance frequency is established, the electronic components are connected according to figure 9.9. The frequency setting of the intermediate frequency (the HP 8341B synthesizer) is determined by subtracting the frequency of the NIST synthesizer (13.7411 GHz or 20.12768 GHz, depending on which NIST synthesizer is used) from the cavity frequency. The power of the intermediate frequency signal is +12 dBm, to match the NIST synthesizer power. Nominal values for other device parameters are list in table 9.4.

The most difficult aspect of the PLL is setting the phase and gain of the lock-in amplifier. Initially, the feedback output is disconnected and the frequency tuned as close to resonance as possible. The phase of the error signal is given earlier in equation (8.10) and shown in figure 8.2. The phase of the lock-in amplifier is set to  $0^\circ$  relative to the maximum error signal and the output of the lock-in amplifier is set to be proportional to the phase of the incoming signal. The frequency is recentered and the feedback connected. The gain of the lock-in amplifier is then increased until the feedback loop begins to oscillate and then decreased by one increment.

The ultimate stability of the PLL, assuming all external noise sources are eliminated, is parts in  $Q \times 10^7$ , limited by intrinsic noise in the modulator component [5]. Because the modulation is at

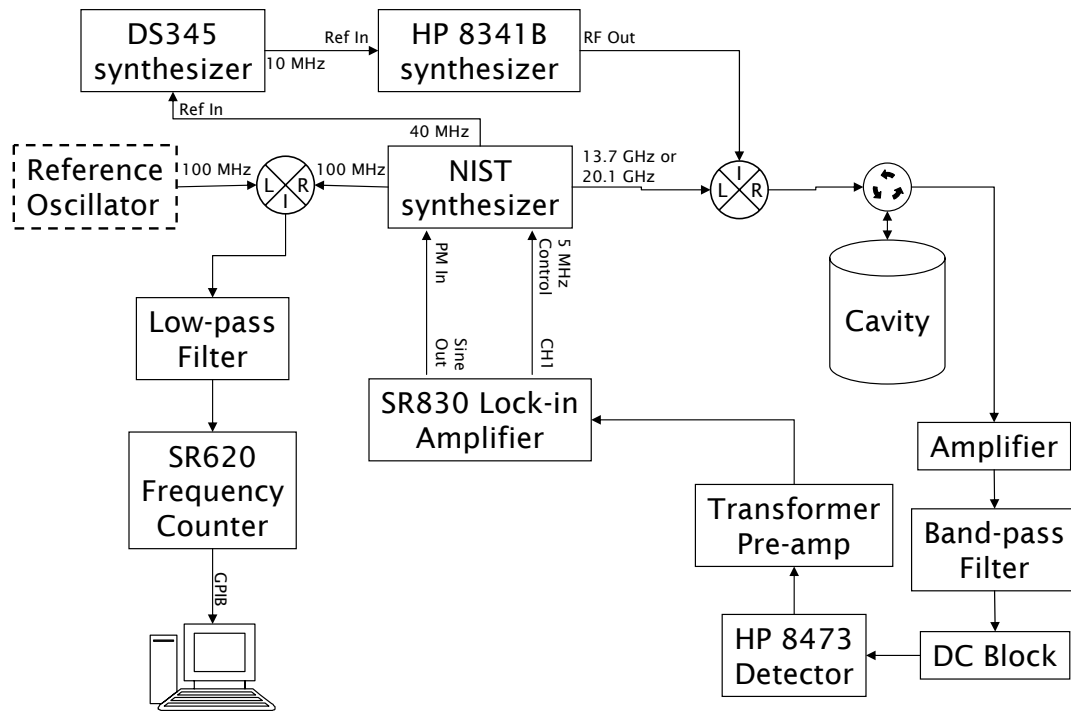


Figure 9.9. Detailed block diagram of the phase-locked loop (PLL). The frequency of the PLL is compared with a reference oscillator in the top left. This reference may be a cesium-beam clock or a second PLL.

Table 9.4. Nominal device settings for the phase-locked loop

| <b>Setting</b>                   | <b>Value</b> |
|----------------------------------|--------------|
| <b>SR 830 lock-in amplifier</b>  |              |
| Reference frequency              | 50 kHz       |
| Reference amplitude              | 100 mV       |
| Reference phase                  | (see text)   |
| Harmonic                         | 1            |
| Sensitivity                      | 200 $\mu$ V  |
| Reserve                          | 100 dB       |
| Time constant                    | 1 s          |
| Filter                           | 6 dB/octave  |
| <b>SR 560 transformer preamp</b> |              |
| Band                             | Low-pass     |
| Frequency                        | 30 Hz        |
| Attenuation                      | 6 dB/octave  |
| <b>SR 620 frequency counter</b>  |              |
| Mode                             | Frequency    |
| Gate factor                      | 1            |
| Gate scale                       | 1 s          |

50 kHz we are especially sensitive to external noise (i.e., acoustic noise) at this frequency. Also, any noise in the generation or transmission of the modulation signal will increase the instability of the entire PLL.

### **Dual-Mode Technique**

One new technique we are introducing for the superconducting cavity stabilized oscillator is the ability to phase lock two modes of the same cavity simultaneously and independently. Because the two phase-locked loops experience the same environment, common-mode rejection of many noise sources should be possible. To run in the two-mode configuration, the layout shown previously in figure 9.9 is duplicated, with the exception that the excitation frequencies of the two PLL are different (one for each mode) and the modulation frequencies of the two loops must also be slightly different to minimize crosstalk between the two circuits.

## **9.4 Auxiliary Systems**

### **9.4.1 Acoustic Noise Abatement**

As explained in section 8.2.2, acoustic noise may cause the resonance frequency of the cavity to fluctuate. One particular noise source is an air conditioner installed directly above our microwave equipment. Unfortunately, we cannot operate the experiment without the air conditioning. The microwave devices (particularly, the amplifiers) are sensitive to temperature. Without the air conditioner, the room temperature rises above 30 °C within a few hours, so operating the experiment without the air conditioner is not feasible.

To reduce the acoustic noise in the system, the dewar is supported by an air-damper table. Additionally, we have added sound-absorbing foam to the walls of the laboratory and have installed a wooden box covered with the foam around the dewar. At the time of this writing, we have not yet tested the efficacy of these measures.

### **9.4.2 Computer Control and Software**

Control of the microwave and temperature equipment is done with a computer via the GPIB interface. Software for the experiment was written by myself and previous researchers using the National Instruments LABVIEW system.

## Bibliography

- [1] W. Faulkner. “The Sound and the Fury.” In *Novels: 1926–1929, Library of America*, volume 164, New York: Library of America (2006). Originally published in 1929.
- [2] J. D. Jackson. *Classical Electrodynamics*. New York: Wiley, third edition (1999).
- [3] V. B. Braginsky, V. P. Mitrofanov, and V. I. Panov. *Systems with Small Dissipation*. Chicago: U. Chicago P. (1985).
- [4] F. Pobell. *Matter and Methods at Low Temperatures*. Berlin: Springer, second edition (1996).
- [5] J. Q. Deng, G. Mileti, R. E. Drullinger, D. A. Jennings, and F. L. Walls. “Noise considerations for locking to the center of a Lorentzian line.” *Physical Review A*, **59**(1):773–777 (1999).  
<http://tf.nist.gov/timefreq/general/pdf/1294.pdf>. Also, NIST Time and Frequency Division publication bin #1294.
- [6] L. M. Nelson and F. L. Walls. “Environmental effects in mixers and frequency distribution systems.” In *IEEE Frequency Control Symposium* (1992). <http://tf.nist.gov/timefreq/general/pdf/971.pdf>. Also, NIST Time and Frequency Division publication bin #971.
- [7] F. L. Walls and J.-J. Gagnepain. “Environmental sensitivities of quartz oscillators.” *IEEE Transactions on Ultrasonics, Ferroelectrics, and Frequency Control*, **39**(2):241–249 (1992).  
<http://tf.nist.gov/timefreq/general/pdf/957.pdf>. Also, NIST Time and Frequency Division publication bin #957.
- [8] W. A. Moer. *Thermal Conductivity Measurements in <sup>4</sup>He Near the Superfluid Transition Temperature*. Ph.D. thesis, University of New Mexico, Albuquerque, NM (1997).
- [9] N.-C. Yeh, D. M. Strayer, V. L. Anderson, and N. Asplund. “Superconducting-Cavity-Stabilized Oscillators (SCSO) for precise frequency measurements.” *Physica B*, **280**:557–558 (2000).
- [10] International Telephone and Telegraph Corp. *Reference Data for Radio Engineers*. Indianapolis: Sams, sixth edition (1975).

There is a crack in everything.

It's how the light gets in.

---

Leonard Cohen, "Anthem"\*

## Chapter 10

### Data for Superconducting Cavities

**Q**UANTITATIVE descriptions of the superconducting cavity stabilized oscillator system consist of two parts. First, the cavity itself must be characterized using spectroscopy. Second, the frequency stability of the integrated phase-locked loop system is recorded and expressed as the Allan variance. This chapter shows the results of these measurements for our system.

#### 10.1 Cavity Characterization

As mentioned previously in section 8.2.1, the figure of merit for the superconducting cavity is the quality factor  $Q$ . We typically calculate  $Q$  by measuring the transmission spectrum of the cavity (see section 9.3.1 and then applying the relation given earlier:

$$Q = f_0 / \Delta f, \quad (10.1)$$

where  $f_0$  is the resonance frequency and  $\Delta f$  is the full width at half maximum of the resonance peak. A typical transmission spectrum is shown in figure 10.1 and results are summarized in table 10.1. The highest  $Q$ 's we have achieved are in the  $10^8$  range for the  $TE_{011}$  mode, although higher should be possible. We suspect we are limited by low signal-to-noise ratios; higher  $Q$  values require weaker coupling to the signal coaxes (equation (9.3)), resulting in less signal reaching the oscilloscope. The oscilloscope we use for spectroscopy measurement sees broadband noise, which can limit our ability to discern the resonance peak. This was particularly true of the 20 GHz

---

\*Reference [1]

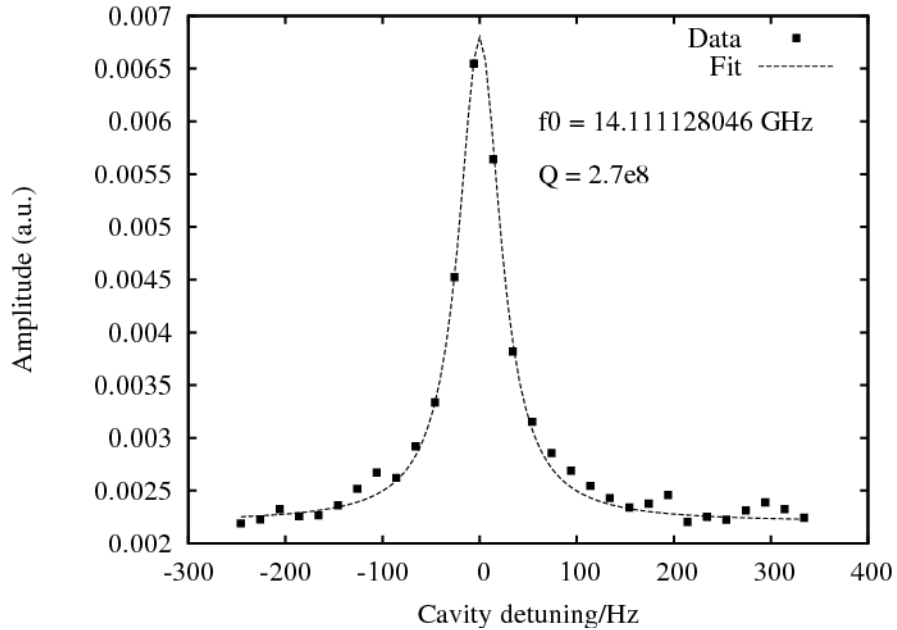


Figure 10.1. Example spectrum of the cavity in the  $TE_{011}$  mode.

Table 10.1. Best measured parameters of the superconducting cavity

| Property               | Symbol     | Value ( $TE_{011}$ ) | Value ( $TE_{013}$ ) |
|------------------------|------------|----------------------|----------------------|
| Resonance frequency    | $f_0$      | 14.1 GHz             | 20.7 GHz             |
| Resonance width (FWHM) | $\Delta f$ | 26 Hz                | 3.0 kHz              |
| Quality factor         | $Q$        | $5.4 \times 10^8$    | $6.9 \times 10^6$    |
| Surface resistance     | $R_s$      | $1.4 \mu\Omega$      | $170 \mu\Omega$      |

signal of the  $TE_{013}$  mode; for this mode we were only able to measure  $Q$  on the order of millions. To improve our signal-to-noise ratio for spectroscopy we purchased band-pass filters at the cavity resonance frequencies, but to date we have not tested the new filters. It should be noted that the key advantage of the phase-locked loop technique is its immunity to broadband noise.

## 10.2 Frequency Stability

The ultimate goal of this portion of the project is to reduce the frequency instability as much as possible. Theoretical estimates for our system suggest fractional frequency instabilities of less than  $10^{-15}$  should be possible (see, for example, table 9.3).

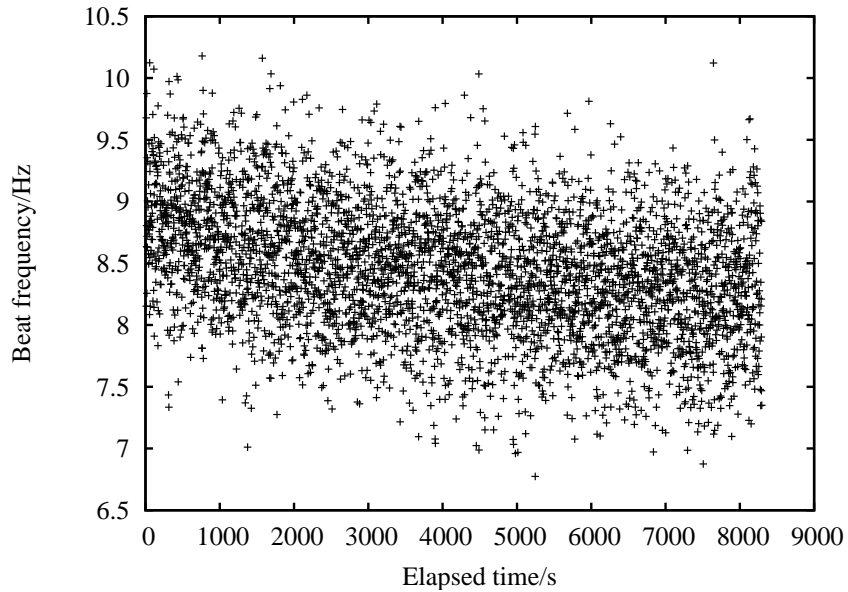


Figure 10.2. Time series of the phase-locked loop frequency for the  $TE_{011}$  mode. The frequency shown is the beat frequency between the 100 MHz outputs of the PLL and a cesium beam clock. The Allan variance plot for this data is shown in figure 10.3.

### 10.2.1 Single Mode

The best phase-locked loop data obtained to date is shown in figure 10.3 for the  $TE_{011}$  mode. The lowest fractional frequency stability of  $\sim 3 \times 10^{-12}$  was reached for measurement times greater than 200 s. The temperature for this run was 3.67 K with temperature fluctuations of about 30  $\mu$ K. The cavity  $Q$  was  $3 \times 10^6$ . (Unfortunately, for the runs with higher  $Q$ , the temperature control was not yet optimized, causing large drifts in frequency.) Given these system parameters, the fractional frequency stability should be able to reach  $10^{-13}$ , which we did not achieve. We believe our stability is limited by acoustic noise and ambient temperature drifts in the laboratory, and we subsequently began infrastructure improvements to reduce these effects (see below).

### 10.2.2 Dual Mode

By duplicating our electronics set up, we can operate the  $TE_{011}$  and  $TE_{013}$  resonance modes simultaneously and compare their frequencies. Figure 10.4 shows the fractional frequency stability for three configurations: each mode when compared to a cesium beam clock and a comparison of the modes with each other. The lack of common-mode instability reduction in the dual-mode

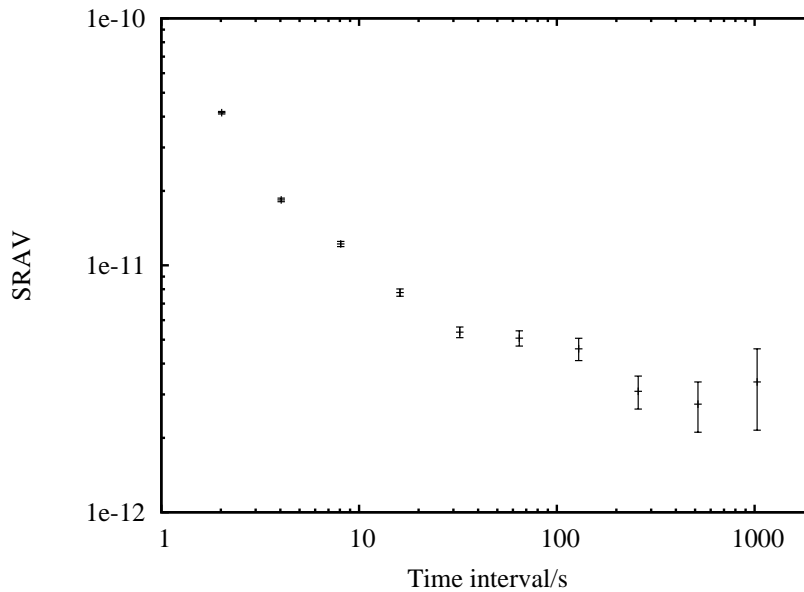


Figure 10.3. Frequency stability of the superconducting cavity stabilized oscillator operating in the 14 GHz mode, from the time series data in figure 10.2. The square root of the Allan variance (SRAV) is shown as a function of the time interval.

configuration suggests the noise sources are affecting the external electronics and not directly affecting the superconducting cavity.

### 10.3 Environmental Noise Sources

The poor frequency stability in the above data caused us to examine noise sources in the laboratory. We identified two primary culprits. The first was acoustic noise. A large air conditioning system is installed on the laboratory ceiling directly above our electronics. The low-frequency noise spectrum of the air conditioner is shown in figure 10.5. Also, the lab is adjacent to an elevator and another large air conditioner.

A second source of noise on long time scales may be the drifting of the ambient temperature in the laboratory. The temperature of the cavity is maintained with submillikelvin stability, but the external electronics have no temperature control and only passive cooling. The room temperature has been observed to fluctuate by about 3 °C over the period of an hour. This variation is likely to effect the sensitive microwave electronics. The synthesizers all use quartz crystals to generate their microwave signals, making them susceptible to temperature variations [2]. Also, the amplifiers,

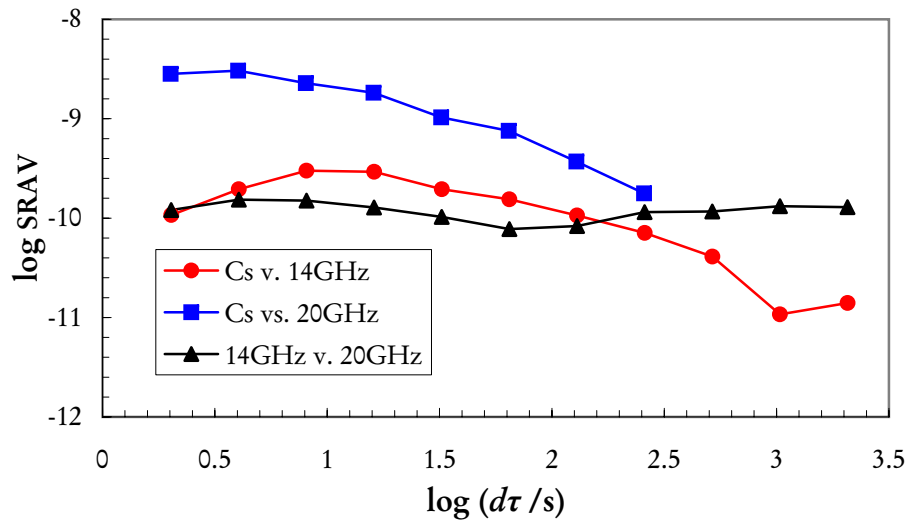


Figure 10.4. Frequency stability of the dual-mode configuration. Shown is the square root of the Allan variance ( $S_{RAV}$ ) as a function of the time interval for the  $TE_{011}$  mode versus a cesium beam clock (red circles), the  $TE_{013}$  mode versus a cesium beam clock (blue squares) and the two modes versus each other (black triangles).

mixers, and coaxial cables are known to show temperature dependence [3].

Although the phase-locked loop circuit is designed to reject most external noise sources, it can not protect against sources which affect the cavity itself, such as those mentioned earlier in table 9.3. Acoustic noise may cause strains in the cavity, altering its dimensions and therefore its resonance frequency. Fluctuations in the incident power may also affect the resonance frequency; power fluctuations may be caused by vibrations in the microwave components and cables.

We do not have a quantitative assessment of these external noise sources at this time, but we believe these effects to be significant, if not dominant, in the experiment. Solving problems such as controlling the ambient temperature and humidity require a large investment in infrastructure which our limited budget does not allow. (For example, precision frequency sources at the Jet Propulsion Laboratory are kept in temperature-, humidity-, and pressure-controlled vaults, which are also electromagnetically shielded.)

After recognizing the seriousness of our noise issues, we began improving the laboratory environment. We installed a new thermostat on the air conditioner with a variable fan speed control, allowing us to reduce the noise generated by the air conditioner without completely turning it off. We also made some effort to reduce acoustic noise in our laboratory by covering

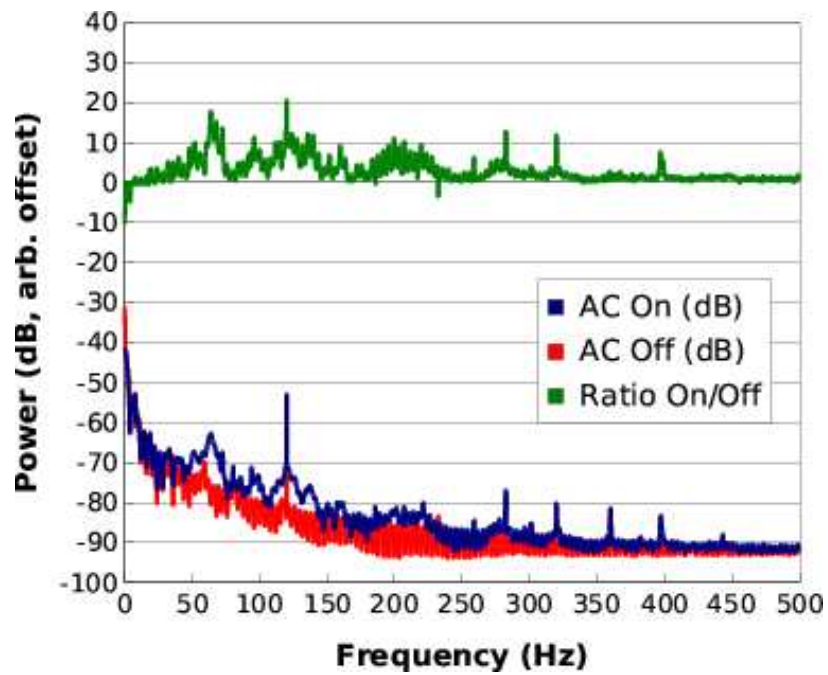


Figure 10.5. Low frequency power spectrum of air conditioner noise. The bottom curves show the acoustic noise spectrum in the laboratory with the air conditioner on and off, in decibels with an arbitrary base. The top curve is the difference of the bottom two curves. Note that most of the noise is at 60 Hz and its harmonics, as expected for an device using AC power.

the walls with sound-absorbing foam, enclosing the dewar in a sound-reducing box, and lowering the dewar into a pit, but we were not able to measure the effectiveness of these improvements before our funding expired. In the future we may also load the pit with sand to further reduce acoustic noise entering the dewar.

Although we have not yet reached the frequency stability necessary for a good clock system, frequency stability of parts in  $10^{12}$  is more than sufficient for other scientific measurements. In the remainder of part II of this thesis, we explain how to use our superconducting cavity resonators to investigate thermodynamic properties of helium-4 gas.

## Bibliography

- [1] L. Cohen. “Anthem.” In *The Future*, Sony Records (1992). Recording number 053226, compact disk, track 5.
- [2] F. L. Walls and J.-J. Gagnepain. “Environmental sensitivities of quartz oscillators.” *IEEE Transactions on Ultrasonics, Ferroelectrics, and Frequency Control*, **39**(2):241–249 (1992).  
<http://tf.nist.gov/timefreq/general/pdf/957.pdf>. Also, NIST Time and Frequency Division publication bin #957.
- [3] L. M. Nelson and F. L. Walls. “Environmental effects in mixers and frequency distribution systems.” In *IEEE Frequency Control Symposium* (1992). <http://tf.nist.gov/timefreq/general/pdf/971.pdf>. Also, NIST Time and Frequency Division publication bin #971.

子曰：『吾嘗終日不食、  
終夜不寢、以思、無益、  
不如學也。』

## Chapter 11

---

孔子《論語》\*

### Thermodynamic Measurements of Helium

**A**LTHOUGH the superconducting cavity system is useful as a frequency reference, the cavity can be used in its own right to perform precise experiments. In this and the following chapters we explain how the high frequency resolution of the system can be used for precise measurements of the dielectric constant and density of helium.

In short, the presence of a gas inside the cavity shifts the resonance frequency of the cavity. The frequency shift relative to the vacuum frequency gives the dielectric constant of the gas. The density can then be calculated from the dielectric constant by means of the Clausius-Mossotti relation, as explained below.

By measuring the density of the helium as a function of pressure and temperature we determine the equation of state. Because of its light mass, the quantum nature helium becomes evident at low temperatures, leading to a superfluid phase when helium-4 is cooled below 2.17 K (called the lambda temperature,  $T_\lambda$ ). Although qualitatively similar to Bose-Einstein condensation, the high density and strong interatomic forces in the superfluid have prevented discovery of a microscopic theory of helium-4 superfluidity.

One of the original goals of the present work was to measure the critical scaling behavior of the superfluid transition [2–5], but this was abandoned because it requires a microgravity environment. (The original intent was to fly the experiment on the International Space Station.) Gravity creates a large pressure gradient in the liquid phases, causing phase separation between the superfluid

---

\*The Master said, "I have been the whole day without eating, and the whole night without sleeping;—occupied with thinking. It was of no use. The better plan is to learn."—Confucius, *The Analects*, Translated by James Legge. Original and translation from [1].

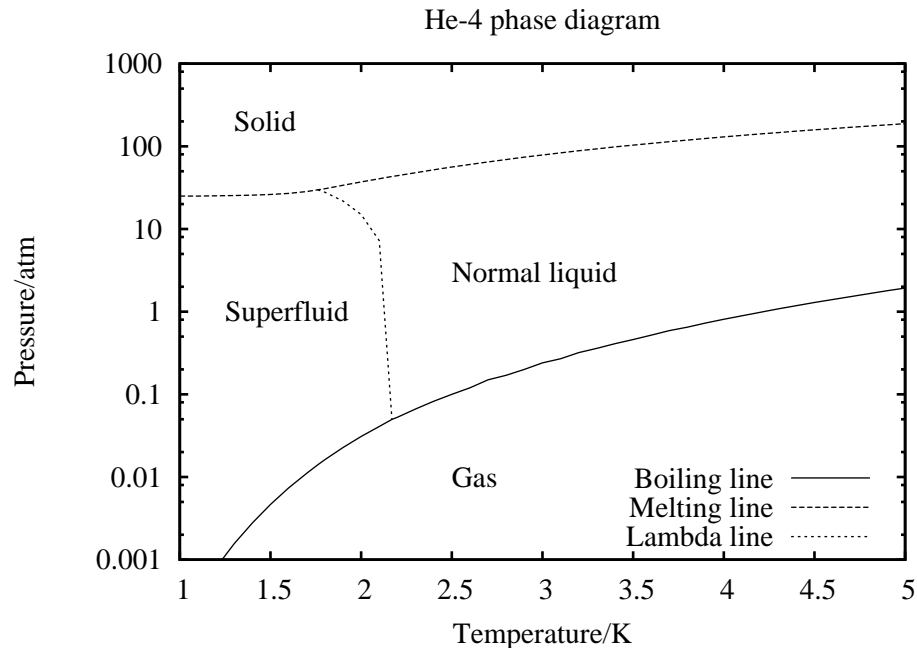


Figure 11.1. Helium-4 phase diagram in the temperature-pressure plane.

and normal liquid phases. Any macroscopic sample will contain both phases near the transition temperature, masking the critical phenomena of the phase transition itself.

Fortunately, in the gas phase the gravity-induced pressure gradient is about a thousand times smaller. Therefore, we can study the thermodynamic properties of helium-4 gas and the liquid-gas transition. The gas phase of helium is worthy of investigation in its own right because it is the simplest possible real gas to study with theoretical methods, having only two electrons and one nucleus. Because of its simplicity, the properties of helium can be predicted to high precision using first-principle numerical calculations (quantum Monte Carlo simulations and the like). With precision measurements we can compare experimental data with these models to validate or disprove them. Alternatively, if we accept the numerical calculations as accurate, our measurements can be inverted to determine the Boltzmann constant to higher precision than previously done. This procedure will be discussed later in this chapter.

## 11.1 General Properties of Helium-4

### 11.2 Equations of State

The key element that we want to measure is the equation of state of helium-4 in the gas phase and the equation defining the boiling line. The equation of state is defined as the relation among the pressure  $p$ , temperature  $T$ , and volume  $V$  of a substance. Several analytical approximations for the equation of state are in common use. We present a few here.

#### 11.2.1 Ideal Gas Law

The prototypical equation of state is the ideal gas law

$$p = \rho RT, \quad (11.1)$$

where  $R$  is the molar gas constant ( $8.314472(15) \text{ J mol}^{-1} \text{ K}^{-1}$ , where the parentheses indicate the uncertainty in the last two digits [6]), and  $\rho$  is the molar density of the substance (moles per unit volume). Molar units are chosen here rather than atomic units for better comparison with the literature.

The ideal gas law is a decent approximation for gases at high temperature and low density and helium obeys the ideal gas law better than most substances. However, near saturation and in the low temperature limit more precise equations of state are needed. An important deficiency of the ideal gas law is that it does not predict any phase changes; a more elaborate equation of state, such as the virial equation of state, is needed to explain phase changes.

#### 11.2.2 Virial Equation

The ideal gas law may be generalized by expanding the right-hand side into a polynomial series in the density.

This new equation is called the virial equation of state. Explicitly,

$$p = \rho RT (1 + B\rho + C\rho^2 + \dots). \quad (11.2)$$

The new coefficients  $B$  and  $C$  are the second and third virial coefficients, respectively. In general

Table 11.1. Literature values of the temperature coefficients of the helium-4 second virial coefficient, for use in equation (11.3)

| Parameter                                       | Berry [7] | Luther [9]           | ITS-90 [10] |
|---|-----------|----------------------|-------------|
| Lower temperature bound/K                       | 2.6       | 4.2                  | 3.0         |
| Upper temperature bound/K                       | 27.1      | 27.0                 | 24.5561     |
| $B_0^*$   | 17.19     | 16.572               | 16.708      |
| $B_1^*$   | -396.2    | -361.72              | -374.05     |
| $B_2^*$   | -48       | -710.43              | -383.53     |
| $B_3^*$   | —         | 5139                 | 1799.2      |
| $B_4^*$   | —         | $-1.750 \times 10^4$ | -4033.2     |
| $B_5^*$   | —         | $2.144 \times 10^4$  | 3252.8      |
| $B(4.2 \text{ K})/\text{cm}^3 \text{ mol}^{-1}$ | -79.9     | -80.297              | -80.281     |

\* $B_n$  has units of ( $\text{cm}^3 \text{ mol}^{-1} \text{ K}^n$ )

$B$  and  $C$  are functions of temperature. Phase transitions appear when the above equation has multiple possible values of  $\rho$  for fixed values of  $p$  and  $T$ . (*Caveat lector!* Some authors use a series in the pressure rather than the density. This is particularly confusing to readers because the symbols for pressure and density are similar,  $p$  and  $\rho$ . The form chosen here is the dominant one in the metrology literature.)

Generally, the virial coefficients are determined empirically by constant volume gas thermometry [7] or dielectric constant gas thermometry [8; 9]. The latter technique is closely related to this work and will be described in detail below in section 11.4.

The virial coefficients are usually cast in an analytical form for ease of interpolation. The form typically found in the literature is a power series in the inverse temperature

$$\frac{B(T)}{\text{cm}^3 \text{ mol}^{-1}} = \sum_{n=0}^{\infty} B_n \left( \frac{T}{\text{K}} \right)^{-n} . \quad (11.3)$$

Note that the dependence on the inverse temperature implies that the interactions between atoms become stronger at low temperatures, as expected. Values of the parameters for two experiments (Berry [7] and Luther et al. [9]) and the defined values from the International Temperature Scale of 1990 (ITS-90) [10; 11] are given in table 11.1 and plotted in figure 11.2.

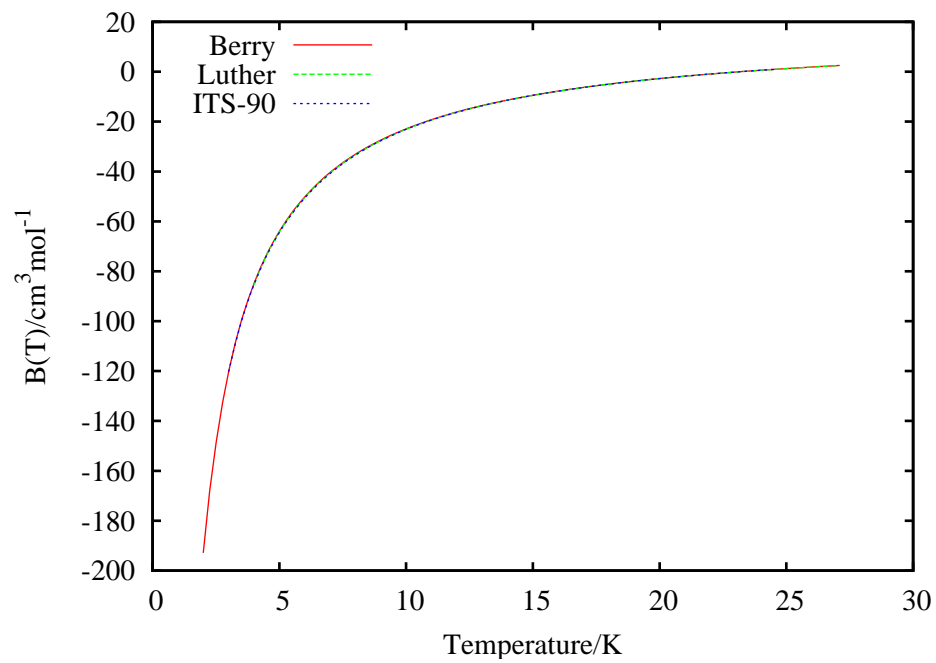


Figure 11.2. Literature values of the temperature dependence of the helium-4 second virial coefficient, from Refs. [7; 9; 10]. The different expressions largely overlap on this scale. Note that  $B$  crosses zero at  $T \sim 24$  K.

Experimentally, the second virial coefficient is determined by measuring the pressure and density along an isotherm and then fitting to the virial equation of state. The discrepancies among the coefficients in table 11.1 are due to differences in the temperature ranges measured. Although not listed in the table, the experiment by Gugan and Michel [8] agrees with Berry's formula to within experimental error.

### 11.2.3 Theoretical Equations of State

Much progress has been made in recent years towards the realization of *ab initio* equations of state for helium-4. These calculations consist of two distinct steps. First, the two body interaction potentials are determined by numerically solving the Schrödinger equation for a two-atom system [12]. Note that many-body effects are neglected, although researchers have recently begun on three-body calculations [13] and solving the relativistic corrections [14] to the potentials. These corrections are necessary for accurate predictions of the normal liquid, superfluid, and solid phase properties. Because of the few constituents in the helium atom, full quantum mechanical calculations of the interatomic potentials are possible with advanced numerical techniques such as quantum Monte Carlo simulations using only the pairwise Coulomb and spin interactions of the constituent particles. One such potential, as calculated by Hurly and Mehl [15] is plotted as a function of distance in figure 11.3. (Note that Hurly and Mehl [15] do not provide an analytical expression, only numerical tables of potential as a function of radius.)

In the classical approximation, the two-body potential can then be used to calculate the virial coefficients using the Mayer cluster expansion or similar techniques [16]. For a quantum-mechanical solution, the virial coefficients are determined from the scattering crosssections for the potential (see, for example, detail in Hurly and Moldover [17]). The crosssections are calculated using partial-wave decomposition with the partial-wave phase shifts given by  $\delta_l(k, r_n)$ , where  $l$  is the angular momentum quantum number,  $k$  is the wave number, and  $r_n$  the radial position of the

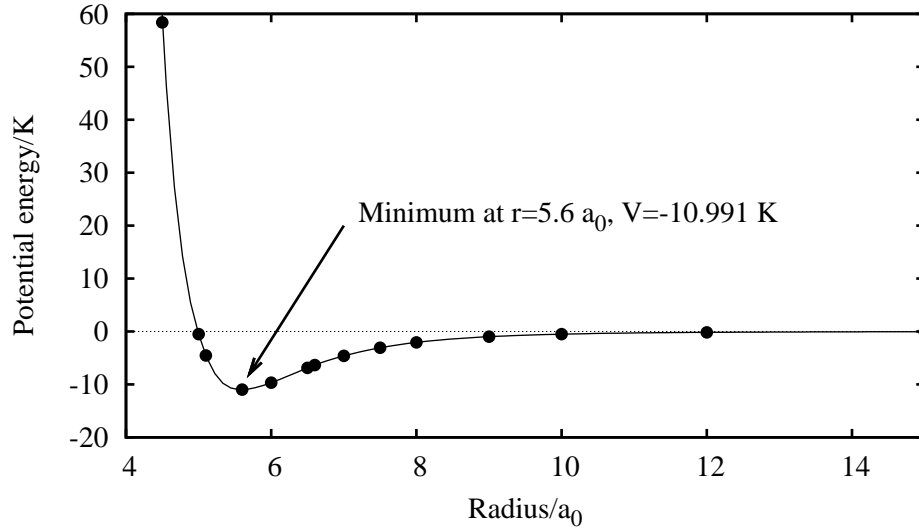


Figure 11.3. Theoretical interaction potential in kelvin of two ground-state  ${}^4\text{He}$  atoms as a function of distance in Bohr radii, using data from Hurly and Mehl [15] (points). The line is a guide to the eye.

$n$ th node in the wavefunction. The second virial coefficient is then given by [17]

$$B(T) = B_{\text{th}}(T) + B_{\text{ideal}}(T) + B_{\text{bound}}(T),$$

$$B_{\text{th}} = \int_0^\infty k \exp\left(-\frac{k^2}{k_B T}\right) \sum_{l=0}^\infty (2l+1) \delta_l(k, r_n \approx \infty) dk,$$

$$B_{\text{ideal}} = -N_A 2^{-5/2} \lambda_t^3,$$

$$B_{\text{bound}} = -N_A 2^{-3/2} \lambda_t^3 [\exp(E_b/k_B T) - 1].$$

The last three equations correspond to thermal average, ideal Bose gas correction, and bound state contributions to the virial coefficient, respectively. Other symbols in the above expressions are Avogadro's number,  $N_A$ , the effective thermal wavelength,  $\lambda_t = \sqrt{2\hbar/mk_B T}$ , and the bound state energy  $E_b$ . Accounting for various numerical approximations in the calculations and uncertainty in the interaction potential, Hurly and Moldover state uncertainties in  $B(T)$  of 9 parts per thousand for  $T \sim 5$  K. For comparison, this is about twice the experimental uncertainty given by Berry [7]. (A recent update to these theoretical calculations was recently published by Hurly and Mehl [15], using an improved potential function and improved numerical code that reduces

the uncertainty by a factor of seven.)

### 11.3 Dielectric Constant–Density Relations

In addition to the  $(p, T, \rho)$  equation of state, we also need an expression relating the density of the gas to its dielectric constant. A commonly used form is the Clausius-Mossotti relation:

$$\frac{\epsilon_r - 1}{\epsilon_r + 2} = A_\epsilon \rho,$$

where  $\epsilon_r$  is the relative dielectric constant of the gas ( $\epsilon_r = 1$  corresponds to the vacuum dielectric constant) and  $A_\epsilon$  is the molar polarizability of the gas.

In many ways the Clausius-Mossotti relation is the dielectric analog of the ideal gas law and has similar limitations. For more precise uses, the Clausius-Mossotti relation may also be expanded as a polynomial series in  $\rho$ , yielding the dielectric virial equation [18]:

$$\frac{\epsilon_r - 1}{\epsilon_r + 2} = A_\epsilon \rho (1 + b\rho + c\rho^2 + \dots), \quad (11.4)$$

where the coefficients  $b$  and  $c$  are called the second and third dielectric virial coefficients, respectively. Unfortunately, the values of the dielectric virial coefficients are not known very precisely. The best values to date are those of White and Gugan [19]:  $b = -0.001(4) \text{ cm}^3/\text{mol}$  and  $c = -2(1) \text{ cm}^6/\text{mol}^2$ , with parentheses indicating the uncertainty in the last digit. The uncertainty in these parameters will limit our determination of  $B$  and  $C$ , as explained below.

### 11.4 Dielectric Constant Gas Thermometry

The phrase dielectric constant gas thermometry (DCGT) refers to the technique of filling a capacitor with a gas of known pressure- and temperature-dependent dielectric constant [9]. The capacitance can be read with high precision using bridge or tunnel-diode oscillator techniques, implying a value for the dielectric constant and hence the temperature.

The analytical starting points of the method are the virial equation of state and the dielectric virial equation. Recalling from above,

$$p = \rho RT(1 + B\rho + C\rho^2 + \dots), \quad (11.5)$$

and

$$\frac{\epsilon - 1}{\epsilon + 2} = A_\epsilon \rho (1 + b\rho + c\rho^2 + \dots). \quad (11.6)$$

The wavelength dependent expression for  $A_\epsilon$  is theoretically calculated to be [20; 21]

$$\begin{aligned} \frac{A_\epsilon}{\text{cm}^3 \text{mol}^{-1}} = & 0.51725407 + 1197.5410 \left( \frac{\lambda}{\text{nm}} \right)^{-2} \\ & + 3.290677 \times 10^6 \left( \frac{\lambda}{\text{nm}} \right)^{-4} + 9.800874 \times 10^9 \left( \frac{\lambda}{\text{nm}} \right)^{-6}, \end{aligned} \quad (11.7)$$

where  $\lambda$  is the wavelength of the incident radiation ( $\lambda \sim 20$  nm for our frequencies). Most DCGT experiments use direct-current or low-frequency measurements and therefore neglect the frequency dependence of  $A_\epsilon$ .

(This physicist is much chagrined by the use of molar units above, but the equivalent atomic constants are known with less precision. However, see section 11.6 below on the Boltzmann constant for a way to remedy this situation.)

Combining the above equations (11.2) and (11.4) to remove the density yields [9]:

$$p = A_1 \eta (1 + A_2 \eta + A_3 \eta^2 + \dots), \quad (11.8)$$

where  $\eta = (\epsilon - 1)/(\epsilon + 2)$  and the coefficients are defined by [8].

$$A_1 = 1/(A_\epsilon/RT + K/3), \quad (11.9)$$

$$A_2 = (B - b)/A_\epsilon, \quad (11.10)$$

$$A_3 = (C - 2Bb + 2b^2 - c)/A_\epsilon^2, \quad (11.11)$$

$$\vdots \quad (11.12)$$

Luther et al. [9] note that the dielectric virial coefficients are about  $10^3$  smaller than the pressure virial coefficients and neglects them in his expressions for  $A_n$ . Gugan and Michel [8], however, include the dielectric virial terms and also adds a constant term  $A_0$ , which if nonzero implies some experimental bias. The parameter  $K$  is an empirical correction for the compressibility of the capacitor and is approximately equal to the inverse of the bulk modulus of the capacitor material, which is on the order of  $10^{-12}$  for niobium and possibly negligible in our experiment.

The uncertainty in our measurements of  $B$  will be dominated by the uncertainty in the second dielectric virial coefficient,  $b = (-1 \pm 4) \times 10^{-3} \text{ cm}^3/\text{mol}$  [19].

Our experiment is useful because for our resonant cavity (neglecting gravity effects, derived later in section 12.1):

$$\epsilon_r - 1 = -2(\Delta f)/f_0, \quad (11.13)$$

where  $\Delta f$  is the gas-induced shift away from the empty cavity frequency  $f_0$ . By measuring the cavity resonance frequency shift we can calculate the dielectric constant of the helium gas. This, along with precise temperature and pressure measurements, allows us to compute the virial coefficients by using equation (11.8).

## 11.5 Virial Coefficients

As mentioned previously in section 11.2.2, the paper by Luther et al. [9] assumes the virial coefficients  $B$  and  $C$  have temperature dependence given by a power series expansion in the inverse temperature:

$$B(T) = \sum_n B_n T^{-n}, \quad \text{and} \quad C(T) = \sum_n C_n T^{-n}, \quad (11.14)$$

following the form suggested in theoretical calculations by Aziz and Slaman [12], and Steur et al. [22]. For values of the coefficients for  $B$ , see table 11.1, above.

Luther et al. measure the capacitance at differing pressures along isotherms. For each value of  $T$  they then do a fit to equation (11.8) to find values of the coefficients  $A_n$  for that particular value of  $T$ . They repeat for several temperatures, then fit these data to equation (11.14) to find the functions  $B(T)$  and  $C(T)$ .

It seems reasonable for us to reproduce these measurements to find  $B(T)$  and  $C(T)$  over the temperature range accessible to us. Our experiment has the particular advantage that it is insensitive to the adsorption of the gas onto the internal surfaces of the apparatus. Because we are using TE cavity modes, the electric field vanishes at the surface and the mode does not “see” any adsorbed atoms; an order-of-magnitude estimate using perturbation theory (see section 12.1) shows this to be a part in  $10^{12}$  effect in the frequency, and therefore, negligible. In contrast, capacitor-based DCGT measurements are sensitive to gas adsorption. Because our experiment is negligibly affected by gas adsorption, we can explore a region of the phase diagram closer to the saturation curve than capacitor systems.

Currently, May et al. at NIST-Gaithersburg are performing room temperature microwave cavity measurements of helium and argon using spheroid copper cavities [20]. It may be interesting to do some room temperature measurements of our own, just for comparison. Their cavities have frequencies of 2–8 GHz and  $Q$  of 10–60 thousand. We have similar  $Q$  values at room temperature, so we may be able to compare with their results.

## 11.6 Boltzmann Constant

In the work discussed above, Luther et al. [9] assume a theoretical value for the molar polarizability  $A_\epsilon$ , although from the form of equation (11.8) it seems possible to extract the value of  $A_\epsilon$  from the data. The CODATA paper defining values of the fundamental physical constants [6] makes this suggestion and adds that the Boltzmann constant may also be measurable through DCGT. A subsequent paper by Fellmuth et al. [23] elaborates on this idea and argues for the feasibility of using DCGT to measure  $k_B$ . Precise determination of Boltzmann’s constant is desirable to firmly link thermodynamic and mechanical energy scales, defining temperature in terms of fundamental quantities rather than experimental artifacts (such as the water triple-point cells currently used). Additionally, Avogadro’s number is related to the Boltzmann constant and the molar gas constant through

$$N_A = R/k_B.$$

Precise measurements of the latter two quantities could define  $N_A$  to higher precision, leading to a better definition of mass and eventual retirement of the SI standard kilogram artifact.

If we abandon the theoretical prediction of  $A_\epsilon$  (equation (11.7)), we can instead relate the molar value of polarizability to the atomic polarizability by

$$A_\epsilon = \frac{R\alpha_0}{3\epsilon_0 k_B}, \quad (11.15)$$

where  $\alpha_0$  is the atomic polarizability,  $\epsilon_0$  is the vacuum permittivity, and  $k_B$  is the Boltzmann constant [6]. Solving this for  $k_B$ :

$$\begin{aligned} k_B &= \frac{\alpha_0}{3\epsilon_0} \left(\frac{A_\epsilon}{R}\right)^{-1} \\ &= \frac{4\pi a_0^3}{3} (1 + m_e/m_\alpha)^3 \alpha_0^* \left(\frac{A_\epsilon}{R}\right)^{-1}, \end{aligned} \quad (11.16)$$

where the second line contains the form preferred by QED theoretical calculations (reduced Rydberg units). In the second line,  $a_0$  is the Bohr radius,  $m_e/m_\alpha$  is the ratio of electron and alpha particle masses,  $\alpha_0^*$  is the atomic polarizability expressed in reduced units.

The usefulness of the second form of the expression above is that all of the quantities except  $A_\epsilon/R$  are known to high precision [6]. In particular, a theoretical expression for  $\alpha_0^*$  is given by Stone [21] (who combines results of Łach [24] and Bhatia [25]):

$$\alpha_0^* = 1.383\,191\,6 + 0.385\,530\,216\omega^2 + 0.127\,538\,95\omega^4 + 0.045\,731\,14\omega^6,$$

where  $\omega$  is the reduced frequency, given by

$$\omega = \frac{4\pi a_0}{\alpha[1 - m_e/(m_\alpha + m_e)]\lambda}.$$

In the expression above,  $\alpha$  is the fine structure constant and  $\lambda$  is the wavelength of the incident radiation.

A precise measurement of  $A_\epsilon/R$  from DCGT using our superconducting cavity system could yield a better empirical value for the Boltzmann constant, which is currently known to 1.8 ppm. All that needs to be done to measure  $k_B$  is to find  $A_\epsilon/R$  by fitting isothermal dielectric constant and pressure data to equation (11.8):

$$p = A_1\eta(1 + A_2\eta + A_3\eta^2 + \dots),$$

$$A_1 = 1/(A_\epsilon/RT + K/3),$$

where  $\eta = (\epsilon_r - 1)/(\epsilon_r + 2)$ . We expect to measure the Boltzmann constant to parts in  $10^8$ , limited by our pressure measurement accuracy.

## Bibliography

- [1] Confucius. “The Analects.” [http://en.wikisource.org/wiki/The\\_Analects?match=zh](http://en.wikisource.org/wiki/The_Analects?match=zh). Translated by James Legge, accessed 23 May, 2007.
- [2] W. Jiang, D. M. Strayer, N.-C. Yeh, J. Huynh, N. Asplund, J. Gatewood, and M. J. Lysek. “Integration of high-resolution frequency control and thermometry for high-precision measurements of physical properties of helium.” *Japan Society of Microgravity Application Journal*, **15 Supp.** II:157 (1999).
- [3] N.-C. Yeh, W. Jiang, and D. M. Strayer. “Application of high-resolution frequency measurements to studies of critical phenomena in helium.” *Japan Society of Microgravity Application Journal*, **15 Supp.** II:136 (1999).
- [4] N.-C. Yeh, W. Jiang, D. M. Strayer, and N. N. Asplund. “Precise measurements of the density and critical phenomena near the phase transitions in helium using high-Q niobium microwave cavities.” *Czech Journal of Physics*, **46**(Suppl. S3) (1996).
- [5] N.-C. Yeh, D. M. Strayer, V. L. Anderson, and N. Asplund. “Superconducting-Cavity-Stabilized Oscillators (SCSO) for precise frequency measurements.” *Physica B*, **280**:557–558 (2000).
- [6] P. J. Mohr and B. N. Taylor. “CODATA recommended values of the fundamental physical constants: 2002.” *Reviews of Modern Physics*, **77**:1–107 (2005). <http://link.aps.org/abstract/RMP/v77/p1>.
- [7] K. H. Berry. “NPL-75: A low temperature gas thermometry scale from 2.6 K to 27.1 K.” *Metrologia*, **15**:89–115 (1979).
- [8] D. Gagan and G. W. Michel. “Dielectric constant gas thermometry from 4.2 to 27.1 K.” *Metrologia*, **16**:149–67 (1980). <http://www.iop.org/EJ/abstract/0026-1394/16/4/002>.
- [9] H. Luther, K. Grohmann, and B. Fellmuth. “Determination of thermodynamic temperature and  $^4\text{He}$  virial coefficients between 4.2 K and 27.0 K by dielectric constant gas thermometry.” *Metrologia*, **33**:341–352 (1996). <http://www.iop.org/EJ/abstract/0026-1394/33/4/8>.
- [10] H. Preston-Thomas. “The International Temperature Scale of 1990 (ITS-90).” *Metrologia*, **27**:3–10 (1990).
- [11] H. Preston-Thomas, P. Bloembergen, and T. J. Quinn, editors. *Supplimentary Information for the International Temperature Scale of 1990*. Sèvres: Bureau International des Poids et Mesures, 1997 reprinted edition (1997).
- [12] R. A. Aziz and M. J. Slaman. *Metrologia*, **27**:211–219 (1990). <http://www.iop.org/EJ/abstract/0026-1394/27/4/005>.
- [13] S. Ujevic and S. A. Vitiello. “Interatomic potential for the condensed phases of helium atoms.” *Physical Review B*, **73**(1):012511 (2006). <http://link.aps.org/abstract/PRB/v73/e012511>.
- [14] W. Cencek, J. Komasa, K. Pachucki, and K. Szalewicz. “Relativistic correction to the helium dimer interaction energy.” *Physical Review Letters*, **95**(23):233004 (2005). <http://link.aps.org/abstract/PRL/v95/e233004>.

- [15] J. J. Hurly and J. B. Mehl. “<sup>4</sup>He thermophysical properties: New ab initio calculations.” *Journal of Research of the National Institute of Standards and Technology*, **112**(2):75–94 (2007).  
<http://nvl.nist.gov/pub/nistpubs/jres/112/2/cnt112-2.htm>.
- [16] R. K. Pathria. *Statistical Mechanics*. Oxford: Butterworth, second edition (1996).
- [17] J. J. Hurly and M. R. Moldover. “Ab initio values of the thermophysical properties of helium as standards.” *Journal of Research of the National Institute of Standards and Technology*, **105**(5):667–688 (2000).  
<http://nvl.nist.gov/pub/nistpubs/jres/105/5/cnt105-5.htm>.
- [18] M. R. Moldover. “Can a pressure standard be based on capacitance measurements?” *Journal of Research of the National Institute of Standards and Technology*, **103**(2):167–175 (1998).
- [19] M. P. White and D. Gegan. “Direct measurements of the dielectric virial coefficients of <sup>4</sup>He between 3 K and 18 K.” *Metrologia*, **29**:37–57 (1992).
- [20] E. F. May, L. Pitre, J. B. Mehl, M. R. Moldover, and J. W. Schmidt. “Quasi-spherical cavity resonators for metrology based on the relative dielectric permittivity of gases.” *Reviews of Scientific Instruments*, **75**:3307–3317 (2004). <http://link.aip.org/link/?RSI/75/3307/1>.
- [21] J. A. Stone and A. Stejskal. “Using helium as a standard of refractive index: Correcting errors in a gas refractometer.” *Metrologia*, **41**:189–197 (2004). <http://www.iop.org/EJ/abstract/0026-1394/41/3/012>.
- [22] P. P. M. Steur, M. Durieux, and G. T. McConville. *Metrologia*, **24**:69–77 (1987).  
<http://www.iop.org/EJ/abstract/0026-1394/24/2/003>.
- [23] B. Fellmuth, C. Gaiser, and J. Fischer. “Determination of the Boltzmann constant—status and prospects.” *Measurement Science and Technology*, **17**(10):R145–R159 (2006). <http://stacks.iop.org/0957-0233/17/R145>.
- [24] G. Łach, B. Jeziorski, and K. Szalewicz. “Radiative corrections to the polarizability of helium.” *Physical Review Letters*, **92**:233001 (2004). <http://link.aps.org/abstract/PRL/v92/e233001>.
- [25] A. K. Bhatia and R. J. Drachman. “Optical properties of helium including relativistic corrections.” *Physical Review A*, **58**:4470–4472 (1998). [http://prola.aps.org/abstract/PRA/v58/i6/p4470\\_1](http://prola.aps.org/abstract/PRA/v58/i6/p4470_1).

The large print giveth, and the small print  
taketh away.

---

Tom Waits, "Step Right Up"\*

## Chapter 12

### Analysis and Preliminary Results

**T**HIS chapter contains derivations for calculating the shift in the cavity resonance frequency caused by a change in the dielectric and preliminary data demonstrating this effect. Two types of perturbations are considered here: first, an isotropic change in the dielectric constant (for example, caused by introducing a gas into the cavity in zero-gravity conditions), and second, the shift caused by gravity-induced density gradient of gas in the cavity. Because neither of these effects is dependent on magnetic properties or the radial and azimuthal components, some simplifications are implied in the following derivation. Both derivations agree with our preliminary data to within the experimental uncertainties.

Two methods were used to calculate the results in this chapter: perturbation theory and WKB theory. Only the perturbation theory calculation is presented here, although the WKB calculation agrees to first order in the dielectric constant shift.

#### 12.1 Perturbation Theory on the EM Wave Equation

The technique followed here is to treat the electromagnetic wave equation in a way analogous to the way Schrödinger equation is treated in quantum perturbation theory. This is reasonable because both equations are Sturm-Liouville partial differential equations.

We begin with the wave equation for the electric field  $\mathbf{E}$ :

$$\nabla^2 \mathbf{E} - \mu\epsilon \frac{\partial^2}{\partial t^2} \mathbf{E} = 0, \quad (12.1)$$

---

\*Reference [1]

where  $\epsilon$  and  $\mu$  are the usual SI quantities. Assuming the electric field has time dependence  $e^{i\omega t}$ , the time derivatives can be evaluated explicitly:

$$\nabla^2 \mathbf{E} + \mu\epsilon\omega^2 \mathbf{E} = 0. \quad (12.2)$$

The field  $\mathbf{E}$  can be decomposed into superpositions of the eigenmodes  $\vec{\mathcal{E}}_\alpha$  of the cavity ( $\alpha = \{\text{TE or TM}\}_{m,n,l}$ ) with eigenfrequencies  $\Omega_\alpha$ :

$$\mathbf{E} = \sum_{\alpha} C_{\alpha} \vec{\mathcal{E}}_{\alpha}.$$

The orthogonality of the modes can be expressed as:

$$\frac{\int dV \vec{\mathcal{E}}_{\alpha}^* \cdot \vec{\mathcal{E}}_{\beta}}{\int dV |\vec{\mathcal{E}}_{\alpha}|^2} = \delta_{\alpha\beta}, \quad (12.3)$$

where the integrals are over the cavity volume and  $\delta_{\alpha\beta}$  is the Kronecker delta function.

The completeness of the modes can be written as

$$\vec{f} = \sum_{\alpha} \vec{\mathcal{E}}_{\alpha} \frac{\int dV \vec{\mathcal{E}}_{\alpha}^* \cdot \vec{f}}{\int dV |\vec{\mathcal{E}}_{\alpha}|^2}, \quad (12.4)$$

where  $\vec{f}$  is some arbitrary electric field.

The perturbation enters in the dielectric constant

$$\epsilon = \epsilon_0(1 + \lambda\chi_e), \quad (12.5)$$

where  $\chi_e = \epsilon/\epsilon_0 - 1$  is the electric susceptibility and  $\lambda$  is a small perturbation parameter ( $\lambda \rightarrow 1$  in the end).

The field and angular frequency of the perturbed system are defined as series in  $\lambda$ :

$$\mathbf{E} = \mathbf{E}_0 + \lambda\mathbf{E}_1 + \lambda^2\mathbf{E}_2 + \dots, \quad (12.6)$$

$$\omega = \omega_0 + \lambda\omega_1 + \lambda^2\omega_2 + \dots. \quad (12.7)$$

The solution proceeds as follows. The above expressions (equations (12.5)–(12.7)) are plugged into the wave equation (equation (12.2)) and terms are grouped in powers of  $\lambda$ . The resulting equations are solved for  $\mathbf{E}_i$  and  $\omega_i$ .

The perturbations we are considering are independent of the radial and azimuthal components, and the only unperturbed modes we are interested in are the  $\text{TE}_{011}$  and  $\text{TE}_{013}$  modes. By symmetry considerations, only  $\text{TE}_{01l}$  modes will couple our perturbations with the unperturbed modes, simplifying some of the calculations to follow.

### 12.1.1 Unperturbed Solution

As shown earlier, the electromagnetic fields of  $\text{TE}_{01l}$  modes are

$$\begin{aligned} H_z &= E_0 J_0(\gamma_{01} r) \sin\left(\frac{l\pi z}{L}\right), \\ E_z &= 0, \\ \mathbf{H}_t &= E_0 \frac{l\pi}{L\gamma_{01}} \cos\left(\frac{l\pi z}{L}\right) J'_0(\gamma_{01} r) \hat{\mathbf{r}}, \\ \mathbf{E}_t &= -E_0 \frac{i\omega\mu}{\gamma_{01}} \sin\left(\frac{l\pi z}{L}\right) J'_0(\gamma_{01} r) \hat{\boldsymbol{\phi}}, \\ \omega_{01l} &= \frac{1}{\sqrt{\mu\epsilon}} \left( \gamma_{01}^2 + \frac{l^2\pi^2}{L^2} \right)^{1/2}, \\ \gamma_{01} &\approx 3.832/R. \end{aligned}$$

We are interested only in the  $l = 1, 3$  cases.

### 12.1.2 First-Order Perturbation

The perturbation proceeds by substituting the perturbed dielectric constant (equation (12.5)), electric field (equation (12.6)) and frequency (equation (12.7)) into the time-independent wave equation (equation (12.2)).

$$\begin{aligned} \nabla^2(\mathbf{E}_0 + \lambda\mathbf{E}_1 + \lambda^2\mathbf{E}_2 + \dots) \\ + \mu(\epsilon_0(1 + \lambda\chi_e))(\omega_0 + \lambda\omega_1 + \lambda^2\omega_2 + \dots)^2(\mathbf{E}_0 + \lambda\mathbf{E}_1 + \lambda^2\mathbf{E}_2 + \dots) = 0 \end{aligned} \quad (12.8)$$

Keeping terms up to first order in  $\lambda$ :

$$\lambda^0 \left[ \nabla^2 \mathbf{E}_0 + \mu \epsilon_0 \omega_0^2 \mathbf{E}_0 \right] + \lambda^1 \left[ \nabla^2 \mathbf{E}_1 + \mu \epsilon_0 \omega_0^2 \mathbf{E}_1 + (\mu \epsilon_0 \omega_0 (\chi_e \omega_0 + 2\omega_1)) \mathbf{E}_0 \right] + \dots = 0. \quad (12.9)$$

As expected, the  $\lambda^0$  coefficient is simply the unperturbed wave equation and therefore zero. In particular  $\mathbf{E}_0$  is one of the eigenmodes. We are interested in  $\mathbf{E}_0 = \vec{\mathcal{E}}_{01l}^{\text{TE}}$  for  $l = 1$  or  $3$ . The corresponding eigenfrequency is  $\omega_0 = \Omega_{01l}^{\text{TE}}$ . (From here the “TE” label will be omitted unless needed for clarity.) The coefficient of  $\lambda^1$  must be zero to match with the right-hand side:

$$\nabla^2 \mathbf{E}_1 + \mu \epsilon_0 \Omega_{01l}^2 \mathbf{E}_1 + (\mu \epsilon_0 \Omega_{01l} (\chi_e \Omega_{01l} + 2\omega_1)) \vec{\mathcal{E}}_{01l} = 0. \quad (12.10)$$

### First-Order Frequency Perturbation

To isolate  $\omega_1$ , take the dot product of each term with  $\vec{\mathcal{E}}_{01l}^*$  and integrate over the cavity volume.

$$\frac{\int dV \vec{\mathcal{E}}_{01l}^* \cdot \nabla^2 \mathbf{E}_1}{\int dV |\vec{\mathcal{E}}_{01l}|^2} + \mu \epsilon_0 \Omega_{01l}^2 \frac{\int dV \vec{\mathcal{E}}_{01l}^* \cdot \mathbf{E}_1}{\int dV |\vec{\mathcal{E}}_{01l}|^2} + \mu \epsilon_0 \Omega_{01l}^2 \frac{\int dV \chi_e |\vec{\mathcal{E}}_{01l}|^2}{\int dV |\vec{\mathcal{E}}_{01l}|^2} + 2\mu \epsilon_0 \Omega_{01l} \omega_1 \frac{\int dV |\vec{\mathcal{E}}_{01l}|^2}{\int dV |\vec{\mathcal{E}}_{01l}|^2} = 0.$$

Various terms can be simplified by applying orthogonality (equation (12.3)). The second term is zero by the requirement that the field perturbations be orthogonal to the unperturbed solution. The first term then becomes zero by orthogonality after integration by parts and by the boundary condition that the field is zero at the cavity walls. Rearranging:

$$\mu \epsilon_0 \Omega_{01l}^2 \frac{\int dV \chi_e |\vec{\mathcal{E}}_{01l}|^2}{\int dV |\vec{\mathcal{E}}_{01l}|^2} + 2\mu \epsilon_0 \Omega_{01l} \omega_1 = 0,$$

$$\omega_1 = -\frac{1}{2} \Omega_{01l} \frac{\int dV \chi_e |\vec{\mathcal{E}}_{01l}|^2}{\int dV |\vec{\mathcal{E}}_{01l}|^2}. \quad (12.11)$$

The above equation gives the first-order correction to the frequency for a given dielectric constant, which may be a function of position. In the case where  $\epsilon$  is uniform (as in zero gravity)

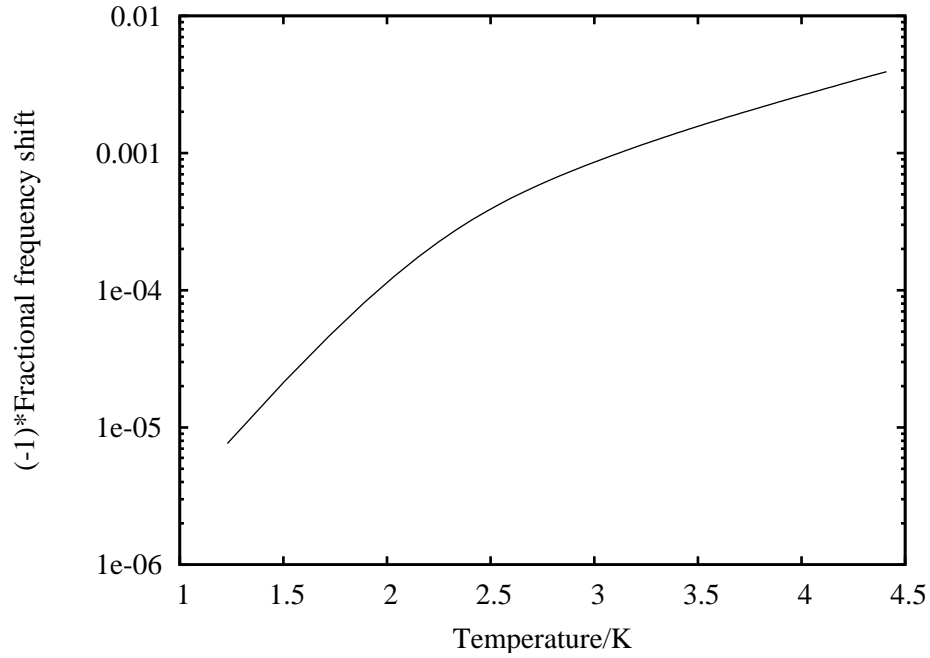


Figure 12.1. Predicted gas-induced frequency shift of the  $TE_{011}$  mode in the presence of helium-4 saturated vapor, as a function of temperature. The presence of the gas decreases the frequency relative to cavity in vacuum; only the magnitude is shown here so that it can be displayed on a log scale. (Thermodynamic data from [2].)

the first-order perturbation correction to the frequency is

$$\omega_1 = -\frac{1}{2}\Omega_{01l}\chi_e = -\frac{1}{2}\Omega_{01l}\left(\frac{\epsilon - \epsilon_0}{\epsilon_0}\right), \quad (12.12)$$

where  $l$  is the label for the unperturbed mode  $TE_{mnl}$  with eigenfrequency  $\Omega_{01l}$ . (The correction for gravity-induced density variations is derived below in section 12.2.) Rewriting this expression in notation from earlier chapters,

$$\frac{f - f_0}{f_0} = -\frac{1}{2}(\epsilon_r - 1),$$

where  $f_0$  is the cavity resonance frequency without gas,  $f$  is the frequency with gas, and  $\epsilon_r$  is the relative dielectric constant of the gas. The magnitude of the predicted frequency shift for  $TE_{011}$  mode in the case of saturated helium-4 vapor is shown in figure 12.1.

### First-Order Field Perturbation

To find the first-order perturbation to the field, take the dot product of each term in equation (12.10) with an arbitrary eigenmode  $\vec{\mathcal{E}}_\alpha^* \neq \vec{\mathcal{E}}_{01l}^*$  and integrate over the cavity volume.

$$\int dV \vec{\mathcal{E}}_\alpha^* \cdot \nabla^2 \mathbf{E}_1 + \mu\epsilon_0 \Omega_{01l}^2 \int dV \vec{\mathcal{E}}_\alpha^* \cdot \mathbf{E}_1 + \mu\epsilon_0 \Omega_{01l}^2 \int dV \chi_e \vec{\mathcal{E}}_\alpha^* \cdot \vec{\mathcal{E}}_{01l} + 2\mu\epsilon_0 \Omega_{01l} \omega_1 \int dV \vec{\mathcal{E}}_\alpha^* \cdot \vec{\mathcal{E}}_{01l} = 0.$$

The last term is zero by orthogonality, and the first term can be intergrated by parts twice:

$$\int dV \nabla^2 \vec{\mathcal{E}}_\alpha^* \cdot \mathbf{E}_1 + \mu\epsilon_0 \Omega_{01l}^2 \int dV \vec{\mathcal{E}}_\alpha^* \cdot \mathbf{E}_1 + \mu\epsilon_0 \Omega_{01l}^2 \int dV \chi_e \vec{\mathcal{E}}_\alpha^* \cdot \vec{\mathcal{E}}_{01l} = 0.$$

The first two terms can be combined after applying the wave equation. Multiplying each term by  $\vec{\mathcal{E}}_\alpha^* / \int dV |\vec{\mathcal{E}}_\alpha|^2$ , summing over the modes  $\alpha \neq \{01l\}$ , and applying the completeness relation (equation (12.3)) yields

$$\mathbf{E}_1 = \sum_{\alpha \neq \{01l\}} \frac{\Omega_{01l}^2}{\Omega_\alpha^2 - \Omega_{01l}^2} \frac{\int dV \chi_e \vec{\mathcal{E}}_\alpha^* \cdot \vec{\mathcal{E}}_{01l}}{\int dV |\vec{\mathcal{E}}_\alpha|^2} \vec{\mathcal{E}}_\alpha.$$

In particular, if  $\chi_e$  is uniform, it factors out of the integral, and  $\mathbf{E}_1 = 0$  by orthogonality. Also, if  $\chi_e$  is independent of the coordinates  $r$  and  $\phi$ , only  $\text{TE}_{01q}$  modes will have nonzero integrals and contribute to the sum.

#### 12.1.3 Second-Order Perturbation

Taking the  $\lambda^2$  terms from equation (12.8):

$$(1/\mu\epsilon_0)\nabla^2 \mathbf{E}_2 + (\omega_1^2 + 2\omega_0\omega_2)\mathbf{E}_0 + (2\omega_0\omega_1)\mathbf{E}_1 + \omega_2^2 \mathbf{E}_2 + 2\omega_0\omega_1\chi_e \mathbf{E}_0 + \chi_e \omega_0^2 \mathbf{E}_1 = 0.$$

Following similar procedures as the first-order calculations, the second-order correction to the frequency is

$$\omega_2 = \frac{3}{2} \frac{\omega_1^2}{\Omega_{01l}} - \frac{1}{2} \sum_{\alpha \neq \{01l\}} \frac{\Omega_{01l}^3}{\Omega_\alpha^2 - \Omega_{01l}^2} \frac{\left| \int dV \chi_e \vec{\mathcal{E}}_{01l}^* \cdot \vec{\mathcal{E}}_\alpha \right|^2}{\left( \int dV |\vec{\mathcal{E}}_\alpha|^2 \right)^2}. \quad (12.13)$$

## 12.2 Gravity Effect on the Local Dielectric Constant

The dielectric virial equation states

$$\frac{\epsilon_r - 1}{\epsilon_r + 2} = A_\epsilon \rho (1 + b\rho + c\rho^2 + \dots),$$

where  $\epsilon_r$  is the relative dielectric constant,  $A_\epsilon$  is the molar polarizability of the gas,  $\rho$  is the molar density, and  $b$  and  $c$  are the second and third dielectric virial coefficients. To simplify later algebra and to aid in interpretation, we introduce a couple of new dimensionless variables:  $\eta = (\epsilon_r - 1)/(\epsilon_r + 2) = \chi_e/(\chi_e + 3)$  and  $s = A_\epsilon \rho$ . Rewriting the previous equation:

$$\eta = s[1 + (b/A_\epsilon)s + (c/A_\epsilon^2)s^2 + \dots].$$

For reference,  $\eta \sim 10^{-3}$  and  $s \sim 10^{-3}$  for saturated helium-4 gas, so we can expand power series in these parameters and expect convergence.

Because  $\chi_e$  appears in the perturbation calculations in the earlier sections, it would be useful to solve the above expression for  $\chi_e$ . A power series should suffice:

$$\chi_e = 3 \frac{\eta}{1 - \eta} = 3 \sum_{i=1}^{\infty} \eta^i.$$

Because  $|\eta|$  is less than unity, the geometric series converges. Applying the dielectric virial equation and grouping in powers of  $s$ :

$$\begin{aligned} \chi_e = 3 \left( s + \left[ 1 + \frac{b}{A_\epsilon} \right] s^2 + \left[ 1 + 2\frac{b}{A_\epsilon} + \frac{c}{A_\epsilon^2} \right] s^3 \right. \\ \left. + \left[ 1 + 3\frac{b}{A_\epsilon} + \left( \frac{b}{A_\epsilon} \right)^2 + 2\frac{c}{A_\epsilon^2} + \frac{d}{A_\epsilon^3} \right] s^4 + \dots \right). \end{aligned} \quad (12.14)$$

The next step is to add the position dependence of the density. From classical thermodynamics (i.e., neglecting Bose-Einstein statistics) the density of the helium gas under uniform gravitational acceleration  $g$  obeys the barometric formula

$$\rho(z) = \rho_0 e^{-mgz/k_B T}.$$

where  $\rho(z)$  is the density at a height  $z$  above the floor of the cavity,  $\rho_0$  is the density at  $z = 0$ ,  $m$  is the mass of a helium atom,  $k_B$  is Boltzmann's constant, and  $T$  is temperature. Letting  $\zeta = mgL/k_B T$  ( $\sim 10^{-4}$ ) and  $s_0$  equal the value of  $s$  at  $z = 0$ :

$$\chi_e(z) = 3 \left\{ s_0 e^{-\zeta(z/L)} + \left[ 1 + \frac{b}{A_\epsilon} \right] s_0^2 e^{-2\zeta(z/L)} + \left[ 1 + 2\frac{b}{A_\epsilon} + \frac{c}{A_\epsilon^2} \right] s_0^3 e^{-3\zeta(z/L)} + \left[ 1 + 3\frac{b}{A_\epsilon} + \left( \frac{b}{A_\epsilon} \right)^2 + 2\frac{c}{A_\epsilon^2} + \frac{d}{A_\epsilon^3} \right] s_0^4 e^{-4\zeta(z/L)} + \dots \right\}.$$

Substituting this into equation (12.11), integrating over the volume of the cavity, and rearranging yields:

$$\begin{aligned} \frac{\omega_1}{\omega_0} = & -\frac{1}{2} \left\{ 3 \left( s_0 + \left[ 1 + \frac{b}{A_\epsilon} \right] s_0^2 + \left[ 1 + 2\frac{b}{A_\epsilon} + \frac{c}{A_\epsilon^2} \right] s_0^3 \right. \right. \\ & \left. \left. + \left[ 1 + 3\frac{b}{A_\epsilon} + \left( \frac{b}{A_\epsilon} \right)^2 + 2\frac{c}{A_\epsilon^2} + \frac{d}{A_\epsilon^3} \right] s_0^4 + \dots \right) \right\} \\ & + \frac{3}{2} s_0 \zeta - \frac{3}{2} s_0^2 \zeta (1 + b/A_\epsilon) + \frac{1}{4} s_0 \zeta^2 - \frac{3}{8l^2 \pi^2} s_0 \zeta^2 + \dots \quad (12.15) \end{aligned}$$

The term in curly brackets is simply the gravity-independent frequency shift. Simplifying,

$$\frac{\omega_1}{\omega_0} = \frac{\omega_1}{\omega_0} \Big|_{g=0} + \frac{3}{2} s_0 \zeta - \frac{3}{2} s_0^2 \zeta (1 + b/A_\epsilon) + \frac{1}{4} s_0 \zeta^2 - \frac{3}{8l^2 \pi^2} s_0 \zeta^2 + \dots \quad (12.16)$$

The second term is  $\sim 10^{-7}$  and the last three terms are  $\sim 10^{-10}$ . The last term above is the largest term that exhibits explicit dependence on the mode.

### 12.2.1 Dead-Space Correction to Density

The final step is to express the above equation in terms of the average density, rather than the density at a specific location; the average density is the quantity relevant to the other thermodynamic variables. Stated another way, the cavity is not a closed volume but is inside a larger sealed can (see figure 9.4). Gas outside the cavity but still inside the can (in the so-called dead space) must be accounted for when calculating the average gas density in finite gravity. The average gas density

inside the can is therefore

$$\begin{aligned}
 \bar{\rho} &= \int dV_{\text{can}} \rho(z) / \int dV_{\text{can}}, \\
 &= \int dz A(z) \rho(z) / \int dz A(z), \\
 &= \int dz A(z) \rho_0 \exp(-mgz/k_B T) / \int dz A(z),
 \end{aligned}$$

where  $A(z)$  is the cross-sectional area of the can and the integral is over the entire height of the can. To get a feel for the size of this correction, we first take the case where  $A(z)$  is constant and calculate the average density over the interval  $z \in (a_1, a_2)$ , where  $a_1$  and  $a_2$  may be positive or negative:

$$\begin{aligned}
 \bar{\rho} &= \int_{a_1}^{a_2} dz A \rho_0 \exp(-mgz/k_B T) / \int_{a_1}^{a_2} dz A, \\
 &= \frac{\rho_0}{a_2 - a_1} \int_{a_1}^{a_2} dz \exp(-mgz/k_B T), \\
 &= \frac{\rho_0}{a_2 - a_1} \left( -\frac{k_B T}{mg} \right) \left[ \exp\left(-\frac{mga_2}{k_B T}\right) - \exp\left(-\frac{mga_1}{k_B T}\right) \right], \\
 &= \rho_0 \left( \frac{2}{a_2 - a_1} \right) \left( \frac{k_B T}{mg} \right) \exp\left[-\frac{(a_2 + a_1) mg}{2 k_B T}\right] \sinh\left[\frac{(a_2 - a_1) mg}{2 k_B T}\right].
 \end{aligned}$$

The terms in square brackets are on the order of  $10^{-4}$ , so power series expansions are reasonable here:

$$\begin{aligned}
\bar{\rho} &= \rho_0 \left[ \frac{2}{(a_2 - a_1)} \frac{k_B T}{m g} \right] \\
&\times \left\{ 1 - \frac{(a_2 + a_1)}{2} \frac{m g}{k_B T} + \frac{1}{2} \left[ \frac{(a_2 + a_1)}{2} \frac{m g}{k_B T} \right]^2 + \dots \right\}, \\
&\times \left\{ \frac{(a_2 - a_1)}{2} \frac{m g}{k_B T} + \frac{1}{6} \left[ \frac{(a_2 - a_1)}{2} \frac{m g}{k_B T} \right]^3 + \dots \right\} \\
&= \rho_0 \left\{ 1 - \frac{(a_2 + a_1)}{2} \frac{m g}{k_B T} + \frac{1}{2} \left[ \frac{(a_2 + a_1)}{2} \frac{m g}{k_B T} \right]^2 + \dots \right\} \\
&\times \left\{ 1 + \frac{1}{6} \left[ \frac{(a_2 - a_1)}{2} \frac{m g}{k_B T} \right]^2 + \dots \right\}, \\
\bar{\rho} &= \rho_0 \left\{ 1 - \frac{(a_2 + a_1)}{2} \frac{m g}{k_B T} + \left[ \frac{1}{2} \left( \frac{a_2 + a_1}{2} \right)^2 + \frac{1}{6} \left( \frac{a_2 - a_1}{2} \right)^2 \right] \left[ \frac{m g}{k_B T} \right]^2 + \dots \right\}.
\end{aligned}$$

For our system  $a_1$  and  $a_2$  are on the order of centimeters, so the second term is  $\sim 10^{-4}$  and the third term is  $\sim 10^{-8}$ , which we will neglect.

For the real system,  $A(z)$  is a piecewise constant function of  $z$ . Calculating  $A(z)$  from the original engineering drawings (figure 12.2) and performing the integration numerically yields a temperature-dependent relation between the average gas density  $\bar{\rho}$  and the density at the height corresponding to the bottom of the cavity  $\rho_0$  (which is needed for the perturbation calculations in the previous section, e.g., equation (12.16)). The density at the bottom of the cavity is related to the average density by

$$\rho_0 = \bar{\rho} \left[ 1 + (5.674 \pm 0.010) \times 10^{-4} \text{ K}^{-1} T \right], \quad (12.17)$$

where the uncertainty in the coefficient is dominated by the uncertainty in the physical dimensions. The total fractional frequency shift from equations (12.17) and (12.16) relative to the zero-gravity case is plotted in figure 12.3.

Combining equations (12.14), (12.16), and (12.17) yields an expression for the frequency shift as a function of the average density in the cavity, the temperature, and the dielectric virial coefficients. This can be inverted to express the density as a function of the frequency shift.



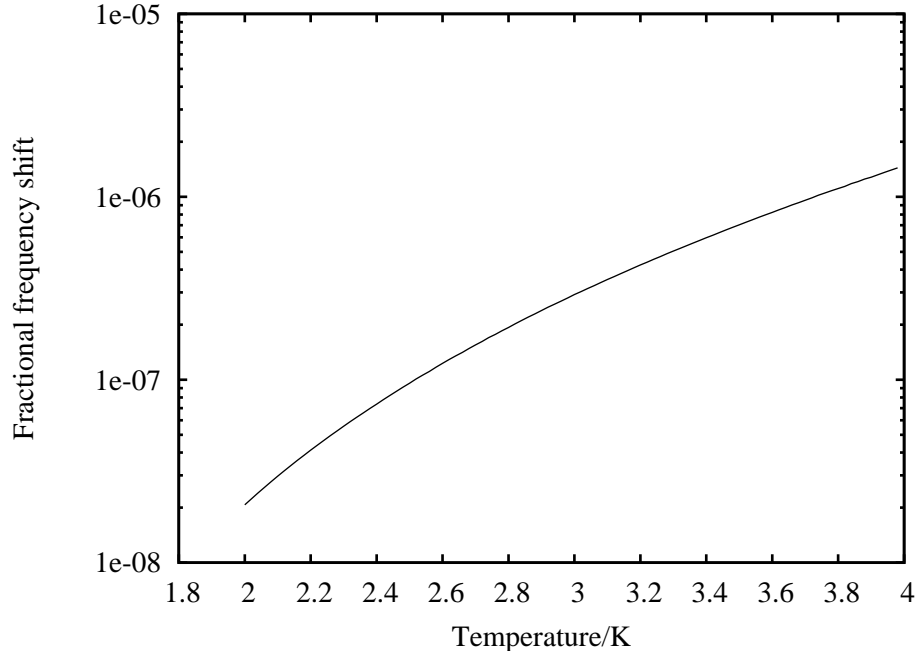


Figure 12.3. Calculated gravity-induced fractional frequency shift for the  $TE_{011}$  as a function of temperature for helium-4 saturated vapor, using thermodynamic data from [2].

### 12.2.2 Liquid Phases

The liquid phases of helium are much more susceptible to gravity effects than the gas phase because the density of the liquid is about a factor of one thousand greater. The large density of the liquid phases invalidates many of the approximations used in the previous sections. For example, the dimensionless quantity  $s = A_\epsilon \rho$  used for the gravity perturbation expansions (e.g., equation (12.16)) is of order unity for the liquid, ruining the convergence of the power series.

The primary gravity effect on liquid phases is the barometric pressure gradient. This is the effect familiar to divers where the pressure increases approximately linearly with depth because of the weight of the fluid above the diver. Specifically, the pressure  $p(z)$  is given by

$$p(z) = p(0) + \int_z^0 \rho(z') g dz' \approx p(0) - \rho g z,$$

where  $z' = 0$  is at the top of the liquid,  $z$  is negative, and the approximation assumes an incompressible fluid. For our cavity height of 28 mm and saturated liquid helium at the lambda point, the change in pressure under Earth gravity is 40 Pa from the bottom to the top of the cavity.

Compared to the saturation pressure of 5.0 kPa, this is on the order of a 1% effect (values from [2]).

The pressure gradient is particularly problematic for studies of the superfluid transition. As seen in the helium-4 phase diagram (figure 11.1 on page 152), the lambda line separating the normal fluid and superfluid phases has a negative value for  $\partial p/\partial T$ . Because of the barometric pressure gradient, a finite sample will span a range of pressures over its height. Near the lambda line, this could result in a pressure-induced phase separation in the liquid, with the top of the liquid (lower pressure) being in the superfluid state while the bottom of the liquid (higher pressure) is in the normal liquid state [3]. In this configuration, only the fluid at exactly the right height in the cavity is at the  $(p, T)$  phase boundary, making it difficult to study properties of the transition.

This limitation is well known and encouraged several space-based experiments of the superfluid transition [4; 5]. Early work on the present experiment was geared towards future microgravity experiments of the critical scaling exponents in the superfluid transition [6–8], but the focus of our experiment shifted to gas phase measurements when suitable microgravity platforms became no longer available.

### 12.3 Equation of State Uncertainties

As described earlier, we can currently measure frequency to parts in  $10^{12}$  precision. With the corrections outlined above, this corresponds to technical limits to the uncertainties in the density of parts in  $10^{10}$ . Using germanium resistance thermometers, we have demonstrated temperature stability of parts in  $10^5$  (as shown in figure 9.6 on page 133). With improved thermometry using paramagnetic-salt thermometers with SQUID readout the temperature resolution can be improved to parts in  $10^9$  or better [9].

The last quantity needed for equation-of-state measurements is pressure. At this time, we have not built the pressure sensor. Plans are to install a Straty-Adams-type capacitance sensor in the cryogenic probe with tunnel-diode oscillator readout, similar to those described in reference [10]. These sensors can have resolutions of parts in  $10^8$ . However, absolute calibration of pressure sensors is only certain to parts in  $10^6$ , limited by the precision of primary pressure standards such as the primary mercury manometers used by NIST [11]. An alternate means of calibration would be to compare the pressure sensor against thermodynamic fixed points. One point could be hard vacuum (assume  $p = 0$ ) and the other would likely be the pressure of the lambda point of helium-4

(the triple point where gas, liquid, and superfluid phases coexist).

The experimental uncertainties expected in the unsaturated gas equation of state measurements are listed in table 12.1.

## 12.4 Proof-of-Concept Data

Before the project stalled, we were able to take some rough proof of concept data to demonstrate the frequency shift. The purpose of the measurement was simply to get order-of-magnitude confirmation that the calculations above were correct before beginning the hardware changes needed to properly fill and monitor the sample gas (see section 9.2.2). To perform these measurements the vacuum can was saturated with helium gas (so that there was liquid helium in the bottom of the can). Temperature was controlled by pumping on the helium bath. No electronic temperature sensors were functioning at this time, so the temperature was implied from the bath pressure. Despite the crudeness of the measurement, general agreement with the predictions was observed. The discrepancies are likely due to the lack of accurate temperature measurement; we estimate the temperature uncertainty to be 5%. The data are presented in table 12.2 and figure 12.4. Because of the large temperature uncertainty in this particular data set, the gravity corrections to the density presented above are negligible at this precision, although for the final version of this experiment these corrections will be necessary.

Table 12.1. Estimated uncertainties for helium equation of state measurements

| Quantity                             | Symbol       | Rel. uncertainty         | Notes                   |
|--------------------------------------|--------------|--------------------------|-------------------------|
| Directly measured quantities         |              |                          |                         |
| Frequency (using spectroscopy)       | $f$          | $10^{-9}$                | —                       |
| Frequency (using PLL)                | $f$          | $10^{-12}$               | conservative estimate   |
| Temperature (using germanium)        | $T$          | $10^{-6}$ 7              | —                       |
| Temperature (using paramagnetic)     | $T$          | $10^{-9}$                | —                       |
| Pressure                             | $p$          | $10^{-8}$ or $10^{-6}$ * | *limited by calibration |
| Local gravity                        | $g$          | $10^{-3}$                | estimate                |
| Assumed values                       |              |                          |                         |
| Second dielectric virial coefficient | $b$          | 1                        | [12]                    |
| Third dielectric virial coefficient  | $c$          | 1                        | [12]                    |
| Molar gas law constant               | $R$          | $10^{-7}$                | [13]                    |
| Boltzmann constant                   | $k_B$        | $10^{-6}$                | (see also below), [13]  |
| Polarizability of He                 | $A_\epsilon$ | $10^{-8}$                | [14; 15]                |
| Derived quantities                   |              |                          |                         |
| Molar density of helium              | $\rho(T, p)$ | $10^{-9}$                | limited by $b$          |
| Second virial coefficient            | $B(T)$       | $10^{-5}$                | limited by $b$          |
| Third virial coefficient             | $C(T)$       | $10^{-2}$                | limited by $b, c$       |
| Boltzmann constant                   | $k_B$        | $10^{-8}$                | limited by $p$          |

Table 12.2. Proof-of-concept data for helium density measurements of saturated helium vapor

| Nominal Pressure<br>(torr) | Temperature*<br>(K) | Predicted $\delta f/f_0^\dagger$<br>( $10^{-4}$ ) | Measured $\delta f/f_0$<br>( $10^{-4}$ ) | Predicted $\rho^\dagger$<br>(mol/m <sup>3</sup> ) | Measured $\rho^\ddagger$<br>(mol/m <sup>3</sup> ) |
|----------------------------|---------------------|---|--|---|---|
| 760                        | $4.2 \pm 0.2$       | -32.7   | -26                                      | 4190  | $3300 \pm 800$                                    |
| 100                        | $2.6 \pm 0.1$       | -5.26   | -3.4                                     | 677   | $440 \pm 100$                                     |
| 70                         | $2.5 \pm 0.1$       | -3.89   | -3.7                                     | 500   | $470 \pm 90$                                      |
| 40                         | $2.2 \pm 0.1$       | -2.42   | -2.5                                     | 312   | $320 \pm 60$                                      |
| 30                         | $2.1 \pm 0.1$       | -1.89   | -2.4                                     | 249   | $310 \pm 60$                                      |

\*Bath temperature calculated from pressure, with estimated uncertainty of 5%

<sup>†</sup>Predicted values based on equation of state data in [2]

<sup>‡</sup>Uncertainties due to temperature uncertainty

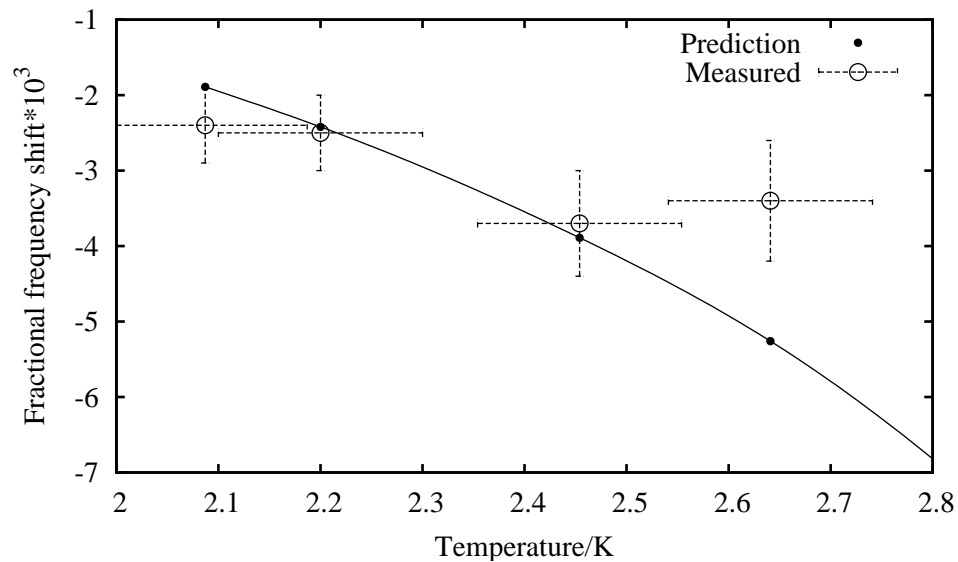


Figure 12.4. Proof-of-concept data for helium density measurements from table 12.2. Predicted values are based on equation-of-state data published by NIST [2] for the specified temperature. The uncertainties in the predictions reflect the uncertainties in the temperature. The data point at 4.2 K is off scale to the bottom right.

## Bibliography

- [1] T. Waits. “Step right up.” In *Small Change*, Elektra/Asylum Records (1976). Recording number 960612-2, compact disk, track 2.
- [2] D. G. Friend. *NIST Thermophysical Properties of Pure Fluids Database, NIST Standard Reference Databases*, volume 12. Gaithersburg, MD: U.S. Department of Commerce (1992). PC software version 3.1.
- [3] G. Ahlers. “Effect of the gravitational field on the superfluid transition in He<sup>4</sup>.” *Physical Review*, **171**(1):275–282 (1968).
- [4] J. A. Lipa, D. R. Swanson, J. A. Nissen, T. C. P. Chui, and U. E. Israelsson. “Heat capacity and thermal relaxation of bulk helium very near the lambda point.” *Physical Review Letters*, **76**(6):944–947 (1996).
- [5] J. A. Lipa, D. R. Swanson, J. A. Nissen, Z. K. Geng, P. R. Williamson, D. A. Stricker, T. C. P. Chui, U. E. Israelson, and M. Larson. “Specific heat of helium confined to a 57 – μm planar geometry near the lambda point.” *Physical Review Letters*, **84**(21):4894–4897 (2000).
- [6] W. Jiang, D. M. Strayer, N.-C. Yeh, J. Huynh, N. Asplund, J. Gatewood, and M. J. Lysek. “Integration of high-resolution frequency control and thermometry for high-precision measurements of physical properties of helium.” *Japan Society of Microgravity Application Journal*, **15 Supp. II**:157 (1999).
- [7] N.-C. Yeh, W. Jiang, and D. M. Strayer. “Application of high-resolution frequency measurements to studies of critical phenomena in helium.” *Japan Society of Microgravity Application Journal*, **15 Supp. II**:136 (1999).
- [8] N.-C. Yeh, W. Jiang, D. M. Strayer, and N. N. Asplund. “Precise measurements of the density and critical phenomena near the phase transitions in helium using high-Q niobium microwave cavities.” *Czech Journal of Physics*, **46**(Suppl. S3) (1996).
- [9] N.-C. Yeh, D. M. Strayer, V. L. Anderson, and N. Asplund. “Superconducting-Cavity-Stabilized Oscillators (scso) for precise frequency measurements.” *Physica B*, **280**:557–558 (2000).
- [10] E. D. Adams. “High-resolution capacitive pressure gauges.” *Reviews of Scientific Instruments*, **64**:601–611 (1993). <http://link.aip.org/link/?RSI/64/601/1>.
- [11] A. P. Müller, C. R. Tilford, and J. H. Hendricks. “A low differential-pressure primary standard for the range 1 Pa to 13 kPa.” *Metrologia*, **42**(6):S187–S192 (2005). <http://stacks.iop.org/0026-1394/42/S187>.
- [12] M. P. White and D. Gagan. “Direct measurements of the dielectric virial coefficients of <sup>4</sup>He between 3 K and 18 K.” *Metrologia*, **29**:37–57 (1992).
- [13] P. J. Mohr and B. N. Taylor. “CODATA recommended values of the fundamental physical constants: 2002.” *Reviews of Modern Physics*, **77**:1–107 (2005). <http://link.aps.org/abstract/RMP/v77/p1>.

- [14] E. F. May, L. Pitre, J. B. Mehl, M. R. Moldover, and J. W. Schmidt. “Quasi-spherical cavity resonators for metrology based on the relative dielectric permittivity of gases.” *Reviews of Scientific Instruments*, **75**:3307–3317 (2004). <http://link.aip.org/link/?RSI/75/3307/1>.
- [15] J. A. Stone and A. Stejskal. “Using helium as a standard of refractive index: Correcting errors in a gas refractometer.” *Metrologia*, **41**:189–197 (2004). <http://www.iop.org/EJ/abstract/0026-1394/41/3/012>.

Don't adventures ever have an end? I suppose not. Someone else always has to carry on the story.

---

J. R. R. Tolkien, *The Lord of the Rings*\*

## Chapter 13

### Future Work and Conclusions

**M**UCH work remains on this project. To date we have proven the feasibility of using our superconducting cavity resonator system for precise frequency measurements and density measurement of helium gas. Although we have only limited scientific data to this point, the hardware has been built and procedures established to allow future researchers to complete the experiment. In this final chapter of part II, we lay out the roadmap for the continuation of the project and summarize the work already accomplished.

#### 13.1 Frequency Stability Measurements

After making infrastructure improvements to the laboratory and purchasing an additional microwave filter, we are near the point of resuming frequency stability measurements.

#### 13.2 Gas-Phase Measurements

##### 13.2.1 Unsaturated Vapor

After installing a pressure sensor, we can begin equation of state measurements of unsaturated helium-4 gas. The measurements will be done along isochores (constant volume/density lines) in the  $(p, T, \rho)$  phase space over a predetermined temperature range (for example, starting at 5 K and going down to 1.7 K in increments of 0.1 K). First, the resonance frequency of the empty cavity would be measured as a function of temperature to provide a baseline for the frequency

---

\*Reference [1]

shift measurements. After this calibration, each run would begin at the maximum temperature by adding a set pressure of helium gas through the fill line. After filling, the low-temperature valve would be closed, fixing the amount of gas in the sample space. The system will take some time to equilibrate at each temperature set point. This settling can be observed by monitoring the pressure and cavity frequency and waiting for them to become constant.

With the system in equilibrium, the pressure and temperature are recorded and the cavity resonance frequency is found using transmission spectroscopy (see section 9.3.1). Spectroscopy allows frequency determination with fractional uncertainty of about  $1/(Q\sqrt{n})$ , where  $Q$  is the quality factor of the cavity (typically,  $10^8$  or higher) and  $n$  is the number of data points in the spectrum (typically,  $n \sim 30$ ); the actual uncertainty in  $f$  is determined by the fitting statistics. If higher precision is required, the phase-locked loop technique (see section 8.2.3) may be used (after estimating the resonance frequency by spectroscopy) to determine the frequency with fractional uncertainties of  $1/(Q \times 10^5)$  or better, limited by the frequency stability. After the measurement of  $p$ ,  $T$  and  $f$ , the temperature is decreased to the next set point and the process repeated. The temperature may be decreased until the helium approaches saturation. We will continue taking data under saturated conditions (see the next section), but the saturated data must be separated from the unsaturated data before the equation-of-state analysis. We can determine whether the system is saturated or not by comparing the temperature and pressure with already published vapor curve data [2].

The advantage of performing the measurements under fixed-volume conditions is that it allows us to empirically determine the gravity-induced barometric and dead-space corrections to the frequency shift (see section 12.2). Because the volume and number of atoms is fixed, the average density of gas in the system is independent of pressure and temperature. This should imply that the resonance frequency of the cavity would be independent of temperature, after accounting for thermal expansion (equation (8.7)) and the temperature dependence of the penetration depth (equation (8.8)). The gravitational acceleration,  $g$ , always appears in the correction terms as the energy ratio  $mgh/k_B T$  (where  $m$  is the mass of the helium atom,  $k_B$  is Boltzmann's constant, and  $h$  is some length parameter) so any residual temperature dependence in the frequency should be the result of these gravity effects. The relation  $f(T)$  for fixed density should give us this correction.

After making the appropriate corrections to the resonance frequency data, we can convert the frequency data into density ( $\rho$ ) data (see section 12.1). Before equation-of-state analysis, the data

must be sorted into isotherms (constant temperature curves). Then, for each value of  $T$  we can fit the  $(p, \rho)$  data to the virial equation (11.2):

$$p = \rho RT (1 + \rho B + \rho^2 C + \dots),$$

and determine the value of the virial coefficients  $B(T)$  and  $C(T)$  for that specific  $T$ .

### 13.2.2 Saturated Vapor Curve

Eventually as the temperature is decreased in the measurements above, the helium will saturate. At this point the fixed-density assumption is no longer valid because liquid will begin condensing in the sample space. Because of the presence of liquid in the system, the form of the gravity correction must be modified in the saturated case compared to the unsaturated case. For the unsaturated gas, the gravity correction to the density yields the average density over the entire sample volume. For the saturated case, we do not want the average density but the density of the vapor at the liquid-gas interface. This requires knowing the height of the interface  $z$  in relation to the cavity.

We will measure  $z$  using a capacitive liquid level sensor. The sensor is a cylindrical coaxial capacitor mounted vertically and connected to the sample space, adjacent to it. As the liquid helium level rises within the sensor, the capacitance  $C$  of the sensor increases linearly with the liquid height because the dielectric constant of the denser liquid is higher than the dielectric constant of the gas (by the Clausius-Mossotti relation, equation (11.3)). The capacitance of the sensor is measured using a tunnel diode oscillator circuit; the oscillation frequency of the circuit is proportional to  $C^{-1/2}$ . The absolute uncertainty in  $z$  is about 100  $\mu\text{m}$  corresponding to uncertainty in the position of the sensor relative to the superconducting cavity. The corresponding relative uncertainty is one part per thousand. In a sense, the liquid level sensor is a low-resolution, low-frequency version of our cavity resonator.

The value of  $z$  can then be used to calculate the density at the position of the liquid-gas interface:

$$\rho(z) = \rho_0 \exp(-m g z / k_B T),$$

where  $\rho_0$  is the value of the density at the bottom of the cavity (found from the frequency via equation (12.16)) and  $z$  is measured relative to the bottom of the cavity and will be negative

(interface below the cavity). The part per thousand uncertainty in  $z$  corresponds to parts in  $10^7$  uncertainty in  $\rho(z)$ .

With the value of  $\rho(z)$ , we will have a complete set of  $(p, T, \rho)$  data for the saturated vapor phase of helium. We can then compare this with other experimental data, such as the curves given in Refs. [2; 3] and theoretical models, such as Ref. [4].

### 13.3 Conclusions

Throughout the course of this work we have built hardware and demonstrated procedures for the characterization of superconducting cavity resonators and shown the feasibility of using our superconducting cavity for precise equation of state measurements of helium-4 gas.

By using the phase-locked loop technique we have demonstrated parts in  $10^{12}$  frequency stability and anticipate an ultimate frequency stability of parts in  $10^{15}$  or better. We have also demonstrated a novel dual-mode locking technique that should allow common-mode noise rejection. We believe our frequency stability is limited by environmental noise sources in the laboratory such as acoustic noise and temperature drifts; we have taken steps to reduce these effects, but have not confirmed the improvements.

In addition to using our superconducting cavity as a frequency reference, we can use the cavity to precisely measure the dielectric constant of helium-4 gas to parts in  $10^9$  uncertainty and, therefore, the density also to parts in  $10^9$ . We have performed a basic proof-of-concept measurement to demonstrate the relationship between cavity frequency and density.

Further work on this project awaits new funding. With new money, the measurements described above can begin immediately and could probably be completed in 12–15 months.

Lastly, the author thanks all those who have helped him on this experiment, particularly Dr. Donald Strayer and Kristjan Stone. The work was directed by Professor Nai-Chang Yeh. Much of the experimental apparatus was built by Nils Asplund. Funding was provided by NASA, with special thanks going to the Graduate Student Researchers Program for supporting the author.

## Bibliography

- [1] J. R. R. Tolkien. *The Lord of the Rings*. Boston: Houghton, one-volume edition (1991).
- [2] D. G. Friend. *NIST Thermophysical Properties of Pure Fluids Database, NIST Standard Reference Databases*, volume 12. Gaithersburg, MD: U.S. Department of Commerce (1992). PC software version 3.1.
- [3] H. Preston-Thomas. "The International Temperature Scale of 1990 (ITS-90)." *Metrologia*, 27:3–10 (1990).
- [4] J. J. Hurly and J. B. Mehl. "<sup>4</sup>He thermophysical properties: New ab initio calculations." *Journal of Research of the National Institute of Standards and Technology*, 112(2):75–94 (2007).  
<http://nvl.nist.gov/pub/nistpubs/jres/112/2/cnt112-2.htm>.

## Appendices to Part II

## Appendix D

### Miscellaneous Constructions for the Helium Experiment

#### D.1 Low Temperature Vacuum Feedthroughs

Minimization of the thermal load to the sample is one of the major design requirements of the helium experiment. To thoroughly heat sink the control and readout wires we pass the wires through the liquid helium bath. This requires the wires to pass through a cryogenically compatible vacuum feedthrough at the top flange of the probe (see figure 9.4).

Our feedthrough design is depicted in figure D.1. The body of the feedthrough is a brass cylinder with an indium flange and bolt circle at one end. The wires (Lakeshore Quad-Twist 36-AWG, Formvar-insulated phosphor bronze) pass through the center of the body. The liquid-helium end of the feedthrough is sealed with Stycast 2850 epoxy.

To construct the feedthroughs, we first machine and clean the body piece. Next we cut the wires to lengths of about 60 cm, using  $\sim 50\%$  more wires than necessary to allow for future additional sensors and to compensate for potential wire failures. The wires are positioned so that approximately one third of the length is on the helium side of the body. The wires are then temporarily taped in place at the vacuum side of the body using electrical tape.

To provide a form for the epoxy, we cut the bulb off of a polyethylene pipette (approximately 2 cm in length and 1 cm in diameter) and pierce a hole in the end bulb. We thread the helium end of the wires through the bulb with the open end of the bulb facing the long end of the brass body. The pipette bulb is pushed along the wires to the body piece, leaving an approximately 5 mm gap between the bulb and the end of the brass body tube. We secure the bulb by taping it to the wires. We suspend the entire assembly on the end of a piece of pipe, with the bulb facing down and the helium end of the wires passing through the pipe.

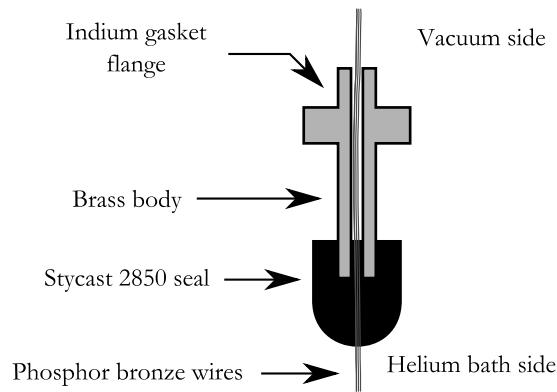


Figure D.1. Cryogenic vacuum feedthrough (not to scale)

Next we mix and outgas the epoxy. Using a pipette, we fill the feedthrough through the center hole, adding enough epoxy to fill the bulb. We move the assembly to a vacuum oven and then pump on it for about 5 minutes to further outgas the epoxy; the pump must be throttled to prevent the epoxy from foaming too quickly and spilling out of the feedthrough. After the gas bubbles dissipate, we bake the feedthrough at 60 °C for 6–8 hours to cure the epoxy.

After the baking is finished, but while the assembly is still warm, we remove the plastic bulb by cutting it and peeling it away from the epoxy; it removes easily. The epoxy must be inspected for defects and may need sanded or cut to remove any excess, particularly near the indium flange or the bolt circle.

Our feedthroughs constructed with this technique have proven to be robust to many vacuum and thermal cycles. The primary mode of failure is by breakage of the wires from mechanical stress, particularly where they enter the epoxy (hence the use of excess wires in the construction). The mechanical stress can be minimized by securing the wires in the assembled probe to prevent excess motion. An additional modification we made to later designs was to add an  $\sim 2$  cm section of shrink tubing around the bundle of wires at the point where they enter the epoxy. The shrink tubing provides some strain relief and alleviates the wire breakage, but these new feedthroughs fail more frequently by cracks in the epoxy after several thermal cycles, perhaps because of differential thermal expansion.

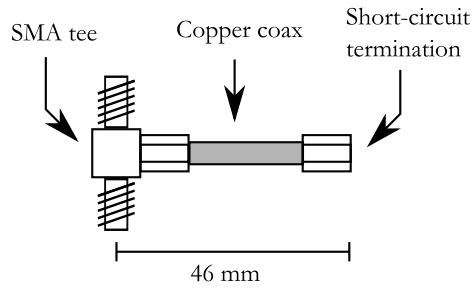


Figure D.2. Drawing of the quarter-wave heat sink tee (not to scale)

## D.2 Quarter-Wavelength Microwave Heat Sinks

One of the major difficulties in the helium experiment is the heat sinking of the microwave signal coaxes. Our need for low dissipation in the microwave system (to improve the signal-to-noise ratio for spectroscopy) necessitated the use of microwave signal coaxes with solid copper inner conductors. However, the gain in electrical conductivity we achieved by using copper carries along the burden of large thermal conductivity. Without heat sinking, our two copper coaxes would conduct approximately 100 mW into the cavity (based on thermal conductivity numbers from [1]).

In order to heat sink the inner conductors of the microwave signal coaxes, we insert tees attached to short-circuited stubs near the bottom of the coax lines. The completed stub consists of a section of 0.141" O.D. rigid copper coaxial cable between a short-circuit termination and a tee coupling, as shown in figure D.2. The transmission coefficient through such an assembly is equal to  $\sin^2(2\pi L/\lambda)$ , where  $L$  is the length of the tee and  $\lambda$  is the wavelength of the radiation. To maximize the microwave signal transmitted through the stubs, the length of the coax was chosen so that the entire assembly was nearly an odd number of quarter wavelengths for both nominal frequencies of interest (14.1 GHz and 20.6 GHz). For our coaxes (filled with polyethylene with a dielectric constant of 2.26), a length of 46 mm gives transmission coefficients of greater than 99% for both modes (see table D.1 and figure D.3). Because the transmission coefficient is a slowly varying function with respect to length, exact lengths and frequencies are not critical. The stubs are inserted into the coaxial lines near the 4 K stage. Several gold-plated copper wires are soldered to the termination and screwed to the 4 K stage to provide thermal anchoring.

Another method of heat sinking the signal coaxes considered in a previous design was the use

Table D.1. Lengths corresponding to transmission maxima for quarter-wave heatsink stubs at the two frequencies of interest, 14.1 GHz and 20.6 GHz

| Number of wavelengths | $L_{14.1}/\text{mm}$ | $L_{20.6}/\text{mm}$ |
|-----------------------|----------------------|----------------------|
| 1/4                   | 3.54                 | 2.42                 |
| 3/4                   | 10.61                | 7.27                 |
| 5/4                   | 17.69                | 12.11                |
| 7/4                   | 24.77                | 16.95                |
| 9/4                   | 31.84                | 21.80                |
| 11/4                  | 38.92                | 26.64                |
| 13/4                  | 46.00*               | 31.48                |
| 15/4                  | 53.07                | 36.33                |
| 17/4                  | 60.15                | 41.17                |
| 19/4                  | 67.23                | 46.01*               |

\*Chosen length

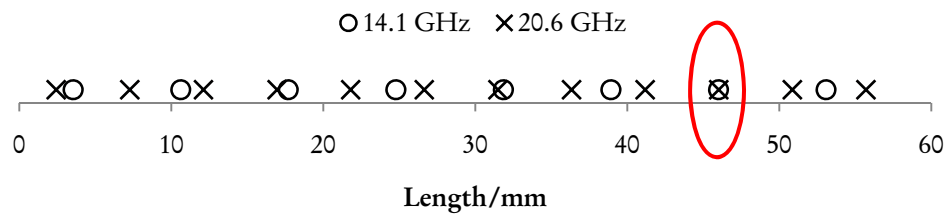


Figure D.3. Graphical representation of table D.1: Lengths of transmission maxima for polyethylene-filled coaxial short-circuit tees at frequencies of 14.1 GHz (circles) and 20.6 GHz (crosses). Possible lengths of the stubs are where the symbols overlap, e.g., at 46 mm.

of short waveguide sections as heat sinks. Because the waveguides contain no interior parts, they can be thermally anchored more easily. This design was attempted by a previous researcher, but the waveguide sections had transmission losses of approximately 20 dB, which we deemed to be too high to be a workable solution.

### D.3 Superconducting Coax Loops

In order to reduce heat conduction between the 4 K stage of the probe and the sample stage, superconducting niobium wire is used for the inner conductor in the low-temperature section of the signal coaxes. The following procedure was devised to construct the most robust signal loops at the end of the coaxes which enters the superconducting cavity. Figure D.4 shows the finished loop.

1. Remove the existing center conductor from a length of 0.085" O.D. stainless steel coax.
2. Solder the outer piece of a male SMA connector to the coax
3. Measure out a piece of 0.020" O.D. niobium wire with length equal to the coax length plus about 1/2".
4. Insert the niobium into the coax with the end near the connector (connector end) flush with the dielectric. Mark the wire where it exits the opposite end (loop end) of the coax.
5. Remove the wire and flatten the loop end of the wire up to the mark made in the previous step. The flattening can be done with a hammer and anvil. (A ball hammer works particularly well). When finished, the flattened part should be approximately 1/16" wide.
6. Reinsert the wire into the coax, leaving about 1/4" protruding through the connector.
7. Prepare the pin for the connector by cutting off a portion of the sheath.
8. Spot weld the pin onto the wire.
9. Push the wire back into the connector to the proper depth.
10. File flat a section of the outer conductor about 1/8" long near the loop to make room for the wire.

11. Bend a U-shaped loop into the flattened section of the wire. The depth of the loop should be about 1/4" and the width comparable to the coax. Trim any excess wire, leaving about 1/8" to overlap the coax.
12. Spot weld the flattened part of the wire to the outer conductor of the coax.
13. With a file, smooth down the weld on the loop so that the loop will pass easily into the sample can.

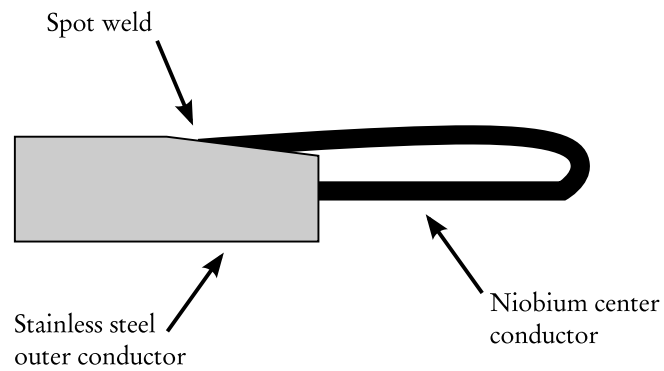


Figure D.4. Construction of superconducting signal loops.

## Bibliography

- [1] *Temperature Measurement and Control Catalog*. Lakeshore Cryogenics, Westerville, OH, ca. 2000.

I never saw any whole, W-H-O-L-E. I saw plenty of holes, H-O-L-E-S. But I didn't really worry. I would get an idea for a scene and shoot it, get another idea and shoot that. I didn't know how they would relate.

---

David Lynch, in an interview with *The New York Times*\*

## Chapter 14

### Concluding Remarks

**F**LUIDS are often the first systems studied in an introductory thermodynamics class (think of ideal gases and basic phase transitions, for example), but the topic is dropped soon after in favor of more tractable systems. This leaves many students (and people who used to be students) with the incorrect impression that fluid thermodynamics is a solved problem when, in fact, the opposite is true. We do not teach fluid-phase physics because it is still largely unsolved except in a few limiting cases (dilute gasses or laminar flow, for example). This is unfortunate because the fluid phases are rich with phenomena.

In this work we have presented experiments on two aspects of fluid-phase physics. In part I, we presented a investigation of the still poorly understood process of boiling. We approached the topic by varying the effective gravity measuring the change in heat transport across the boiling liquid. We discovered that the previously assumed power-law dependence of the heat transfer on gravity is incorrect and that a linear dependence describes our experimental data. We also found behavior in the high-heat-flux regime that differs from the canonical picture of boiling.

In part II, we discussed progress on an experiment to measure the equation of state for helium-4 gas at low temperatures. The experiment leverages the high frequency stability and resolution of superconducting cavities to measure the dielectric constant and density of helium gas to parts in  $10^9$  uncertainty. These measurement will allow us to also calculate the virial coefficients of the gas, which we can compare with theoretical models of the helium interaction potentials. An additional measurement that may be possible is the determination of Boltzmann's constant to parts in  $10^8$ . These measurements could begin in short order once new funding is acquired.

---

\*Reference [1]

Thanks go to Professor Nai-Chang Yeh and her research group members past and present: Andy Fu, Ching-Tzu Chen, Andrew Beyer, Cameron Hughes, Marcus Teague, Pierre Seneor, Slobodan Mitrovic, Jason Briceño, Kristjan Stone, Michael Cheung, Michael Turk, Scott Medling, Janet Sheung, Huan Yang, Sheila Stone, Loly Ekmekjian, and the incorrigible Nils Asplund. Special thanks also go to Dr. Donald Strayer of the Jet Propulsion Laboratory for his guidance and helping hand. Lastly, the author thanks NASA for funding the work presented here.

## Bibliography

- [1] D. Lim. "David Lynch returns: Expect moody conditions, with surreal gusts." *New York Times* (2006).  
<http://www.nytimes.com/2006/10/01/movies/01lim.html?ex=1317355200&en=fb5663bd7dc96d11&ei=5088&partner=rssnyt&emc=rss>. Published online, 1 Oct. 2006.